

Cenozoic Tectonic and Geomorphic Evolution of the Red River Region, Yunnan Province, China

by

Lindsay M. Schoenbohm

B.S. Geology
Carleton College, Northfield, MN, 1997

SUBMITTED TO THE DEPARTMENT OF EARTH, ATMOSPHERIC, AND PLANETARY SCIENCES IN PARTIAL FULFILLMENT OF THE REQUIREMENTS FOR THE DEGREE OF

DOCTOR OF PHILOSOPHY
AT THE
MASSACHUSETTS INSTITUTE OF TECHNOLOGY

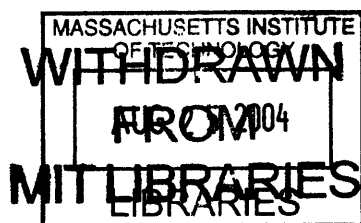
FEBRUARY 2004

© 2004 Massachusetts Institute of Technology. All rights reserved.

Signature of Author: _____
Department of Earth, Atmospheric and Planetary Sciences
January 15, 2004

Certified by: _____
B. Clark Burchfiel
Schlumberger Professor of Geology
Thesis Supervisor

Accepted by: _____
Maria T. Zuber
E.A. Griswold Professor of Geophysics and Planetary Science
Department Head



LINDGREN

Cenozoic Tectonic and Geomorphic Evolution of the Red River Region, Yunnan Province, China

by

Lindsay Schoenbohm

Submitted to the Department of Earth, Atmospheric and
Planetary Sciences on January 15th, 2004,
in Partial Fulfillment of the Requirements for the Degree of
Doctor of Philosophy in Geology

ABSTRACT

This thesis outlines the Cenozoic development of the Red River region, exploring regional landscape evolution and tectonic accommodation of the India-Eurasia collision, focusing on the Oligo-Miocene, left-lateral Ailao Shan shear zone and the active, right-lateral Red River fault on the northeast margin of the shear zone, along which the Red River has incised a deep valley. Oligo-Miocene fluvial and alluvial conglomerates in the valley record shear zone unroofing: pervasive, syn-depositional shortening indicates transpressional exhumation. A low-relief landscape, developed in Late Miocene time, was probably uplifted in Pliocene time, triggering the incision of the Red River and isolating the low-relief landscape from modern base level. On the basis of stratigraphic data, river incision began in Pliocene time or later. Tributary longitudinal profiles indicate two-phase incision, the result of pulsed plateau growth or trunk channel adjustments to changing climate conditions. Paleo-Red River reconstruction indicates ~1400 m river incision, 1400-1500 m surface uplift and 750 m vertical displacement across the northern part of the Red River fault. Minimum right-lateral displacement on the fault is 40 km, 15-16 km of which predates river incision, plateau growth and development of other regional fault systems. Long term average slip-rate is a minimum of ~5 mm/yr. Rotation of a crustal fragment around the eastern Himalayan syntaxis, bounded on the east by the Xianshuihe-Xiaojiang fault system, causes deflection of the Red River fault, accommodated by distributed shear along strike of the Xianshuihe-Xiaojiang fault system. The Red River fault has decreased in regional importance since the initiation of the Xianshuihe-Xiaojiang fault system during growth of the southeast plateau margin. Cosmogenic ²⁶Al and ¹⁰Be basin-wide erosion rate and burial ages indicate a background incision rate of ~0.05 to 0.10 mm/a, lower than the long-term incision rate minimum of ~0.26 mm/a. Cosmogenically-determined incision rate approximately doubles to ~0.20 mm/a in the region of maximum dip-slip displacement on the Red River fault. This thesis also develops a new cosmogenic tool for quantitative landscape analysis: using depth dependence data for multiple cosmogenic nuclides from a single site to constrain an erosion history. This method is applied in the Dry Valleys region of Antarctica.

Thesis supervisor: Dr. B. Clark Burchfiel
Title: Schlumberger Professor of Geology

Biographical Notes

I was born on June 21st, 1976, in Lafayette, Indiana, to Richard Beyer Schoenbohm and Leah Ruth Schoenbohm. My family moved to Appleton, Wisconsin in 1980, where I attended public schools. My sister, Laurel Jean Schoenbohm, was born in 1982. I graduated from Appleton High School East in 1994, and was the valedictorian of my class. I attended Carleton College in Northfield, Minnesota, where I majored in Geology. I was National Merit Scholar, and received the Duncan Stewart award from the Geology faculty at Carleton College. I graduated *magna cum laude* in 1997, with honors distinction for my senior thesis research on the Heart Mountain Fault of northwest Wyoming. I worked as a lab technician at the Large Lakes Observatory in Duluth, Minnesota for one year.

I arrived at MIT to begin work on this PhD in the fall of 1998. I was awarded the Robert Schrock fellowship during my first year at MIT. I have been a teaching assistant once for Field Geology, twice for Introduction to Geology, taught by both Dr. John Southard and Dr. Sam Bowring, and twice for Structural Geology, taught by my advisor, Dr. Clark Burchfiel. The remainder of my support while at MIT has come from NSF funded research assistantships.

I move on from MIT to a postdoctoral position at the Institut für Geowissenschaften at Potsdam Universität in Germany, where I will conduct research in Argentina and western China, in collaboration with Dr. Manfred Strecker.

Acknowledgements

So many have contributed to the successful completion of my PhD at MIT that it is impossible to thank everyone, and I apologize for any oversights here.

First, I would like to thank the members of my committee, particularly my advisor, Clark Burchfiel, for guiding and supporting my field research, and for allowing me the freedom to pursue my interests in landscape evolution and cosmogenic dating. Thanks also to Kelin Whipple for serving as an unofficial advisor, folding me in with the rest of his geomorphology group. I've learned from Darryl Granger (Purdue University) about much more than cosmogenic dating, and was glad to have him as a member of my thesis committee. The same goes for Mark Kurz (WHOI), who has been a valued colleague and friend since my embarking on a second generals project with him. Thanks also to Wiki Royden and Kip Hodges; their comments have greatly improved this thesis. I'd like to express my thanks to the other faculty I've interacted with over the years, particularly John Southard, Sam Bowring, Dave Mohrig and Rob van der Hilst at MIT, Peter Clift at WHOI and John Geissman at the University of New Mexico.

A number of people put me on the path to MIT, beginning with Connie Roop in an 8th grade earth science class. Her enthusiasm for geology and pretty much everything else is contagious. At Carleton, I was further inspired by professors Mary Savina, Bereket Haileab, Dave Bice and especially Julie Maxson. I was privileged to share my time there with a number of fantastic students, including Alison Anders, Dave Bitner, Carrie Elliot, Noah Finnegan, Karen (Bobbitt) Gran, Brian Klawiter, Dave Mitchell, Sara (Gran) Mitchell, Anders Noreen, George Oliver, and Kati Szramek, many of whom are now pursuing PhD's at other institutions. Ed Beutner at Franklin and Marshall College was also an important early influence, as the primary advisor on my senior thesis.

At MIT, fellow students have been incredibly important to my success and to my general happiness. The adage that you learn as much from other students as from your classes or professors is certainly true with this smart, cohesive group. Bridget Bergquist, Amy Draut, Steve DiBenedetto, Astri Kvassness, Amy McKnight and John Thurmond, the "frobenius" crew, got me through differential equations and beyond. I'm grateful for a strong group of geology women who have inspired and supported me over the years, including: Julie Baldwin, Marin Clark, Lindy Elkins, Becky Flowers, Jenny Matzel, Kirsten Nicolaysen, Rebecca Saltzer, and Karen Viskupic. Special thanks also to the other students working on the southeast margin: Eric Kirby, Marin Clark, Sinan Akciz, Christopher Studnicki-Gizbert and Will Ouimet. Sinan and Christopher read through last-minute drafts of this thesis, and I thank them for that. Thanks to all the other students I've interacted with over the years at MIT, including Jeremy Boyce, Simon Brocklehurst, Chris Carr, Ben Crosby, Greg Gerbi, Marc Hesse, Jose Hurtado, Joel Johnson, Greg Lawson, Maureen Long, Bill Lyons, Kate Ruhl, Taylor Schildgen, Blair Schoene, Noah Snyder, Jim VanOrman, Arthur White, and Cameron Wobus. Thanks to a number of non-students as well, including Daniel Sheehan, and my heat-tolerant officemates, Jim Crowley and Jahandar Ramezani.

I spent fully nine months of the last five and a half years in China and I owe an incredible debt to my colleagues, both Chinese and American, who made these five field seasons possible. Chen Liangzhong was our primary colleague in China, and become an important mentor and a good friend. Yin Jiyun accompanied us for one season and I appreciate his expertise and generosity as well. Our excellent driver, Koh Jianle, kept us safe through all five field seasons without a single accident and only one close call, an exceptional record in China. But more important, Lao Koh was always ready to laugh, and to point out “Neogene” rocks as we drove by. I spent one field season in Yunnan with Marin Clark and was incredibly enriched by the experience. I thank her for that. Finally, I would like to thank my field assistants, Josh Feinberg and Michael Stewart. I cannot imagine two better companions: both are among the most generous, considerate and hilarious people I know.

Finally, I wish to thank my closest friends and family, including Bridget Bergquist, Simon Brocklehurst, Greg Hoke, Kate Jesdale, Maren Peterson, Noah Snyder, and Michael Stewart. My many aunts and uncles, Grammy Rueger and Grandma and Grandpa Schoenbohm have always been supportive and understanding throughout my long education. Finally, most important of all, my deepest thanks to my sister, Laurel, and to my parents, Richard and Leah Schoenbohm. My parents have made this all possible.

Lindsay Schoenbohm
January 15th, 2004

*To my father,
for his love of science*

*To my mother,
who doesn't believe in plate tectonics*

Table of Contents

Title Page.....	1
Abstract.....	3
Biographical Notes.....	4
Acknowledgements.....	5
Dedication.....	7
Table of Contents.....	8
Chapter 1: Introduction.....	9
Chapter 2: Transpressional exhumation of the Ailao Shan shear zone as recorded by Cenozoic sedimentary rocks, Yunnan Province, China.....	19
Chapter 3: The Red River fault and the active tectonics of the southeast margin of the Tibetan Plateau.....	69
Chapter 4: Geomorphic constraints on surface uplift, exhumation, and plateau growth in the Red River region, Yunnan Province, China.....	119
Chapter 5: Cosmogenically determined incision rates along the Red River, Yunnan Province, China.....	185
Chapter 6: Depth dependence of cosmogenic ^3He and ^{21}Ne in Antarctic sandstone bedrock: implications for exposure and erosion history.....	201
Chapter 7: Conclusion.....	231

Introduction

Motivation

The India-Eurasia continental collision is the most spectacular example of active mountain building, plateau development and continental-scale strike-slip faulting on Earth, with deformation extending well beyond the Himalaya and the Tibetan plateau, deep into the Asian continent. Models for development of the collision zone tend to fall under two categories: those that emphasize the lateral extrusion of relatively undeformed crustal blocks with strain localized along major shear zones, and those that emphasize crustal thickening, plateau growth and diffuse deformation. These models, while not mutually exclusive, do represent fundamentally different views of the nature of continental deformation. Although satellite image interpretation, geodynamic modeling and reconnaissance field studies have significantly advanced our understanding of Asian tectonics and of controls on crustal deformation, resolution of these opposing viewpoints also depends on detailed knowledge of the temporal and spatial patterns of deformation in all regions of the collision zone.

This thesis focuses on a critically important area within the India-Eurasia collision zone, the Red River region of Yunnan Province, China, situated on the southeast margin of the Tibetan plateau. This region has been complexly deformed as a result of the Cenozoic collision. The Ailao Shan shear zone, which guides the course of the Red River, is an Oligo-Miocene, ductile, left-lateral strike-slip shear zone that is interpreted by many researchers to have played a role in accommodating lateral extrusion of Indochina in mid-Cenozoic time (Tapponnier et al., 1990; Leloup et al., 1995; Harrison et al., 1996; Leloup et al., 2001; Gilley et al., 2003). The Red River fault, approximately coincident with the northeast edge of the shear zone, is an active, right-lateral structure which has also been interpreted as a younger, extrusion-related structure (Allen et al., 1984; Leloup et al., 1995; Replumaz et al., 2001). Other studies, however, emphasize additional active faults which affect the region, including the Xianshuihe-Xiaojiang fault system, which accommodates rotation of a crustal fragment around the eastern Himalayan syntaxis and appears to deflect the Red River fault where the two fault systems intersect (Allen et al., 1991; Wang et al., 1998). In addition to the surface expression of strike-slip faulting, the southeastern margin of the Tibetan plateau has experienced crustal thickening and corresponding surface uplift in Late Cenozoic time, possibly a result of the flow of weak lower crust from beneath Tibet

into this region (Royden, 1996; Royden et al., 1997; Clark and Royden, 2000; Clark, 2003). These competing processes have shaped the tectonic and landscape development of the Red River region.

The following chapters of this thesis formulate a comprehensive, integrated history of both the tectonic and geomorphic development of the Red River region, based on newly mapped structural relationships and quantitative landscape analysis. Results are interpreted in the context of two questions related to the nature of continental deformation: (1) the role of strike-slip shear zones in accommodating continental collision, and (2) the topographic development of the southeastern plateau margin. This study also seeks to develop the tools of quantitative landscape analysis, particularly the use of paleo-river channels to reconstruct elevated landscapes, and cosmogenic dating techniques to constrain river incision rates and to assess the erosional history of a region.

Role of strike-slip shear zones in accommodating the India-Eurasia collision

The importance of major strike-slip faults across the entire collision zone in Asia was first promoted by Molnar and Tapponnier (1975) on the basis of seismicity and Landsat imagery, opening debate on questions of how convergence was partitioned between crustal thickening and lateral extrusion, and whether deformation was rigid or diffuse within the intervening crustal blocks. Tapponnier et al. (1982) published an influential experiment in which the collision was modeled by the convergence of a rigid India with a deformable Asia, represented by layered plasticine. This analogue model, to a first order, produced a strong resemblance to the modern Asian structural configuration, although it was vertically confined and so could not incorporate the effects of crustal thickening. On this basis, Tapponnier et al., (1982; 1986) proposed that in the early stages of the collision, approximately during formation of the South China Sea from 32 to 17 Ma, Indochina was extruded to the southeast (present coordinates), bounded to the northeast by the Ailao Shan shear zone. Deformation migrated north in Miocene and Pliocene time, when, according to this model, a crustal block began to extrude, bounded by the left-lateral Altyn Tagh fault in the north and the right-lateral Red River fault to the southwest, partially reactivating and reversing the sense of slip on the older Ailao Shan shear zone.

Chapter 1- Introduction

A series of papers elaborated on the “extrusion model” over the subsequent two decades. Avouac and Tapponnier (1993) and Peltzer and Saucier (1996) published numerical models that emphasized the rigid nature of the intervening crustal blocks, and Peltzer and Saucier (1996) argued that up to 80% of convergence between India and Eurasia could be taken up along major strike-slip faults. Another series of studies focused on the field relationships and geochronology of the major shear zones, including important work on the Ailao Shan shear zone and Red River fault (Schärer et al., 1990; Harrison et al., 1992; Lacassin et al., 1993; Leloup et al., 1993; Leloup and Keinast, 1993; Schärer et al., 1994; Leloup et al., 1995; Harrison et al., 1996; Zhang and Schärer, 1999; Leloup et al., 2001; Replumaz et al., 2001; Gilley et al., 2003). In general, these studies supported the extrusion hypothesis, establishing the Ailao Shan shear zone as an Oligo-Miocene, left-lateral, ductile feature with a probable displacement of several hundred kilometers. It was also confirmed that the Red River fault is an active, or recently active, right-lateral structure, but displacement appears to be less than originally envisioned by the extrusion model (Allen et al., 1984; Leloup et al., 1995; Replumaz et al., 2001). A shortcoming of these studies, however, is a lack of consideration of the way in which the Ailao Shan shear zone and Red River fault interact with other regional geologic features, probably a product of limited field mapping and the underlying assumption that deformation should be concentrated on these major structures.

Despite the popularity of the extrusion model, a number of other authors have argued, from a variety of perspectives, for an interpretation of Asian tectonics in which deformation is diffusely or sometimes continuously distributed. Models in which the Asian lithosphere is treated as a deforming, thin viscous sheet (England and Houseman, 1988; Houseman and England, 1993) find that convergence can be primarily accommodated through crustal thickening, with only minor spreading or rotation of thickened crust around the eastern Himalayan syntaxis. A distinct class of models, discussed further below, take into account rheological variations in crustal behavior with depth (Royden, 1996; Royden et al., 1997; Shen et al., 2001), and also predict distributed deformation, much of which is taken up by flow within a weak crustal layer. Other authors (Cobbold and Davy, 1988; Davy and Cobbold, 1988; Dewey et al., 1989; England and Molnar, 1990) suggest the region east of the eastern syntaxis has been undergoing broad, right-lateral shear and clockwise rotation along left-lateral faults throughout the development of the

collision zone. Wang and Burchfiel (1997) and Wang et al. (1998) document field evidence for widespread contractional deformation in Yunnan overlapping with the period of deformation along the Ailao Shan shear zone, and for modern rotation around the eastern Himalayan syntaxis, bounded by the Xianshuihe-Xiaojiang fault system. Rotation around the syntaxis is confirmed, at least in the short term, by GPS data (King et al., 1997; Chen et al., 2000). In this interpretation, rotation and broadly distributed deformation dominate the structural history of this region, with fault systems and principle stress orientations evolving as the syntaxis migrated from a position southwest to a position northwest of this region (Wang and Burchfiel, 1997; Wang et al., 1998). Thus, although major strike-slip faults clearly play a role in the Cenozoic development of the India-Eurasia collision, the degree of partitioning of convergence between lateral extrusion, rotation and crustal thickening, and spatial and temporal variations in this strain partitioning, remain open and hotly debated topics.

Plateau formation and growth

As the largest elevated landmass on Earth, the Tibetan plateau is profoundly important for Asian tectonics and for Cenozoic climate change (Raymo et al., 1988; Ruddiman and Kutzbach, 1989). A number of theories (partially reviewed in Harrison et al., 1992) for formation of the plateau have been proposed, including under-thrusting of India beneath the entire plateau, continental injection, distributed shortening, and detachment of the mantle lithosphere resulting in buoyant uplift of the plateau. Recently, viscous models with a depth-dependent rheology have successfully reproduced the flat-topped, steep sided morphology of the Tibetan plateau as well as strain patterns observed in geologic and geodetic data (Royden, 1996; Royden et al., 1997; Shen et al., 2001). These models suggest the presence of a weak lower-crustal channel beneath Tibet which flows in response to lateral pressure gradients; as a result, lower crust is driven from beneath Tibet into adjacent regions. Where blocked by strong lithosphere (such as the Sichuan basin), channel flow is impeded, and a steep topographic margin develops in the absence of significant surface shortening (Burchfiel et al. 1995; Clark and Royden, 2000; Kirby et al., 2002; 2003; Clark 2003). However, between the Sichuan basin and the eastern Himalayan syntaxis, relatively unimpeded channel flow is hypothesized to have resulted in crustal thickening and long wave-length uplift of the southeastern margin of the Tibetan plateau (Clark and Royden, 2000; Clark, 2003). Surface uplift in this region has important implications for regional climate

change (e.g. Ruddiman and Kutzbach, 1989), for landscape development and for subsequent structural deformation.

Quantitative tools of landscape analysis: river profiles and cosmogenic dating

The pace of research at the intersection of tectonics and climate-controlled surface processes has accelerated over the last decade as workers have increasingly realized the importance of such interactions in long-term orogenic evolution. Substantial advances in the use of geomorphic features and processes for unraveling tectonic relationships have come about in part because of the availability of digital topographic data and high-resolution satellite imagery, along with appropriate computing and software resources. Analysis of river longitudinal profiles has proven particularly valuable in a number of studies for recording temporal and spatial variations in rock uplift rate (e.g., Whipple and Tucker, 1999; Snyder et al., 2000; Kirby and Whipple, 2001; Whipple and Tucker, 2002; Lague and Davy, 2003; Wobus et al., 2003; Whipple, in press). Advances in quantitative landscape analysis have also come from the refinement of cosmogenic surface exposure dating and from low-temperature thermochronology (e.g., Noller et al., 2000; Burbank and Anderson, 2001). Cosmogenic dating is a particularly powerful tool for constraining the age of landforms, erosion rate, river incision, mass wasting, soil production, paleo-elevation and erosion history.

Structure of the thesis

In general, the Chapters in this thesis progress chronologically through the tectonic and landscape evolution of the Red River Region. They are also grouped by technique, from primarily field mapping in Chapters 2 and 3, to application of river longitudinal profile analysis in Chapter 4, and to cosmogenic dating techniques in Chapters 5 and 6. The conclusion in Chapter 7 draws these observations together to outline a comprehensive history of development of the Red River region in the context of the major topics discussed in the preceding sections.

Chapter 2 explores the exhumation of the Ailao Shan shear zone as recorded by the deposition and deformation of a narrow band of Cenozoic sedimentary rocks along the northeast margin of the shear zone. The core of this chapter is detailed maps produced at two localities within the Cenozoic strata, which establish the unroofing history of the shear zone and the concurrent

Chapter 1- Introduction

structural setting. Structural relationships clearly indicate syn-depositional contraction within the basin, and therefore point to tranpressional exhumation of the shear zone. This is consistent with the regional interpretation by Wang and Burchfiel (1997), who link shortening in the Lanping-Simao fold and thrust belt to the southwest to exhumation of the shear zone, and is inconsistent with models indicating transtensional unroofing of the shear zone (Leloup et al., 1995; Harrison et al., 1996; Leloup et al., 2001, Gilley et al., 2003). Mapped relationships also indicate that at least 30 km left-lateral displacement occurred north of the northern boundary of the shear zone along a parallel fault, and that total displacement along the shear zone may be less than ~190 km since the first exposure of shear zone gneiss, probably in Early Miocene time. The study also shows that if displacement is hundreds of kilometers, it must have occurred on or southwest of the northeast margin of the shear zone. These observations are consistent with regionally distributed deformation. This chapter also suggests links between erosion along the Red River and the spatial and temporal patterns of exhumation.

Chapter 3 focuses on the active tectonics of the southeast margin of the Tibetan plateau, interpreting the Red River fault, Xianshuihe-Xiaojiang fault system and other active faults in the context of new mapping along the Red River fault, and the possible presence of weak lower crust, hypothesized to result from southeast directed flow of material from beneath Tibet (Clark and Royden, 2000). The active fault systems of the southeastern plateau margin accommodate displacement at a high angle to the inferred southeasterly flow direction within the lower crust, suggesting a decoupling of transport directions in the mid to lower crust. This chapter establishes that the Red River fault was active prior to regional surface uplift. The initiation of rotation around the eastern Himalayan syntaxis may be linked to the intrusion of weak lower crust, with the Red River fault becoming less important as the Xianshuihe-Xiaojiang fault system developed.

Chapter 4 examines the landscape morphology of the Red River region, identifying an upland, low-relief landscape continuous with a regional low-relief landscape, which was elevated through growth of the southeastern margin of the Tibetan plateau (Clark, 2003). The Red River, along with the other major rivers of the southeastern plateau margin, has deeply incised the upland landscape. Techniques are developed in this chapter to reconstruct the paleo-drainage

Chapter 1- Introduction

system developed on the upland landscape, which is used to determine the magnitude and distribution of the vertical component of displacement along the Red River fault, and to constrain the total amount of river incision and corresponding surface uplift. Channel profiles are used to define two distinct phases of river incision which could result from pulsed plateau uplift, but likely reflect the interaction of regional climate change and plateau development.

Chapter 5 applies cosmogenic basin-wide erosion rate and burial dating techniques to determine incision rate along the Red River. Results indicate the background incision rate is lower than the long-term average, consistent with tributary longitudinal profile analysis in Chapter 4 which suggests incision rate is decreasing toward the present. Incision rate patterns also correlate with the distribution of vertical displacement along the Red River fault established in Chapter 4.

Chapter 6 further explores cosmogenic dating techniques for constraining landscape evolution, but in a different field setting. Sandstone bedrock cores from the Dry Valleys region of Antarctica are analyzed for cosmogenic ^{21}Ne and ^3He concentrations and combined with previously published ^{26}Al and ^{10}Be data for the same cores (Brown et al, 1992; Brook, 1994). Anomalous depth dependence for the stable nuclides (^{21}Ne and ^3He) in one core suggests a complicated erosion history. Modeling indicates that erosion rates must have been higher in the past, probably 5 times higher prior to ~ 1.3 Ma. A scenario of long exposure at low erosion rates punctuated by rapid removal of material at ~ 1.3 Ma also produces good correspondence between modeled profiles and measured data. These results have implications for the long-term stability of climate and erosion rates in the Dry Valleys region. This study demonstrates for the first time that erosion history can be extracted from a single sampling site, with important applicability to landscape evolution studies.

With the exception of Chapter 5, each of the body chapters of this thesis is written for separate publication. As such, there is some unavoidable overlap among the papers. Chapter 2 will be submitted to *Tectonics* and Chapter 3 to the *Journal of Geophysical Research*. Chapter 4 is in press at *GSA Bulletin*. Chapter 6 will be submitted to *Earth and Planetary Science Letters*.

REFERENCES

- Allen, C.R., Gillespie, A.R., Han Yuan, Sieh, K.E., Zhang Buchun, Zhu Chengnan, 1984, Red River and associated faults, Yunnan Province, China: Quaternary geology, slip rates, and seismic hazard: *Geological Society of America Bulletin*, v. 95, p. 686-700.
- Allen, C.R., Luo, Z., Qian H., Wen X., Zhou H., Huang W., 1991, Field study of a highly active fault zone: the Xianshuihe-Xiaojiang fault of southwestern China: *Geological Society of America Bulletin*, v. 103, p. 1178-1199.
- Avouac, J-P, and Tapponnier, P., 1993, Kinematic model of active deformation in central Asia: *Geophysical Research Letters*, v. 20, p. 895-898.
- Brook, E.J., 1994, Surface Exposure Geochronology Using Cosmogenic Nuclides: Applications in Antarctic Glacial Geology: Doctoral Dissertation, Woods Hole Oceanographic Institution MIT Joint Program in Oceanography/Applied Ocean Science and Engineering, WHOI-93-50, 232 p.
- Brown, E.T., Brook, E.J., Raisbeck, G.M., Yiou, R., Kurz, M., 1992, Effective attenuation lengths of cosmic rays producing ^{10}Be and ^{26}Al in quartz: implications for exposure age dating: *Geophysical Research Letters*, v. 19 p. 369-372.
- Burbank, D. W. and Anderson, R. S., eds., 2000, *Tectonic Geomorphology*: Blackwell Science, 274 p.
- Burchfiel, B.C., Chen, Z., Liu, Y., and Royden, L.H., 1995, Tectonics of the Longmen Shan and adjacent regions: *International Geology Review*, v. 37, p. 661-735.
- Chen, Z., Burchfiel, B.C., Liu, Y., King, R.W., Royden, L.H., Tang, W., Wang, E., Zhao, J. and Zhang, X., 2000, Global Positioning System measurements from eastern Tibet and their implications for India/Eurasia intercontinental deformation: *Journal of Geophysical Research*, v. 105, no. B7, p. 16215-16227.
- Clark, M.K., 2003, Late Cenozoic Uplift of Southeastern Tibet [PhD Thesis]: Massachusetts Institute of Technology, 226 p.
- Clark, M.K. and Royden, L.H., 2000, Topographic ooze: Building the eastern margin of Tibet by lower crustal flow: *Geology*, v. 28, p. 703-706.
- Cobbold, P.R., and Davy, P., 1988, Indentation tectonics in nature and experiment 2. Central Asia: *Geological Institute, University of Uppsala*, v. 14, p. 143-162.
- Davy, P., and Cobbold, P.R., 1998, Indentation tectonics in nature and experiment 1. Experiments scaled for gravity: *Geological Institute, University of Uppsala*, v. 14, p. 129-141.
- Dewey, J., Cande, S., and Pitman, W.C., III, 1989, Tectonic evolution of the India-Eurasia collision zone: *Eclogae Geologicae Helveticae*, v. 82, p. 717-734.
- England, P.C., and Houseman, G.A., 1988, The mechanics of the Tibetan Plateau: *Philosophical Transactions of the Royal Society of London A*, v. 326, p. 301-320.
- England, P., and Molnar, P., 1990, Surface uplift, uplift of rocks, and exhumation of rocks: *Geology*, v. 18, p. 1173-1177.
- Gilley, L.D., Harrison, T.M., Leloup, P.H., Ryerson, F.J., Lovera, O.M., Wang J-H, 2003, Direct dating of left-lateral deformation along the Red River shear zone, China and Vietnam: *Journal of Geophysical Research*, v. 103, No. B2, 10.1029/2001JB001726.
- Harrison, T.M., W Chen, Leloup, P.H., Ryerson, F.J., and Tapponnier, P., 1992, An Early Miocene transition in deformation regime within the Red River fault zone, Yunnan, and its significance for the Indo-Asian tectonics: *Journal of Geophysical Research*, v. 97, p. 7159-7182.
- Harrison, T.M., Leloup, P.H., Ryerson, F.J., Tapponnier, P., Lacassin, R., and Chen Wenji, 1996, Diachronous initiation of transtension along the Ailao Shan-Red River shear zone, Yunnan and Vietnam, in Yin, A., and Harrison, T.M., eds., *The Tectonic Evolution of Asia*, Cambridge University Press, New York, p. 208-226.
- Houseman, G., and England, P., 1993, Crustal Thickening Versus Lateral Expulsion in the Indian-Asian Continental Collision: *JGR*, v. 98, p. 12233-12249.
- King, R.W., Shen, F., Burchfiel, B.C., Royden, L.H., Wang E., Chen Z., Liu Y., Zhang X.-Y., Zhao J.-X., and Li Y., 1997, Geodetic measurement of crustal motion in southwest China: *Geology*, v. 25, no. 2, p. 179-182.
- Kirby, E., and Whipple, K.X., 2001, Quantifying differential rock-uplift rates via stream profile analysis: *Geology*, v. 29, p. 415-418.
- Kirby, E., Reiners, P.W., Krol, M.A., Whipple, K.X., Hodges, K.V., Farley, K.A., Tang, W., Chen, Z., 2002, Late Cenozoic evolution of the eastern margin of the Tibetan Plateau: Inferences from $^{40}\text{Ar}/^{39}\text{Ar}$ and (U/Th)/He thermochronology: *Tectonics*, v. 21, 10.1029/2000TC001246.

Chapter 1- Introduction

- Kirby, E., Whipple, K.X., Tang W., and Chen Z., 2003, Distribution of active rock uplift along the eastern margin of the Tibetan Plateau: Inferences from bedrock channel longitudinal profiles, *Journal of Geophysical Research*, v. 108, doi:10.1029/2001JB000861.
- Lacassin, R., Replumaz, A., Leloup, P.H., 1998, Hairpin river loops and strike-slip sense inversion of southeast Asian strike-slip faults: *Geology*, v. 26, p. 703-706.
- Lauge, D., and Davy, P., 2003, Constraints on the long-term colluvial erosion law by analyzing slope-area relationships at various tectonic uplift rates in the Siwalik Hills (Nepal): *Journal of Geophysical Research*, v. 106, no. B11, p. 26561-26591.
- Leloup, P.H., and Kienast, J.R., 1993, High temperature metamorphism in a major Tertiary ductile continental strike-slip shear zone: The Ailao Shan-Red River (P.R.C.): *Earth and Planetary Science Letters*, v. 118, p. 213-234.
- Leloup, P.H., Harrison, T.M., Ryerson, F.J., Chen W., Li Q., Tapponnier, P., and Lacassin, R., 1993, Structural, petrological and structural evolution of a Tertiary ductile strike-slip shear zone, Diancang Shan, Yunnan: *Journal of Geophysical Research*, v. 98, p. 6715-6743.
- Leloup, P.H., Lacassin, R., Tapponnier, P., Schärer, U., Zhong D., Liu X., Zhang L., Ji S., Phan T.T., 1995, The Ailao Shan-Red River shear zone (Yunnan, China), Tertiary transform boundary of Indochina: *Tectonophysics*, v. 251, p. 3-84.
- Leloup, P.H., Arnaud, N., Lacassin, R., Kienast, J.R., Harrison, T.M., Phan Trong, T.T., Replumaz, A., and Tapponnier, P., 2001, New constraints on the structure, thermochronology, and timing of the Ailao Shan-Red River shear zone, SE Asia: *Journal of Geophysical Research*, B, v. 106, p. 6683-6732.
- Molnar, P., and Tapponnier, P., 1975, Cenozoic tectonic of Asia: Effects of a continental collision: *Science*, v. 189, p. 419-426.
- Noller, J.S., Sowers, J.M., and Lettis, W.R., eds., 2000, *Quaternary Geochronology; methods and applications: AGU Reference Shelf*, 582 p.
- Peltzer, G., and Saucier, F., 1996, Formation and evolution of strike-slip faults, rifts, and basins during India-Asia collision: An experimental approach: *Journal of Geophysical Research*, v. 93, p. 15085-15117.
- Raymo, M.E., Ruddiman, W.F., and Froelich, P.H., 1988, Influence of Late Cenozoic mountain building on ocean geochemical cycles: *Geology*, v. 16, p. 649-653.
- Replumaz, A., Lacassin, R., Tapponnier, P., and Leloup, P.H., 2001, Large river offsets and Plio-Quaternary dextral strike-slip rate on the Red River fault (Yunnan, China): *Journal of Geophysical Research*, B, v. 106, 819-836.
- Royden, L.H., 1996, Coupling and decoupling of crust and mantle in convergent orogens: Implications for strain partitioning in the crust: *Journal of Geophysical Research*, B, v. 101, p. 17 679-17 705.
- Royden, L.H., Burchfiel, B.C., King, R.W., Wang, E., Chen Z., Shen F., Liu Y., 1997, Surface deformation and lower crustal flow in eastern Tibet: *Science*, v. 276, p. 788-790.
- Ruddiman, W.F. and Kutzbach, J.E., 1989, Forcing of Late Cenozoic northern hemisphere climate by plateau uplift in southern Asia and the American west: *Journal of Geophysical Research*, v. 94, p. 18409-18427.
- Schärer, U., Zhang L., Tapponnier, P., 1994, Duration of strike-slip movements in large shear zones: the Red River belt, China: *Earth and Planetary Science Letters*, v. 126, p. 379-397.
- Schärer, U., Tapponnier, P., Lacassin, R., Leloup, P.H., Zhong D., and Ji S., 1990, Intraplate tectonics in Asia: a precise age for large-scale Miocene movement along the Ailao Shan-Red River Shear Zone, China: *Earth and Planetary Science Letters*, v. 97, p. 65-77.
- Shen, F.L., Royden, L.H., and Burchfiel, B.C., 2001, Large-scale crustal deformation of the Tibetan Plateau: *Journal of Geophysical Research* B, v. 106, p. 6793-6816.
- Snyder, N.P., Whipple, K.X., Tucker, G.E., and Merritts, D.J., 2000, Landscape response to tectonic forcing: DEM analysis of stream profiles in the Mendocino triple junction region, northern California: *Geological Society of America Bulletin*, v. 112, p. 1250-1263.
- Tapponnier, P., Peltzer, G., Armijo, R., Le Dain, A.-Y., and Cobbold, P., 1982, Propagating extrusion tectonics in Asia: New insights from simple experiments with plasticine: *Geology*, v. 10, p. 611-616.
- Tapponnier, P., Peltzer, G., and Armijo, R., 1986, On the mechanics of the collision between India and Asia, *in* Coward, M.P. and Ries, A.C., eds., *Collision Tectonics*, Geological Society Special Publication 19, p. 115-157.
- Tapponnier, P., Lacassin, R., Leloup, P.H., Schärer, U., D. Zhong, X. Liu, S. Ji, L. Zhang and J. Zhong, 1990, The Ailao Shan/Red River metamorphic belt: Tertiary left-lateral shear between Indochina and south China: *Nature*, v. 343, p. 431-437.
- Wang, E., and Burchfiel, B.C., 1997, Interpretation of Cenozoic tectonics in the Right-Lateral accommodation zone between the Ailao Shan shear zone and the Eastern Himalayan Syntaxis: *International Geology Review*, v. 39, p. 191-219.

Chapter 1- Introduction

- Wang, E., Burchfiel, B.C., Royden, L.H., Chen L., Chen J., Li W., Chen Z., 1998, Late Cenozoic Xianshuihe-Xiaojiang, Red River and Dali fault systems of southwestern Sichuan and central Yunnan, China: Boulder, Colorado, Geological Society of America Special Paper 327.
- Whipple, K.X., in press, Bedrock rivers and the geomorphology of active orogens: *Annual Review of Earth and Planetary Sciences*, v. 32.
- Whipple, K.X., and Tucker, G.E., 1999, Dynamics of the stream-power river incision model: Implications for height limits of mountain ranges, landscape response timescales, and research needs: *Journal of Geophysical Research*, v. 104, p. 17 661-17 674.
- Whipple, K.X., and Tucker, G.E., 2002, Implications of sediment-flux-dependent river incision models for landscape evolution: *Journal of Geophysical Research*, v. 107, no. B2, 10.1029/2000JB000044.
- Wobus, C.W., Hodges, K.V., and Whipple, K.X., 2003, Has focused denudation sustained active thrusting at the Himalayan topographic front? *Geology*, v. 31, p. 861-864.
- Zhang, L.-S. and Schärer, U., 1999, Age and origin of magmatism along the Cenozoic Red River shear belt, China: *Contributions to Mineralogy and Petrology*, v. 134, p. 67-85.

**Transpressional exhumation of the Ailao Shan
shear zone as recorded by Cenozoic sedimentary rocks,
Yunnan Province, China**

Lindsay Schoenbohm^{1*}
B. Clark Burchfiel¹
Chen Liangzhong²
Josh Feinberg³
Michael Stewart⁴
Yin Jiyun²

¹Massachusetts Institute of Technology, Dept. of Earth, Atmospheric and Planetary Sciences, 77
Massachusetts Ave., Cambridge, MA 02139

²Yunnan Institute of Geological Sciences, 131 Baita Rd., Kunming, Yunnan, China

³University of California, Berkeley, Department of Earth and Planetary Sciences, 269 McCone
Hall, Berkeley, CA 94720

⁴Maine Maritime Academy, Castine, ME 04420

* E-mail: schoenbl@mit.edu

ABSTRACT

Cenozoic sedimentary rocks preserved along the northeast side of the Ailao Shan shear zone record the nature and timing of exhumation of shear zone rocks. Field mapping indicates that the lower part of the Cenozoic strata consists of Early Oligocene lacustrine red mudstone and gypsum and the upper part consists of Late Oligocene to Miocene fluvial conglomerate, inter-bedded with rare sandstone and fine-grained fossil leaf-bearing intervals. Sediment derived from shear zone gneiss is present only in the upper part of the section. Our observations are consistent with geochronologic results indicating that deformation began as early as 34 Ma (Gilley et al., 2003) with the onset of rapid cooling at approximately 25 Ma (Harrison et al., 1996). Exhumation must have ended before the formation of a regional low-relief erosion surface and the onset of brittle deformation along the Red River fault, probably in Early Pliocene time. Rapid exhumation of the Ailao Shan shear zone has been interpreted to have occurred in transtension, accommodated by a normal fault on the northeast margin of the shear zone (Harrison et al., 1996). However, we observe consistent and pervasive shortening structures within the Cenozoic strata, including a southwest-dipping reverse fault along the northeast margin of the shear zone, thrust faults defined by thick gouge zones within weak Cenozoic lithologies that dip 45° SW, and a NE-dipping reverse fault along the northeast side of the Red River valley. These faults are associated with pervasively folded and sheared Cenozoic strata. These structures are distinct from sub-vertical deformational features associated with the active Red River fault. We also observe that the older Cenozoic rocks were deformed, eroded and redeposited in the upper part of the section. This syn-depositional deformation indicates significant shortening occurred during exhumation of the shear zone. Our field data thus suggest mid-Cenozoic transpressional exhumation of the Ailao Shan shear zone. Focused erosion along the Red River, established by Late Oligocene time, may have contributed to deeper exhumation of the northeast part of the shear zone.

INTRODUCTION

The Ailao Shan shear zone (Fig. 1), a long, narrow belt of amphibolite-grade mylonitic gneiss running the length of the southeast margin of the Tibetan Plateau, is a profound crustal discontinuity, and has been an important element in the tectonic development of the India-

Eurasia collision. In some models, the shear zone is viewed as an intracontinental transform fault, responsible for the extrusion of Indochina in response to the collision (Tapponnier et al., 1982; 1986; Avouac and Tapponnier, 1993; Leloup et al., 1995; 2001). However, the importance of the shear zone has been minimized by others, in favor of tectonic models in which deformation is widely distributed in Southeast Asia, emphasizing spreading of thickened crust (England and Houseman, 1989; Houseman and England, 1993), rotation around the eastern Himalayan syntaxis (Wang and Burchfiel, 1997; Wang E. et al., 1998) or broad right-lateral shear (Dewey et al., 1989). The nature of exhumation of the shear zone is also controversial, and has been variously linked to opening of the South China Sea and models that emphasize transtensional exhumation (Brias et al., 1993; Leloup et al., 1995; Harrison et al., 1996; Leloup et al., 2001), or to contemporaneous regional shortening and transpressional exhumation (Wang and Burchfiel, 1997), or to both synchronous or non-synchronous transpression and transtension (Leloup and Kienast, 1993; Leloup et al., 1995). A clearer understanding of the Ailao Shan shear zone, particularly its unroofing history and the relationship between exhumation and regional tectonics, is important in understanding the evolution of the India-Eurasia collision, particularly (1) the way in which southeast Asia responded to the collision, (2) the role of strike-slip shear zones in general in Asian tectonics; and (3) the nature of deformation of continental crust, whether diffuse and continuous, or localized on a few major lithospheric-penetrative faults.

Because of its importance in Asian tectonics, the Ailao Shan shear zone has been the focus of many studies, particularly into the thermochronology, petrology and structure of the shear zone, potential offset markers and regional volcanism (Schärer et al., 1990; Harrison et al., 1992; Leloup and Kienast, 1993; Lacassin et al., 1993; Schärer et al., 1994; Leloup et al., 1995; Harrison et al., 1996; Chung et al., 1997; Wang P. et al., 1998; Zhang and Schärer, 1999; Wang et al., 2001; Leloup et al., 2001). The Red River fault, a brittle, right-lateral structure coincident with the northeast margin of the Ailao Shan shear zone, has also been documented in a number of studies (Allen et al., 1984; Wang E. et al., 1998; Replumaz et al., 2001; Chapter 3). Cenozoic sedimentary rocks preserved in a long, linear belt along the northeastern margin of the shear zone, however, have not been studied (Fig. 1b). These strata preserve a unique record of the unroofing history of the shear zone and provide insight into the timing and concurrent structural setting of exhumation. Through detailed mapping of these rocks, we determine the sequence of

events in the evolution of the Ailao Shan shear zone and demonstrate that this region underwent shortening during unroofing of the shear zone. On this basis, exhumation of the shear zone was through transpression, consistent with regional structural observations and geochronology. We establish that the Red River fault plays no role in unroofing of the shear zone. Finally, we suggest that focused erosion along the paleo-Red River, established by Late Oligocene time, could be partially responsible for deeper exhumation along the northeast side of the Ailao Shan shear zone.

GEOLOGIC SETTING

Regional geologic framework

The southeast margin of the Tibetan Plateau has been extensively deformed as a result of the India-Asia collision. Several Tertiary shear zones traverse this region, including the Ailao Shan, the Chong Shan and the Gaoligong Shan shear zones (Fig. 1; Wang and Burchfiel, 1997; Akciz et al., 2003a; 2003b). The Ailao Shan shear zone collectively refers to a narrow belt (< 20 km-wide) of metamorphic rocks that outcrop in Vietnam as the Day Nui Con Voi, in southern and central Yunnan as the Ailao Shan, in northern Yunnan as the Diancang Shan, and in northernmost Yunnan as the Xue Long Shan (Fig. 1a, Tapponnier et al., 1990; Leloup et al., 1995). Altogether the shear zone stretches more than 1000 km from the South China Sea to the eastern margin of the Tibetan Plateau. All four metamorphic bodies share a steep foliation and sub-horizontal stretching lineation and contain abundant left-lateral shear sense indicators (Tapponnier et al., 1990; Leloup et al., 1993; 1995; 2001).

The Ailao Shan shear zone defines a profound geologic discontinuity, separating Indochina to the southwest from South China to the northeast. Adjacent to the shear zone, the eastern part of the Indochina block is covered by Triassic to Early Cenozoic continental red beds up to 8 km thick in the Lanping-Simao basin, deformed in Middle Eocene to pre-Pliocene time (Fig. 1; Leloup et al. 1995; Wang and Burchfiel 1997). The region of South China adjacent to the Ailao Shan shear zone consists mainly of Permian carbonates and basalts, Early Mesozoic shallow marine carbonates of the Yangtze platform and, in the Chuxiong basin, Jurassic and Cretaceous non-marine redbeds (Leloup et al. 1995, Fig. 1b).

The regional fault systems active today in Yunnan (Fig. 1) are distinct from the older shear zones, and include the left-lateral Xianshuihe-Xiaojiang fault system (Allen et al., 1991; Wang E. et al., 1998; Shen et al., 2003), the largely left-lateral and extensional Dali fault system (DFS Fig. 1a; Allen et al., 1984; Leloup et al., 1993; Wang E. et al., 1998) and the right-lateral Red River fault (Allen et al., 1984; Leloup et al., 1995; Wang E. et al., 1998; Replumaz et al., 2001; Chapter 3). The Red River fault is of particular interest as it is generally coincident with the northeast margin of the Ailao Shan shear zone. The precise relationship between the ductile, sinistral mylonites of the Ailao Shan shear zone and the active, brittle, dextral Red River fault is not well established. We therefore follow Wang E. et al. (1998) in using nomenclature which distinguishes between these structures, and refer to each separately as the Ailao Shan shear zone (ASSZ) or the Red River fault (RRF). The Red River fault has experienced at least 40 km right-lateral offset, probably since Middle-Miocene or Pliocene time (Chapter 3), with a minor oblique extensional component on the northern part of the fault. Vertical displacement in this region, however, is less than ~750 m (Schoenbohm et al., in press and Chapter 4). The limited amount of vertical displacement adjacent to the Ailao Shan contrasts with the Diancang Shan, which lies along the southwestern margin of the modern Dali Fault system (Fig. 1a). Northeast-southwest extension in this region has significantly exhumed this part of the shear zone, resulting in rapid cooling recorded by $^{40}\text{Ar}/^{39}\text{Ar}$ thermochronology at ~5 Ma (Leloup et al., 1993; Wang E. et al., 1998)

The Ailao Shan shear zone is situated within the southeast margin of the Tibetan Plateau. The region is characterized by a low-relief upland landscape continuous with both the Tibetan Plateau and the south Asian coastal margin (Fig. 1a; Clark 2003). The upland landscape is perched above deeply incised rivers of the southeastern margin of the plateau, including the Salween, Mekong, Yangtze, and Red Rivers and their major tributaries (Clark, 2003; Clark et al., in press; Schoenbohm et al., in press and Chapter 4). This morphology is suggestive of long-wave-length surface uplift associated with growth of the Tibetan plateau, and subsequent river incision. Clark and Royden (2000) argued that this results from the flow of weak lower crust from beneath Tibet to the southeast, thickening the crust and producing isostatic surface uplift. On the basis of stratigraphic evidence, incision of the Red River as a response to surface uplift began in Pliocene time or later (Chapter 3).

Ailao Shan shear zone

Gneisses of the Ailao Shan segment of the Ailao Shan shear zone are amphibolite grade with well-developed, steeply northeast dipping foliation and sub-horizontal lineation (Tapponnier et al., 1990; Leloup et al., 1995). Mylonites preserve abundant evidence for left-lateral ductile shear (Tapponnier et al., 1990; Lacassin et al., 1993; Leloup et al., 1995). The magnitude of offset, difficult to determine because of the lack of well-correlated geologic features, is estimated to be 700 ± 200 km (Leloup et al., 1995; Chung et al., 1997; Leloup et al., 2001). Peak metamorphic conditions are 550-780°C and 3-7 kbar (Leloup et al., 1993; Leloup and Kienast, 1993), indicating ~18 km exhumation (Leloup and Kienast, 1993). To the northeast, these high-grade gneisses are juxtaposed along the Red River fault with unmetamorphosed strata of the Yangtze platform and Chuxiong basin (Fig. 1b). The fault along the southwest side of the Ailao Shan shear zone separates high grade gneisses from a belt of low-grade schists containing numerous lenses of ultramafic rock (Bureau of Geology, Yunnan, 1990; Leloup et al., 1995). Further southwest, rocks of the Lanping-Simao redbed basin are unmetamorphosed (Fig. 1; Bureau of Geology, Yunnan, 1990). The Ailao Shan shear zone is thus deeply exhumed in comparison to the immediately adjacent rocks of South China and Indochina.

Extensive geochronology has constrained the timing of deformation and exhumation within the shear zone; most of the existing data is summarized by Leloup et al. (2001), Wang P. et al. (1998, 2001) and Gilley et al. (2003). Dating of monazite inclusions in synkinematic garnet indicates shearing occurred between 34 and 21 Ma (Gilley et al., 2003). $^{40}\text{Ar}/^{39}\text{Ar}$ thermochronology shows rapid cooling of the Ailao Shan segment of the shear zone between ~25 and 17 Ma (Harrison et al., 1996). Presumably, there was a lag of up to a few million years between the onset of tectonically driven erosional exhumation of the shear zone and the first record of rapid cooling in shear zone rocks because of heat advection during unroofing. Tectonically driven rapid exhumation of the shear zone may have continued beyond the youngest ages (~17 Ma) recorded by $^{40}\text{Ar}/^{39}\text{Ar}$ feldspar thermochronology which correspond to ~200°C (Harrison et al., 1996). Interestingly, these data indicate that cooling was diachronous both along strike (older to the southeast in Vietnam) and across the shear zone (older along the northeast side) (Harrison et al., 1996). Zircon and apatite fission-track data indicate rapid cooling from 13-

10 Ma (Bergman et al., 1997; Leloup et al., 2001), but it is unclear whether these data record continued left-lateral shear and exhumation in the Ailao Shan or a distinct cooling event possibly related to early right-lateral displacement on the Red River fault. The low-relief upland landscape must have formed locally after exhumation of the shear zone, therefore not before 17 Ma (Harrison et al., 1996) and possibly not before ~10 Ma (Bergman et al., 1997) if there was significant exhumation of the shear zone at that time (Schoenbohm et al., in press and Chapter 4). However, the local landscape must have formed before river incision and regional surface uplift, probably in Pliocene time (note that on a regional scale, the low-relief landscape may vary in origin and age; Clark et al., 2003; Schoenbohm et al., in press and Chapter 4). The preservation of the low-relief relict landscape on the crest of the Ailao Shan and adjacent regions, and the establishment of less than 750 m vertical displacement along the Red River fault means that all tectonically driven erosional exhumation of the shear zone must pre-date establishment of the relict landscape and is unrelated to displacement along the modern Red River fault.

The spatial and temporal relationships between the Ailao Shan shear zone and the Lanping-Simao fold and thrust belt suggest that the shear zone may have been at least partially exhumed in a transpressional setting (Leloup and Kienast, 1993; Leloup et al., 1995; Wang and Burchfiel, 1997). Structures within the fold and thrust belt are generally southwest vergent, and exposures of older rocks to the northeast suggest a northeastward deepening décollement which probably merges with the Ailao Shan shear zone (Leloup et al., 1995; Wang and Burchfiel, 1997). Eocene-Oligocene rocks are folded with older strata, but Pliocene and possibly Late Miocene deposits are relatively undeformed, indicating the fold and thrust belt was active from middle to Late Eocene time to no later than Pliocene time (Wang and Burchfiel, 1997). This period overlaps with that inferred for activity along the Ailao Shan shear zone. Transpression, with some degree of partitioning between coeval strike-slip shearing in the Ailao Shan shear zone and contractional deformation of the Lanping-Simao fold and thrust belt may therefore be partly (Leloup and Kienast, 1993; Leloup et al., 1995) or entirely (Wang and Burchfiel, 1997) responsible for unroofing of the shear zone.

In contrast, thermochronologic data, petrologic and structural observations along the northeast margin of the shear zone, and data from the South China Sea have been used to argue for transtensional exhumation of the Ailao Shan shear zone (Brias et al., 1993; Harrison et al., 1996, Leloup et al., 2001). Partly on the basis of diachronous cooling of the shear zone indicated by thermochronologic data, Harrison et al. (1996) proposed that the shear zone was exhumed through “zipper tectonics,” in which a small amount of rotation of the Indochina block during left-lateral shear resulted in an extensional component which progressed along the shear zone from the South China Sea to the northern tip of the Ailao Shan, producing an increasing gradient in extension from northwest to southeast. A small degree of rotation of Indochina is consistent with seafloor magnetic anomaly interpretation by Brias et al. (1993). Harrison et al. (1996) proposed that exhumation primarily occurred on a normal fault along the northeast margin of the shear zone coincident with strands of the modern Red River fault. Modeling of cross-strike thermochronologic data indicates deeper exhumation of the northeast margin of the shear zone, also consistent with this model (Harrison et al., 1996). This interpretation, however, has been challenged by other authors, particularly the causal relationship between continental tectonics and opening of the South China Sea (Holt et al., 1995; Hall, 1996; Packham, 1996; Wang and Burchfiel, 1997), nor has this scenario been confirmed through detailed analysis of the nature of the northeast boundary of the shear zone. Additionally, as we develop below, deeper exhumation on the northeast side of the shear zone may be related to focused river incision rather than to an exhumation-related normal fault.

In summary, the Ailao Shan shear zone may have been active as a left-lateral structure since ~34 Ma or earlier (Gilley et al., 2003), and the shear zone was rapidly exhumed from ~18 km depth (Leloup and Kienast, 1993) from probably a few million years prior to the youngest cooling age at ~25 Ma, through the feldspar closure temperature at 17 Ma (Harrison et al., 1996). Contemporaneous regional shortening in the Lanping-Simao fold and thrust belt suggest a regionally transpressive setting. However there is potentially contradictory evidence for extension along the northeast margin of the shear zone. To explore the nature of deformation and the exhumation record along the northeast boundary of the shear zone we studied Cenozoic sedimentary rocks in the Red River valley which record the exhumation and concurrent structural setting of the Ailao Shan shear zone.

STRATIGRAPHY AND DEFORMATION OF CENOZOIC SEDIMENTARY ROCKS

A narrow belt of Cenozoic conglomerate, sandstone, mudstone and gypsum is preserved adjacent to the Ailao Shan shear zone in the Red River valley (Fig. 1b; Bureau of Geology, Yunnan, 1990; Wang E. et al., 1998). As discussed further below, these strata contain Oligocene and Miocene fossils and sedimentary units that appear to both predate and postdate exhumation of shear zone gneiss: they span the time during which the Ailao Shan shear zone was actively unroofing. The lower part of the section contains lacustrine and fine-grained fluvial strata and the upper part is dominated by fluvial sediments. The entire section is extensively deformed both by Ailao Shan related structures and by activity along the Red River fault.

The Cenozoic sedimentary rocks are well preserved from the town of Mosa in the north, through a major bend in the shear zone near the town of Yuanjiang and farther southeast along the river across the border into Vietnam (Fig. 1b). The original basin was probably very narrow because sedimentary rocks of similar age on the Yangtze platform to the north (Bureau of Geology, Yunnan, 1990) are local deposits, and are unrelated to the strata along the Red River. Because detailed mapping is necessary to unravel the stratigraphy and structure of these sedimentary rocks, we focused our study on two locations with good access and exposure at Yuanjiang and ~100 km southeast at the town of Nansa (Figs. 2 and 3). Because of the sub-tropical climate and high population, most of the map area is either vegetated or cultivated and exposure is generally limited to road-cut and riverside outcrops. Though we have firmly established the underlying structural and depositional relationships, because of limited outcrop, some of the aspects of the mapping are open to interpretation, particularly the extrapolation of contacts. We have indicated actual outcrop in each of the map areas (Figs. 2 and 3), and have thoroughly documented relationships where observed in outcrop.

Our mapping efforts focused on answering the following questions: (1) What is the contact along the northeast margin of the Ailao Shan shear zone, where unmodified by the Red River fault? (2) What is the unroofing sequence of the Ailao Shan shear zone as recorded by the Cenozoic sedimentary succession ? (3) What structural setting do these sedimentary rocks record during their deposition? These questions are addressed below as we describe the results of our mapping.

Nansa Map Area

In the Nansa map area (~35 km long, ~5 km wide, Figs. 2 and 4 F-J), Cenozoic sedimentary rocks are deposited on Triassic rocks of the Yangtze platform and are bounded to the southwest by the Ailao Shan shear zone and a strand of the Red River fault.

Stratigraphy

Pre-Cenozoic rocks. Throughout the Nansa area, Cenozoic strata are deposited unconformably on Triassic units of the Yangtze platform and, in the northern corner of the map area, on Permian basalt and limestone (Bureau of Geology, Yunnan, 1990). Triassic rocks comprise two units: massive black or gray cliff-forming limestone with common calcite veining (T₂), and a package of tan siltstone, sandstone, carbonate, shale, rare coal and greenish or purple shale (T₃) (Bureau of Geology, Yunnan, 1990). In this region, T₃ strata are slightly metamorphosed, evident primarily by the growth of fine-grained muscovite in more aluminous rocks. A strand of the Red River fault separates T₂ and T₃ units.

Early Oligocene lacustrine strata: Wubang Mudstone. The base of the Cenozoic section consists of red mudstone (Fig. 5g), gypsum (Fig. 5h) and occasional carbonate rocks, and is well-exposed near the town of Wubang (Fig. 2), after which we name the unit. These rocks are uniformly fine-grained, lacking in both sand and cobble interbeds. In a few exposures southwest of Nansa (Fig. 2), cobbles of varying lithology have been incorporated into the Wubang Mudstone through down-slope sliding and mixing. These deposits however, are confined to the upper few meters of exposure, follow the hillslope, are highly disturbed, and thus can be distinguished from the fine-grained Wubang mudstone. Gypsum within the Wubang Mudstone is massive and white to gray in color in some places, but in other places it exhibits black, gray and white laminations on the centimeter scale. Carbonate intervals are poorly exposed, but are generally tan, laminated, and do not contain obvious fossils. Because these rocks are relatively weak, they have been intensely sheared, both by the Red River fault, and as we will argue below, by older deformation. In a particularly good exposure near Nansa (Fig. 2), mudstone and gypsum are vertically foliated and boudinaged. In smaller outcrops, these rocks nearly always display a shear fabric, which is related to adjacent structures (see further discussion below), and gypsum is

ductilely folded (Fig. 5h). We infer a lacustrine origin for these rocks based on the association of fine-grained mud and evaporite deposits, but intense deformation has obscured any further evidence for this interpretation, such as fossils, sedimentary structures, and exposed contacts with the surrounding rocks.

These lacustrine strata of the Wubang Mudstone are in probable depositional contact with T₃ sedimentary rocks. Though we were unable to observe the contact in outcrop, near Wubang (Fig. 2) we bracketed the contact and observed low dips (~13°) in relatively undeformed red mudstone adjacent to T₃ limestone with no apparent structural discontinuity in between (Location 2, Fig. 2). This unit is thicker to the northwest near Nansa and pinches out ~3 km southeast of Wubang (near Location 4, Fig. 2 and cross section H, Fig. 4). This may reflect the original depositional extent, or the unit may have been erosionally removed in the southeast. The Wubang Mudstone is capped in at least one place (Location 4, Fig. 2) by the overlying Ailao Shan Conglomerate (described below). The Wubang Mudstone is assigned an Eocene-Oligocene age on Chinese geologic maps (Bureau of Geology, Yunnan, 1990) through correlation to similar units elsewhere in Yunnan dated with ostracode fossils (Wang E. et al., 1998), but it has not been directly dated in this map area. Because this unit may be local, and correlation to similar rocks elsewhere in Yunnan therefore may be inappropriate, we prefer to define the age of the Wubang mudstone in relation to other units and deformational events in the Nansa region. These strata are younger than Triassic rocks on which they are deposited, and are also younger than metamorphism of T₃ rocks adjacent to the Ailao Shan gneiss. We argue below that this metamorphism is related to early activity along the Ailao Shan shear zone, and therefore this unit is younger than the earliest phase of strike-slip deformation, ~34 Ma (Gilley et al., 2003). These strata are older than the Oligo-Miocene conglomerates which we discuss below. We therefore tentatively assign deposition of the Wubang mudstone to Early Oligocene time.

Oligocene-Miocene fluvial strata: Langdun Formation. We identified three distinct, conformable units within this part of the section which we describe below from the base to the top. The section is exposed relatively well in road cuts northeast of the town of Langdun (Fig. 2) and we call these rocks the Langdun Formation. Each informal member is given a descriptive name

Limestone Conglomerate. This dominantly fluvial conglomerate forms the lowest member of the Langdun Formation and contains clasts derived from Yangtze platform rocks, primarily T₂ limestone (Fig. 5e, and Table 1). Because of the high carbonate content of the unit, it tends to be very well lithified. In most places, the Limestone Conglomerate is a mix of medium sand- to cobble-sized sediment, and clasts are generally well-rounded. Finer, carbonate sand-dominated horizons do occur, but are uncommon except in the upper part of the section, and sedimentary structures, such as cross-bedding and flame structures, are sometimes observed. We also find poorly sorted deposits with angular, locally derived pebble-sized clasts in a fine groundmass, particularly on the hill to the northeast of Nansa (Figs. 2 and 5f). This unit is in unconformable depositional contact with T₂ limestone, but never with T₃ units or Ailao Shan gneiss across the most active strands of the Red River fault. In some places the contact between the Limestone Conglomerate and T₂ limestone is a karst surface: irregularities and cavities in the limestone are filled with blocky, angular, matrix supported clasts of T₂, which grades upwards into fluvial facies Limestone Conglomerate. We observed this relationship to the northeast of the Funke reverse fault, southeast of the town of Funke (Fig. 2). The thickness of the Limestone Conglomerate varies along and across the valley, but the maximum thickness observed was ~1 km. The sedimentology of these strata, and their confinement to the narrow Red River valley, suggest they are dominantly fluvial in origin, related to an axial river system, with intermingling coarser alluvial fan deposits. We did not find fossils in this unit in the Nansa region, but did find them in the Yuanjiang map area (see below).

A defining characteristic of the Limestone Conglomerate is that it does not contain material derived from the Ailao Shan shear zone. Therefore, the limestone conglomerate must pre-date the first arrival of Ailao Shan gneiss at the Earth's surface. However, the presence of this unit indicates that (1) the Red River was established as a through-going, axial drainage system at this time, and (2) tectonically driven erosional exhumation of the shear zone was probably underway, stripping the cap rocks from the exhuming shear zone gneisses which were still at depth at this time, causing an influx of coarser material and debris flow deposits into the basin.

Transitional Sandstone. This member of the Langdun Formation is a sandstone (Fig. 5d), approximately 200 m thick, which pinches out to northwest and southeast and is not observed in the Yuanjiang map area. The sandstone is relatively poorly sorted, and contains both fine-grained layers and cobble lags throughout. Bedding is apparent at the 10's of centimeters scale, and rare cross-bedding is present. The Limestone Conglomerate grades upward into the Transitional Sandstone, and the sandstone grades upward into the Ailao Shan Conglomerate, a relationship which is best observed near fossil site RR99-13 (Fig. 2). Fossils are common in the fine-grained, organic-rich layers of the Transitional Sandstone. This unit is also likely fluvial in origin, and is similar in appearance to fine-grained point bar and slow-moving channel deposits on the modern Red River.

Ailao Shan Conglomerate. This member of the Langdun Formation contains abundant clasts derived from the Ailao Shan shear zone (Fig. 5a-c). The Ailao Shan Conglomerate is essentially identical in sedimentology to modern deposits along the Red River, but is easily distinguished by better lithification and extensive deformation. Some horizons within the conglomerate are well-sorted and well-rounded, with sandy interbeds (Fig. 5b-c, and Table 1, e.g., Yuanjiang 9), while elsewhere the unit is poorly sorted with boulders >1m in diameter (Fig. 5a, and Table 1, e.g. Nansa 120a). In general, this unit contains significantly larger clasts than the Limestone Conglomerate. The stratigraphy of this member is complex, with intermingling fluvial sediments and further fluvial reworking, and outcrop is poor, precluding the establishment of a more detailed stratigraphy. Where observed, paleo-current indicators suggest flow to the southeast, but conclusive examples are rare because of deformation and poor exposure. This unit is deposited para-conformably on the Transitional Sandstone (best observed near fossil site RR99-13 and southwest of the Funke reverse fault, Fig. 2)), or where this member is absent, directly on the Limestone Conglomerate (best observed immediately east of Nansa). The Ailao Shan Conglomerate is in both structural and depositional contact with the Early Oligocene Wubang Mudstone and T₃ rocks (Location 4, Fig. 2). We infer a fluvial origin for the Ailao Shan Conglomerate, with a contribution of coarser-grained, poorly-sorted debris flow material from tributaries which drained the rapidly exhuming Ailao Shan shear zone. These coarse deposits were presumably subsequently reworked by the axial drainage system.

The presence of Ailao Shan cobbles is a defining characteristic of the Ailao Shan Conglomerate. Deposition of this unit indicates the first arrival of shear zone gneiss at the Earth's surface; all sediment subsequently deposited in the adjacent basin will contain at least some material derived from the shear zone. Ailao Shan gneiss and leucogranite is unlike any other lithology within the Yangtze platform adjacent to the Red River fault, and so is easily identified. The Ailao Shan Conglomerate often contains material derived from the Yangtze platform, but once Ailao Shan rocks were exposed and began to be eroded and deposited in the adjacent basin, this material dominated the sediment load of the axial drainage system.

The Ailao Shan Conglomerate contains re-worked clasts of the Limestone Conglomerate member (Fig. 6e) confirming that (1) this unit is younger than the Limestone Conglomerate, as our mapping indicates, and that (2) older Cenozoic strata were subject to reworking, and therefore deformation, exposure, erosion and redeposition, during deposition of younger parts of the sedimentary section.

Fossils. In the Nansa map area, we collected macroscopic plant fossils from the Transitional Sandstone and the Ailao Shan Conglomerate. These were identified by a Chinese paleobotanist, Dr. Li, and correlated with other known fossil flora localities in Yunnan at Xiaolongtan, Jianchuan and Jinggu (Li, personal communication 2002). Details are given in Appendix A. Localities RR99-19, RR00-1 and RR00-15 are northeast of Langdun (Fig. 2) in roughly correlative positions, and yield Miocene ages. At one fossil locality closer to Nansa (Fig. 2, RR99-13), however, fossils indicate a Late Oligocene to Early Miocene age. Fossils in the Ailao Shan Conglomerate (Fig. 2, RR00-13 near Wubang and RR00-105 near the southeast end of the map area) are Miocene in age. These fossils thus indicate that the Limestone Conglomerate and Transitional Sandstone are probably Late Oligocene to Miocene in age and the Ailao Shan Conglomerate was probably deposited entirely in Miocene time in the Nansa region.

Structure

Red River fault. In order to identify earlier deformational features, it is first necessary to recognize the youngest deformation, that associated with the Red River fault. However, we discuss these observations only briefly here, as they are explored in greater detail in Chapter 3 of

this thesis. In the Nansa region, the Red River fault comprises several major strands, marked by sub-vertical gouge zones and displacement of modern geomorphic features. One major fault separates Ailao Shan gneiss from slightly metamorphosed T₃ rocks (Fault A, Fig. 2), and another major fault strand separates T₃ from T₂ (Fault B, Fig. 2). Both faults show evidence for right-lateral displacement of tributaries to the Red River. Neither of the major faults, nor the minor faults in this area show evidence for dip-slip displacement. Between Nansa and Wubang (Fig. 2), lacustrine mudstone and gypsum is intensely deformed, with a sub-vertical, pervasive shear fabric between the two major strands of the Red River fault. Any pre-Red River fault fabric has been destroyed in these fault zones. These observations are further discussed in Chapter 3 of this thesis.

Ailao Shan contact. In the Nansa map area, the contact between the Ailao Shan gneiss and the adjacent country rock is an active, sub-vertical strand of the Red River fault (Fault A, Fig. 2). Between Nansa and Wubang, Wubang mudstone is sub-vertically foliated immediately adjacent to this contact. Southeast of Wubang, T₃ sedimentary rocks adjacent to the contact are also sheared and gypsum is injected along fault splays. Streams which cross this contact are consistently offset right-laterally. If the original contact between the Ailao Shan gneiss and Yangtze platform rocks was a distinct structure or was different in character, it has been modified by this active strand of the Red River fault.

Another major strand of the Red River fault separates T₂ and T₃ sedimentary rocks (Fault B, Fig. 2). Streams are offset right-laterally where they cross this fault, and rocks on either side of the fault display sub-vertical shear fabrics. However, the juxtaposition of Triassic units across this fault suggests earlier left-lateral displacement along Fault B. Faults A and B bound a narrow sliver of T₃ rocks. The nearest exposure of T₃ rocks northeast of Fault B is near Nansa (Location 1, Fig. 2). If these units can be matched, they record ~30 km left-lateral displacement (the amount necessary to restore the most southeasterly exposure of T₃ rocks within the sliver to a position adjacent to T₃ rocks near Nansa, see Location 1 note, Fig. 2). However, low-grade metamorphism affected this sliver of rocks and indicates minor exhumation from shallow crustal levels. The sub-surface extent of this unit is not known, and therefore no unique piercing point can be established across this fault. This deformation is related to exhumation of the Ailao Shan

shear zone because (1) right-lateral displacement on the Red River fault cannot account for this juxtaposition, and (2) it is reasonable to expect that narrow slivers of rock will be exhumed or displaced left-laterally adjacent to the Ailao Shan shear zone, which may have accommodated 700 ± 200 km left-lateral displacement and ~ 18 km exhumation of shear zone rocks (Leloup and Kienast, 1993; Leloup et al., 1995).

Reverse faults on northeast side of valley: Funke reverse fault. The Funke fault (Figs. 3 and 6g) is a steep ($\sim 80^\circ$), southwest-vergent reverse fault along the northeast side of the valley between Nansa and just to the southeast of Langdun, named after a nearby village. This fault is associated with overturned Cenozoic strata between Nansa and Funke (Fig. 6h), but appears to die out to the southeast of Langdun, where it is truncated by a sub-vertical strand of the Red River fault (Fault C, Fig. 2). Limestone Conglomerate and Transitional Sandstone rocks up to a few hundred meters below the reverse fault display a strong fabric sub-parallel to the fault, with gouge development, grain-size reduction and apparent rotation of cobbles (Fig. 6h). This fabric is enhanced by erosion. Above the contact, rocks are relatively less deformed. Northeast of Langdun, several reverse faults bounding slices of Limestone Conglomerate and Transitional Sandstone are present (Location 3, Fig. 2), though exposure is poor and the faults cannot be traced far to the northwest or southeast. Langdun Formation rocks adjacent to these faults appear to be less deformed, though gouge is still present along the faults and minor fault splays within the conglomeratic units are present. The Funke reverse fault involves all three Oligo-Miocene fluvial units and therefore post-dates deposition of these rocks or is syn-depositional. We have not observed a similar structure in the Yuanjiang map area, but Chinese geologic maps (Bureau of Geology, Yunnan, 1990) indicate reverse faulting involving Cenozoic sedimentary rocks may continue to the north of Nansa towards the town of Honghe (Fig. 1b). This is supported by our preliminary observations at Honghe where steep, north-dipping reverse faults and associated folds are present. If this fault is associated with exhumation of the Ailao Shan shear zone, it probably has a component of strike-slip displacement as well, though we could not constrain this further.

Thrust fault on southwest side of valley: Wubang thrust fault. We mapped a moderately dipping ($\sim 45^\circ$) zone of intensely sheared rock well-exposed near Wubang, for which we name

the structure (Figs. 2 and 6a). The Wubang thrust dips southwest toward the Ailao Shan shear zone, but is separated by ~1 km from the contact with the shear zone rocks. This thrust places Wubang Mudstone over Ailao Shan Conglomerate (Fig. 6b), and may have a significant strike-slip separation as well. Conglomeratic rocks below the thrust are disturbed, and some cobbles, particularly those larger than ~20 cm, are fractured. However, deformation above the thrust, within the Wubang Mudstone, is more extensive. We observed gouge zones and foliated mudstone and gypsum with a shear fabric subparallel to the Wubang thrust up to several hundred meters southwest of the thrust. The Wubang thrust fault is truncated or overprinted by the Red River fault between Nansa and Wubang and in other localities to the southeast. Here, subvertical fabrics predominate, related to recent deformation. The presence of Ailao Shan Conglomerate in the footwall of this fault (Fig. 6b), indicates that shortening must post-date or occur during deposition of the conglomerate. At one location (Location 4, Fig. 2), however, relatively undeformed Ailao Shan Conglomerate depositionally overlies the Wubang Mudstone. The contact is exposed along a valley to the east side of this deposit. This relationship suggests that at least part of the Ailao Shan Conglomerate was deposited after development of the Wubang thrust fault. On the basis of these observations, thrusting along this fault occurred during deposition of the Ailao Shan Conglomerate. Similar relationships are present in the Yuanjiang area.

Extensive folding and deformation of Cenozoic section. Folding and small-scale faults occur in nearly every outcrop of the Cenozoic strata. Bedding is often difficult to identify because of pervasive shearing and associated rotation of clasts, particularly in sand-poor parts of the section. Folds are therefore rarely traceable over even the length of an outcrop, and were primarily identified by the presence of regions of opposing dip separated by regions in which bedding could not be determined. Some of the pervasive folding and shearing of the Cenozoic section is probably related to displacement along strands of the Red River fault, particularly small scale folds developed immediately adjacent to the active faults. However, folding and deformation may also be related to earlier episodes of deformation. On a large scale, the Cenozoic section is broadly deformed into a syncline, overthrust on the northeast and southwest by the Funke reverse fault and the Wubang thrust respectively (Figs 2 and 4 F-H), and this deformation is thus distinct from that associated with the Red River fault.

Yuanjiang Map Area:

The Yuanjiang map area (~40 km long, ~6 km wide, Figs. 3 and 4) is comparable to the Nansa map area in a number of ways. The Cenozoic stratigraphy is similar, though at Yuanjiang the Transitional Sandstone is absent, the Limestone Conglomerate contains clasts from a wider variety of Yangtze Platform lithologies, and there is very little Wubang Mudstone. The Cenozoic units rest on rocks of the Yangtze Platform and are bounded to the southwest by the Ailao Shan shear zone. The map area is divided into two parts by the Yuanjiang basin. To the southeast of the Yuanjiang basin, Tertiary strata are capped by ~300 m of relatively undeformed Quaternary sediment.

Stratigraphy

Pre-Cenozoic rocks. Northwest of the Yuanjiang basin, Cenozoic rocks are deposited on T₃ strata (Fig. 3) which are essentially identical to the T₃ rocks in the Nansa area, and consist of coarse sandstone, tan siltstone, shale, occasional carbonate rocks, and a distinctive purple and green shale. To the northeast of the Red River fault, T₃ strata are unmetamorphosed. To the southwest they are slightly higher grade, evidenced by the presence of quartzite and phyllite. Southeast of Yuanjiang, Cenozoic rocks rest on a variety of Proterozoic, Silurian and Devonian lithologies of the Yangtze platform, mostly limestone and shallow-marine deposits. T₃ strata are present in a sliver between these units and the Ailao Shan shear zone.

Early Oligocene lacustrine strata: Wubang Mudstone. Only limited outcrops of extensively deformed red mudstone and gypsum are present in the Yuanjiang map area (Fig. 3). These rocks appear very similar to the Wubang Mudstone in the Nansa map area: they consist of fine-grained red mudstone, black, gray and white gypsum, and occasional green mudstone which is probably the un-oxidized equivalent of the red mudstone. Massive gypsum dominates the unit in some places, particularly near Location 2 (Fig. 3). Deformation has obscured the stratigraphic relationship between this unit and the rest of the Cenozoic rocks. As at Nansa, we see no evidence for any coarse grained material within this unit, and because it is unmetamorphosed, it must be younger than the slightly metamorphosed T₃ rocks with which it is associated. Because of the similar lithology and structural position, we correlate these rocks with the better constrained Early Oligocene lacustrine rocks in the Nansa map area, and therefore assume the

age and relationship of the Wubang Mudstone with the pre-Cenozoic and Oligo-Miocene section to be equivalent. This unit was probably deposited in Early Oligocene time on slightly metamorphosed T₃ strata, was either of limited original extent, or was subsequently almost entirely erosionally removed, and today is found only in a few places in intensely sheared contact with T₃ rocks and Oligocene-Miocene fluvial sedimentary rocks.

Oligocene-Miocene fluvial strata: Langdun Formation. Two distinct, conformable units correlative with the Limestone Conglomerate and the Ailao Shan Conglomerate described in the Nansa map area are also present in the Yuanjiang map area.

Limestone Conglomerate. Because of the similar composition, sedimentary facies, stratigraphic position, and the presence of comparable fossils (see discussion below and Appendix A), we equate this unit with the Limestone Conglomerate in the Nansa region. In the Yuanjiang area, the Limestone Conglomerate consists of well-sorted, fluvial conglomerate and sandstone (Fig. 5e) with occasional occurrences of angular, locally derived debris flow units (Fig. 5f). The unit is particularly well-exposed near Location 4 (Fig. 3), where it is dominated by rounded, fist-sized clasts. At fossil sites RR00-18 and RR00-19 (Fig. 3), the Limestone Conglomerate is finer grained, and bedding is more apparent. Bed thickness ranges from 10 cm to ~1m. Fine-grained, fossil bearing horizons are common at these two locations, and clasts are generally under 5 cm in diameter (Table 1). This unit is found only in two locations, however, northwest of the Yuanjiang basin (both near Location 2, Fig. 3). Here, the Limestone conglomerate is well-rounded and well-sorted. Clast lithology throughout the Yuanjiang map area is dominated by T₂ limestone and other rocks from the Yangtze platform (Table 1, e.g., Yuanjiang 1). Interestingly, the closest occurrence of T₂ limestone is ~40 km *downstream* of this unit (Bureau of Geology, Yunnan, 1990), as a result of right-lateral displacement along the Red River fault, a relationship explored in Chapter 3 of this thesis. The unit is almost certainly in depositional contact with Yangtze platform rocks to the northeast of the Red River fault, although the contact was not exposed in the map area. The original contact between the Limestone Conglomerate and T₃ units immediately between the Red River fault and the Ailao Shan shear zone was probably also depositional, but today it has been modified by deformation related to the Red River fault (Location 2, Fig. 2).

Ailao Shan Conglomerate. This fluvial conglomerate contains abundant clasts derived from the Ailao Shan shear zone, and because of this, and the similar sedimentary facies and stratigraphic position, we correlate this unit with the Ailao Shan Conglomerate in the Nansa map area. Southeast of Yuanjiang, clasts are particularly well-rounded, well-sorted and imbricated (Fig. 5b). In this area, the Ailao Shan Conglomerate is appears to be conformably deposited on Limestone Conglomerate (Location 4, Fig. 3). The contact is not exposed, but bedding within the Limestone Conglomerate below the contact and the Ailao Shan Conglomerate above are sub-parallel to the contact. These exposures bracket the position of the contact to within a few meters. Deposition of the Ailao Shan Conglomerate signals the arrival of shear zone gneiss at the Earth's surface, which subsequently dominates the clast composition of the adjacent axial drainage system, though material continued to be contributed to the basin from the Yangtze platform as well. Northwest of Yuanjiang, the Ailao Shan Conglomerate is almost always deposited directly on T₃, indicating the Limestone Conglomerate was erosionally removed, or it never was present in that region. Here, the conglomerate is generally well-rounded and well-sorted. To the northwest, the conglomerate is finer grained, dominated by sandy horizons, and bedding is usually clearly defined.

Fossils. Fossils collected from the Limestone Conglomerate in one locality southeast of Yuanjiang (Fig. 3, RR00-18) are Miocene in age and correlate to fossils from the Nansa map area. Fossils from the Langdun Formation are therefore Miocene in age with the exception of one locality in the Nansa area which is Late Oligocene to Early Miocene in age (see above). The depositional age of the sedimentary rocks may vary along the length of the shear zone, and the time at which shear zone rocks reached the surface may have varied as well. Thus, in the Nansa map area, the Limestone Conglomerate and Transitional Sandstone may be slightly older (Late Oligocene to Miocene) than at Yuanjiang, where fossils in the Limestone Conglomerate indicate only Miocene deposition.

Quaternary fluvial sediments. Southeast of Yuanjiang, ~300 m of horizontally bedded, coarse boulder conglomerates are deposited on a sub-horizontal unconformity, capping deformed rocks of the Langdun Formation and T₃ rocks. These poorly consolidated sediments could be recent

fluvial deposits, but because of the large clast size (up to 1 meter) and because the clasts are nearly exclusively derived from the Ailao Shan shear zone, they may be the incised remnants of alluvial fans which stretched from the Ailao Shan across the entire Red River valley. Large modern alluvial fans are common in this region today, and partially fill the modern Yuanjiang basin. The age of these deposits is uncertain, but Chinese maps assign them to the Quaternary (Bureau of Geology, 1990), which is consistent with the lack of lithification and a lack of deformation except immediately adjacent to the Red River fault (Location 3, Fig. 3). The presence of these sediments indicates a beveling of pre-Quaternary sedimentary rocks, followed by local deposition of this unit, and subsequent incision along the Red River.

Structure

Red River fault. Northwest of Yuanjiang (Fault A, Fig. 3) the Red River fault consists of a single, sub-vertical main strand marked by an extensive gouge zone up to 100 m across. Both Langdun Formation and T₃ rocks are involved in this deformation, and are penetratively deformed. A major tributary to the Red River follows this fault zone into the Yuanjiang basin (Fig. 3). Several faults strike oblique to the main strand and show evidence for extension: three faults are to the northwest of Mandan and two faults are southwest of Fault A near the Yuanjiang basin (Fig. 3). An important normal fault, adjacent to the Ailao Shan shear zone near the northwest end of the map area, merges with the main strand to the southeast (Fault C, Fig 3). Strata between the Ailao Shan shear zone rocks and the Fault A are folded obliquely to the main strand, about approximately east-west trending axes, consistent with right-lateral shear. These folds are defined by the folded contact between the Ailao Shan Conglomerate and the T₃ rocks, discussed below. The precise geometry of these folds is difficult to determine because of uncertainty as to the original geometry of this contact. South of Yuanjiang, a single main fault (Fault B, Fig. 3) is marked by an extensive gouge zone, similar to that along Fault A. Slivers of T₃, Wubang Mudstone and Langdun Formation are closely interleaved, particularly near the southeast end of the map area. Foliation within this deformed zone is sub-vertical. Several tributaries to the Red River flow along this fault zone and are offset right-laterally. We observed one fold adjacent to Fault B (near fossil site RR00-19) with an east-west axial orientation, consistent with right-lateral shear. The two main faults northwest and southeast of Yuanjiang (Faults A and B, Fig. 3) are not aligned, but rather interact to produce the Yuanjiang pull-apart

basin. The implications of these observations for the Red River fault are explored in Chapter 3 of this thesis.

Ailao Shan contact. In the northwestern part of the Yuanjiang map area, a steeply dipping normal fault (Fault C, Fig. 3) has modified the contact between the Ailao Shan shear zone and rocks to the northeast. Elsewhere, however, the original contact is preserved. It is poorly exposed, and we were unable to observe the contact in outcrop. However, we constrained the dip of the contact by carefully locating outcrops in valleys and on adjacent ridges and find that the contact dips steeply to the southwest ($\sim 80^\circ$). This fault is associated with displacement along the Ailao Shan shear zone, and therefore probably has accommodated a large amount of left-lateral slip. However, exhumation of the shear zone has also been accommodated along this structure, and unless it has been significantly rotated, the original contact therefore has a reverse sense separation. Furthermore, this observation indicates that the Red River fault is a distinct structure from the older fault responsible for unroofing the Ailao Shan shear zone

Reverse faults on southwest side of valley: Mandan and Zhega reverse faults. Structurally similar to the Wubang thrust fault in the Nansa map area (Fig. 2), these thick zones of gouge and sheared rock are well-developed and traceable along almost the entire length of the map area (Fig. 3). Both northwest and southeast of Yuanjiang, the faults dip moderately ($\sim 45^\circ$) to the southwest and the gouge marking the faults can be up to several hundred meters thick. These faults may have accommodated an unknown amount of strike-slip displacement if they are associated with the Ailao Shan shear zone, but older-over-younger relationships and the dip of these faults also suggest thrust-sense separation. Northwest of Yuanjiang the Mandan thrust fault lies between the Ailao Shan shear zone and the main strand of the Red River fault, and is localized in a distinctive purple and green phyllite horizon within the T₃ rocks (Fig. 6d). It is truncated by active strands of the Red River fault near the Yuanjiang basin. A complicated backthrust along this fault (Location 2, Fig. 3 and cross section B, Fig. 4) folds Limestone Conglomerate and Ailao Shan Conglomerate. The rocks in the vicinity of this backthrust are sheared parallel to the opposing structures which define the backthrust. Deformation is concentrated along the Mandan thrust fault, but is observed locally throughout the region between the Ailao Shan shear zone and the Mandan fault. Southeast of the Yuanjiang basin, the

Zhega fault is well-developed (Fig. 3). This fault is defined by a thick (~200 m) gouge zone which dips to the southwest towards the Ailao Shan shear zone (Fig. 6c). The sheared zone cuts Limestone Conglomerate near fossil site RR00-18 (Fig. 3) and passes into T₃ rocks to the southeast. Deformation is not confined to the Zhega fault, but occurs throughout the region between the Ailao Shan shear zone and the main strand of the Red River fault (Fault B), and T₃ is thrust over Limestone Conglomerate.

Deformation associated with these faults affects T₃ rocks, Wubang Mudstone, Limestone Conglomerate (Fig. 6c) and Ailao Shan Conglomerate, and therefore post-dates deposition of these units. In many places the Mandan fault places T₃ sedimentary rocks above Ailao Shan Conglomerate. As in the Nansa map area, however, relatively undeformed Ailao Shan Conglomerate is also deposited on T₃ strata between the Red River fault and the Ailao Shan shear zone (Location 1, Fig. 3). The contact between these two units is exposed in a few localities, and is clearly depositional. Bedding within these deposits of Ailao Shan Conglomerate are generally low (less than 20°) but T₃ strata below are more strongly deformed. Because Ailao Shan Conglomerate was apparently deposited both before and after thrusting along the Mandan fault, we infer that thrusting in this extensively gouge-marked zone occurred syn-depositionally.

Extensive folding and deformation of Cenozoic section. A number of broad folds in this region, defined by the basal contact of the Ailao Shan Conglomerate, are consistent with an origin related to right-lateral displacement along the Red River fault. However, pervasive deformation within the Cenozoic section may have been caused by older deformation as well. In one exceptional outcrop, well-bedded Limestone Conglomerate is folded with a sub-horizontal axial plane, with a fold axis of 210° (Fig. 6f). We suspect that the entire Cenozoic section may be deformed in a similar way, but because of the sparseness of outcrop and deep weathering this can not be confirmed.

DISCUSSION

From the mapped relationships in the study area a sequence of depositional and deformational events and their interrelationships can be established. This sequence has important implications

for the exhumation of the Ailao Shan shear zone as well as for the broader tectonic development of the southeastern margin of the Tibetan Plateau.

Existing Framework

Deposition and deformation northeast of the Ailao Shan shear zone can be correlated with regional events and thermochronologic studies of the shear zone to define 5 stages of development (Fig. 7). (1) Early deformation along the Ailao Shan shear zone (from ~34 Ma, Gilley et al., 2003) without significant unroofing of the shear zone. Left-lateral shearing was probably close to strike-slip at this time with no oblique component. (2) Early cooling within the Ailao Shan shear zone, resulting from an oblique component to left-lateral displacement, but before Ailao Shan gneisses were exhumed to the Earth's surface. From $^{40}\text{Ar}/^{39}\text{Ar}$ thermochronologic data, this period began some time before ~25 Ma in the southeast and progressed northwest along the shear zone (Harrison et al., 1996). (3) Continued exhumation of the Ailao Shan shear zone resulting in the arrival at the Earth's surface of Ailao Shan gneisses. Timing of this stage is not directly addressed by existing thermochronology, but probably lags behind the onset of rapid exhumation by a few million years and may continue beyond the youngest cooling ages recorded by $^{40}\text{Ar}/^{39}\text{Ar}$ (~17 Ma, Harrison et al., 1996) or fission-track methods (10-13 Ma; Bergman et al., 1997). (4) Reduction of relief of the Ailao Shan shear zone after cessation of tectonically driven erosional exhumation and development of the regional low-relief landscape (Schoenbohm et al., in press and Chapter 4). This period is younger than the youngest rapid cooling along the shear zone recorded by $^{40}\text{Ar}/^{39}\text{Ar}$ data (~17 Ma, Harrison et al., 1996) and may also be younger than a rapid cooling interval recorded by fission-track data (~10 Ma, Bergman et al., 1997; Leloup et al., 2001). (5) Development of the active Red River fault (Allen et al., 1984; Wang E. et al., 1998; Replumaz et al., 2001) and ~1.5 km surface uplift and river incision (Schoenbohm et al., in press and Chapter 4) probably in Pliocene time (Leloup et al., 1993; Wang E. et al., 1998; Replumaz et al., 2001; Chapter 3). These constraints form a framework for understanding relationships indicated by our mapping of Cenozoic sedimentary rocks, and in turn, new constraints developed in this study help to refine the regional framework.

History of deposition and deformation recorded by Cenozoic strata

Early Deformation, Stage 1

Displacement of slightly metamorphosed slices of T₃ sedimentary rocks along the northeast side of the Ailao Shan shear zone in both the Yuanjiang and Nansa map areas (Figs. 2 and 3) are the earliest indication, outside of the shear zone gneiss, of deformation associated with left-lateral strike-slip movement along the Ailao Shan shear zone (Fig. 7, Stage 1a). In the Nansa map area (Fig. 2, Location 1), we cannot define a unique piercing point, but displacement could be 10's of km's (the current apparent offset is ~30 km in a left-lateral sense, but this fault was reactivated right-laterally by the Red River fault, with potentially greater than 40 km displacement (Chapter 3), so total left-lateral displacement could be 70 km or more. The right-lateral reactivation of an older, left-lateral fault is similar to relationships observed on the Jianshui, Quijiang and possibly Chuxiong faults to the northeast (Burchfiel and Wang, 2003), and indicates that left-lateral deformation was not confined entirely to within the Ailao Shan shear zone, but extended on at least a few faults into the region to the northeast of the shear zone.

Lacustrine mudstone and gypsum (Wubang Mudstone), deposited on slightly metamorphosed T₃ strata in the Nansa map area (Fig. 2) place further important constraints on the timing and structural style of early deformation along the Ailao Shan shear zone (Fig. 7, Stage 1b). Because these Cenozoic strata are unmetamorphosed, their deposition must post-date exhumation of metamorphosed T₃ rocks, which occurred during left-lateral displacement along the shear zone. However, the fine-grained character of the Wubang rocks, despite their proximal position to the Ailao Shan shear zone, precludes significant development of relief or exhumation of the shear zone or other rocks during their deposition. The lacustrine rocks are locally preserved, present only in the northwestern part of the Nansa map area and in isolated locations in the Yuanjiang map area. On the basis of these constraints, we interpret these strata to have been deposited in sag ponds or small pull-apart basins along strands of the early Ailao Shan shear zone after minor exhumation of T₃ rocks, but before rapid exhumation began. Geochronological constraints, as outlined above, indicate this period was from ~34 Ma (Gilley et al., 2003) to before ~25 Ma, depending on location (Harrison et al., 1996), and indicate the strata are Early Oligocene in age.

Exhumation of the Ailao Shan shear zone, Stages 2 and 3

Late Oligocene to Miocene sedimentary rocks of the Langdun Formation are fluvial conglomerates mixed with occasional debris flow deposits, very similar to the depositional setting found today along the Red River. They reflect the presence of significant relief in the area, and are the product of erosion of Yangtze platform and Ailao Shan rocks (Fig. 7, Stage 2 and 3). Ailao Shan derived clasts are found only in the upper part of the section, in the Ailao Shan Conglomerate, confirming that the arrival of the shear zone gneiss at the Earth's surface lagged behind the onset of rapid exhumation. (Fig. 7, Stage 3) The Langdun Formation thus spans exhumation prior to (stage 2) and after (stage 3) exposure of deeper structural levels of the Ailao Shan shear at the Earth's surface. The Late Oligocene to Early Miocene age based on plant macrofossils is consistent with geochronology indicating rapid cooling during the same time period (25-17 Ma, Harrison et al., 1996). Our data also indicate that exposure of shear zone gneiss may have been earlier in the Nansa region, where fossils in the Transitional Sandstone are Late Oligocene to Miocene, while fossils in the stratigraphically lower Limestone Conglomerate in the Yuanjiang region are Miocene. This is broadly consistent with diachronous unroofing of the shear zone as interpreted by Harrison et al. (1996).

Today the Ailao Shan shear zone separates rocks of the Yangtze platform from Indochina sedimentary rocks. However, prior to the arrival of the gneiss at the Earth's surface, South China and Indochina rocks must have been in direct contact, as they are farther north near Midu (Fig. 1). It is therefore surprising that clasts which comprise the Limestone Conglomerate appear to be derived exclusively from the Yangtze platform to the northeast, in most cases dominated by T₂ limestone. This suggests Yangtze platform rocks capped the Ailao Shan gneiss prior to exhumation of the shear zone, as we have schematically illustrated in Figure 7, Stage 2. These capping rocks were eroded and deposited in the adjacent basin during early rapid cooling of shear zone rocks, and a drainage divide must have separated the Cenozoic basin from potential Indochina source rocks (Fig. 7, Stage 2). Sediment derived from these capping rocks is identical in composition to rocks of the Yangtze platform to the northeast, suggesting that if there was significant displacement on the Ailao Shan shear zone at that time, it must have been to the southwest, probably along the Indochina-South China contact.

Similar analysis for the Ailao Shan Conglomerate is difficult because not enough is known of the lateral distribution of rock types within the Ailao Shan shear zone to match cobbles in the conglomerate with possible source rocks in the shear zone. However, given the current shear zone geometry, gneisses are only present southwest of the Red River fault to the Vietnamese town of Pho Lu (Leloup et al., 2001, termination of shear zone is just beyond southeast corner of Figure 1b) approximately 150 km from the southeast end of the Nansa map area. Right-lateral displacement along the Red River fault would reduce the apparent left-lateral displacement by at least 40 km (Chapter 3). Though we cannot constrain total left-lateral displacement on the Ailao Shan shear zone, these data suggest that displacement since the deposition of the Ailao Shan Conglomerate (Miocene) can be no greater than ~190 km. However, it is unclear how the Ailao Shan and Day Nui Con Voi in Vietnam relate, and how the geometry and current exposure of the shear zone in Vietnam may have been affected by young normal faulting, and therefore this displacement remains speculative.

The fluvial nature of the Langdun formation and the correlation of rocks at Yuanjiang and Nansa indicates that a through-going river was established around the same time that rapid exhumation of the shear zone began. During deposition of the Early Oligocene lacustrine rocks of the Wubang Mudstone, an axial river had not yet been established. The Red River has apparently existed in approximately the same location since Oligocene time throughout exhumation of the shear zone, establishment of the low-relief landscape, surface uplift and subsequent river incision. This speaks to the persistence of large rivers along major crustal discontinuities, a topic we will return to below.

Mapped relationships indicate that the Cenozoic section was syn-depositionally shortened. This is expected, because deposition of the Landun Formation (Late Oligocene to Miocene) overlaps with the period of rapid cooling (25-17 Ma; Harrison et al., 1996), and presumed tectonically driven erosional exhumation of the Ailao Shan shear zone. It is therefore likely that any rocks adjacent to the deforming shear zone would also be deformed as they were being deposited. The original contact between rocks of the Ailao Shan shear zone and the Yangtze platform dips 80° SW where it is unmodified by the younger Red River fault in the Yuanjiang map area (Fig. 3). Approximately 1 km to the northeast of this contact are other southwest dipping structures (~45°)

defined by thick gouge zones, present throughout the map area (Mandan and Zhelong thrust faults, Fig. 3 and Wubang thrust fault, Fig. 2). These faults affect T₃ strata, Early Oligocene lacustrine mudstone and gypsum, the Limestone Conglomerate and the Ailao Shan Conglomerate. In many places, deformed Ailao Shan Conglomerate is in the footwall of these faults. Northwest of Yuanjiang (Location 1, Fig. 3) and in one place near Wubang in the Nansa map area (Location 4, Fig. 2), relatively undeformed Ailao Shan Conglomerate also positionally overlies deformed sediment between these faults and the Ailao Shan shear zone. Thrust sense displacement along these faults thus occurred during deposition of the Ailao Shan conglomerate, and also therefore during exhumation of the shear zone. Near Nansa (Fig. 2), Triassic T₂ limestone of the Yangtze platform is also thrust above the Cenozoic section, overturning the section between Nansa and Langdun (Funke reverse fault, Fig. 2). This shortening must post-date deposition of the Limestone Conglomerate, Transitional Sandstone and at least the lower part of the Ailao Shan Conglomerate, but could be coeval with later Ailao Shan Conglomerate deposition. A strong argument for syn-depositional deformation come from clasts derived from the Limestone Conglomerate found in the Ailao Shan Conglomerate. These clast indicate deformation and subsequent erosion and redeposition of parts of older parts of the Cenozoic section within younger parts. Our field data thus indicate shortening during deposition of the Late Oligocene to Miocene Langdun Formation, and during exhumation of the Ailao Shan shear zone.

The thrust and reverse faults we observe in the Nansa and Yuanjiang areas, particularly where they converge on the basin from both sides, provide a mechanism for forming and deepening the basin and placing it in a low structural position: the basin has been re-exhumed by surface uplift and river incision in the Pliocene or later (Schoenbohm et al., in press and Chapter 4). Numerical modeling of asymmetrical basins bounded by high-angle reverse faults shows that deep, narrow basins can form adjacent to similar faults, narrowing and deepening as they develop (Zhang and Bott, 2000). The Ventura basin in California, which is overthrust from both the north and south by the San Cayetano and Oak Ridge faults respectively (Niño et al., 1998), may be an analogue for this basin.

Post tectonically driven erosional exhumation, Stages 4 and 5

After the cessation of tectonically driven erosional exhumation and rapid cooling, the Ailao Shan shear zone probably was of high relief, and so continued to erode, and sediments derived from the shear zone may have been deposited in an adjacent, but now undeforming basin during this time (Fig. 7, Stage 4). This period began sometime after 17 Ma (Harrison et al., 1996), but because the lower temperature (<200°C) cooling history of the shear zone is poorly constrained, timing is uncertain. Eventually the area was reduced to low relief and relatively low elevation (Schoenbohm et al., in press and Chapter 4). Finally, probably in Pliocene time, the Red River fault developed, modifying the original contact between the Ailao Shan and the Yangtze platform (Fig. 7, Stage 5). The area also experienced ~1.5 km surface uplift and was incised by the Red River, re-exposing the Cenozoic basin (Schoenbohm et al., in press and Chapter 4).

Exhumation of the Ailao Shan shear zone

The nature of exhumation of the Ailao Shan shear zone is a central question motivating this study. The shear zone was exhumed from ~18 km depth (Leloup and Kienast, 1993). Most of the exhumation probably occurred during rapid cooling from before ~25 to after ~17 Ma (Harrison et al., 1996). In this study, we show that Ailao Shan rocks reached the surface in Miocene time. Rocks of the Yangtze platform to the northeast and the Langping-Simao basin to the southwest are largely unmetamorphosed, meaning that exhumation was concentrated in the Ailao Shan shear zone, a zone < 20 km wide and hundreds of kilometers long (Fig. 1)

Transpressional (Wang E. et al., 1998) and transtensional (Harrison et al., 1996) exhumation mechanisms have been suggested, or a combination of both (Leloup and Kienast, 1993; Leloup et al., 1995). In any scenario, the strike-slip component along the shear zone is the most important: if left-lateral displacement is 700 ± 200 km (Leloup et al., 1995), a small oblique component, either extensional or contractional, can result in significant exhumation. Transpression and transtension, however, will result in different deformation patterns and have different implications for the regional tectonic setting.

This study demonstrates that the northeast margin of the shear zone was undergoing shortening during exhumation, evidenced by syn-depositional thrust and reverse faults and folding of

adjacent Oligocene and Miocene strata. The spatial and temporal relationship between the Ailao Shan and the Lanping-Simao fold and thrust belt also implies shortening during unroofing of the shear zone (Leloup et al., 1995; Wang E. et al., 1998). On this basis, it is reasonable to argue for a transpressional exhumation mechanism.

Contradictory evidence from the northeast side of the shear zone has been used in support of a transtensional exhumation model. Previous workers have argued on the basis of triangular facets and the steepness of the northeast side of the range that the Red River fault has a significant extensional component (Allen et al., 1984; Leloup et al., 1995; Replumaz et al., 2001) and the Ailao Shan shear zone has been recently partially exhumed by activity on the Red River fault (Leloup et al., 1995; Harrison et al., 1996). However, Schoenbohm et al. (in press and Chapter 4) have demonstrated that post-Miocene vertical displacement is less than ~750 m on the northern part of the active fault, and is negligible in the southeast near Nansa. Because the low-relief landscape has not yet been erosionally removed from the crest of the Ailao Shan, there has been no significant exhumation of the shear zone along the Red River fault since Pliocene time (Schoenbohm, in press and Chapter 4). Furthermore, we have established in this study that the original contact between the Ailao Shan shear zone and the Yangtze platform is distinct from the Red River fault and is a steeply southwest dipping reverse fault. Recent activity along the Red River fault therefore plays no role in the exhumation of the Ailao Shan shear zone.

Another line of argument in favor of transtensional exhumation is the sharp contrast between amphibolite grade Ailao Shan gneiss and unmetamorphosed Yangtze platform rocks to the northeast, which could be the result of an extensional fault. The contrast in metamorphic grade is less pronounced on the southwest side of the Ailao Shan. An extensional fault would also explain cross-strike thermochronologic data indicating deeper exhumation along the northeast side (Harrison et al., 1996). However, transpressional exhumation can also produce these features. Transpression exhumes deep crustal rocks by producing (1) a vertical conduit through wrenching, and (2) vertical flow from contraction (Fossen and Tikoff, 1998). Rocks within the shear zone are extruded in a steep, narrow crustal channel, and are much more strongly exhumed within the shear zone than without, creating the grade contrast (Tikoff and Teyssier, 1994; Dewey et al., 1989; Fossen and Tikoff, 1998). Examples of transpressional exhumation of

narrow shear zones include: the Great Slave Lake shear zone in Canada (Hoffman, 1987; Hanmer, 1988), the Alpine Fault in New Zealand (Sibson et al., 1979; Walcott, 1998; Claypool et al., 2002), the Coast shear zone in Alaska and Canada and the Idaho shear zone in western Idaho (McClelland et al., 2000) and the Karakoram fault zone in China and Pakistan, particularly in the Pangong region (Searle, 1996; Searle et al., 1998; Dunlap et al., 1998). Deeper exhumation along one portion of a shear zone may result from strain partitioning across the zone, and/or potentially from the interaction with surface processes.

Transpression must be coupled with erosion to exhume a shear zone. In most cases, rock uplift associated with vertical extrusion of the shear zone channel would produce surface uplift and greater relief which would in turn promote higher erosion rates. In case of the Ailao Shan, we suggest that the Red River was an important erosive agent, and was in fact developed in its present location as early as Oligocene time, around the same time that exhumation began. At that time the Yangtze and other major Tibetan rivers may have flowed through the Red River to the South China Sea, increasing the drainage area and the erosive potential of the Red River (these rivers were subsequently diverted during early surface uplift and development of the eastern Plateau margin (Clark et al., in press)). Erosion along the Red River and its tributaries could cause deeper exhumation along the northeast margin of the shear zone, as erosion has been argued to play a role in shaping exhumation patterns in other regions (e.g. Zeitler et al., 2001; Koons et al., 2002). Interestingly, each of the three major, deeply exhumed shear zones of the southeastern plateau margin, the Gaoligong Shan, the Chong Shan and the Ailao Shan, is associated with a major river, the Salween, Mekong and Red Rivers respectively. Lacassin et al. (1998) and Wang and Burchfiel (1997) present evidence of the antiquity of the Salween and Mekong rivers, suggesting the rivers may have been in their present location during exhumation of the Ailao Shan shear zone as well. Though the structural grain of this region probably guides the location of major rivers, there is a potential relationship between major, continental scale rivers and the exhumation of deep crustal rocks along major strike-slip shear zones.

Implications for Asian tectonics

Field data presented in this paper and regional observations (Wang and Burchfiel, 1997) are consistent with transpressional rather than transtensional exhumation of the Ailao Shan shear

zone. However, the reconstruction of magnetic sea-floor anomalies in the South China Sea has been used to support transtension along the Ailao Shan shear zone during extrusion of Indochina (Brias et al., 1993; Harrison et al., 1996). This interpretation (Tapponnier et al., 1986; Tapponnier et al., 1990; Avouac and Tapponnier, 1993; Brias et al., 1993; Leloup et al., 1995; Harrison et al., 1996; Leloup et al., 2001; Gilley et al., 2003) assumes that a straightforward link can be made between oceanic and continental tectonics, and that sea-floor spreading can be directly related to displacement along the Ailao Shan shear zone. Because of the inconsistency of this evidence with transpressional exhumation of the shear zone, we join other authors (Northrup et al., 1995; Hall, 1996; Packham, 1996; Wang and Burchfiel, 1997) rejecting a straightforward link between oceanic and continental plate tectonics. Instead, seafloor spreading may be affected by plate interactions along the eastern plate boundary of Eurasia resulting in the formation of extensional basins along the entire Asian margin (Northrup et al., 1995; Packham, 1996), making any relationship between opening of the South China Sea and movement along the Ailao Shan shear zone difficult to interpret. What then accounts for diachronous cooling along the Ailao Shan shear zone, if not extension related to opening of the South China Sea, after the model of Harrison et al. (1996)? We do not have a definitive answer to this question, but suspect that the answer lies in the partitioning of strain between the Ailao Shan shear zone and the Lanping-Simao fold and thrust belt. Wang and Burchfiel (1997) argued that left-lateral displacement on the Ailao Shan shear zone was progressively transferred to shortening structures within the fold and thrust belt, and that the relative amount of displacement accommodated within the shear zone decreases to the southeast. Younger cooling ages in the northwest Ailao Shan may correspond to more deeply exhumed rocks, or to a larger component of vertical extrusion, while older cooling ages toward the southeast may correspond to a greater shortening component, more horizontally oriented strain, and slightly less overall exhumation. Foliation orientation roughly supports this, with steeper orientations reported in the northwest, but detailed thermobarometry and further study of the relationship between shortening in the Lanping-Simao basin and the Ailao Shan shear zone would be necessary to test this scenario.

We confirm that the southeastern margin of the Tibetan Plateau region was shortening in an approximately northeast-southwest direction (current coordinates) during left-lateral displacement along the Ailao Shan shear zone. Deformation was distributed throughout the

Lanping-Simao fold and thrust belt to the southwest of the shear zone (Wang and Burchfiel, 1997). To the northeast, we observe faults within the Red River valley with probable 10's of kilometers of left-lateral displacement, and Burchfiel and Wang (2003) report at least two similar faults farther northeast, the Quijiang and Jianshui faults (Fig. 1b), with 6 to 25 km left-lateral displacement. However, most displacement must have occurred on or southwest of the northeast margin of the Ailao Shan shear zone, on the basis of sediment provenance for the Cenozoic strata within the Red River valley. Finally, clast provenance for the Ailao Shan Conglomerate suggests no more than ~190 km left-lateral displacement along the northeast margin of the shear zone since deposition of that unit began, probably in Early Miocene time. The Ailao Shan shear zone is unquestionably an important crustal discontinuity, and extrusion of Indochina probably occurred southwest of the shear zone. However, deformation is not confined to the shear zone, but instead occurs over a region nearly 300 kilometers wide (Fig. 1). Such deformation must be taken into account by models for the tectonic evolution of this region.

CONCLUSIONS

Detailed mapping of Cenozoic sedimentary rocks preserved along the northeast margin of the Ailao Shan shear zone reveals important information about the exhumation of the shear zone and its relationship to regional landscape and tectonic development. Results of this study, integrated with other regional studies (particularly Leloup et al., 1995; Harrison et al., 1996; Wang E. et al., 1998; Leloup et al., 2001; Gilley et al., 2003), suggest the following regional development (Fig. 7). In Early Oligocene time, displacement without significant exhumation began along the Ailao Shan shear zone. Slices of T₃ sediment were displaced left-laterally up to 10's of kilometers and were slightly exhumed along strands of this fault system, and lacustrine rocks of the Wubang Mudstone were deposited in sag or pull-apart basins. In Late Oligocene time, rapid exhumation began and the through-going Red River was established. Sediment from source areas in the Yangtze platform and from units capping the Ailao Shan shear zone, probably also Yangtze Platform sediment, was deposited in the Limestone Conglomerate member of the Langdun Formation. In Miocene time, high-grade Ailao Shan gneiss and leucogranite were exhumed and cobbles from the Ailao Shan began to be deposited in the Ailao Shan Conglomerate member of the Langdun Formation. The basin was structurally depressed by thrust faulting of opposing dip on the flanks of the basin. Exhumation ceased along the shear zone probably in Late Miocene

time, and relief was reduced in the region through erosion of the Ailao Shan and adjacent terrain. In Pliocene time, the region was re-exhumed by surface-uplift driven incision along the Red River, and the Red River fault became active, further deforming basin strata and complicating older relationships.

Our study demonstrates that the northeast margin of the shear zone experienced shortening during exhumation of the Ailao Shan, consistent with shortening in the Lanping-Simao fold and thrust belt at the same time (Wang and Burchfiel, 1997), indicating a tranpressional regime during exhumation. Further, erosional removal of exhumed shear zone rocks along the paleo-Red River, established in approximately its present course by Late Oligocene time, provides an explanation for deeper exhumation (Harrison et al., 1996) along the northeast side of the shear zone. The Red River fault plays no significant role in exhumation of the shear zone. While the Ailao Shan shear zone is undeniably important in the tectonic evolution of southeast Asia, our results are consistent with diffuse deformation and partitioning of strain across a region up to 300 kilometers wide.

APPENDIX A: FOSSILS

Altogether 56 plant macrofossil species were collected at 7 localities. All fossils were assigned a Miocene age except for RR99-13 which is reported to be Oligocene to Early Miocene in age. Fossils were identified by Professor Li Di Yun of the Yunnan Institute for Geological Sciences. Twenty species correlate to fossils from the Yunnan Xiaolongtan Miocene flora. *Dryophyllum* is an extinct fossil which correlates to the Yunnan Jianchuan flora. Eleven species correlate to the Yunnan Jinggu flora.

Nansa map area: Ailao Shan Conglomerate

RR00-13, 8 species, N1 (Miocene)

Neckera sp.	shanwanica	Wu et Feng
Andropogon sp.		
Cyperacites sp.		
Graminites sp.		
Monocotyphyllum sp.		
Pheobe sp.		
Phyllites sp.		
Potamogten sp.		

Chapter 2- Exhumation of the Ailao Shan shear zone

RR00-105, 3 species, N1 (Miocene)

Magnolia sp.	miocenica	Hu et Chaney
Phoebe sp.		
Sequoia sp.	Chinensis	Endo emend. Wang et Li

Nansa Transitional Sandstone

RR99-13, 24 species, N11/E3 (Aquitanian/Oligocene, ~23 Ma)

Acer sp.		
Alangium sp.	aequalifolium	(Goeppert) Kryshfovich et Borsuk
Albizia sp.		
Amelanchier sp.	wongii	Chaney
Betula sp.	dissecta	Tao
Calocedrus sp.	lantenoisii	Laurent
Cassia sp.	suffruticosa	Kone et Both
Cinnamomum sp.		
Dalbergia sp.	lucida	Geng
Dyophyllum sp.	fushunense	Chen
	parvum	Tao
	relongtanense	Colani
	yunnanense	Colani
Fraxinus sp.		
Gleditschia sp.	integra	
Indigofera sp.	praesanguis	Tao
Machilus sp.	ugoana	Huzioka
Magnolia sp.	latifolia	Tao
Monocotyphyllum sp.		
Nathaphoebe sp.	precavaleriei	Li
Phyllites sp.		
Pinus sp.		
Quercus sp.		
Sophora sp.	paraflavescens	Geng et Liu
Spiraea sp.	protolunbergi	Tanai et Suzuki
Typha sp.	lesquereuxii	Cockerell
Zelkova	speciosa	D. Y. Li
	ungeri	Kovats

RR99-19, 30 species, N1 (Miocene)

Acer sp.	florinii	Hu et Chaney
	paxii	Franch
Alangium sp.	aequalifolium	(Goeppert) Kryshfovich et Borsuk
Alnus sp.		
Betula sp.	mioluminifera	Hu et Chaney
Cassia sp.	oblonga	Zhou
	suffruticosa	Koen. et Roth
Cinnamomum sp. lanceolatum		(Unger) Heer
	naitoanum	Huzioka et Takahasi
Cyclobalanopsis sp.	praegilva	Huzike
Cyperacites sp.		
Desmodium sp.	pardemosum	Tao
	pulchellum	(L.) Benth
Drmosia sp.	xiaolong	Tanensis Zhou
Fagus sp.	chinensis	Li

Chapter 2- Exhumation of the Ailao Shan shear zone

Graminites sp.		
Hamamelis sp.	miomollis	Hu et Chaney
Jasminum sp.	paralanceolarium	Li
Laurus sp.	obovalis	Tao
Litsea sp.	grabani	Hu et Chaney
	rubesens	Tao
Machilus sp.	ugoana	Huzioka
Magnolia sp.	latifolia	Tao
	Miocenica	Hu et Chaney
Nothaphoebe sp.	precavaleriei	Li
Passiflora sp.		
Phoebe sp.	megaphylla	Chen et Tao
	Pseudolanecolata	Colani
Podogonium sp.	oehuingense	(Koenig) Kirchh
Phragmites sp.	yuanjiangensis	D. Y. Li
Phyllites sp.		
Quercus sp.	latifolia	Li
	sinomiocenicum	Hu et Chaney
Sequoia sp.	chinensis	Wang et Liu
Sophora sp.	miojaponica	Hu et Chaney
	paraflavescens	Geng et Liu
Spiraea sp.		
Typha sp.	lesgereuxii	Cockerell
	latissima	Al. Braun
Uvaria sp.	yunnanensis	Li

RR00-1, 20 species, N1 (Miocene)

Cassia sp.	suffruticosa	Koen et Roth
Berchemia sp.	miofloribunda	Hu et Chaney
	polyphylla	Wall.
	pubescens	Burkill
Carpinus sp.		
Cinamomum sp.		
Cyclobalanopsis sp.	praegilva	Huzioka
Cyperacites sp.		
Dalbergia sp.	prekupeana	Tao
Distylium sp.		
Dryophyllum sp.	dewalquei	Sep. et Mar.
Juglans sp.		
Lithocarpus sp.	reniifolium	Tao
Nothaphoebe	precavalerieir	Li
Passiflore sp.		
Pheobe sp.	pseudoalaceolata	Colani
Phragmites sp.		
Phyllites sp.		
Quercus sp.	lantenoisii	Colani
Robinia sp.		
Sabalites sp.	taishhuensis	Takahashi
Sophora sp.	paraflovescens	Grenget Liu

RR00-15, 18 species, N1 (Miocene)

Acer sp.	miofranchetii	Hu et Chaney
Ailanthus sp.		
Alangium sp.	aequalifolium	(Geopp.) Krysht et Bors.
Berchemia sp.	yunnanensis	Franck
Castanopsis sp.	indica	(Koxb) A.D.C.

Chapter 2- Exhumation of the Ailao Shan shear zone

Cyperacites sp.		
Desmodium sp.		
Lithocarpus sp.	neriifolium	Tao
Litsea sp.		
Magnolia sp.	miocenica	Hu et Chaney
Myrica sp.		
Nothopheobe sp.		
Phoebe sp.	pseudolanceolata	Colani
Phyllites sp.		
Pueraria sp.	prethomsorii	Tao
Quercus sp.	lanteroisii	Colani
Quercus sp.	sinomiocenica	Hu et Chaney
Robinia sp.		
Sophora sp.		

Yuanjiang Limestone Conglomerate

RR00-18, 8 species, N1 (Miocene)

Cassia	suffruticosa	Koen et Roth
Cyperacites sp.		
Graminites sp.		
Monocotyphyllum sp.		
Nyssa sp.		
Phragmites sp.	yunnanensis	
Typha	lesquereuxii	Cockerell

REFERENCES CITED

- Akciz, S., Burchfiel, B. C., Crowley, J.L., Chen, L., and Yin, J., 2003, Structural and geochronological constraints on the exhumation of the metamorphic rocks along the Chong Shan shear zone, Western Yunnan, China: Geological Society of America, 2003 annual meeting, Seattle, WA.
- Akciz, S., Burchfiel, B. C., Crowley, J.L., Chen, L., and Yin, J., 2003, Gaoligong And Chong Shan shear zones, Yunnan, and accommodation of the northward movement of India relative to Indochina during mid-Cenozoic time: AGU 2003 Fall Meeting, San Francisco, CA.
- Allen, C.R., Gillespie, A.R., Han Yuan, Sieh, K.E., Zhang Buchun, Zhu Chengnan, 1984, Red River and associated faults, Yunnan Province, China: Quaternary geology, slip rates, and seismic hazard: Geological Society of America Bulletin, v. 95, p. 686-700.
- Allen, C.R., Luo, Z., Qian H., Wen X., Zhou H., Huang W., 1991, Field study of a highly active fault zone: the Xianshuihe-Xiaojiang fault of southwestern China: Geological Society of America Bulletin, v. 103, p. 1178-1199.
- Avouac, J-P, and Tapponnier, P., 1993, Kinematic model of active deformation in central Asia: Geophysical Research Letters, v. 20, p. 895-898.
- Bergman, S.C., Leloup, P.H., Tapponnier, P., Schärer, U., and O'Sullivan, P., 1997, Apatite fission track thermal history of the Ailao Shan-Red River shear zone, China: paper presented at meeting, European Union of Geoscience, Strasbourg, France
- Brias, A., Patriat, P., and Tapponnier, P., 1993, Updated interpretation of magnetic anomalies and seafloor spreading stages in the South China Sea, implications for the Tertiary tectonics of SE Asia: Journal of Geophysical Research, B, v. 98, p. 6299-6328.
- Burchfiel, B.C., and Wang, E., 2003, Northwest-trending, middle Cenozoic, left-lateral faults in southern Yunnan, China and their tectonic significance: Journal of Structural Geology, v. 25, p. 781-792.
- Bureau of Geology and Mineral Resources of Yunnan Province, 1990, in Regional Geology of Yunnan Province, Beijing, Geological Publishing House, 728 p.

Chapter 2- Exhumation of the Ailao Shan shear zone

- Chung, S-L, Lee, T-Y, Lo, C-H, Wang, P-H, Chen, C-Y, Yem, N.T., Hoa, T.T., and Genyao W., 1997, Intraplate extension prior to continental extrusion along the Ailao Shan-Red River shear zone: *Geology*, v. 25, p. 311-314.
- Clark, M.K, and Royden, L.H., 2000, Topographic ooze: Building the eastern margin of Tibet by lower crustal flow: *Geology*, v. 28, p. 703-706.
- Clark, M.K., Schoenbohm, L.M., Royden, L.H., Whipple, K.X., Burchfiel, B.C., Zhang, X., Tang, W., Wang, E., Chen, L., in press, Surface Uplift, tectonics, and erosion of eastern Tibet from large-scale drainage patterns: *Tectonics*.
- Clark, M.K., 2003, Late Cenozoic Uplift of Southeastern Tibet [PhD Thesis]: Massachusetts Institute of Technology, 226 p.
- Claypool, A.L., Klepeis, K.A., Dockrill, B., Clark, G.L., Zwingmann, H., and Tulloch, A., 2002, Structure and kinematics of oblique continental convergence in northern Fiordland, New Zealand: *Tectonophysics*, v. 359, p. 329-358.
- Dewey, J., Cande, S., and Pitman, W.C., III, 1989, Tectonic evolution of the India-Eurasia collision zone: *Eclogae Geologicae Helveticae*, v. 82, p. 717-734.
- Dunlap, W.J., Weinberg, R.F., and Searle, M.P., 1998, Karakoram fault zone rocks cool in two phases: *Journal of the Geological Society, London*, v. 155, p. 903-912.
- England, P., Houseman, G., 1989, Extension During Continental Convergence, With Application to the Tibetan Plateau: *Journal of Geophysical Research*, v. 94, p. 17561-17579.
- Fossen, H., and Tikoff, B., 1998, Extended models of transpression and transtension, and application to tectonic settings, in Holdsworth, R.E., Strachan, R.A. and Dewey, J.F. (eds): *Continental Transpressional and Transtensional Tectonics*, Geological Society, London, Special Publications, v. 135, p. 15-33.
- Gilley, L.D., Harrison, T.M., Leloup, P.H., Ryerson, F.J., Lovera, O.M., Wang J-H, 2003, Direct dating of left-lateral deformation along the Red River shear zone, China and Vietnam: *Journal of Geophysical Research*, v. 103, No. B2, 10.1029/2001JB001726.
- Hall, R., 1996, Reconstructing Cenozoic SE Asia: in Hall, R., and Blundell, D., (eds), *Tectonic Evolution of Southeast Asia*, Geological Society Special Publication No. 106, p. 153-184.
- Hanmer, S., 1988, Great Slave Lake shear zone, Canadian shield: reconstructed vertical profile of a crustal-scale fault zone: *Tectonophysics*, v. 149, p. 245-264.
- Harrison, T.M., W Chen, Leloup, P.H., Ryerson, F.J., and Tapponnier, P., 1992, An Early Miocene transition in deformation regime within the Red River fault zone, Yunnan, and its significance for the Indo-Asian tectonics: *Journal of Geophysical Research*, v. 97, p. 7159-7182.
- Harrison, T.M., Leloup, P.H., Ryerson, F.J., Tapponnier, P., Lacassin, R., and Chen Wenji, 1996, Diachronous initiation of transtension along the Ailao Shan-Red River shear zone, Yunnan and Vietnam, in Yin, A., and Harrison, T.M., eds., *The Tectonic Evolution of Asia*, Cambridge University Press, New York, p. 208-226.
- Hoffman, P.F., 1987, Continental transform tectonics: Great Slave Lake shear zone (ca. 1.9 Ga), northwest Canada: *Geology*, v. 15, p. 785-788.
- Holt, W.E., Li M., and Haines, A.J., 1995, Earthquake strain rates and instantaneous relative motions within central and eastern Asia: *Geophysical Journal International*, v. 122, p. 569-593.
- Houseman, G., and England, P., 1993, Crustal Thickening Versus Lateral Expulsion in the Indian-Asian Continental Collision: *JGR*, v. 98, p. 12233-12249.
- Koons, P.O., Zeitler, P.K., Chamberlain, C.P., Craw, D., Meltzer, A.S., 2002, Mechanical links between erosion and metamorphism in Nanga Parbat, Pakistan Himalaya: *American Journal of Science*, v. 302, no. 9, p. 749-733.
- Lacassin, R., Leloup, P.H., and Tapponnier, P., 1993, Bounds on strain in large Tertiary shear zones of SE Asia from boudinage restoration: *Journal of Structural Geology*, v. 15, p. 677-692.
- Lacassin, R., Replumaz, A., Leloup, P.H., 1998, Hairpin river loops and strike-slip sense inversion of southeast Asian strike-slip faults: *Geology*, v. 26, p. 703-706.
- Leloup, P.H., and Kienast, J.R., 1993, High temperature metamorphism in a major Tertiary ductile continental strike-slip shear zone: The Ailao Shan-Red River (P.R.C.): *Earth and Planetary Science Letters*, v. 118, p. 213-234.
- Leloup, P.H., Harrison, T.M., Ryerson, F.J., Chen Wenji, Li Qi, Tapponnier, P., and Lacassin, R., 1993, Structural, petrological and structural evolution of a Tertiary ductile strike-slip shear zone, Diancang Shan, Yunnan: *Journal of Geophysical Research*, v. 98, p. 6715-6743.
- Leloup, P.H., Lacassin, R., Tapponnier, P., Schärer, U., Zhong Dalai, Liu Xiaohan, Zhang Liangshang, Ji Shaocheng, Phan Trong Trinh, 1995, The Ailao Shan-Red River shear zone (Yunnan, China), Tertiary transform boundary of Indochina: *Tectonophysics*, v. 251, p. 3-84.

Chapter 2- Exhumation of the Ailao Shan shear zone

- Leloup, P.H., Arnaud, N., Lacassin, R., Kienast, J.R., Harrison, T.M., Phan Trong, T.T., Replumaz, A., and Tapponnier, P., 2001, New constraints on the structure, thermochronology, and timing of the Ailao Shan-Red River shear zone, SE Asia: *Journal of Geophysical Research*, B, v. 106, p. 6683-6732.
- Lewis, D.W., 1984, *Practical Sedimentology*: Hutchison Ross Publications, Stroudsburg, Penn.
- Li Diyun, Professor, personal communication, Yunnan Institute of Geological Sciences, 131 Baita Road, Kunming, Yunnan, P.R.China.
- McClelland, W.C., Tikoff, B., and Manduca, C.A., 2000, Two-phase evolution of accretionary margins: examples from the North American Cordillera: *Tectonophysics*, v. 326, p.37-55.
- Niño, F., Chéry, J., and G., J.-P., 1998, Mechanical modeling of compressional basins: origin and interaction of faults, erosion and subsidence in the Ventura basin, California: *Tectonics*, v. 17, p. 955-972.
- Northrup, C.J., Royden, L.H., Burchfiel, B.C., 1995, Motion of the Pacific plate relative to Eurasia and its potential relation to Cenozoic extension along the eastern margin of Eurasia: *Geology*, v. 23(8), p. 719-722.
- Packham, G., 1996, Cenozoic SE Asia: reconstructing its aggregation and reorganization: in Hall, R., and Blundell, D., (eds), *Tectonic Evolution of Southeast Asia*, Geological Society Special Publication No. 106, p. 123-152.
- Replumaz, A., Lacassin, R., Tapponnier, P., and Leloup, P.H., 2001, Large river offsets and Plio-Quaternary dextral strike-slip rate on the Red River fault (Yunnan, China): *Journal of Geophysical Research*, B, v. 106, 819-836.
- Royden, L.H., 1996, Coupling and decoupling of crust and mantle in convergent orogens: Implications for strain partitioning in the crust: *Journal of Geophysical Research*, B, v. 101, p. 17 679-17 705.
- Royden, L.H., Burchfiel, B.C., King, R.W., Wang, E., Chen Z., Shen F., Liu Y., 1997, Surface deformation and lower crustal flow in eastern Tibet: *Science*, v. 276, p. 788-790.
- Schoenbohm, L.M., Whipple, K.X., Burchfiel, B.C., and Chen, L., in press, Geomorphic constraints on surface uplift, exhumation, and plateau growth in the Red River region, Yunnan Province, China: *GSA Bulletin*.
- Searle, M.P., 1996, Geological evidence against large-scale pre-Holocene offsets along the Karakoram Fault: Implications for the limited extrusion of the Tibetan plateau: *Tectonics*, v. 15, p. 171-186.
- Searle, M.P., Weinberg, R.F. and Dunlap, W.J., 1998, Tranpressional tectonics along the Karakoram fault zone, northern Ladakh: constraints on Tibetan extrusion, in Holdsworth, R.E., Strachan, R.A. and Dewey, J.F. (eds): *Continental Transpressional and Transtensional Tectonics*, Geological Society, London, Special Publications, v. 135, p. 307-326.
- Sibson, R.H., White, S.H., and Atkinson, B.K., 1979, Fault rock distribution and structure within the Alpine fault zone: a preliminary account: in Walcott, R.I., and Cresswell, M.M. (eds), *The Origin of the Southern Alps*, Royal Society of New Zealand Bulletin, v. 18, p. 55-65.
- Schärer, U., Zhang L., Tapponnier, P., 1994, Duration of strike-slip movements in large shear zones: the Red River belt, China: *Earth and Planetary Science Letters*, v. 126, p. 379-397.
- Schärer, U., Tapponnier, P., Lacassin, R., Leloup, P.H., Zhong Dalai, and Ji Shaocheng, 1990, Intraplate tectonics in Asia: a precise age for large-scale Miocene movement along the Ailao Shan-Red River Shear Zone, China: *Earth and Planetary Science Letters*, v. 97, p. 65-77.
- Shen J., Wang Y., and Song F., 2003, Characteristics of the active Xiaojiang fault zone in Yunnan, China: a slip boundary for the southeastward escaping Sichuan-Yunnan block of the Tibetan Plateau: *Journal of Asian Earth Sciences*, v. 21, p. 1085-1096.
- Tapponnier, P., Peltzer, G., Armijo, R., Le Dain, A.-Y., and Cobbold, P., 1982, Propagating extrusion tectonics in Asia: New insights from simple experiments with plasticine: *Geology*, v. 10, p. 611-616.
- Tapponnier, P., Peltzer, G., and Armijo, R., 1986, On the mechanics of the collision between India and Asia, in Coward, M.P. and Ries, A.C., eds., *Collision Tectonics*, Geological Society Special Publication 19, p. 115-157.
- Tapponnier, P., Lacassin, R., Leloup, P.H., Schärer, U., D. Zhong, X. Liu, S. Ji, L. Zhang and J. Zhong, 1990, The Ailao Shan/Red River metamorphic belt: Tertiary left-lateral shear between Indochina and south China: *Nature*, v. 343, p. 431-437.
- Tikoff, B., and Teyssier, C., 1994, Strain modeling of displacement-field partitioning in transpressional orogens: *Journal of Structural Geology*, v. 16, p. 1575-1588.
- Walcott, R.I., 1998, Modes of oblique compression: Late Cenozoic tectonics of the South Island of New Zealand: *Reviews of Geophysics*, v. 36, p. 1-26.
- Wang, Erchie, and Burchfiel, B.C., 1997, Interpretation of Cenozoic tectonics in the Right-Lateral accommodation zone between the Ailao Shan shear zone and the Eastern Himalayan Syntaxis: *International Geology Review*, v. 39, p. 191-219.
- Wang, Erchie, Burchfiel, B.C., Royden, L.H., Chen Liangzhong, Chen Jishen, Li Wenxin, Chen Zhiliang, 1998, Late Cenozoic Xianshuihe-Xiaojiang, Red River and Dali fault systems of southwestern Sichuan and central Yunnan, China: Boulder, Colorado, Geological Society of America Special Paper 327.

Chapter 2- Exhumation of the Ailao Shan shear zone

- Wang, Pei-Ling, Ching-Hua Lo, Tung-Yi Lee, Sun-Lin Chung, Ching-Ying, Lan, Nguyen Trong Yem, 1998, Thermochronological evidence for the movement of the Ailao Shan-Red River shear zone: A perspective from Vietnam: *Geology*, v. 26, p. 887-890.
- Wang, Pei-Ling, Ching-Hua Lo, Sun-Lin Chung, Tung-Yi Lee, Ching-Ying Lan, Trang Van Thang, 2001, Onset timing of left-lateral movement along the Ailao Shan-Red River shear zone: $^{40}\text{Ar}/^{39}\text{Ar}$ dating constraint from the Nam Dinh Area, northeastern Vietnam: *Journal of Asian Earth Sciences*, v. 18, p. 281-292.
- Zhang G.-B., and Bott, M.H.P., 2000, Modelling the evolution of asymmetrical basins bounded by high-angle reverse faults with application to foreland basins: *Tectonophysics*, v. 322, p. 203-218.
- Zhang, Lian-Sheng and Schärer, U., 1999, Age and origin of magmatism along the Cenozoic Red River shear belt, China: *Contributions to Mineralogy and Petrology*, v. 134, p. 67-85.
- Zeitler, P.K., Meltzer, A.S., Koons, P.O., Craw, D., Hallet, B., Chamberlain, C.P., Kidd, W.S.F., Park, S.K., Seeber, L., Bishop, M., and Shroder, J., 2001, Erosion, Himalayan geodynamics, and the geomorphology of metamorphism: *GSA Today*, v. 11, p. 4-9.

Table 1. Langdun Formation lithologic and sedimentologic data

	Ailao Shan Conglomerate								
	Yuanjiang 9	Nansa 90	Nansa 94a	Nansa 94b	Nansa 95	Nansa 96	Nansa 120a	Nansa 120b	Nansa 120c
Gneiss/leucogranite ¹	0.37	0.84	0.08	0.08	0.06	0.34	1.00	0.88	0.70
Black/gray limestone	0.05	0.04	0.12	0.18	0.32	0.20	0.00	0.00	0.00
Basalt	0.05	0.00	0.04	0.00	0.04	0.00	0.00	0.00	0.04
Sandstone/siltstone	0.53	0.12	0.76	0.72	0.52	0.46	0.00	0.12	0.26
Conglomerate	0.00	0.00	0.00	0.02	0.06	0.00	0.00	0.00	0.00
Purple siltstone	0.00	0.00	0.00	0.00	0.00	0.00	0.00	0.00	0.00
Purple sandstone	0.00	0.00	0.00	0.00	0.00	0.00	0.00	0.00	0.00
Angular ²	0.14	0.05	0.06	0.05	0.23	0.03	0.24	0.30	0.11
Round	0.72	0.82	0.69	0.61	0.65	0.75	0.51	0.53	0.57
Matrix	0.14	0.12	0.25	0.33	0.12	0.22	0.25	0.17	0.32
Mud to Granule ³	0.20	0.12	0.25	0.33	0.12	0.22	0.25	0.18	0.32
Pebble	0.50	0.23	0.22	0.43	0.31	0.23	0.12	0.55	0.24
Cobble	0.30	0.58	0.48	0.24	0.50	0.55	0.42	0.27	0.42
Boulder	0.00	0.07	0.04	0.00	0.07	0.00	0.21	0.00	0.01

	Ailao Shan Conglomerate				Limestone Conglomerate			
	Nansa 120d	Nansa 121	Nansa 122	Nansa 213	Yuanjiang 1	Yuanjiang 8	Nansa 19	Nansa 99
Gneiss/leucogranite	0.94	1.00	1.00	0.27	0.00	0.00	0.00	0.00
Black/gray limestone	0.00	0.00	0.00	0.20	0.07	0.69	0.80	0.62
Basalt	0.00	0.00	0.00	0.02	0.02	0.00	0.00	0.38
Sandstone/siltstone	0.06	0.00	0.00	0.49	0.76	0.28	0.20	0.00
Conglomerate	0.00	0.00	0.00	0.02	0.00	0.03	0.00	0.00
Purple siltstone	0.00	0.00	0.00	0.00	0.02	0.00	0.00	0.00
Purple sandstone	0.00	0.00	0.00	0.00	0.13	0.00	0.00	0.00
Angular	0.25	0.26	0.32	0.04	0.42	0.42	0.30	0.22
Round	0.49	0.46	0.34	0.76	0.50	0.36	0.57	0.64
Matrix	0.25	0.28	0.34	0.20	0.08	0.22	0.13	0.14
Mud to Granule	0.25	0.28	0.39	0.24	0.26	0.38	0.20	0.34
Pebble	0.49	0.35	0.22	0.32	0.72	0.50	0.64	0.47
Cobble	0.25	0.33	0.29	0.40	0.02	0.08	0.16	0.14
Boulder	0.00	0.04	0.09	0.04	0.00	0.04	0.00	0.05

Note: Data given as fraction of total. Data collected through random selection of ~50 clasts at each site. Clasts were identified, measured and assessed for roundness. Site locations on Figs. 2 and 3.

¹Gneiss/leucogranites derive from the Ailao Shan shear zone. Lithologic associations are as follows: Black and gray limestone = Triassic (T₂); Basalt = Permian; Conglomerate = Limestone Conglomerate member of the Langdun formation; Purple siltstone = Devonian; Purple sandstone = Sinian (Bureau of Geology, Yunnan, 1990). Sandstones and siltstones could derive from a variety of units and can't be further identified.

²Rounding determined qualitatively. Matrix refers to sand size material and smaller for which rounding was not determined.

³Grain size assigned according to Udden-Wentworth grain size scale (Lewis, 1984).

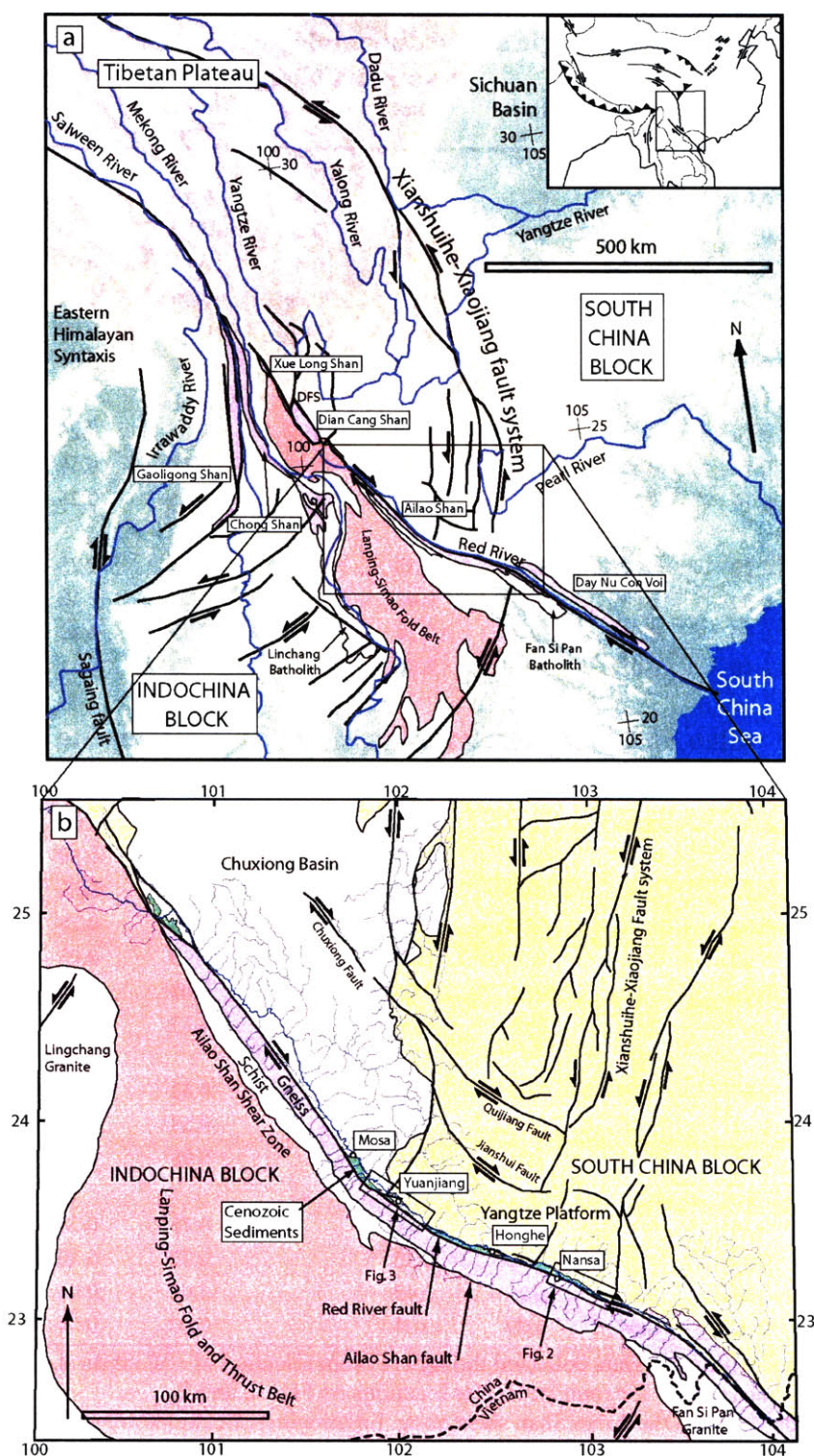


Figure 1. a) Regional topography and generalized geology of southeastern margin of the Tibetan Plateau. Major shear zones include the Xue Long Shan, Dian Cang Shan, Ailao Shan and Day Nui Con Voi, which collectively comprise the Ailao Shan shear zone, and the Chong Shan and Gaoligong Shan shear zones in western Yunnan. The Red River fault runs along the northeast side of the Ailao Shan, through Vietnam to the South China Sea. b) Generalized map of Ailao Shan region, including the Ailao Shan shear zone (both schists and gneiss), South China (Chuxiong basin and Yangtze platform) and Indochina (Lingchang granite and Lanping-Simao redbed basin). Figs. 2 and 3 indicated with boxes. Note Cenozoic sediments in green.

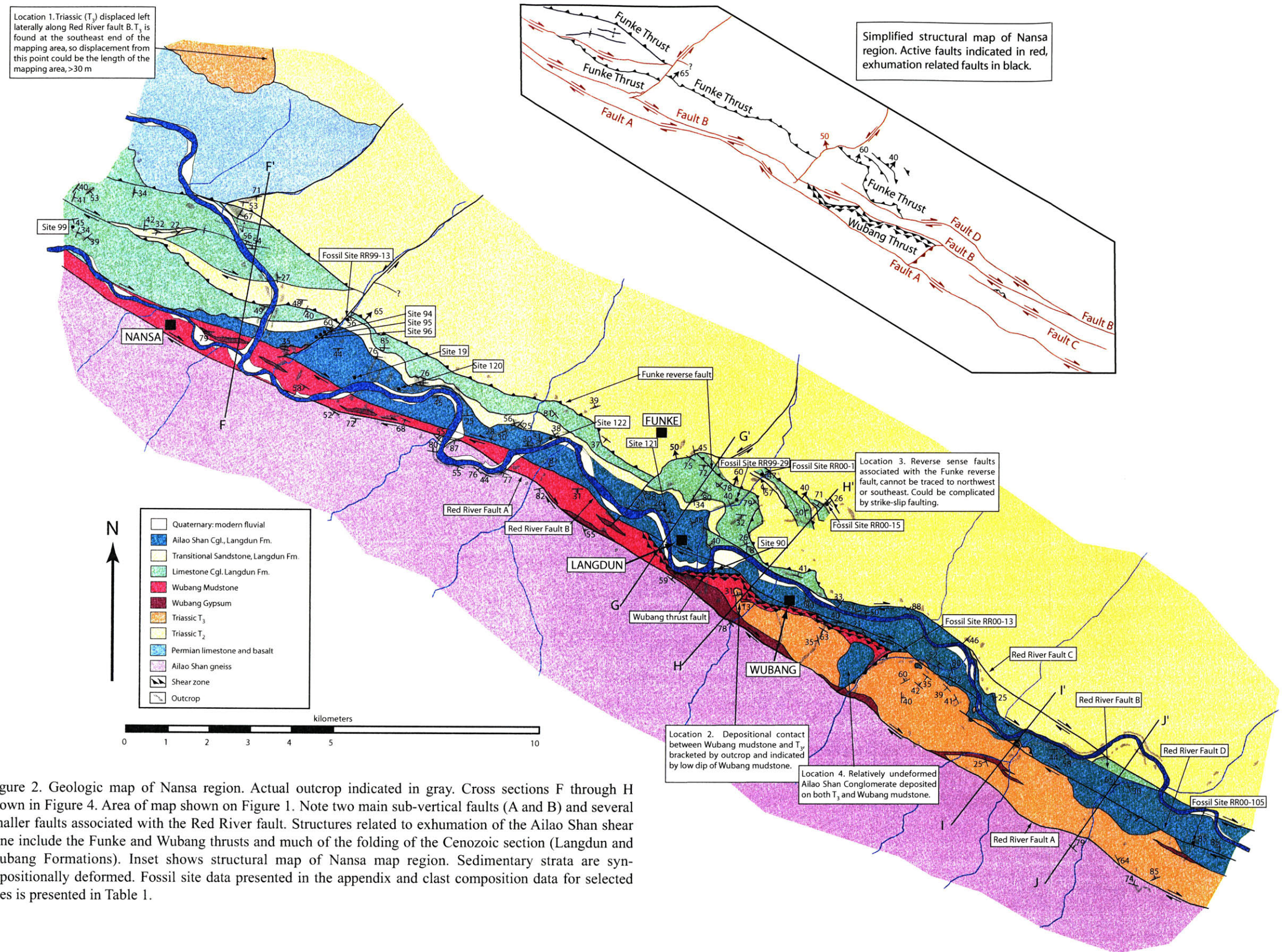


Figure 2. Geologic map of Nansa region. Actual outcrop indicated in gray. Cross sections F through H shown in Figure 4. Area of map shown on Figure 1. Note two main sub-vertical faults (A and B) and several smaller faults associated with the Red River fault. Structures related to exhumation of the Ailao Shan shear zone include the Funke and Wubang thrusts and much of the folding of the Cenozoic section (Langdun and Wubang Formations). Inset shows structural map of Nansa map region. Sedimentary strata are syn-depositionally deformed. Fossil site data presented in the appendix and clast composition data for selected sites is presented in Table 1.

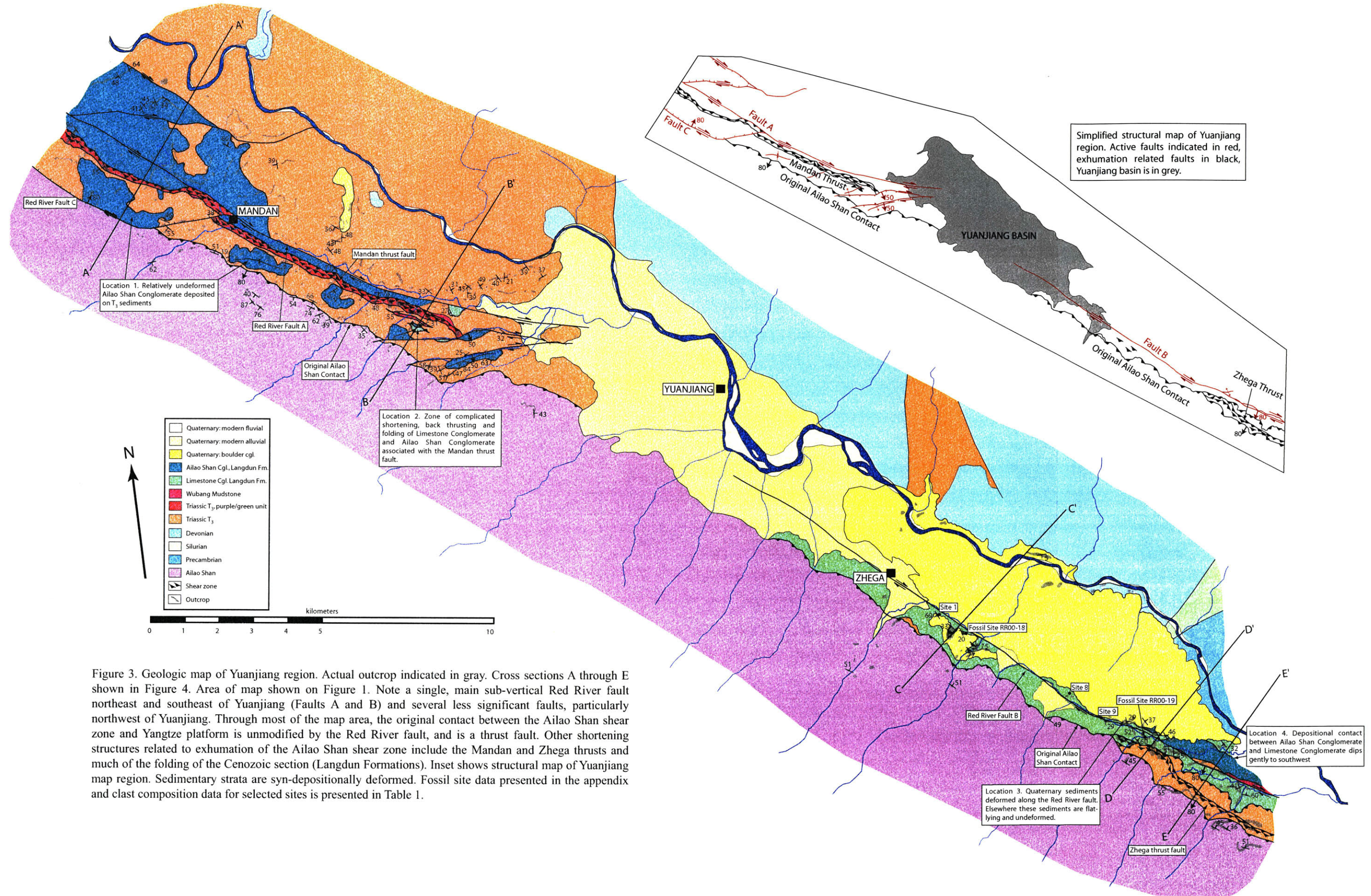


Figure 3. Geologic map of Yuanjiang region. Actual outcrop indicated in gray. Cross sections A through E shown in Figure 4. Area of map shown on Figure 1. Note a single, main sub-vertical Red River fault northeast and southeast of Yuanjiang (Faults A and B) and several less significant faults, particularly northwest of Yuanjiang. Through most of the map area, the original contact between the Ailao Shan shear zone and Yangtze platform is unmodified by the Red River fault, and is a thrust fault. Other shortening structures related to exhumation of the Ailao Shan shear zone include the Mandan and Zhega thrusts and much of the folding of the Cenozoic section (Langdun Formations). Inset shows structural map of Yuanjiang map region. Sedimentary strata are syn-depositionally deformed. Fossil site data presented in the appendix and clast composition data for selected sites is presented in Table 1.

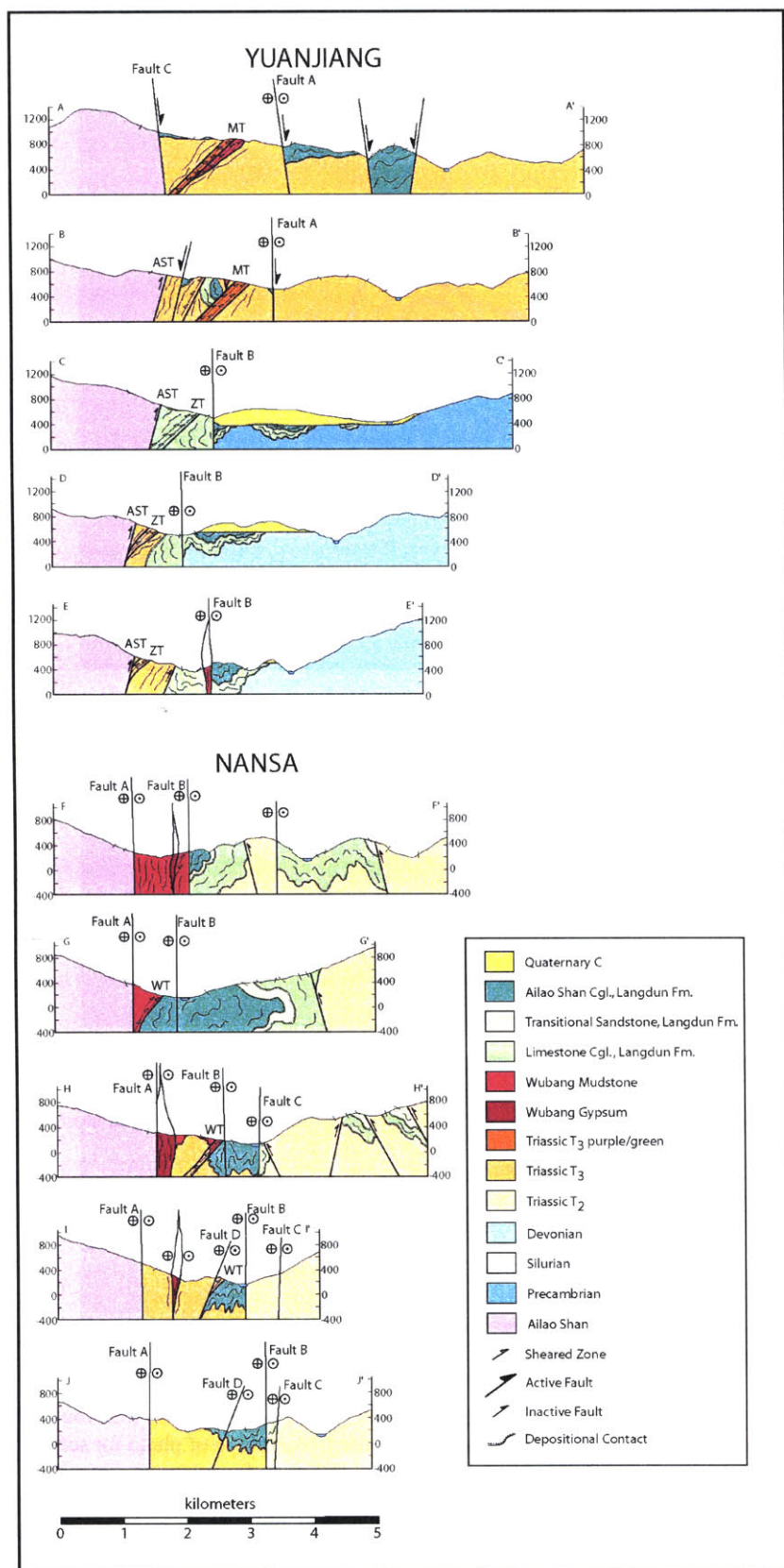


Figure 4. Cross sections from northwest to southeast. Section locations marked on Figure 2 (F through J) and Figure 3 (A through E). No vertical exaggeration. MT = Mandan thrust; ZT = Zhega thrust; WT = Wubang thrust.

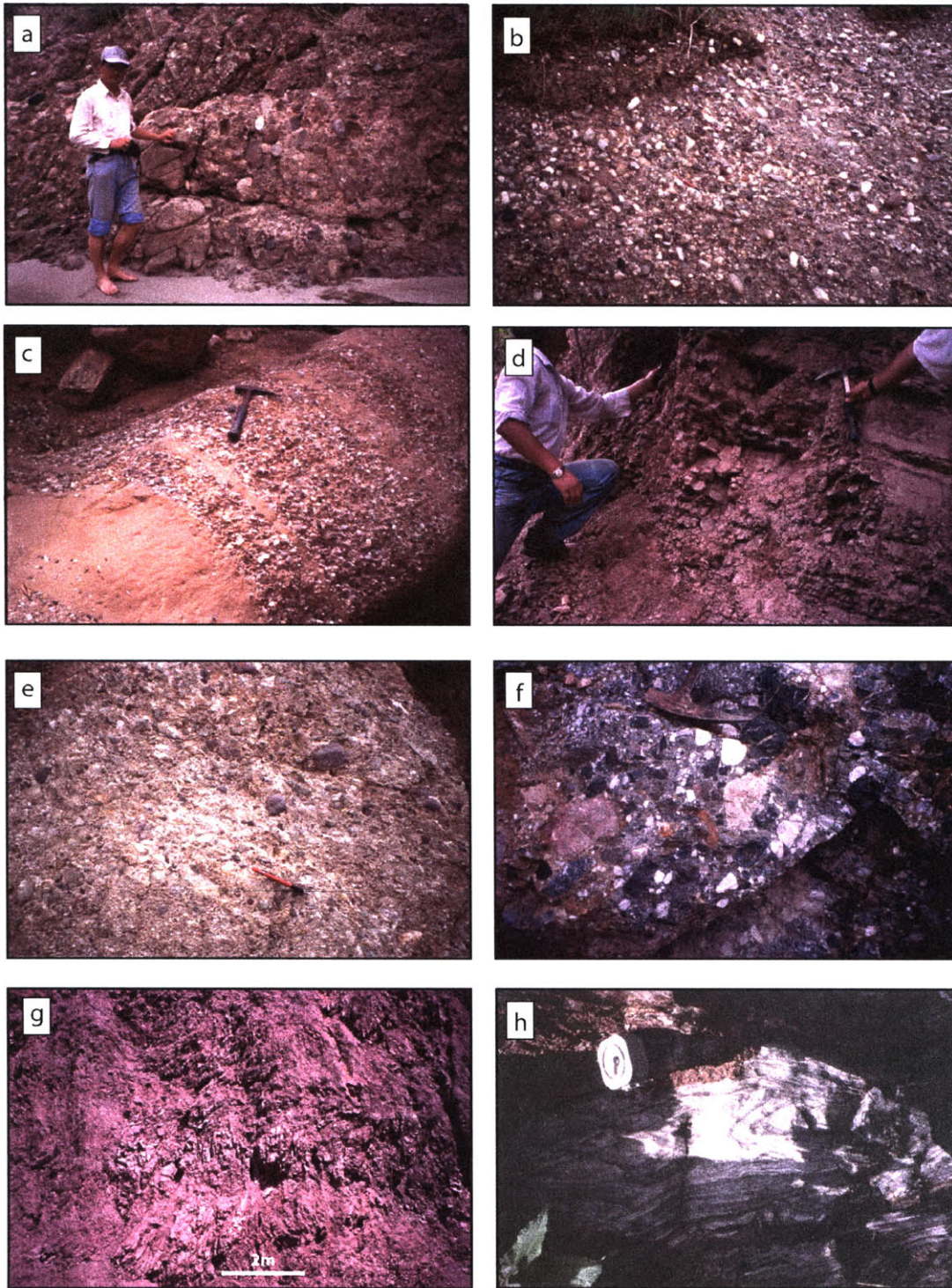


Figure 5. Cenozoic stratigraphy. a) Coarse facies of Ailao Shan Conglomerate, Langdun Formation, Nansa. b) Well-rounded, well-sorted facies of Ailao Shan Conglomerate, Langdun Formation, Yuanjiang. Red pencil near center of photo for scale. c) High sand content facies of Ailao Shan Conglomerate, Langdun Formation, Nansa. Hammer for scale. d) Transitional Sandstone, Langdun Formation, fossil locality RR99-13, Nansa. e) Well-sorted, well-rounded fluvial member of Limestone Conglomerate, Langdun Formation, Yuanjiang. Red pencil for scale. f) Angular, debris flow member of Limestone Conglomerate, Langdun Formation, Nansa. Hammer for scale. g) Red lacustrine mudstone, Wubang Formation, deformation associated with Red River fault, Nansa. h) Lacustrine gypsum, Wubang Formation, deformation associated with Red River fault, Nansa. Compass for scale.

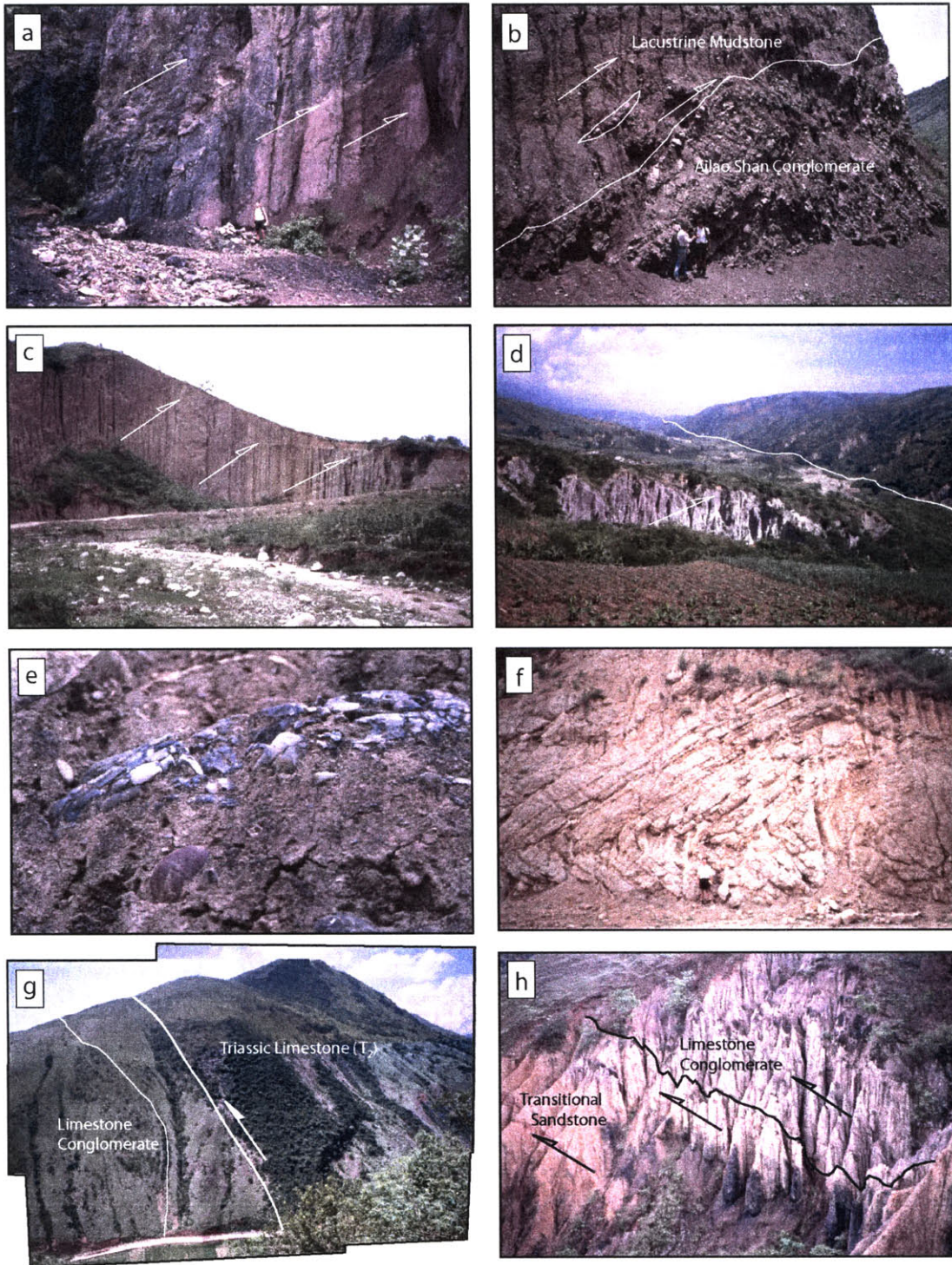
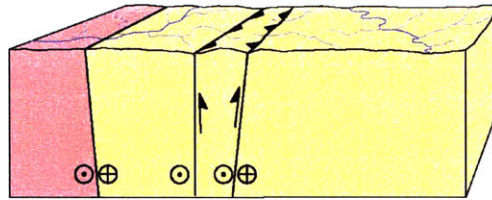


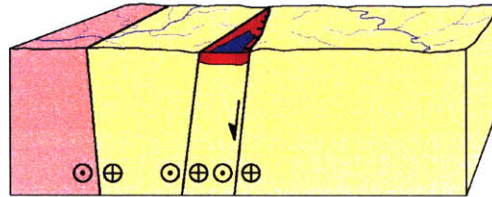
Figure 6. Examples of shortening structures in Cenozoic rocks. a) Wubang thrust developed in Wubang Mudstone, Nansa. View to northwest. b) Wubang thrust carries Wubang Mudstone over Ailao Shan Conglomerate, Nansa. View to northwest. c) Zhega thrust developed in Limestone Conglomerate, southeast of Yuanjiang. View to northwest. d) Mandan thrust developed in purple/green phyllitic member of Triassic (T₃), northwest of Yuanjiang. Red River fault marked with white line across tributary valley. View to northwest. e) Cobble of Limestone Conglomerate within Ailao Shan Conglomerate, Nansa. f) Folds developed in Limestone Conglomerate, Yuanjiang. g) Funke thrust fault on northeast side of Nansa valley, overturns Limestone Conglomerate. View to northwest. h) Overturned Limestone Conglomerate and Transitional Sandstone below Funke thrust fault. View to northwest.

Chapter 2- Exhumation of the Ailao Shan shear zone

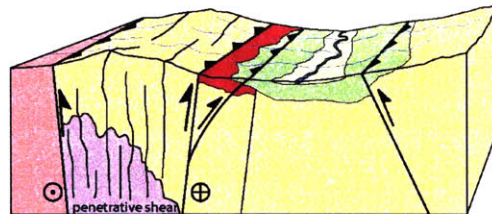
STAGE 1a: Early-Oligocene
Beginning of left-lateral displacement and minor early exhumation.



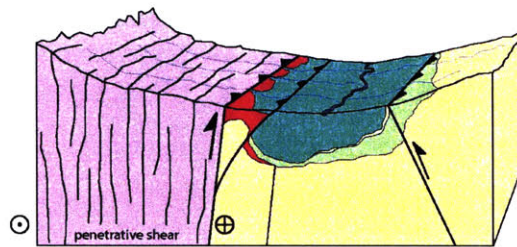
STAGE 1b: Early-Oligocene
Continued left-lateral displacement and deposition of lacustrine mudstone and gypsum in pull-apart or sag basins.



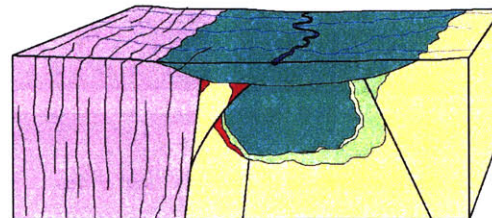
STAGE 2: Late-Oligocene
Beginning of rapid exhumation before Ailao Shan gneisses reach the surface. Deposition of Limestone Conglomerate and Transitional Sandstone. Establishment of Red River.



STAGE 3: Early-Miocene
Continued exhumation, Ailao Shan reaches the surface. Deposition of Ailao Shan Conglomerate.



STAGE 4: Late-Miocene
Cessation of exhumation, filling of basin and formation of low-relief landscape.



STAGE 5: Pliocene
Surface uplift, re-exhumation of basin and right-lateral displacement along Red River fault

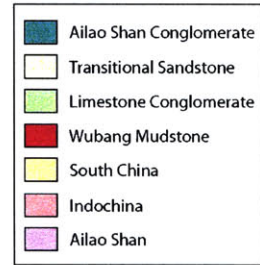
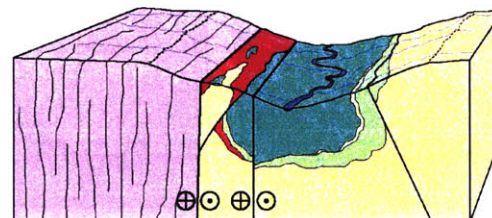


Figure 7. Evolution of Red River region. See text for elaboration on the development during each stage. Block diagrams based most closely on cross sections G and H from Nansa map area (Fig. 3), but are broadly applicable along the northeast edge of the Ailao Shan shear zone.

The Red River fault and the active tectonics of the southeast margin of the Tibetan plateau

Lindsay M. Schoenbohm^{1*}

B. Clark Burchfiel¹

Chen Liangzhong²

Josh M. Feinberg³

Michael C. Stewart⁴

Yin Jiyun²

¹Massachusetts Institute of Technology, Dept. of Earth, Atmospheric and Planetary Sciences, 77 Massachusetts Ave., Cambridge, MA 02139

²Yunnan Institute of Geological Sciences, 131 Baita Rd., Kunming, Yunnan, China

³University of California, Berkeley, Department of Earth and Planetary Sciences, 269 McCone Hall, Berkeley, CA 94720

⁴Maine Maritime Academy, Castine, ME 04420

* E-mail: schoenbl@mit.edu

ABSTRACT

Detailed mapping of field relationships along the Red River fault reveal information about the distribution and magnitude of slip along the fault, about its interactions with other regional faults systems, and the relationship between river incision and growth of the eastern margin of the Tibetan Plateau. The Red River fault is complex, consisting of up to four strands, and is dominated by right-lateral strike-slip displacement. Evidence for an extensional component to displacement is strongest along the northern part of the fault, and decreases to the southeast to zero at a point ~100 km SE of a major bend in the fault. Results of this study indicate dextral displacement on the Red River fault is probably at least ~40 km, 15-16 km of which predates incision of the Red River in Pliocene time or later, and probably also predates plateau growth and development of other regional fault systems. Long-term average slip-rate on the Red River fault is a minimum of ~5 mm/yr. However, the regional active tectonics are characterized by rotation of the upper crust around the eastern Himalayan syntaxis, bounded to the east by the Xianshuihe-Xiaojiang fault system, which deflects but does not cut the Red River fault. The distributed nature of the Xianshuihe-Xiaojiang fault system as it approaches the Red River fault is important for accommodating shearing across the strong crustal anisotropy formed by the Red River fault and Ailao Shan shear zone. The southeast plateau margin may have grown through the flow of weak lower crust from beneath Tibet into adjacent regions, resulting in surface uplift, river incision, and the formation of a detachment zone in the mid to lower crust. The Xianshuihe-Xiaojiang fault system initiated during growth of the southeast plateau margin. The Red River has been decreasing in regional importance since establishment of modern tectonic rotation around the eastern Himalayan syntaxis.

Keywords: Red River fault, Xianshuihe-Xiaojiang fault system, Dali fault system, southeast Asia, extrusion, plateau growth

INTRODUCTION

The Red River fault, together with the Ailao Shan shear zone and the Red River (Fig. 1), which extend from Tibet to the South China Sea, are remarkably prominent features of the landscape and the geology, easily recognizable on any map or satellite image of the southeast margin of the

Tibetan Plateau. The Red River fault has been viewed as a major, intra-continental fault zone that penetrates the lithosphere, today accommodating southeastward extrusion of the South China block (Tapponnier et al., 1982; 1986, Avouac and Tapponnier, 1993; Leloup et al., 1995; Replumaz et al., 2001). However, alternate interpretations view the Red River fault as a passive marker, deflected by rotation of an internally deforming region around the eastern Himalayan syntaxis, bounded by the Xianshuihe-Xiaojiang fault system (King et al., 1997; Wang et al., 1998; Chen et al., 2000). Additionally, recent modeling and geomorphic studies suggest that the southeastern margin of the Tibetan plateau may have grown in Miocene and Pliocene time through pressure-gradient-driven flow of weak mid to lower crust from beneath Tibet into the adjacent regions, thickening the crust and causing isostatic surface uplift in the absence of upper crustal shortening (Royden, 1996; Royden et al., 1997; Clark and Royden, 2000; Clark et al., in press; Schoenbohm et al., in press and Chapter 4). If true, faults active today, such as the Red River fault and the Xianshuihe-Xiaojiang fault system, may be detached in the mid to lower crust. In the context of these contrasting interpretations, it is crucial to understand the magnitude and timing of displacement along the Red River fault, the interaction of the Red River fault with other active faults of the southeast part of the plateau, and the temporal relationship between the active faults and regional surface uplift.

In this study, we reinterpret the role of the Red River fault in accommodating deformation of the southeast margin of the Tibetan Plateau in light of new data. We present detailed, field mapping along the Red River fault which yields important information about fault morphology, the distribution and amount of displacement along the fault, the northwest termination of the Red River fault, its interactions with the Xianshuihe-Xiaojiang system, and the timing of incision of the Red River. These data are integrated with existing data to interpret the regional active fault systems in the context of surface uplift, plateau growth, and the possibility of a detachment zone in the mid to lower crust.

GEOLOGIC SETTING

Regional Geology

The southeast margin of the Tibetan Plateau has been extensively deformed as a result of the India-Eurasia collision. During mid-Cenozoic time, several major shear zones, including the

Ailao Shan shear zone, accommodated deformation, rotation and extrusion of crustal blocks (Tapponnier et al., 1986, 1990; Leloup et al., 1995; Harrison et al., 1996; Wang and Burchfiel, 1997). The Ailao Shan shear zone is a long (>1000 km), narrow (<20 km) zone of amphibolite facies gneiss and mylonite with abundant left-lateral shear sense indicators which stretches discontinuously from southeastern Tibet to the South China Sea (Fig. 1; Tapponnier et al., 1990; Leloup et al., 1993; 1995; 2001). The shear zone is interpreted to have accommodated 700 ± 200 km displacement of Indochina to the southeast (present coordinates) relative to South China (Leloup et al., 1995) active by at least 34 Ma (based on dating of monazite inclusions in syn-kinematic garnet, Gilley et al., 2003). The shear zone was rapidly exhumed in transtension (Harrison et al., 1992; Leloup et al., 1995; Harrison et al., 1996) or transpression (Wang and Burchfiel, 1997; Chapter 2) from before ~25 Ma and continuing to at least ~17 Ma (Harrison et al., 1996). Limited fission track data may also indicate a period of rapid cooling between 13 and 10 Ma (Bergman et al., 1997; Leloup et al., 2001), but it is unclear if this is related to late-stage, left-lateral exhumation of the shear zone or to early displacement on the Red River fault.

The Ailao Shan shear zone is a major crustal discontinuity, separating rocks of Indochina to the southwest from the South China block to the northeast (Fig. 1). Adjacent to the shear zone the Yangtze platform consists of mainly of Permian carbonate and basalt, Mesozoic shallow marine carbonates and, in the Chuxiong basin, Jurassic and Cretaceous non-marine redbeds (Fig. 1b; Bureau of Geology, Yunnan, 1990; Leloup et al. 1995). A narrow belt of highly deformed Oligocene and Miocene lacustrine and fluvial sediments which record the unroofing history of the Ailao Shan shear zone are preserved to the northeast of the shear zone along the Red River valley (Fig. 1b; Wang et al., 1998; Chapter 2). To the immediate southwest of the shear zone is the Lanping-Simao Mesozoic and early-Cenozoic redbed basin, deformed into an early- to mid-Cenozoic fold and thrust belt (Fig. 1; Bureau of Geology, Yunnan, 1990; Leloup et al., 1995; Wang et al., 1998).

The fault systems active today, including the Red River fault, Xianshuihe-Xiaojiang fault system and the Dali fault system, are distinct from the older, mid-Cenozoic system. The right-lateral Red River fault (Fig. 1) is approximately coincident with the northeast margin of the Ailao Shan shear zone from central Yunnan southeast to the South China Sea, but reverses the sense of

displacement recorded in the Oligocene and Early Miocene shear zone mylonites (Allen et al., 1984; Leloup et al., 1995; Wang et al., 1998; Replumaz et al., 2001). Both features are prominently bent near the intersection with the Xianshuihe-Xiaojiang fault system (Fig. 1). The Ailao Shan shear zone and Red River fault are linked, but the deformation they accommodate, the nature of that accommodation, and probably also the conditions in the mid to lower crust while they were active may be very different. We therefore follow Wang et al. (1998) in using nomenclature to distinguish these two structures. The term Ailao Shan shear zone in our usage refers only to the belt of high grade gneiss and mylonite with left-lateral shear sense indicators, while the Red River fault is the brittle, right-lateral structure within the Red River valley to the northeast of the shear zone (Fig. 1).

Considerable controversy surrounds the morphology and distribution of displacement on the Red River fault. Pioneering work by Allen et al. (1984) suggested that for much of its length, slip is partitioned between two faults, with dip-slip extensional displacement concentrated on the “Range Front fault” between the Ailao Shan shear zone and rocks of the Yangtze platform, and with most of the right-lateral strike-slip displacement occurring on the “Mid Valley fault” a few hundred meters to the northeast. Subsequent reconnaissance mapping by Wang et al. (1998) and satellite image interpretation by Replumaz et al. (2001) have revealed a more complicated fault system. Strike-slip displacement estimates range between 5.3 and 57 km with slip-rates from 2 to 10 mm/yr (Fig. 2; Allen et al., 1984; Weldon et al., 1994; Leloup et al., 1995; Wang et al., 1998; Replumaz et al., 2001). These previous studies will be assessed on a site by site basis below. The distribution of dip-slip extensional displacement on the Red River fault is also controversial. Wang et al. (1998) argue that normal faulting occurs only north of the bend in the fault (Fig. 1). In their interpretation, the slip vector is close to parallel to the fault southeast of the bend and therefore has a minor oblique component northwest of the bend. This is confirmed by Schoenbohm et al., (in press, and Chapter 4) who have constrained the distribution and magnitude of dip-slip displacement by reconstructing the drainage network developed on a low-relief landscape perched today high above the Red River valley. Disruption of this network records any vertical displacement on the Red River fault since river incision began, essentially serving as a sub-horizontal marker. Schoenbohm et al. (in press and Chapter 4) found ~750 m vertical displacement near the town of Ejia (Fig. 1) north of the major bend, with displacement

decreasing to near zero northwest toward the Midu basin and southeast toward Yuanjiang (Fig. 1b). Displacement south of the bend is negligible. The timing of initiation of the Red River fault is unknown, though most studies assume that displacement recorded by the tributary network must post-date the onset of river incision (Allen et al., 1984; Leloup et al., 1995; Replumaz et al., 2001), which is in Pliocene time or later (Schoenbohm et al., in press, and Chapter 4). Leloup et al., (1993) link the onset of rapid cooling in the Diancang Shan massif at 4 to 5 Ma to initiation of the Red River fault, but as discussed below, the Diancang Shan massif was exhumed by faults of the extensional Dali fault system (Fig. 1a) and the relationship between this fault system and the Red River fault is unclear.

The Xianshuihe-Xiaojiang fault system is a convex, NW- to N-S-trending network of seismically active left-lateral faults which cut across the older structural fabric of the southeast plateau margin (Fig. 1; Allen et al., 1991; Wang et al., 1998; Shen et al., 2003). In Sichuan Province and Tibet, displacement appears to be concentrated on one or two faults, but as the system approaches the Red River region in Yunnan, it branches into multiple strands with complicated step-over and interference relationships (Wang et al., 1998; Shen et al., 2003). Displacement consistently sums to ~60 km across the entire fault zone, and the Red River, Red River fault and Ailao Shan shear zone are deflected, but not offset, ~60 km left-laterally where the Xianshuihe-Xiaojiang fault system projects across them (Wang et al., 1998). Left-slip occurs on multiple northeast-striking faults to the southwest in southern China and Indochina. These faults are less well known, but displacement determined by river “dogleg” offsets on three of these faults, the Mengxing, Nam Ma and Wanding faults, are 24 km, 12 km and 9.5 km respectively (Fig. 1a; Lacassin et al., 1998). As there are a number of other active faults in this region, including the easternmost Dien Bien Phu fault in Vietnam, displacement southwest of the Red River may be of a similar magnitude to that on the Xianshuihe-Xiaojiang fault system. The relationship between faults on either side of the Red River fault, however, is unclear, leading in part to the very different models for the region discussed below. Structural basins along the left-lateral fault system contain Quaternary and Late Pliocene age deposits, and on this basis Wang et al. (1998) infer 2-4 Ma for the inception of the fault system, yielding a slip rate of 15-30 mm/yr. Shen et al. (2003) inferred a similar rate on the basis of trenching and radiocarbon dating: a combined 16 mm/yr for both the east and west Xiaojiang faults, with probable displacement on other fault

strands as well. In contrast, geodetic slip rates are slightly lower (12 ± 4 mm/yr, King et al., 1997 and ~ 10 mm/yr, Chen et al., 2000). The reason for the discrepancy is unclear, but possibilities include that short-term slip rates (geodetic) are slightly lower than the long term average (geologic), or that basin sediments are not well dated and may stretch into the early Pliocene time, allowing for a slightly earlier initiation of the fault system (5 to 6 Ma) (Wang et al., 1998).

Much of Yunnan is in extension today, particularly across the Dali fault system northwest of the Red River fault (Fig. 1a; Leloup et al., 1993; Wang et al., 1998), and the Tengchong volcanic field to the southwest (Fig. 1a; Wang and Burchfiel, 1997; Wang et al., 1998). The Dali Fault system is a complicated region of dip-slip and strike-slip faulting along north-northeast- and northwest-trending faults. Extension on the western side of the Dali region is particularly impressive in the Diancang Shan, which is bounded on three sides by detachment faults (Leloup et al., 1993; Wang et al., 1998). The gneissic core of the range is interpreted to be the probable northwest continuation of the Ailao Shan shear zone (Tapponnier et al., 1990; Leloup et al., 1993). Strike-slip faulting also accommodates rotation of crustal fragments within the Dali region (Wang et al., 1998). Sedimentary deposits in extensional basins within the fault system suggest a Quaternary or Pliocene initiation (Wang et al. 1998). Geochronological data in the Diancang Shan indicate rapid cooling of the massif between 4 and 5 Ma (Leloup et al., 1993), though the authors regard this as the result of normal displacement along the northwest continuation of the Red River fault rather than initiation of the Dali Fault system.

Regional models

Probably the most influential conceptual model for development of this region is the “extrusion model” (Tapponnier et al., 1982, 1986) which has been refined over the past two decades on the basis of mapping, geochronology and modeling studies (Tapponnier et al., 1990; Schärer et al., 1990; Avouac and Tapponnier, 1993; Brias et al., 1993; Leloup and Keinast, 1993; Leloup et al., 1995; Harrison et al., 1996; Peltzer and Saucier, 1996; Leloup et al., 2001). This model hypothesizes significant extrusion of Indochina during early- to mid-Cenozoic time, resulting in development of the Ailao Shan shear zone. Harrison et al. (1996) argue for transtensional exhumation of the shear zone on a fault they consider to be the same structure as the modern Red River fault. According to the extrusion model, since approximately Pliocene time (Leloup et al.,

1993), the sense of tectonic displacement reversed, and Tibet and South China have been extruding to the east and southeast, bounded on the southwest side by the Jiali fault system (Fig. 1a inset) and the reactivated Red River fault and on the north side by the Altyn Tagh fault (Fig. 1a inset; Tapponnier et al., 1982; 1986; Avouac and Tapponnier, 1993; Peltzer and Saucier, 1996). Modeling studies suggest that regions of the eastern plateau margin are internally rotated, though only to a small degree, during extrusion, resulting in left-lateral displacement along the Xianshuihe-Xiaojiang fault system and the Kunlun fault (Fig. 1a inset; Avouac and Tapponnier, 1993; Peltzer and Saucier, 1996). The bend in the Red River fault is thought to originate through interaction with the Xianshuihe-Xiaojiang fault, but Replumaz et al. (2001) argue that left-lateral displacement is mostly absorbed in shortening north of the Red River fault and is not transferred across the fault in any way. Predicted displacement rate on the Red River fault today, according to this model, is $\sim 10 \pm 5$ mm/yr toward N110°E (Peltzer and Saucier, 1996), resulting in 7.5 ± 4 mm/yr dextral slip and an associated extensional component (Replumaz et al., 2001). Both the Ailao Shan shear zone and Red River fault, parts of a single structure in the model, are viewed as sub-vertical, crustal scale features.

Alternate models argue for rotation around the eastern Himalayan syntaxis rather than southeast directed extrusion, and emphasize complex regional deformation (England and Houseman, 1989; Dewey et al., 1989; Houseman and England, 1993; Wang and Burchfiel, 1997; Wang et al., 1998). Wang et al. (1998) present evidence for Pliocene-Quaternary rotation around the eastern Himalayan syntaxis of a region bounded to the east by the Xianshuihe-Xiaojiang fault system in Sichuan and Yunnan, and by the Dien Bien Phu fault in Vietnam. In this model, the rotating fragment is strongly internally deformed. The Dali fault system, for example, accommodates east-west extension and rotation within the larger rotating crustal fragment (Wang et al., 1998). Regions to the southeast of the syntaxis are in overall extension, while regions to the northeast are in compression (Wang et al., 1998; Wang and Burchfiel, 2000). GPS data support this model, at least in the short term, showing consistent velocity vectors parallel to the Xiaojiang and Dien Bien Phu faults both north and south of the Red River (King et al., 1997; Chen et al., 2000). Wang et al. (1998) argue that the Red River fault acts as a passive marker in this rotating system, and is deflected ~ 60 km by shear, producing the prominent bending of the Red River fault, Ailao Shan shear zone and Red River as well as structures farther to the southwest. Right-slip along the

fault may result from rotation, just as right-slip is produced on several faults to the northeast which are bounded on either end by left-lateral strands of the Xianshuihe-Xiaojiang fault system (Fig. 1b; Burchfiel and Wang, 2003). A component of displacement on the Red River fault may also result from east-west extension in the Dali region and between strands of the Xianshuihe-Xiaojiang fault system (Wang et al., 1998).

An additional important factor to consider in unraveling recent deformation of the southeast margin of the Tibetan plateau is the growth of the plateau itself. The southeast margin is characterized by an elevated, low-relief landscape, which forms a continuous carapace from the Tibetan plateau to the south Asian coastal margin, and is deeply incised by the major rivers of the eastern plateau (Clark and Royden, 2000). The elevation of this landscape through surface uplift suggests crustal thickening. However, throughout the southeast margin region there is little evidence for crustal shortening at the Earth's surface. The effect is particularly dramatic in the Longmen Shan, adjacent to the Sichuan basin (Fig. 1a), where GPS and geologic studies (Burchfiel et al., 1995; King et al., 1997; Chen et al., 2000; Kirby et al., 2000) have demonstrated insignificant Cenozoic upper crustal shortening (<3mm/yr, Chen et al., 2000) despite a topographic front nearly as steep as the Himalayan front (Clark and Royden, 2000). On the southeast plateau margin, there are regions of local shortening with transpressive bends or steps along the Xianshuihe-Xiaojiang fault system (Wang et al., 1998), but little indication elsewhere of active regional crustal shortening. The lack of correspondence between surface shortening and apparent crustal thickening is a crucial observation for recent studies (Royden, 1996; Royden et al., 1997; Clark and Royden, 2000) which suggest crustal thickening may occur through the extrusion of weak lower crust from beneath the Tibetan Plateau into the mid to lower crust of the southeastern margin. This intruded material thickens the crust, resulting in isostatic surface uplift with no accompanying upper crustal shortening. According to these models, gravitational potential energy drives the flow from areas of higher to lower (Clark and Royden, 2000). In the Red River region, there is clear evidence for surface uplift. By reconstructing the river network developed on the low-relief, perched landscape, Schoenbohm et al., (in press, and Chapter 4) demonstrated 1400-1500 m surface uplift near the Chinese-Vietnamese border, with the total amount of surface uplift increasing toward Tibet. If the lower crustal flow models are correct, ~1500 m surface uplift implies ~9 km crustal thickening (assuming Airy isostasy)

through the addition of low viscosity material. The implied presence of weak crustal material beneath the southeast part of the plateau should affect the faults observed at the surface.

MOTIVATION

In the context of limited existing data on, and competing models for, active tectonics of the southeast plateau margin, a clear understanding of the Red River fault is fundamentally important. We focus on several questions: (1) What is the magnitude, distribution and nature of strike-slip and dip-slip displacement along the Red River fault? Many aspects of the Red River fault are still poorly known, particularly the role of the major bend in shaping fault morphology and the pattern of displacement. (2) How does the Red River fault interact with the Xianshuihe-Xiaojiang fault system? Is it possible for displacement on the Xianshuihe-Xiaojiang fault system to pass across the Red River fault without visible surface structures? (3) How does the Red River fault interact with the Dali fault system? Proponents of the extrusion model link it to fault systems in Tibet, and so advocate that the fault continues in some way to the northwest (Tapponnier et al., 1982; 1986; Leloup et al., 1993; 1995). In other interpretations, the Red River fault is truncated by the Dali fault system (Wang et al., 1998). (4) What are the mutual relationships among faulting, surface uplift and river incision in this region? What do these imply for dynamic connections between the active tectonics of the southeastern plateau margin and the proposed intrusion of weak mid to lower crust?

RESULTS: STRUCTURAL RELATIONSHIPS ALONG THE RED RIVER FAULT

Strategy

In order to address these fundamental, unresolved questions about the Red River fault and its relationship to other regional fault systems and surface uplift, we conducted detailed field mapping in a number of locations (Fig. 1). We also relied on remotely sensed imagery (CORONA), DEM analysis, and existing maps (Allen et al., 1984; Bureau of Geology, Yunnan, 1990; Replumaz et al., 2001). Data from Nansa (~100 km southeast of the bend; called Atu by Allen et al., 1984 and Replumaz et al., 2001), Yuanjiang (at the bend), Ejia (~150 km north of the bend) and Wudingshan (at the northern termination of the Ailao Shan gneiss) are useful for understanding the differences in fault morphology relative to the bend (Fig. 1b). We explored interactions between the Red River fault and Xianshuihe-Xiaojiang fault system at Yuanjiang

and Nansa, which bracket the zone in which the faults interact (Fig. 1b). Cenozoic sediments preserved along the fault in these map areas reveal much about both the Red River fault and earlier deformation related to exhumation of the Ailao Shan shear zone. These findings are discussed in Chapter 2 of this thesis, though we review data relevant to the Red River fault here. We also conducted field studies in the Midu basin and near the southern end of Erhai Lake (Fig. 1a) to assess the northern continuation (or termination) of the Red River fault where it intersects the Dali fault system. Data from the Wudingshan region (Fig. 1b) constrain the timing of incision of the Red River. We describe our results from southeast to northwest.

Nansa map area

Faults: In the Nansa region, two major strands of the Red River fault are present (Fig. 3). The southwest strand is sub-vertical and separates Ailao Shan shear zone gneiss from Cenozoic sedimentary rocks and Triassic rocks of the Yangtze platform (Fault A, Fig. 3). The northeast strand, also sub-vertical, juxtaposes an Upper Triassic Yangtze platform unit (T_3 , low-grade phyllite, quartzite and minor carbonate) against a Middle Triassic unit (T_2 , massive black and gray limestone) (Fault B, Fig. 3). Both faults are marked by gouge zones. Near Nansa, the faults are ~100-200 m apart, separated by Early Oligocene lacustrine mudstone and gypsum: deformation in this region is continuous between the two faults (Fig. 4a), and the lacustrine sediments are intensely sheared, with distributed gouge zones developed throughout (Figs. 4b and 4c). Both faults reactivate older structures: the southwest fault is the original contact between Ailao Shan shear zone rocks and the adjacent terrain and thus probably accommodated 10's or 100's of kilometers displacement. The northeast strand records left-lateral displacement as well, juxtaposing the two Triassic units (Chapter 2), although a unique displacement cannot be determined. This reactivation of older, left-lateral structures by right-lateral displacement in recent times is also present along several faults 50 to 70 km north of the map area (Burchfiel and Wang, 2003). In the northern corner of the map area a right-lateral strike-slip fault (Fault C, Fig. 3) offsets an older thrust fault. Near the town of Wubang, a small thrust fault oblique to and between the major fault strands (Fault D, Fig. 3) appears to accommodate minor local shortening. In the southeast part of the map area, two minor faults are present, one between the two major faults (Fault E between A and B, Fig. 3), and one fault along the northeast side of the valley (Fault F northeast of Fault B, Fig. 3) which merges with the northeast major fault (Fault B,

Fig. 3). Cenozoic rocks are extensively folded and sheared throughout the Nansa region. However, much of this deformation is probably older than initiation of the Red River fault and is syn-depositional, related directly to exhumation of the Ailao Shan shear zone (Chapter 2).

Displacement: Stream offsets in the Nansa region are minor, generally <1 km. Just to the northwest, however, a major ridge deflects tributaries along its entire ~16 km length (Figs. 2 and 3). Allen et al. (1984) noted this ridge, but argued that when the Red River was at a higher elevation, tributaries flowed across the top of the ridge. With continued river incision, the tributaries preferentially incised weak rocks along the fault, abandoning their courses over the crest: the 16 km long ridge thus results from stream capture and erosion within a zone underlain by weak rock and does not reflect total strike-slip displacement. However, we agree with Replumaz et al. (2001) that the simplest interpretation, and that most consistent with data elsewhere, treats this feature as a shutter ridge which records a minimum ~16 km displacement. Replumaz et al. (2001) observe another major shutter ridge near the town of Honghe (Fig. 1) which indicates ~22 km geomorphic displacement (Fig. 2).

According to our mapping, an older thrust fault on the northeast side of the basin is offset right-laterally ~5 km by a minor strand of the Red River fault (Fig. 2; Fault C, Fig. 3). Because we do not consider this to be one of the major, through-going faults within the Nansa region, displacement across the entire fault system at Nansa is probably significantly greater than 5 km.

Xianshuihe-Xiaojiang related faults: Two faults, which we interpret to be the continuation of strands of the Xiaojiang fault system, are present in the map area (Faults 1 and 2, Fig. 3). Both faults strike NNE and dip west ~50-60°. Left-lateral displacement on the eastern fault is <1 km and on the western fault is <500 m. Both faults merge and are lost within the intensely sheared zone between the two major strands of the Red River fault (Faults A and B), and neither fault offsets the northeast contact of Ailao Shan shear zone. Both faults project into a major strand of the Xiaojiang fault system to the north (Wang et al., 1998).

Yuanjiang map area

Faults: This map area consists of a southeastern and northwestern part, separated by the Yuanjiang basin (Fig. 5). To the southeast, the Red River fault is a single fault strand, marked by a gouge zone ~100 m thick with a northeast dip of ~80° (Fault B, Fig. 5; Fig. 6a). In one place, cenozoic sedimentary rocks (Oligo-Miocene fluvial conglomerates) are folded about an E-W trending axis (Fig. 5), consistent with a right-lateral structural setting. These folded sediments are truncated by deposition of a boulder conglomerate which is locally deformed along the Red River fault, but elsewhere is flat lying (Fig. 5). Folding of the truncated sediments must pre-date deposition of the boulder conglomerate, which is likely Quaternary in age because it is undeformed and unlithified, but we know of no more definite age for this unit. This fault projects to the northwest along the southwest side of the Yuanjiang basin. In this part of the map area there is no evidence of an active fault between this fault (Fault B) and the Ailao Shan shear zone.

To the northwest of the Yuanjiang basin, the Red River fault consists of a single dominant sub-vertical fault strand marked by a thick gouge zone (Fault A, Fig. 5; Fig. 6b). This fault projects to the southeast into the northern part of the Yuanjiang basin and does not connect directly with the main fault to the southeast of the basin (Fault B). Several minor fault strands trend parallel or slightly oblique to the main fault. Near the Yuanjiang basin, two faults striking approximately east-west and dipping ~50° to the south accommodate south-side down normal displacement, and together with the main fault strand, form a horst on the west side of the basin (Faults F and G, Fig. 5 and inset). A pair of minor normal faults to the northwest form a graben (Faults C and D, Fig. 5). Cenozoic strata and the Triassic Yangtze platform rocks south of the main fault strand are folded about E-W-trending axes, consistent with right-lateral displacement (Fig. 5). Near the northwest end of the map, Fault E dips ~80° northeast, coincides with well-developed triangular facets, and has a significant component of dip-slip. This fault merges to the southeast with the main Red River fault strand (Fault A). Southeast of the point at which these faults merge, triangular facets are less well-developed and the morphological break does not correspond to the Ailao Shan-Yangtze Platform contact, but rather to a steeply dipping marble horizon within the Ailao Shan gneiss. The contact here between the Ailao Shan and Yangtze Platform is an inactive, steeply southwest dipping (~80°) reverse fault.

Displacement: Tributaries to the Red River are displaced up to 5.5 km southeast of Yuanjiang (Figs. 2 and 5). Northwest of Yuanjiang a large tributary is offset a maximum of ~15 km, but the stream flows through the alluviated Yuanjiang basin, and it is unclear if the Red River fault controls this part of the river course. A more conservative estimate for displacement recorded by this tributary is probably ~8 km, the length of the river where it flows through a confined, fault controlled valley (Figs. 2 and 5). Based on a trenching study on a single strand of the Red River fault northwest of this region, near Gasa (Fig. 1b) Weldon et al. (1994) estimated a maximum slip-rate of 2.7 mm/yr on that strand and a range 1-4 mm/yr across the entire fault system (cited in Duong and Feigl, 1999, Fig. 2).

Though we were unable to observe direct geologic offsets in the Yuanjiang map area, clasts in Cenozoic strata appear to be displaced right-laterally from possible source areas across the Red River fault (Fig. 7). These fluvial sediments only incorporate sediment from sources that were originally adjacent or upstream. At three localities in the southeastern part of the map area (Figs. 5 and 7) a detailed analysis of sediment composition was made. Cobbles at site LC1 include basalt and distinctive black and gray limestone and a variety of other sandstones and siltstones. Site LC8 comprises 69% black and gray limestone with some non-diagnostic sandstones and siltstones. Site ASC9 is dominated by clasts derived from the Ailao Shan shear zone, but also contains black and gray limestone and basalt clasts. Though it is difficult to specifically identify the source unit for most cobbles within the conglomerates, the above highlighted lithologies are sufficiently unique within the Yangtze craton that they can be used for this purpose. Basalt clasts are Permian (correlative to the Emei Shan flood basalts) and black and gray limestone is derived from a distinctive Middle Triassic unit (T_2). Comparison of sample localities and the location of appropriate source rocks within the Red River basin suggests right-lateral displacement: the best constraints come from T_2 limestones, whose nearest occurrence is ~40 km downstream near the town of Honghe (Figs. 2 and 7), and from Permian basalt which occurs ~29 km downstream. However, we cannot uniquely determine the source of these conglomerates. It is possible that during Late Oligocene-Early Miocene (Chapter 2) deposition of these conglomerates, Permian basalt and T_2 limestone were more widespread on the Yunnan plateau, or were being eroded from rocks which capped the Ailao Shan shear zone (Chapter 2). The minimum displacement of 40 km indicated by this data is therefore considered tentative.

Xianshuihe-Xiaojiang related faults: Directly north of the Yuanjiang basin at least 5 discrete faults across ~4km of outcrop are the westernmost faults related to the Xianshuihe-Xiaojiang fault system. These closely-spaced sub-vertical faults strike $\sim 10^\circ$ and project northward directly to a major strand of the Xiaojiang fault (Wang et al., 1998). Displacement on each fault appears to be small (10's of meters), but they involve unconsolidated Quaternary sediment and are or were recently active. These faults are located in a region in which Replumaz et al. (2001) identify a right-lateral fault which they call the "Yuanjiang fault" with a strike sub-parallel to the Red River fault, and therefore at a high angle to the active faults we observe. We suspect that, using satellite imagery, Replumaz et al. (2001) mapped an inactive fault which is identified on Chinese maps (Bureau of Geology, Yunnan, 1990). This fault does indeed have a morphologic expression, but this may result from differential weathering along an older structure. While we cannot rule out the existence of this fault, our field observations of multiple strands of N-S-striking cross-cutting faults at a high angle which cut Quaternary unconsolidated sediments argues that the "Yuanjiang fault" is not currently active.

Ejia map area

Faults: The Red River fault is relatively simple near the town of Ejia (Figs. 8 and 9a), where there is a single fault strand dipping $\sim 70\text{-}80^\circ$ northeast, marked by a gouge zone. South of Ejia, the fault branches to two major strands, both of which deflect tributaries (Fig. 2). Evidence for normal faulting and footwall uplift includes triangular facets and dramatically steep lower reaches of tributaries (Schoenbohm et al., in press and Chapter 4). In this region, the Red River flows ~ 10 km to the east of Ejia and its tributaries are deeply incised. Between the incised tributaries and adjacent to the Ailao Shan are several flat benches at $\sim 1200\text{-}1400$ m elevation, at least 400 m above the modern river, including the bench on which the town of Ejia is built (Figs. 8 and 9b). These benches may be former tributary valley floors, stranded during incision. Replumaz et al. (2001) indicate a number of antithetic faults on the northeast side of the benches, but we could find no evidence for these faults in the field.

Displacement: Because the course of the Red River lies far east of Ejia, tributaries down stream of the fault are more entrenched than in most places where the Red River fault and the Red River

are nearly coincident. Tributaries near Ejia and to the north are offset up to 5 km, with some even showing apparent left-slip displacement, probably the result of upstream tributary capture (Fig. 8). In this region, tributaries appear to flow along the Red River fault either upstream or downstream to a tributary that crosses the mass of rocks between the fault and the river. South of Ejia, however, tributaries flow along both strands of the Red River fault and are displaced 18 to 25 km (Fig. 2). In this region, Replumaz et al. (2001) exploited the deep entrenchment of tributaries both upstream and downstream of the fault, and found a statistical best fit between upstream and downstream tributaries by restoring 25 km of right-lateral displacement. They obtained a secondary minimum of 41 km displacement (Fig. 2).

Wudingshan map area

Faults: In the southern part of the Wudingshan map area (Fig. 10), the Red River fault is marked by a thick gouge zone under the town of Damagie. Northward, the fault bifurcates, with one strand separating Ailao Shan gneiss from Yangtze platform sediments. The southwest strand, however, slices through rocks of the Ailao Shan shear zone, the only place where such a relationship is observed along the entire fault system. A minor normal fault, which dips $\sim 60^\circ$ east, is coincident in places with the northeast fault (Fig. 11a). Gneisses of the Ailao Shan shear zone terminate northwest of Wudingshan, and rocks of South China (Chuxiong basin) and Indochina (Langping-Simao basin) are directly juxtaposed along a complex boundary. The active Red River fault continues to the northwest along or close to this boundary.

Displacement: Allen et al. (1984) noted that to the northwest of Wudingshan, the Red River approaches the Red River fault, flows along it for 5.3 km, then turns east, away from the fault (Figs. 2 and 10). They interpret this to indicate 5.3 km right-lateral displacement. However, Leloup et al. (1995) and Replumaz et al. (2001) suggest a number of alternate tributary reconstructions in this region. Replumaz et al. (2001) propose matching the tributary which drains the Midu basin with the intersection of the main river and the Red River fault near Wudingshan, yielding ~ 20 km displacement (Figs. 1b and 2), which we also find to be the simplest and most robust reconstruction. However, the number of complicated tributary captures in this region precludes a simple offset analysis.

Wang et al. (1998) described slivers of Permian rocks usually found only west of the Ailao Shan shear zone displaced right-laterally to the east side of the Ailao Shan. Here they are depositionally overlain by Pliocene sediments (Fig. 12). The minimum offset required to restore these strata to a position adjacent to Permian strata southwest of the Red River fault is ~16 km (Fig. 12; Bureau of Geology, Yunnan, 1990; Wang et al., 1998). A maximum displacement based on current exposure is ~41 km, determined by matching the northwest-most outcrop of Permian rocks on either side of the fault (Figs. 2 and 12). However, Permian rocks may continue to the northwest under the Midu basin, yielding a larger possible offset. Chinese geologic maps indicate that Pliocene sediments are deposited across one of the faults which bounds a sliver of Permian rocks (Bureau of Geology, Yunnan, 1990; Wang et al., 1998). We were unable to observe this relationship in outcrop because of poor exposure and limited time, but if this relationship is correct, then displacement of these slivers must predate deposition of the Pliocene sediments. Wang et al. (1998) also use Triassic granitic rocks in a similar way. Existing maps indicate intrusive contacts for these bodies in both Indochina and Yangtze Platform rocks (Bureau of Geology, Yunnan, 1990). However, the Triassic age assigned these bodies (Bureau of Geology, Yunnan, 1990) presents an apparent contradiction: ~700 km left-lateral displacement occurred on the boundary between Indochina and South China in the mid-Cenozoic, therefore these granites must either be younger than that displacement (i.e., not Triassic), or they must be in fault contact with the surrounding rock rather than in intrusive contact. Until this conflict is resolved through further mapping and geochronology, these rocks should not be used to measure displacement on the Red River fault.

Timing of river incision: In the Wudingshan region, Pliocene sediments are deposited on a sub-horizontal surface several hundred meters above the modern level of the Red River, which in turn is ~200 m lower in elevation than the low-relief landscape on either side of the valley (Fig. 10). The Pliocene age of these sediments is constrained by plant fossils (Bureau of Geology, Yunnan, 1990). The strata comprise sandstones and conglomerate, with finer-grained fossil-bearing intervals (Fig. 11b). Conglomeratic horizons contain a variety of lithologies, including material derived from the Ailao Shan shear zone and from both Indochina and South China sedimentary strata. In many places these rocks are well-cemented, probably related to a high limestone-clast component, but in other places lithification is poor. Deformation appears to be

more intense in the less lithified units. In general, conglomerate clasts are well-rounded and relatively small (<10 cm diameter), but rare interbeds of more angular clasts are present. Tan sandstones, siltstones and mudstones are common, as are organic rich, fossil-bearing layers. Channel structures were observed as well. The contact between the Pliocene sediments and Triassic strata is depositional, and outcrops in several locations near Wudingshan, Damagie (Fig. 10) and along a road connecting the two cities. These Pliocene sediments are gently folded in some places and intensely sheared in others. Some deformation is probably related to the Red River fault, but much is the result of down-slope sliding and internal deformation of these poorly consolidated sediments as they are undermined by down-cutting of the Red River. Evidence for the latter interpretation includes the prevalence of low-angle shear planes within the sediment sub-parallel to the hillslope.

In our interpretation, these Pliocene fluvial sediments were deposited by the paleo-Red River at a time when the Red River was flowing in a broad, open valley slightly lower in elevation than the landscape on either side. The Red River has subsequently incised the landscape, abandoning its former valley, stranding these sediments high above the modern river. These sediments are similar to Oligo-Miocene conglomerates in the Nansa and Yuanjiang regions, which is expected if they are both paleo-Red River sediments (Chapter 2). These Pliocene sediments, however, are in general finer grained and contain Pliocene age fossils. These sediments are also in a different structural position, perched above the Red River on the low-relief landscape, compared to those in Nansa and Yuanjiang, which are folded deep into the valley, below the elevation of the low-relief landscape. Because these sediments are Pliocene in age, river incision must have begun in Pliocene time or later.

Midu map area

Faults: North of the termination of the Ailao Shan gneiss at Wudingshan, the Red River fault separates rocks of the Lanping-Simao basin (Indochina block) and the Chuxiong basin (South China block). South of the Midu basin, two faults lie in parallel valleys, each marked by thick gouge zones (Fig. 13). The south flowing tributary from the Midu basin starts in the eastern valley, cuts across the ridge separating the two, flows down the western valley, then cuts farther west and eventually joins the Red River which flows southeast from the Weishan basin (Fig. 13).

The eastern fault places Triassic rocks of the Chuxiong basin against rocks of the Indochina block, while the western fault is within Indochina strata. For this reason, the eastern fault is considered the dominant structure, but the modern activity along these faults is difficult to extract from their older history as left-lateral structures.

Within the Midu basin (Fig. 13), the eastern fault follows the east side of the basin, marked by deformed sediments. The western fault is more difficult to trace into the Midu basin (Fig. 13). There are several faults farther west which may represent splays or sub-parallel strands. In particular, a small basin to the west is bounded by one such fault on its eastern edge (Fig. 13). The basin is filled with deformed coal bearing sediments of probable Quaternary age (Bureau of Geology, Yunnan, 1990) and is overlain by fine-grained, flat-lying alluvial deposits (Fig. 14a). Displacement along this fault has apparently blocked the basin outlet for part of its history, allowing accumulation of coal-bearing sediments, and has also caused deformation and tilting of the basin. Recently the outlet has been breached, either through fluvial processes or because of movement along the fault, and the basin is currently being incised. Other faults in this area correlate to a number of small Quaternary basins and probably have a small component of normal displacement.

North of the Midu basin, the probable continuation of the Red River fault can be traced from the northwestern corner of the basin through a narrow valley and into the Erhai basin to the north (Figs. 13 and 14c). It is unclear if this fault is active, though we did observe at least one possible tributary that is offset right-laterally (Fig. 14b). This fault continues north into the Erhai basin where it juxtaposes Indochina rocks with fine-grained Quaternary lacustrine sediments (Fig. 13), suggesting recent activity. The northward continuation of this fault is unclear, but it may trend along the east side of Erhai Lake forming a prominent scarp (Fig. 13).

Interaction of the Red River fault with the Dali Fault System: The Chenghai fault, a northeast trending, left-lateral fault which is part of the Dali fault system, forms a steep topographic scarp along the north side of the Midu basin (Wang et al., 1998). The Chenghai fault truncates the eastern strand of the Red River fault and offsets it left-laterally ~7 km to where it continues through the valley and into the Erhai basin to the north (Figs. 13 and 14d). Left-lateral

displacement on the Chenghai fault is probably transferred to extension, accommodated by structures on the southwest side of the basin, and thus is responsible for the formation of the Midu basin (Fig. 13 inset). It is less clear how right-lateral displacement on the Red River fault is accommodated, and we will explore this topic further in the discussion.

DISCUSSION

We now return to the principal questions motivating this study, considering questions about the recent structural, geomorphic and geodynamic development of the southeast margin of the Tibetan Plateau.

The magnitude and distribution of displacement on the Red River fault

Fault morphology: The number of faults and the way in which slip is partitioned on the strands of the Red River fault varies along its length and depends on local conditions: we do not observe two distinct faults with consistent partitioning of strike- and dip-slip, as originally proposed by Allen et al. (1984). Near Nansa, ~100 km southeast of the major bend in the fault, our mapping demonstrates two principle faults, neither of which shows evidence for dip-slip displacement, and a number of other small, sub-parallel faults (Fig. 3). In the vicinity of the bend, at Yuanjiang, there is a single major fault strand on either side of a right step-over, with multiple subsidiary faults (Fig. 5). Some of these faults show evidence for normal displacement, particularly a fault in the northwest which follows the Ailao Shan-Yangtze platform contact (Fault E, Fig. 5). North of the bend, the fault consists of two strands until just southeast of Ejia, where they merge again, forming a single trace with clear evidence for normal-sense displacement (Fig. 8). At Wudingshan, the fault bifurcates again, and a local fault farther east has clear normal sense displacement (Fig. 10), though it is not as well-developed as at Ejia. The faults continue northwest as two strands, though the eastern strand is probably the dominant structure, into the Midu basin, where the eastern strand is truncated and offset ~7 km left-laterally by the Chenghai fault (Fig. 13).

Our mapping indicates strong expression of normal faulting at Ejia, decreasing to the northwest toward the Midu Basin, and decreasing to the southwest as well, where evidence for dip-slip displacement is strong at Yuanjiang but is absent at Nansa (Fig. 1). This is consistent with the

river reconstruction work of Schoenbohm et al. (in press and Chapter 4) which determines precisely the same distribution of normal displacement, reaching a maximum of ~750 m near Ejia. It is also consistent with the hypothesis of Wang et al. (1998) that slip is approximately parallel to the segment southeast of the bend, resulting in an extensional component to slip northwest of the bend.

The origin of the Yuanjiang basin (Fig. 1) is important because of its position at a critical kinematic point, the bend in the Red River fault. On the basis of satellite image interpretation, Replumaz et al. (2001) proposed the existence of the “Yuanjiang fault,” which should lie between Gasa and Yuanjiang (Fig. 1), “shortcutting” and essentially straightening the bend. In this model, the Yuanjiang basin forms as a result of interactions at the intersection of the Red River and Yuanjiang faults. However, our mapping indicates that the northwest-southeast feature observed by Replumaz et al. (2001) is probably an older, inactive fault: we identify instead a series of north-south trending left-lateral faults in the same location which involve unconsolidated Quaternary material and are therefore currently or recently active. Further, the distribution of normal faulting along the length of the fault suggests that the bend is an integral part of the kinematics of the fault system, and there is no need to “shortcut” the bend. Rather, we interpret the Yuanjiang basin as a complex extensional pull-apart structure, partly the result of a step-over in the Red River fault (Fig. 5 inset). The two major faults on either side of the Yuanjiang basin do not meet or align: the southeast fault projects along the south side of the basin, while the northeast fault projects through the northern part of the basin. Both these faults dip in the same direction, toward the northeast ~80°. Two faults south of and sub-parallel to the fault northwest of Yuanjiang dip 50-60° in the opposite direction, toward the southwest (Fig. 5). These faults together define a graben and horst structure, and account partially for the formation of the Yuanjiang basin. The basin may also partly result from down-warping of the hanging wall in response to normal faulting (Fig. 5), which is supported by tributary profile analysis by Schoenbohm et al. (in press and Chapter 4), or from differential left-lateral displacement on highly distributed southernmost strands of the Xianshuihe-Xiaojiang fault system (Fig. 5 inset).

Strike-slip displacement: Stream offsets along the Red River fault (Fig. 2), range from just a few meters up to 25 km, and are determined by correlating tributary or main channel segments which

are displaced along the fault. This analysis is complicated for offsets greater than the characteristic stream spacing, because channels can be captured by originally upstream channels as they are moved past each other by displacement on the fault. For this reason, the length of “dog-leg” channels or shutter ridges record only the minimum displacement on the fault, which in the case of the Red River appears to be ~25 km southeast of Ejia (Fig. 2). Replumaz et al. (2001) circumvent this problem by statistically matching channel segments on either side of the fault in the Ejia and Wudingshan regions: they obtained a best fit correspondence through restoration of ~25 km displacement: this is an actual displacement value, not a minimum. Replumaz et al. (2001) also propose a river reconstruction in the region between Ejia and Midu which yielded ~20 km displacement. Minimum displacement near Honghe (~22 km) and Nansa (~16 km) are in a similar range. These data permit the possibility that displacement is not uniform along the Red River fault, being greatest near Ejia, (~25 km), decreasing northwest to 20 km between Ejia and Midu and to the southeast to ~22 km at Honghe and ~16 km at Nansa. However, given that the latter values only provide a minimum constraint on the displacement, we consider the more conservative case in our analysis below that the magnitude of displacement is constant at ~25 km along the entire length of the fault (Replumaz et al., 2001).

The Red River drainage network probably began to record displacement on the Red River fault only after the Red River began to incise the landscape (Allen et al., 1984; Replumaz et al., 2001). Though rivers can record strike-slip displacement in the absence of deep entrenchment, non-entrenched rivers are less likely to record displacement of the magnitude observed here (up to 25 km) because displaced tributaries can more easily change their course and reorganize for greater transport efficiency in response to strike-slip faulting. Pliocene age paleo-Red River sediment near Wudingshan (Figs. 1 and 10) indicates that the river was not incised at the time of their deposition, and therefore incision began in Pliocene time or later.

Given ~25 km displacement since Pliocene time (<5.3 Ma), the long-term average slip-rate is a minimum of ~5 mm/yr. If the Red River began to incise more recently, the corresponding slip-rate would be higher. However, slip-rate may not be constant with time, and in particular may be decreasing toward the present. In the Midu basin, the Red River fault is truncated and offset by the Chenghai fault, and therefore slip cannot be occurring along the Red River fault in that

region unless it is accommodated in some unknown way. A trenching study on a single strand of the Red River fault by Weldon et al. (1994) estimated a maximum slip rate of 2.7 mm/yr on that strand and a range 1-4 mm/yr across the entire fault system (cited in Duong and Feigl, 1999). Strike-slip rates appear to die out toward the South China Sea, where geodetic data in Vietnam indicate probably a small amount of dextral displacement across the fault (1-5 mm/yr) though uncertainties are very large (Duong and Feigl, 1999). Seismic reflection profiles in the Gulf of Tonkin show no sign of Pliocene faulting (Rangin et al., 1995). A recent, low slip-rate also could explain the lack of historic seismicity along the fault (Allen et al., 1984). These data collectively suggest slip-rate may have been higher in the past than it is today.

Our data also suggest an older, pre-Pliocene or pre-river incision history for the Red River fault. South of Yuanjiang, Late Oligocene/Early Miocene fluvial conglomerates contain clasts that could be derived from sources currently located ~40 km downstream, indicating a possible ~40 km right-lateral displacement (Figs. 5 and 7). The extent of possible source regions during deposition of the conglomerate, however, is uncertain, and so this magnitude of displacement is considered tentative. If correct, this geologically recorded displacement (~40 km) exceeds geomorphically recorded displacements (~25 km) by at least 15 km. At the northern termination of the Ailao Shan gneiss, slivers of Permian limestone are right-laterally displaced a minimum of 16 km (Figs. 2 and 12). The faults originally bounding the slivers appear to be inactive since the deposition of Pliocene age sediments (Figs. 10 and 12; Bureau of Geology, Yunnan, 1990), though we were unable to confirm this in the field. If this relationship is correct, the geologically recorded ~16 km displacement predates ~25 km displacement recorded by offset rivers. A tentative, minimum value for total geologic displacement on the Red River fault is ~40 km, at least 15 to 16 km of which pre-dates river incision. Though data are sparse and uncertain, displacement appears to be roughly consistent along the length of the fault.

Displacement on the Red River fault of at least 15-16 km may have begun before the onset of river incision because tentative offset geologic markers record greater displacement than do the rivers. This displacement may have been continuous with that recorded by the Red River, or it could result from an older, temporally distinct event. If deformation was continuous, the long term slip rate (~5 mm/yr) and the tentative total dextral displacement (~40 km) yield an initiation

of the fault system at approximately 8 Ma or earlier. Unfortunately, we know of no direct constraints on the timing of initiation of the Red River fault which could confirm this. Leloup et al. (1995) argue that vertical displacement on the Red River fault is related to exhumation of the Diancang Shan massif, which began to cool rapidly between 4 and 5 Ma, based on $^{40}\text{Ar}/^{39}\text{Ar}$ data (Leloup et al., 1993). However, vertical displacement on the Red River fault is only a maximum of 750 m near Ejia and decreases in magnitude to the northwest (Schoenbohm et al., in press and Chapter 4): a much more extensive exhumation of the Diancang Shan (>4 km; Leloup et al., 1993) is probably unrelated. The faults in the Dali region form a kinematically distinct system (Wang et al., 1998); while the two fault systems are probably related in some way today, they may not have originated at the same time. Another possibility is that displacement recorded by geologic markers corresponds to a distinct, earlier faulting episode. Rapid cooling recorded by apatite and zircon fission-track thermochronology at 13-10 Ma (Bergman et al., 1997; Leloup et al., 2001) could be the result of early displacement on the Red River fault, though this is difficult to ascertain because of the limited context for the data. The reason for, and timing of, the possible pre-river incision displacement of at least 15-16 km remains unresolved.

Interaction of the Red River fault and the Xianshuihe-Xiaojiang fault system

As the Xianshuihe-Xiaojiang fault system approaches the Red River fault (Fig. 1a), deformation becomes more diffuse. Near Nansa, there are two faults with displacement <1 km which project northward into eastern strands of the Xiaojiang fault system (Fig. 3). These faults cut one strand of the Red River fault, but die out before reaching the second strand and the Ailao Shan shear zone. In the Yuanjiang region, there are a series of north-striking faults across a ~4 km wide transect which project northward into a western strand of the Xianshuihe-Xiaojiang fault (Figs. 1 and 5). The faults displace unconsolidated Quaternary sediment and are currently or recently active, although displacement on any one of the faults is relatively minor (10's of meters). Our mapping thus demonstrates that the Ailao Shan shear zone and most of the strands of the Red River fault are not cut by the Xianshuihe-Xiaojiang fault system: rather, the fault system becomes progressively more diffuse as it approaches the Red River, resulting in tens and possibly hundreds of faults, each with minor displacement, in the ~100 km wide region of intersection.

The Xianshuihe-Xiaojiang fault system is among the most seismically active fault systems in the world (Allen et al., 1991), with ~60 km displacement (Wang et al., 1998) and slip-rates estimated from 10 to 30 mm/year (King et al., 1997; Wang et al., 1998; Chen et al., 2000). Although these faults slice through older geologic features elsewhere, they do not cut the Red River fault or the Ailao Shan shear zone. The Red River fault and probably more importantly the Ailao Shan shear zone must form a profound crustal discontinuity. How is displacement on the Xianshuihe-Xiaojiang fault system then accommodated? Is it absorbed at the intersection with the Red River fault, or does the shear continue across the fault and Ailao Shan shear zone in the absence of any obvious structures?

Replumaz et al. (2001), in supporting the extrusion model, argued for the first case, that displacement is absorbed by a combination of deflection of the Red River fault and shortening northeast of the Red River. However, this region is in overall extension, with numerous extensional basins along strands of the Xianshuihe-Xiaojiang fault system (Wang et al., 1998, Shen et al., 2003), and extension in the Dali region (Wang and Burchfiel, 1997; Wang et al., 1998). Replumaz et al. (2001) proposed recent shortening in Cenozoic sediments along the Red River, but discussion in Chapter 2 of this thesis demonstrates that this shortening is related to exhumation of the Ailao Shan shear zone in Oligocene and Miocene time.

Because of these data, and for reasons expanded on below, we favor the second interpretation, in which shear, manifested by counterclockwise rotation, continues across the Red River fault. Southwest of the Red River fault and the Ailao Shan are less well-studied northeast-striking, active left-lateral faults, and their displacement may be of about the same magnitude as on the Xianshuihe-Xiaojiang fault system (Lacassin et al., 1998; Wang et al., 1998). Wang et al. (1998) argue that the Xianshuihe-Xiaojiang fault system and these faults together bound a crustal fragment which rotates around the eastern Himalayan syntaxis. Geodetic data support this interpretation, indicating rotation of this region at ~10 mm/yr, with velocity vectors at a high angle to the Red River fault (King et al., 1997; Chen et al., 2000). In this interpretation, the Red River fault is a passive marker, deflected by regional left-lateral shear (King et al., 1997; Wang et al., 1998; Chen et al., 2000).

Although the continuation of shear across the Red River fault and Ailao Shan shear zone is a kinematic challenge, the phenomenon is not unique. Particularly because of the growing body of GPS data, a number of regions have been identified where strain is transmitted in the absence of obvious accommodating structures. GPS data from the eastern margin of the Tibetan plateau indicates a zone of right-lateral shear, 8-10 mm/yr over 500 km, must exist between the Longmen Shan and the northeast part of the plateau (Fig. 1a; Chen et al., 2000). A number of small faults affect this region, but their history is poorly known and there is no obvious way in which the velocity gradient is accommodated (Chen et al., 2000). A similar situation in Greece has been identified, partly with the aid of GPS data, in which a broad zone of right-shear appears to cross central Greece, linking the North Anatolian fault with the West Hellenic subduction zone (Kahle et al., 1998), though again, there is no expression of a through-going structure parallel to the velocity gradient in the upper crust. The North Anatolian fault appears to terminate in a series of extensional faults, and a number of reactivated extensional and strike-slip faults may serve to accommodate this shear (Reuther et al., 1993; Dinter and Royden, 1993; Kahle et al., 1998; Kiratzi, 2002). Perhaps the best analogue is the Garlock fault and the Eastern California shear zone. The east-west striking, left-lateral Garlock fault trends orthogonally across the broadly deforming, right-lateral Eastern California shear zone (Dokka and Travis, 1990a; 1990b). None of the faults of the Eastern California shear zone cut the Garlock fault, except the southern Death Valley fault zone, despite geodetic studies which indicate that right-lateral shear continues across the Garlock fault (McClusky et al., 2001; Miller et al., 2001)

In our conceptual model (Fig. 15), the anisotropic zone defined by the Ailao Shan shear zone and the Red River fault is rotated between a series of blocks defined by strands of the Xianshuihe-Xiaojiang fault system. The distributed nature of the Xianshuihe-Xiaojiang fault system in the vicinity of the Red River fault is an indication of how the shear is accommodated. In order not to open gaps between the blocks and the shear zone, deformation must occur on a large number of discrete faults; this essentially breaks the blocks up into smaller and smaller sub-blocks until there is nearly continuous contact between the blocks and the anisotropic zone. The anisotropic zone undergoes a small amount of lengthening, which could easily occur within the strongly foliated gneisses of the Ailao Shan shear zone. Although left-lateral faults are not present

immediately south of the Ailao Shan shear zone (except for the Dien Bien Phu fault), this deformation may be broadly distributed or otherwise hidden within the Lanping-Simao fold and thrust belt (Fig. 1).

Interaction of the Red River fault and the Dali fault system

The Red River fault terminates to the northwest within the Dali fault system. Our mapping indicates that the Red River fault is offset left-laterally ~7 km by the Chenghai fault in the Midu basin (Fig. 13). The Red River fault, however, shows evidence for recent activity between Midu and Wudingshan, and possibly along its northward continuation from the northwest corner of the basin. This suggests two possible interpretations. The Chenghai could be very young and active, having truncated and displaced the Red River fault only recently. This scenario is more attractive if slip-rate on the Red River fault is lower in the present than suggested by the average long-term slip-rate. Alternatively, slip on the Red River fault may be absorbed in some way near the intersection of the Chenghai and Red River faults, though it is not clear how this might occur. Further, there is no direct connection between the northernmost trace of the Red River fault and the faults associated with the Diancang Shan massif. The possible extension of the Red River fault is along the east side of Erhai Lake, whereas the faults bounding the Diancang Shan lie to the west by several kilometers (Wang et al., 1998), and these faults show no evidence for right-lateral displacement (Leloup et al., 1993; Wang et al., 1998). Finally, the Qiaohou fault (Fig. 1) has been proposed to be the northern continuation of the Red River fault (Tapponnier et al., 1990; Leloup et al., 1995). However, field observations indicate that displacement on this fault is probably left-lateral (Wang et al., 1998). The Red River fault clearly does not pass through the Dali region, but rather is displaced or terminates in some way. This is inconsistent with aspects of the extrusion model, which connect the Red River fault through the Diancang Shan and Qiaohou fault to the Jiali fault system in Tibet (Tapponnier et al., 1990; Leloup et al., 1995).

Plateau growth, river incision and the active fault systems

The southeast margin of the Tibetan plateau appears to have experienced surface uplift in Cenozoic time, associated in some way with Cenozoic growth of the Tibetan Plateau itself. Recent studies have suggested that surface uplift in this region results from the extrusion of weak crust from beneath the Tibetan plateau into adjacent regions, thickening the crust at mid to lower

crustal levels, causing isostatic surface uplift (Clark and Royden, 2000). This hypothesis appears to be supported in a number of ways by structural and geomorphic relations in the Red River region, which we discuss below.

Important evidence for lower crustal flow comes from the presence of a low-relief landscape perched above the deeply incised rivers of the southeastern plateau margin (Clark and Royden, 2000; Clark, 2003; Schoenbohm et al., in press, and Chapter 2). This low-relief landscape was presumably elevated through regional surface uplift, triggering incision along the Yangtze River, the Red River, and other major rivers of the southeast margin (Clark et al., in press; Clark, 2003). By reconstructing the paleo-Red River tributary network developed on the low-relief landscape, Schoenbohm et al. (in press and Chapter 4) demonstrated 1400 ± 100 m river incision and an associated 1400-1500 m surface uplift near the Chinese-Vietnamese border. The amount of surface uplift probably increases in magnitude towards Tibet and decreases toward zero where the perched, low-relief landscape merges with the modern coastal plain. Surface uplift in this region has occurred in the absence of upper crustal shortening. In fact, much of Yunnan is currently undergoing extension, particularly in the Dali and Tengchong regions (Leloup et al., 1993; Wang and Burchfiel, 1997; Wang et al., 1998). Shortening within Cenozoic fluvial conglomerates along the Red River occurred in Oligocene-Early Miocene time, and thus predates surface uplift in this region. Surface uplift in the absence of upper crustal shortening suggests crustal thickening may occur at mid to lower crustal levels (Burchfiel et al., 1995; Kirby et al., 2000; Chen et al., 2000; Clark and Royden, 2000; Kirby et al., 2002; Clark, 2003)

Incision along the Yangtze and major tributaries near the edge of the Tibetan Plateau in late-Miocene time (7-13 Ma) is implied by the apatite (U-Th)/He data of Clark (2003). River incision is the result of surface uplift, and thus constrains the timing of plateau growth, although there may be a relatively short lag time (~1 Ma?) between the beginning of surface uplift and the onset of river incision. Kirby et al. (2002) use (U-Th)/He and $^{40}\text{Ar}/^{39}\text{Ar}$ data to similarly infer uplift of the plateau adjacent to the Sichuan basin in late Miocene or early Pliocene time (10-12 Ma in the Longmen Shan, western edge of Sichuan basin, and 5-7 Ma in the Min Shan, northern edge of Sichuan basin). In the Red River region, Pliocene, paleo-Red River sediments, deposited on a regional low-relief landscape and perched above the modern Red River, indicate river incision

must have begun in Pliocene time or later (<5.3 Ma). These data together imply that plateau growth began in the Middle to Late Miocene near Tibet, propagated southeastward, and reached the Red River region possibly in latest-Miocene or in Early Pliocene time. This is consistent with the flow of lower crustal material from beneath the Tibetan plateau towards the southeast.

Along the eastern and southeastern margin of the Tibetan plateau, there is a consistent mismatch between upper crustal structure and apparent gradients in crustal thickness (Burchfiel et al., 1995; Clark and Royden, 2000; Kirby et al., 2000, Chen et al., 2000). This is particularly impressive in the Longmenshan region, in which the steep range front suggests considerable shortening between the plateau and the Sichuan basin (Burchfiel et al., 1995) but both geologic (Burchfiel et al., 1995; Kirby et al., 2000) and geodetic (King et al., 1997; Chen et al., 2000) studies demonstrate minimal shortening across this boundary (<3 mm/a). On the southeast margin, the topographic gradient (Clark and Royden, 2000) approximates the gradient in crustal thickness (Li and Mooney, 1998); both elevation and crustal thickness decrease to the southeast. The upper crust, in contrast, is currently rotating around the eastern Himalayan syntaxis (King et al., 1997; Wang et al., 1998; Chen et al., 2000). The Xianshuihe-Xiaojiang fault system and Dien Bien Phu fault strike obliquely across the slope of the surface topography (Fig. 1). The lack of correspondence between crustal thickness and surface features suggests different processes are operating at different crustal depths. If pressure-gradients related to crustal thickness drive lower crustal flow, then the transport direction in the mid to lower crust in this region should be to the southeast, parallel to the gradient in crustal thickness (Li and Mooney, 1998) and roughly parallel to the topographic gradient (Clark and Royden, 2000). The upper crust, however, rotates around the eastern Himalayan syntaxis (King et al., 1997; Wang et al., 1998; Chen et al., 2000) suggesting the development of a regional detachment zone in the mid to lower crust.

Finally, although timing can only be broadly constrained, there does appear to be an overlap in the age of initiation of the Xianshuihe-Xiaojiang fault system, the Dali Fault system, and surface uplift in the Red River region. The Diancang Shan massif within the Dali region began rapidly cooling at 4-5 Ma (Leloup et al., 1993), presumably as a result of, and lagging slightly behind, the initiation of extension within the Dali Fault system. The initiation of the Xianshuihe-Xiaojiang fault system is 2-4 Ma on the basis of the age of sediments in fault bounded basins, but

is ~6 Ma if calculated using geologic offset and the geodetically determined slip-rate of ~10 mm/yr (Chen et al., 2000). The overlap in age of these faults systems and their kinematic links suggest they initiated at approximately the same time, probably around 4 to 6 Ma. River incision in the Red River region is constrained to be younger than 5.3 Ma, but probably lags slightly behind the onset of surface uplift. On the basis of these preliminary timing constraints, the fault systems which currently dominate upper crustal deformation in Yunnan initiated during growth of the southeast plateau margin, suggesting they are linked. Crustal thickening through lower crustal flow suggests a linking mechanism: the development of a detachment zone in the weak mid to lower crust could be a trigger for the initiation of the Dali Fault system and the Xianshuihe-Xiaojiang fault system.

Lateral extrusion vs. lower crustal flow and rotation

The flow of weak crustal material from beneath the Tibetan plateau into the southeast margin region (Royden, 1996; Royden et al., 1997; Clark and Royden, 2000), supported by evidence presented and compiled in this study, is incompatible with the extrusion model, in which rigid crustal blocks are translated laterally, bounded by lithospheric penetrative structures (Tapponnier et al., 1982; 1986). However, our data demonstrate that the long-term average slip-rate on the Red River fault is a minimum of 5 mm/yr, though geodetic and geologic data suggest the slip-rate is slower at present (Allen et al., 1984; Weldon et al., 1994; Rangin et al., 1995; Duong and Feigl, 1999). Displacement along the Red River fault is ~25 km since Pliocene time, and total displacement is probably more than 40 km. These data suggest the Red River fault is not simply a passive marker, but rather plays an important role in the development of the southeast margin region.

Right-lateral displacement on the rotated segment of the Red River fault could result from counterclockwise rotation within the left-lateral system (Wang et al., 1998), similar to the Jianshui, Quijiang and possibly Chuxiong faults to the northeast which are reactivated right-laterally between strands of the Xianshuihe-Xiaojiang fault system (Fig. 1b; Burchfiel and Wang, 2003). If the Red River fault is rotated ~20° along a ~170 km length (from Yuanjiang to near the Vietnamese border, Fig. 1a), the result of ~60 km deflection of the fault by the Xianshuihe-Xiaojiang fault system, simple trigonometric relationships indicate right-lateral displacement of

~10 km. However, we argue above that bending of the Red River fault is the result of distributed shear along strands of the Xianshuihe-Xiaojiang fault system (Fig. 15). If this geometry is correct, slip is zero at the boundaries of the shearing region, and within this region the amount of displacement depends on the density and exact placement of faults, but should be relatively minor. Additionally, in both scenarios, displacement both northwest and southeast of the rotated segment cannot be accounted for, which is inconsistent with evidence compiled in this study that displacement along the entire Red River fault is roughly uniform. We therefore do not consider rotation of the Red River fault to account for a significant proportion of the recorded right-lateral displacement.

Right-lateral displacement could also result from extension within the Dali fault system and between strands of the Xianshuihe-Xiaojiang fault system (Wang et al., 1998). This extension is difficult to quantify because the geometry of these faults is not well known, but we make a rough estimate here. We consider that most of the east-west extension probably occurs on three faults: the east and west bounding faults of the Dian Cang Shan massif, and the Chenghai fault (Fig. 1a). Data for the best studied fault, the eastern boundary of the Dian Cang Shan, suggests 6.3 km vertical displacement (Leloup et al., 1993) along a fault dipping ~50-60° to the east (Leloup et al., 1993; Wang et al., 1998), which corresponds to 3.6 to 5.3 km horizontal, east-west extension. The western bounding fault of the Dian Cang Shan is very poorly known, but may have accommodated a comparable amount of vertical and horizontal displacement. Along the Chenghai fault, reconnaissance field work and preliminary DEM analysis suggest ~2 km displacement based on the presence of the low-relief landscape at an elevation of ~3000 m to the east of the Chenghai fault, 1500 m above the floor of a basin to the west. The basin is filled with ~500 m sediment (Wang et al., 1998), yielding a total vertical displacement of ~2 km. The fault dips ~45° to the west (observed by BCB), and thus horizontal, east-west extension is ~2 km along this fault. The maximum east-west extension accommodated by these faults is ~13 km. This translates to ~18 km right-lateral displacement on the Red River fault, which strikes N45°W near this extending region. If extension occurs on additional faults, then we have probably underestimated the associated amount of displacement on the Red River fault. Though this estimate is preliminary, it suggests that a significant proportion of the current right-lateral slip on the Red River fault could result from extension in the Dali region. Furthermore, the Red River

fault currently cannot be traced into Tibet, but rather is truncated by faults of the Dali fault system.

Not all of the post-Pliocene displacement on the Red River fault, however, can be accounted for by extension in the Dali region, and geologic data suggest at least 15-16 km right-lateral displacement which predates extension in the Dali region, river incision, and probably surface uplift. This earlier displacement could be related to a poorly defined cooling event between 10 and 13 Ma (Bergman et al., 1997; Leloup et al., 2001), or could be continuous with modern activity on the Red River fault. Both the origin and significance of this pre-plateau growth right-lateral displacement are uncertain, but is consistent with predictions of the extrusion model (Tapponnier et al., 1982; 1986; 1990; Avouac and Tapponnier, 1993; Replumaz et al., 2001)

The solution to this apparent contradiction between the extrusion model (Tapponnier et al., 1982; 1986) and models for plateau growth through lower crustal flow (Royden, 1996; Royden et al., 1997; Clark and Royden, 2000) may rely on temporal distinctions. In mid-Cenozoic time, significant lateral extrusion of Indochina probably occurred along the Ailao Shan shear zone (Leloup et al., 1995; Leloup et al., 2001). In Late Miocene to Early Pliocene time, however, crustal structure may have changed drastically in the eastern margin region through the rheological evolution of the crust through the introduction of weak lower crust, extruded from beneath Tibet, possibly resulting in the formation of a detachment zone in the mid to lower crust. In this context, the Red River fault may have accommodated lateral extrusion in some way prior to growth of this region of the plateau, but since Pliocene time, the Xianshuihe-Xiaojiang fault system has developed and has gradually become the dominant structure on the southeast plateau margin. The Red River fault, in turn, would have gradually diminished in regional importance, and its slip-rate would be declining toward relatively slow values at present (Fig. 16).

CONCLUSIONS

The Red River fault consists of several strands, and in places some of the active strands lie along the northeastern contact of the Ailao Shan shear zone. The fault is prominently deflected by counterclockwise shear at its intersection with the Xianshuihe-Xiaojiang fault system. Displacement on the Red River fault north of the bend has an extensional component, with

maximum dip-slip offset of ~750 m near the town of Ejia (Fig. 1; Schoenbohm et al., in press and Chapter 4). There is no evidence for the existence of the “Yuanjiang fault” proposed by Replumaz et al. (2001). There is no evidence for normal displacement on the Red River fault southeast of the Yuanjiang basin. Geologic and geomorphic displacements on the Red River fault are probably ~40 km, 15-16 km of which apparently predates river incision and probably also surface uplift within the Red River region and development of the Xianshuihe-Xiaojiang fault system. The long term average slip-rate is a minimum of ~5 mm/yr, but modern slip-rates may be slower (Allen et al., 1984; Weldon et al., 1994; Rangin et al., 1995; Duong and Feigl, 1999).

The left-lateral Xianshuihe-Xiaojiang fault system is active, with slip-rates ranging from 10 to 30 mm/yr (Wang et al., 1998; Chen et al., 2000; Shen et al., 2003) and forms the eastern boundary of a crustal fragment that rotates clockwise around the Eastern Himalayan syntaxis. Shear appears to be taken up on discrete faults southwest of the Red River fault (King et al., 1997; Wang et al., 1998; Chen et al., 2000) with similar displacement magnitudes (Lacassin et al., 1998). The Red River fault is rotated within this system (Wang et al., 1998). The region is also undergoing extension (Wang et al., 1998), probably contributing a significant portion of the right-lateral displacement on the Red River fault. Displacement on the Xianshuihe-Xiaojiang fault system is transferred across the Red River fault and Ailao Shan shear zone to faults to the southwest in the absence of any discrete obvious upper crustal structure or structures which would accommodate this transfer, a phenomenon observed in a number of other crustal settings. The Xianshuihe-Xiaojiang fault system becomes increasingly distributed near the Red River fault, which may allow for the transmittal of shear across the Ailao Shan shear zone (Fig. 15).

Data presented in this study are consistent with growth of the eastern margin of the Tibetan plateau through pressure-gradient-driven flow of weak material from beneath Tibet into adjacent regions (Royden, 1996; Royden et al., 1997; Clark and Royden, 2000; Clark, 2003), resulting in surface uplift, river incision and the possible development of a weak horizon in the mid to lower crust. The Xianshuihe-Xiaojiang fault system appears to have initiated during growth of the southeast plateau margin, suggesting the presence of a detachment zone was an important factor in establishing modern upper crustal tectonics because it allowed decoupling of the upper and mid to lower crust transport directions. The Red River was probably active before growth of the

plateau in this region, and may be decreasing in regional importance since the establishment of the crustal fragment that rotates around the eastern Himalayan syntaxis (Fig. 16). This study emphasizes the dramatic change in behavior of the crust from mid-Cenozoic time, when lateral extrusion seems to have been the dominant mode of crustal deformation (Tapponnier et al., 1990; Leloup et al., 1995; Leloup et al., 2001), to today, when surface uplift, lower crustal flow, and detachment between the upper and lower crust appear to predominate.

REFERENCES

- Allen, C.R., Gillespie, A.R., Han Yuan, Sieh, K.E., Zhang Buchun, Zhu Chengnan, 1984, Red River and associated faults, Yunnan Province, China: Quaternary geology, slip rates, and seismic hazard: *Geological Society of America Bulletin*, v. 95, p. 686-700.
- Allen, C.R., Luo, Z., Qian H., Wen X., Zhou H., Huang W., 1991, Field study of a highly active fault zone: the Xianshuihe-Xiaojiang fault of southwestern China: *Geological Society of America Bulletin*, v. 103, p. 1178-1199.
- Avouac, J-P, and Tapponnier, P., 1993, Kinematic model of active deformation in central Asia: *Geophysical Research Letters*, v. 20, p. 895-898.
- Bergman, S.C., Leloup, P.H., Tapponnier, P., Schärer, U., and O'Sullivan, P., 1997, Apatite fission track thermal history of the Ailao Shan-Red River shear zone, China: paper presented at meeting, European Union of Geoscience, Strasbourg, France
- Brias, A., Patriat, P., and Tapponnier, P., 1993, Updated interpretation of magnetic anomalies and seafloor spreading stages in the South China Sea, implications for the Tertiary tectonics of SE Asia: *Journal of Geophysical Research*, B, v. 98, p. 6299-6328.
- Burchfiel, B.C., and Wang, E., 2003, Northwest-trending, middle Cenozoic, left-lateral faults in southern Yunnan, China and their tectonic significance: *Journal of Structural Geology*, v. 25, p. 781-792.
- Burchfiel, B.C., Chen, Z., Liu, Y., and Royden, L.H., 1995, Tectonics of the Longmen Shan and adjacent regions, Central China: *International Geology Review*, v. 37, p. 661-735.
- Bureau of Geology and Mineral Resources of Yunnan Province, 1990, in *Regional Geology of Yunnan Province*, Beijing, Geological Publishing House, 728 p.
- Chen, Z., Burchfiel, B.C., Liu, Y., King, R.W., Royden, L.H., Tang, W., Wang, E., Zhao, J. and Zhang, X., 2000, Global Positioning System measurements from eastern Tibet and their implications for India/Eurasia intercontinental deformation: *Journal of Geophysical Research*, v. 105, no. B7, p. 16215-16227.
- Clark, M.K., and Royden, L.H., 2000, Topographic ooze: Building the eastern margin of Tibet by lower crustal flow: *Geology*, v. 28, p. 703-706.
- Clark, M.K., Schoenbohm, L.M., Royden, L.H., Whipple, K.X., Burchfiel, B.C., Zhang, X., Tang, W., Wang, E., Chen, L., in press, Surface Uplift, tectonics, and erosion of eastern Tibet from large-scale drainage patterns: *Tectonics*.
- Clark, M.K., 2003, Late Cenozoic Uplift of Southeastern Tibet [PhD Thesis]: Massachusetts Institute of Technology, 226 p.
- Dewey, J., Cande, S., and Pitman, W.C., III, 1989, Tectonic evolution of the India-Eurasia collision zone: *Eclogae Geologicae Helveticae*, v. 82, p. 717-734.
- Dinter, D.A., and Royden, L., 1993, Late Cenozoic extension in northeastern Greece: Strymon Valley detachment complex and Rhodope metamorphic core complex: *Geology*, v. 21, p. 45-48.
- Dokka, R.K., and Travis, D.J., 1990a, Late Cenozoic strike-slip faulting in the Mojave Desert, California: *Tectonics*, v. 9, p. 311-340.
- Dokka, R.K., and Travis, D.J., 1990b, Role of the Eastern California shear zone in accommodating Pacific-North American plate motion: *Geophysical Research Letters*, v. 17, p. 1323-1326.
- Duong, C.c., and Feigl, K.L., 1999, Geodetic measurement of horizontal strain across the Red River fault near Tha Ba, Vietnam, 1963-1994: *Journal of Geodesy*, v. 73, p. 298-310.

Chapter 3- Active tectonics of the southeast margin of the Tibetan plateau

- England, P., Houseman, G., 1989, Extension During Continental Convergence, With Application to the Tibetan Plateau: *Journal of Geophysical Research*, v. 94, p. 17561-17579.
- Gilley, L.D., Harrison, T.M., Leloup, P.H., Ryerson, F.J., Lovera, O.M., Wang J-H, 2003, Direct dating of left-lateral deformation along the Red River shear zone, China and Vietnam: *Journal of Geophysical Research*, v. 103, No. B2, 10.1029/2001JB001726.
- Harrison, T.M., W Chen, Leloup, P.H., Ryerson, F.J., and Tapponnier, P., 1992, An Early Miocene transition in deformation regime within the Red River fault zone, Yunnan, and its significance for the Indo-Asian tectonics: *Journal of Geophysical Research*, v. 97, p. 7159-7182.
- Harrison, T.M., Leloup, P.H., Ryerson, F.J., Tapponnier, P., Lacassin, R., and Chen Wenji, 1996, Diachronous initiation of transtension along the Ailao Shan-Red River shear zone, Yunnan and Vietnam, *in* Yin, A., and Harrison, T.M., eds., *The Tectonic Evolution of Asia*, Cambridge University Press, New York, p. 208-226.
- Houseman, G., and England, P., 1993, Crustal Thickening Versus Lateral Expulsion in the Indian-Asian Continental Collision: *JGR*, v. 98, p. 12233-12249.
- Kahle, H.-G., Straub, C., Reilinger, R., McClusky, S., King, R., Hurst, K., Veis, G., Kastens, K., and Cross, P., 1998, The strain rate field in the eastern Mediterranean region, estimated by repeated GPS measurements: *Tectonophysics*, v. 294, p. 237-252.
- King, R.W., Shen, F., Burchfiel, B.C., Royden, L.H., Wang E., Chen Z., Liu Y., Zhang X.-Y., Zhao J.-X., and Li Y., 1997, Geodetic measurement of crustal motion in southwest China: *Geology*, v. 25, no. 2, p. 179-182.
- Kirby, E., Whipple, K.X., Burchfiel, B.C., Tang, W., Berger, G., Sun, Z., and Chen, Z., 2000, Neotectonics of the Min Shan, China: Implications for mechanisms driving Quaternary deformation along the eastern margin of the Tibetan Plateau: *GSA Bulletin*, v. 112, p. 375-393.
- Kirby, E., Reiners, P.W., Krol, M.A., Whipple, K.X., Hodges, K.V., Farley, K.A., Wenqing Tang, Zhiliang Chen, 2002, Late Cenozoic evolution of the eastern margin of the Tibetan Plateau: Inferences from $^{40}\text{Ar}/^{39}\text{Ar}$ and (U/Th)/He thermochronology: *Tectonics*, v. 21, 10.1029/2000TC001246.
- Kiratzis, A.A., 2002, Stress tensor inversions along the westernmost North Anatolian Fault Zone and its continuation into the North Aegean Sea: *Geophysical Journal International*, v. 151, p. 360-376.
- Lacassin, R., Replumaz, A., Leloup, P.H., 1998, Hairpin river loops and strike-slip sense inversion of southeast Asian strike-slip faults: *Geology*, v. 26, p. 703-706.
- Leloup, P.H., and Kienast, J.R., 1993, High temperature metamorphism in a major Tertiary ductile continental strike-slip shear zone: The Ailao Shan-Red River (P.R.C.): *Earth and Planetary Science Letters*, v. 118, p. 213-234.
- Leloup, P.H., Harrison, T.M., Ryerson, F.J., Chen Wenji, Li Qi, Tapponnier, P., and Lacassin, R., 1993, Structural, petrological and structural evolution of a Tertiary ductile strike-slip shear zone, Diancang Shan, Yunnan: *Journal of Geophysical Research*, v. 98, p. 6715-6743.
- Leloup, P.H., Lacassin, R., Tapponnier, P., Schärer, U., Zhong Dalai, Liu Xiaohan, Zhang Liangshang, Ji Shaocheng, Phan Trong Trinh, 1995, The Ailao Shan-Red River shear zone (Yunnan, China), Tertiary transform boundary of Indochina: *Tectonophysics*, v. 251, p. 3-84.
- Leloup, P.H., Arnaud, N., Lacassin, R., Kienast, J.R., Harrison, T.M., Phan Trong, T.T., Replumaz, A., and Tapponnier, P., 2001, New constraints on the structure, thermochronology, and timing of the Ailao Shan-Red River shear zone, SE Asia: *Journal of Geophysical Research*, B, v. 106, p. 6683-6732.
- Li, S. and Mooney, W.D., 1998, Crustal structure of China from deep seismic sounding profiles: *Tectonophysics*, v. 288, p. 105-113.
- McClusky, S.C., Bjornstad, S.C., Hager, B.H., King, R.W., Meade, B.J., Miller, M.M., Monastero, F.C., and Souter, B.J., 2001, Present day kinematics of the Eastern California shear zone from a geodetically constrained block model: *Geophysical Research Letters*, v. 28, no. 17, p. 3369-3372.
- Miller, M.M., Johnson, D.J., Dixon, T.H., and Dokka, R.K., 2001, Refined kinematics of the Eastern California shear zone from GPS observations, 1993-1998: *Journal of Geophysical Research*, v. 106, no. B2, p. 2245-2263.
- Peltzer, G., and Saucier, F., 1996, Formation and evolution of strike-slip faults, rifts, and basins during India-Asia collision: An experimental approach: *Journal of Geophysical Research*, v. 93, p. 15085-15117.
- Rangin, C., Klein, M., Roques, D., Le Pichon, X., and Trong, L.V., 1995, The Red River fault system in the Tonkin Gulf, Vietnam: *Tectonophysics*, v. 243, p. 209-222.
- Replumaz, A., Lacassin, R., Tapponnier, P., and Leloup, P.H., 2001, Large river offsets and Plio-Quaternary dextral strike-slip rate on the Red River fault (Yunnan, China): *Journal of Geophysical Research*, B, v. 106, 819-836.
- Reuther, C.-D., Ben-Avraham, Z., and Grasso, M., 1993, Origin and role of major strike-slip transfers during plate collision in the Central Mediterranean: *Terra Nova*, v. 5, p. 249-257.

Chapter 3- Active tectonics of the southeast margin of the Tibetan plateau

- Royden, L.H., 1996, Coupling and decoupling of crust and mantle in convergent orogens: Implications for strain partitioning in the crust: *Journal of Geophysical Research*, B, v. 101, p. 17 679-17 705.
- Royden, L.H., Burchfiel, B.C., King, R.W., Wang, E., Chen Z., Shen F., Liu Y., 1997, Surface deformation and lower crustal flow in eastern Tibet: *Science*, v. 276, p. 788-790.
- Schoenbohm, L.M., Whipple, K.X., Burchfiel, B.C., and Chen, L., in press, Geomorphic constraints on surface uplift, exhumation, and plateau growth in the Red River region, Yunnan Province, China: *GSA Bulletin*.
- Schärer, U., Tapponnier, P., Lacassin, R., Leloup, P.H., Zhong Dalai, and Ji Shaocheng, 1990, Intraplate tectonics in Asia: a precise age for large-scale Miocene movement along the Ailao Shan-Red River Shear Zone, China: *Earth and Planetary Science Letters*, v. 97, p. 65-77.
- Shen J., Wang Y., and Song F., 2003, Characteristics of the active Xiaojiang fault zone in Yunnan, China: a slip boundary for the southeastward escaping Sichuan-Yunnan block of the Tibetan Plateau: *Journal of Asian Earth Sciences*, v. 21, p. 1085-1096.
- Tapponnier, P., Peltzer, G., Armijo, R., Le Dain, A.-Y., and Cobbold, P., 1982, Propagating extrusion tectonics in Asia: New insights from simple experiments with plasticine: *Geology*, v. 10, p. 611-616.
- Tapponnier, P., Peltzer, G., and Armijo, R., 1986, On the mechanics of the collision between India and Asia, *in* Coward, M.P, and Ries, A.C., eds., *Collision Tectonics*, Geological Society Special Publication 19, p. 115-157.
- Tapponnier, P., Lacassin, R., Leloup, P.H., Schärer, U., D. Zhong, X. Liu, S. Ji, L. Zhang and J. Zhong, 1990, The Ailao Shan/Red River metamorphic belt: Tertiary left-lateral shear between Indochina and south China: *Nature*, v. 343, p. 431-437.
- Wang, E., and Burchfiel, B.C., 1997, Interpretation of Cenozoic tectonics in the Right-Lateral accommodation zone between the Ailao Shan shear zone and the Eastern Himalayan Syntaxis: *International Geology Review*, v. 39, p. 191-219.
- Wang, E., and Burchfiel, B.C., 2000, Late Cenozoic to Holocene deformation in southwestern Sichuan and adjacent Yunnan, China, and its role in formation of the southeastern part of the Tibetan Plateau: *GSA Bulletin*, v. 112, no. 3, p. 413-423.
- Wang, E., Burchfiel, B.C., Royden, L.H., Chen L., Chen J., Li W., Chen Z., 1998, Late Cenozoic Xianshuihe-Xiaojiang, Red River and Dali fault systems of southwestern Sichuan and central Yunnan, China: Boulder, Colorado, Geological Society of America Special Paper 327.
- Weldon, R., Sieh, K., Zhu, C., Han, Y., Yang, J., and Robinson, S., 1994, Slip rate and recurrence interval of earthquake on the Hong He (Red River) Fault, Yunnan, P.R.C.: *International Workshop on Seismotectonics and Seismic hazard in SE Asia*, p. 244-248.

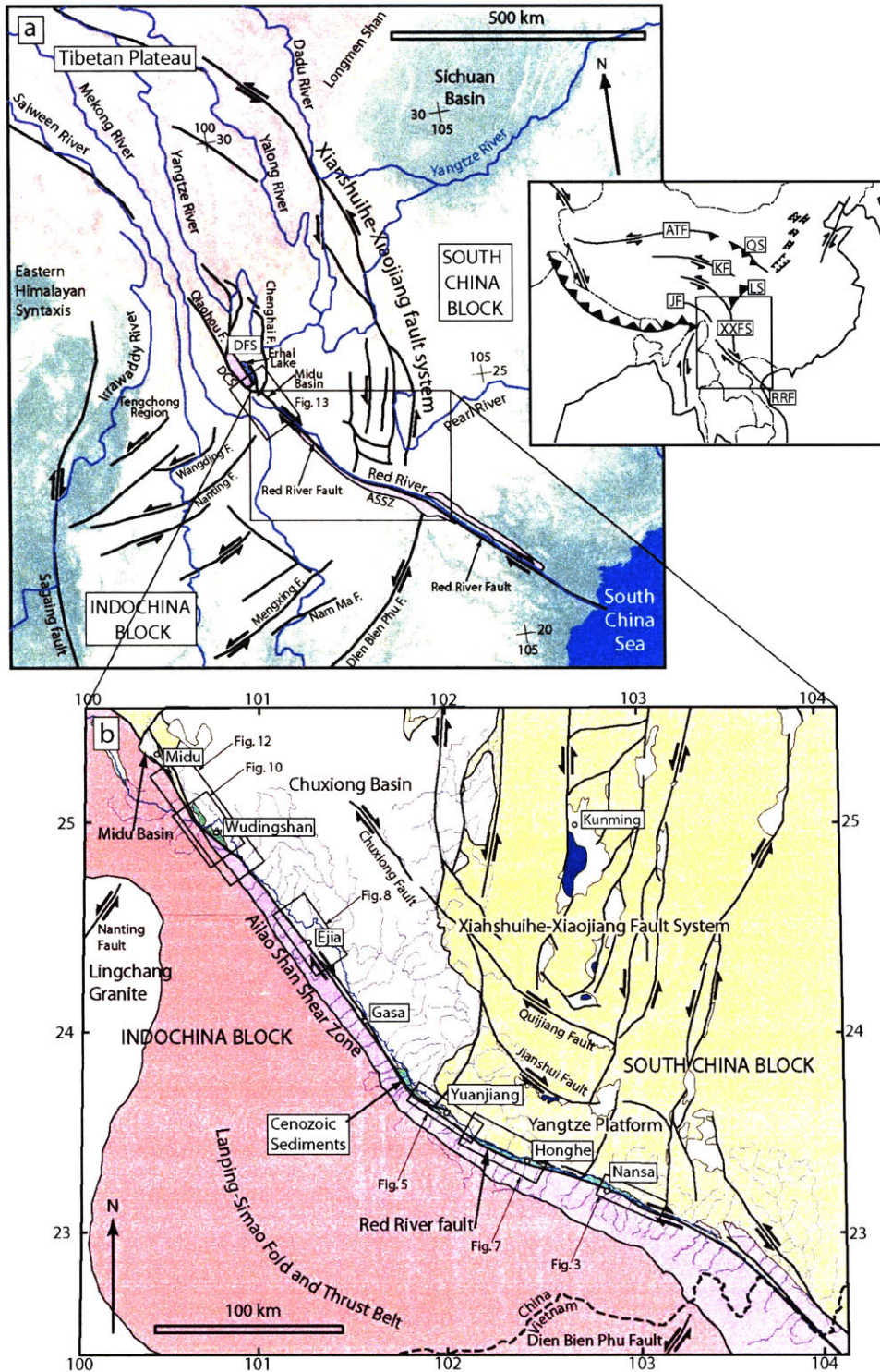


Figure 1. a) Regional topography and generalized geology of southeastern margin of the Tibetan Plateau. DCS = Dian Cang Shan, ASSZ = Ailao Shan shear zone. Inset: ATF = Altyn Tagh Fault, QS = Qilian Shan, KF = Kunlun fault, JF = Jiali Fault, LS = Longmen Shan, XXFS = Xianshuihe-Xiaojiang fault system, RRF = Red River fault. Figure 13 marked with box. b) Generalized map of Red River region, Red River drainage system marked in blue. Figures 3, 5, 7, 8, 10 and 12 marked with boxes.

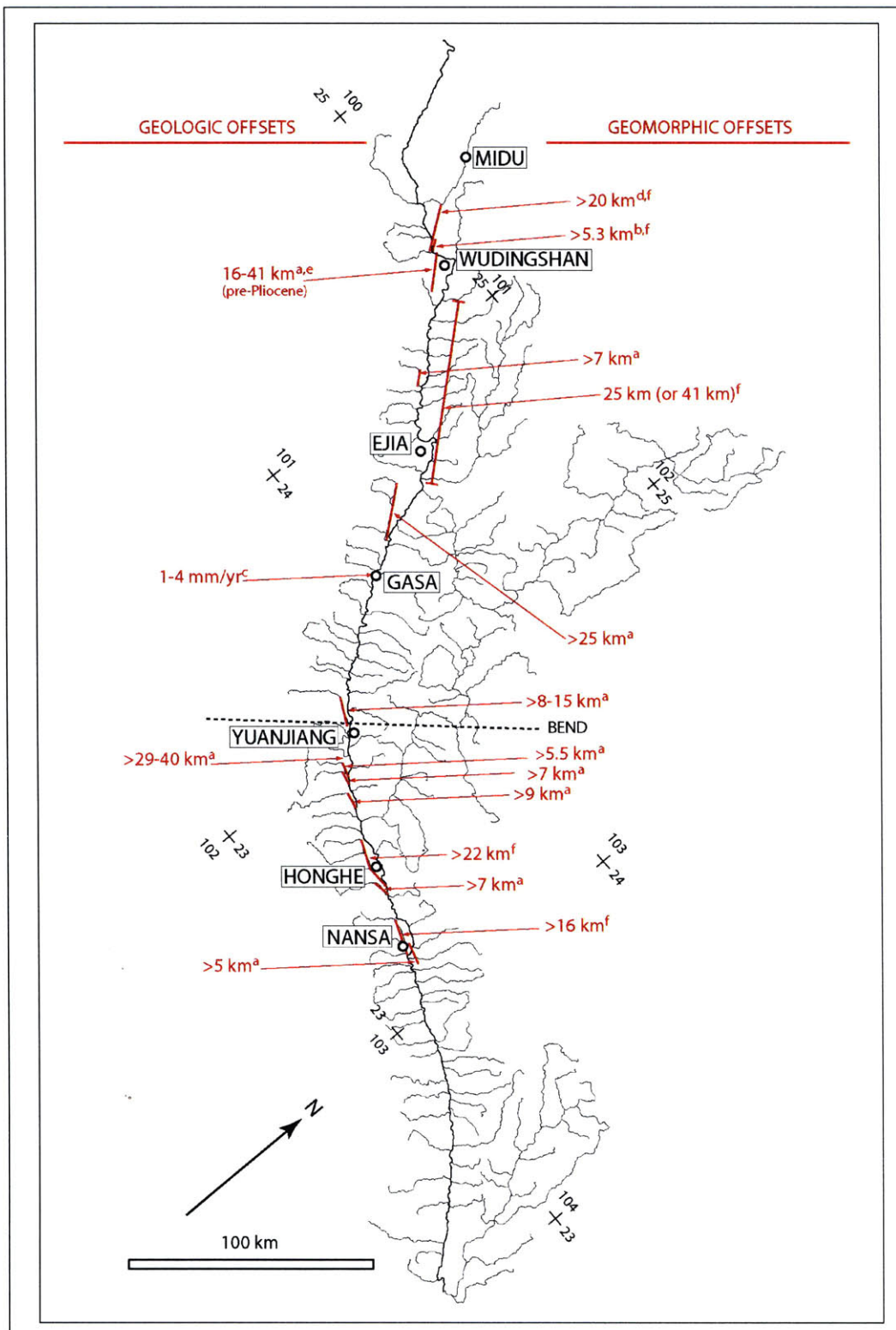


Figure 2. Geologic and geomorphic (deflected tributary) displacement along the Red River fault. Displacement references: a) this study; b) Allen et al., 1984; c) Weldon et al., 1994; d) Leloup et al., 1995; e) Wang et al., 1998; f) Replumaz et al., 2001.

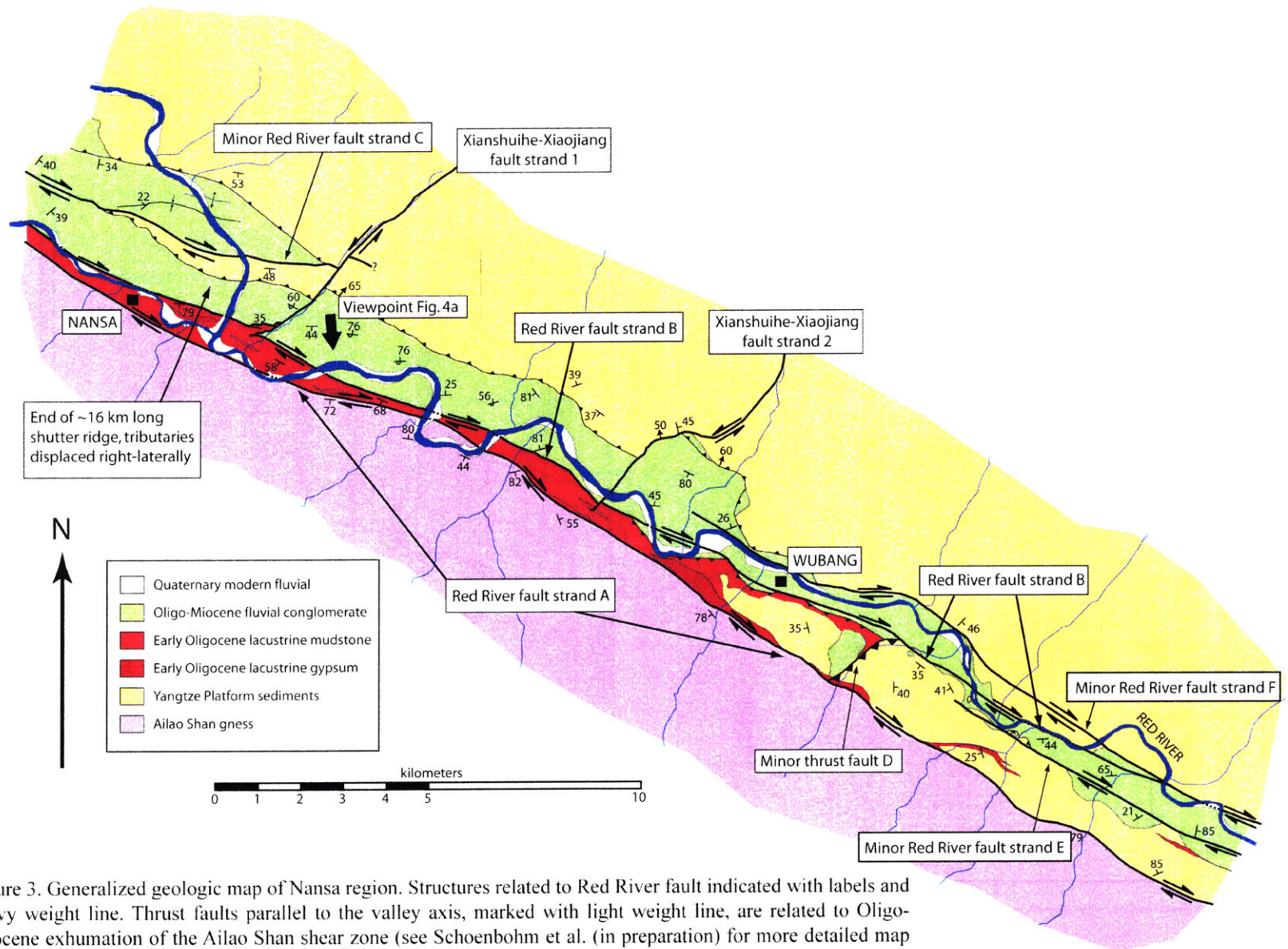


Figure 3. Generalized geologic map of Nansa region. Structures related to Red River fault indicated with labels and heavy weight line. Thrust faults parallel to the valley axis, marked with light weight line, are related to Oligo-Miocene exhumation of the Ailao Shan shear zone (see Schoenbohm et al. (in preparation) for more detailed map and discussion). Note ~5 km displacement on a minor fault strand near the northwest end of mapping area and two left-lateral faults which project to strands of the Xianshuihe-Xiaojiang fault system. See Fig. 1b for location.

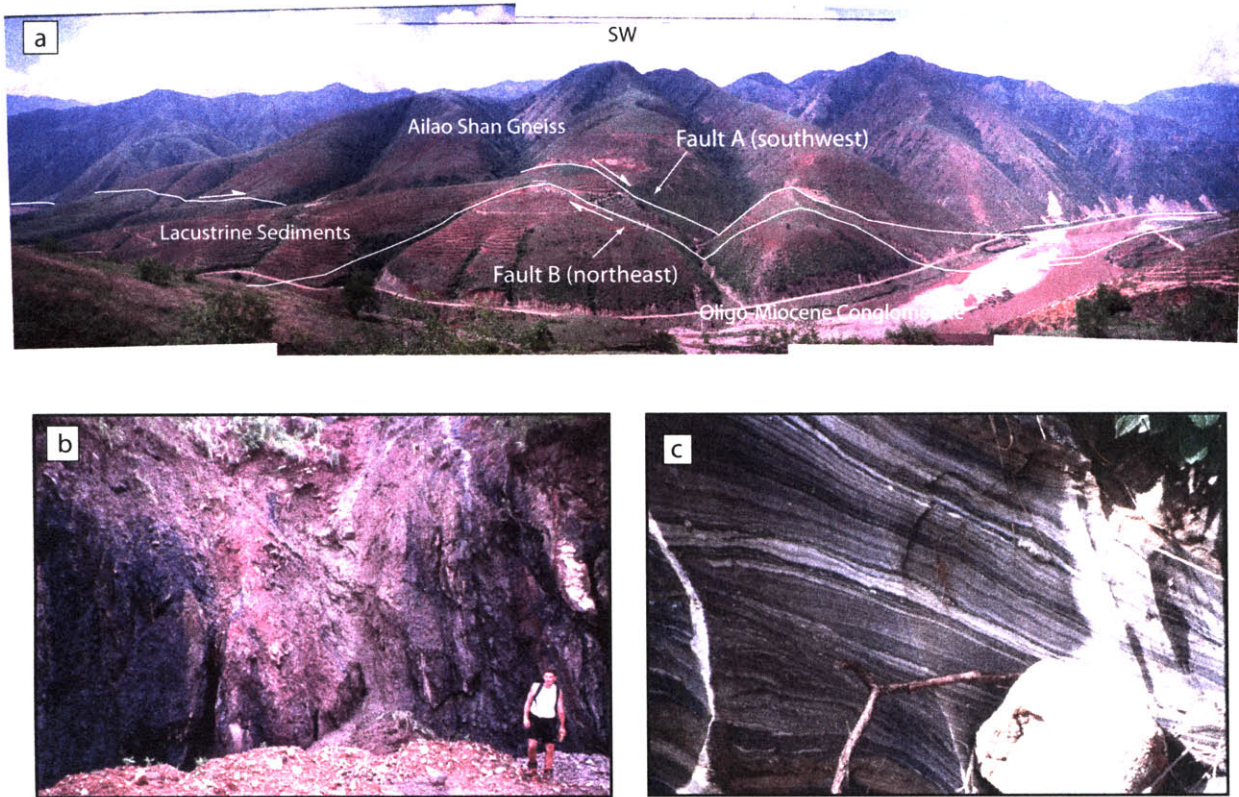


Figure 4. a) Red River fault in Nansa region, view to southwest, Ailao Shan in background, Red River in foreground, flows to left. Red River consists here of two strands (see Figure 3). The southwest fault (Fault A, Fig. 3) separates Ailao Shan gneiss from Oligocene lacustrine sediments (mudstone and gypsum). The northeast fault (Fault B, Fig. 3) separates lacustrine sediments from Oligo-Miocene fluvial conglomerate. Deformation is nearly continuous between two faults. Viewpoint for this photo shown in Figure 3. b) Sheared Oligocene lacustrine mudstone near Nansa, view to southeast. c) Sheared Oligocene lacustrine gypsum, view ~30 cm across, looking straight down. Foliation trends northwest-southeast.

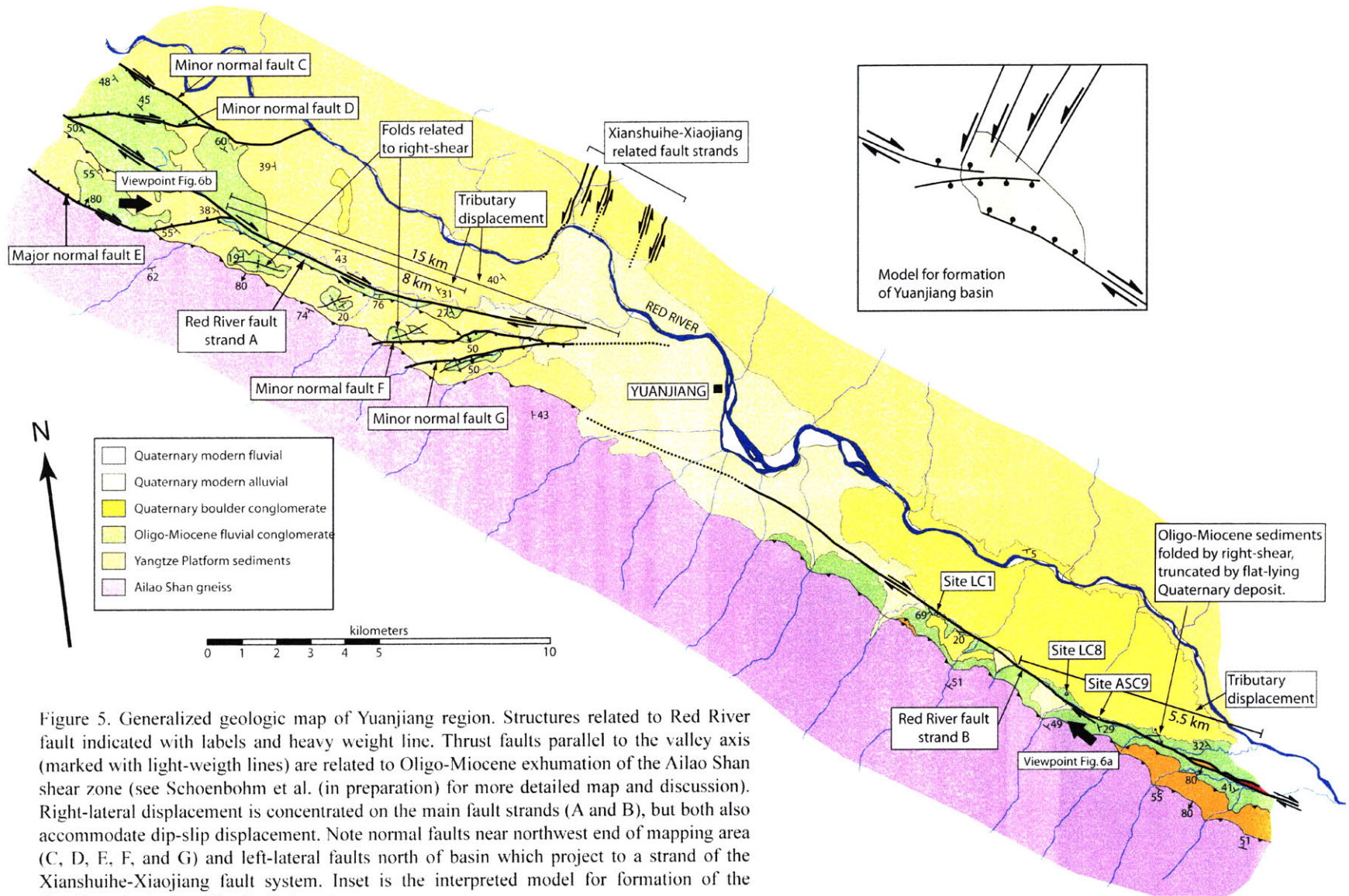


Figure 5. Generalized geologic map of Yuanjiang region. Structures related to Red River fault indicated with labels and heavy weight line. Thrust faults parallel to the valley axis (marked with light-weight lines) are related to Oligo-Miocene exhumation of the Ailao Shan shear zone (see Schoenbohm et al. (in preparation) for more detailed map and discussion). Right-lateral displacement is concentrated on the main fault strands (A and B), but both also accommodate dip-slip displacement. Note normal faults near northwest end of mapping area (C, D, E, F, and G) and left-lateral faults north of basin which project to a strand of the Xianshuihe-Xiaojiang fault system. Inset is the interpreted model for formation of the Yuanjiang basin. See Fig. 1b for location

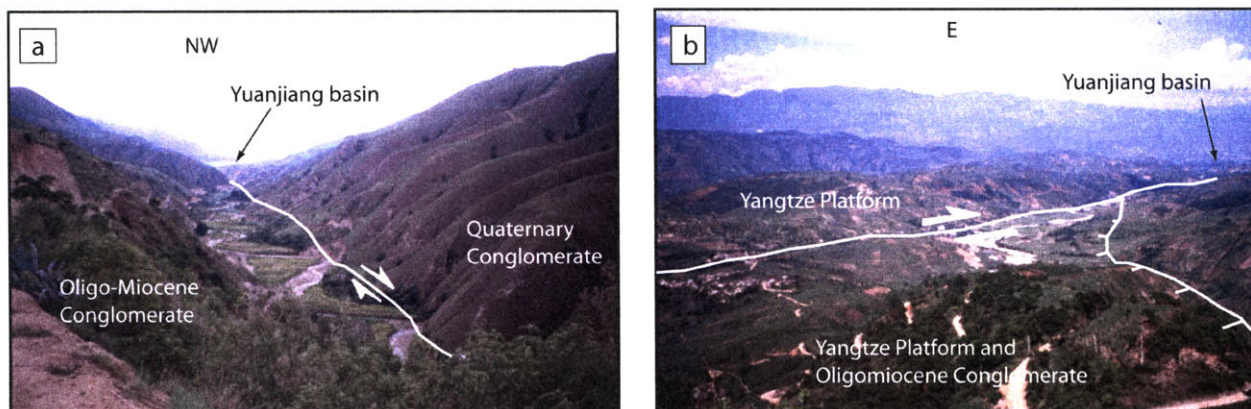


Figure 6. a) Red River fault southeast of Yuanjiang, view to NW to Yuanjiang basin. Tributaries flow along valley, deflected up to 7 km. Fault may have an extensional component. b) Red River fault northwest of Yuanjiang, view to east across Red River valley. Normal fault cuts away from main fault to the west. Viewpoints marked in Figure 5.

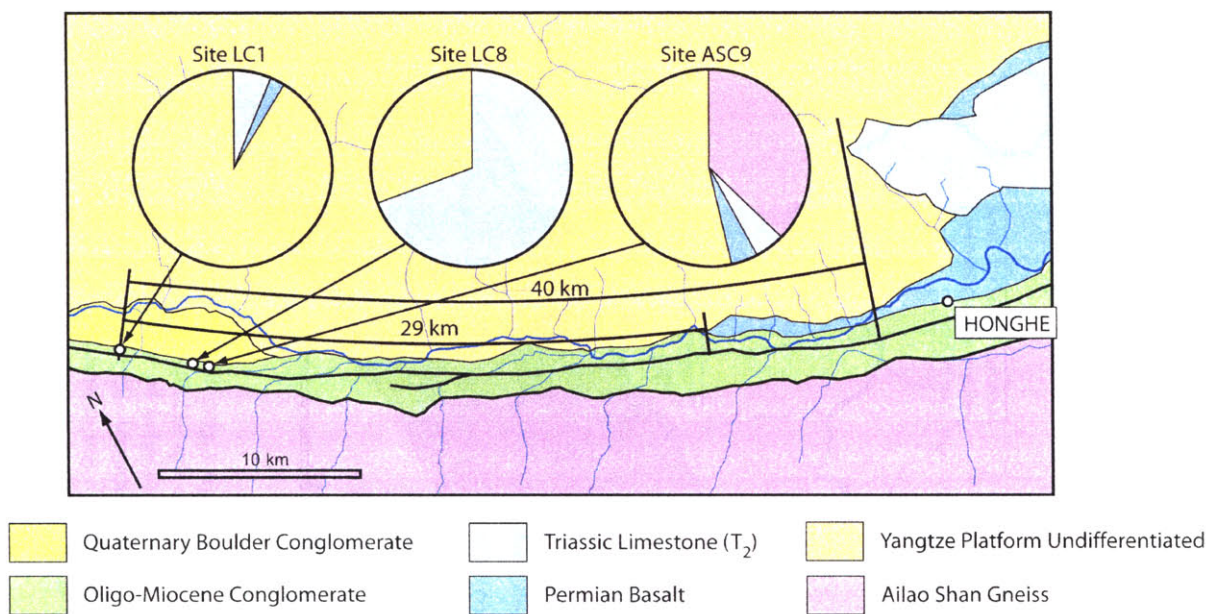


Figure 7. Displacement between Oligo-Miocene fluvial conglomerates and their source. Active faults marked with heavy weight line. Cobble composition for Site LC1, Site LC8 and Site ASC9 given in pie charts. See Figure 1b for location.

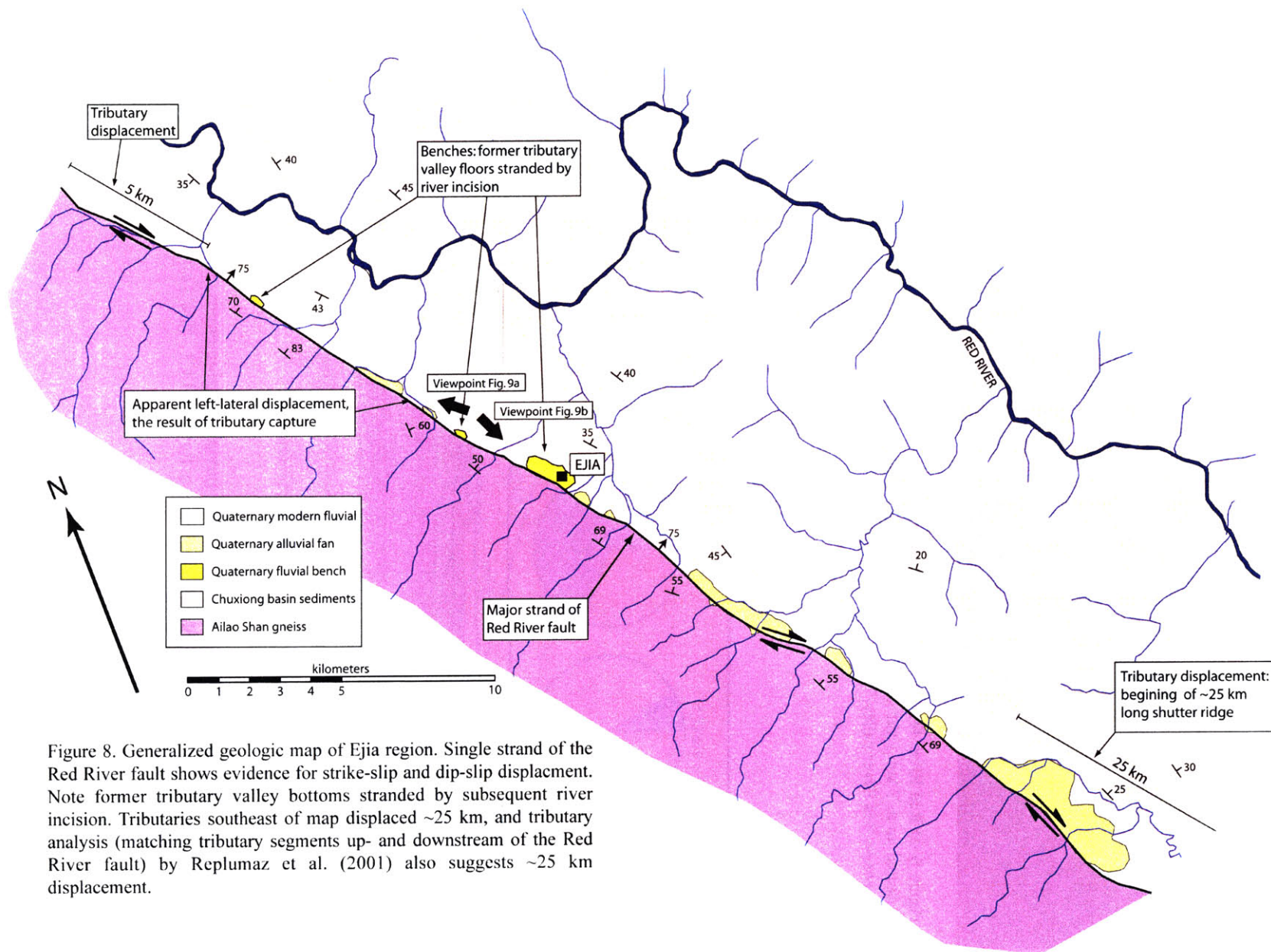


Figure 8. Generalized geologic map of Ejia region. Single strand of the Red River fault shows evidence for strike-slip and dip-slip displacement. Note former tributary valley bottoms stranded by subsequent river incision. Tributaries southeast of map displaced ~25 km, and tributary analysis (matching tributary segments up- and downstream of the Red River fault) by Replumaz et al. (2001) also suggests ~25 km displacement.

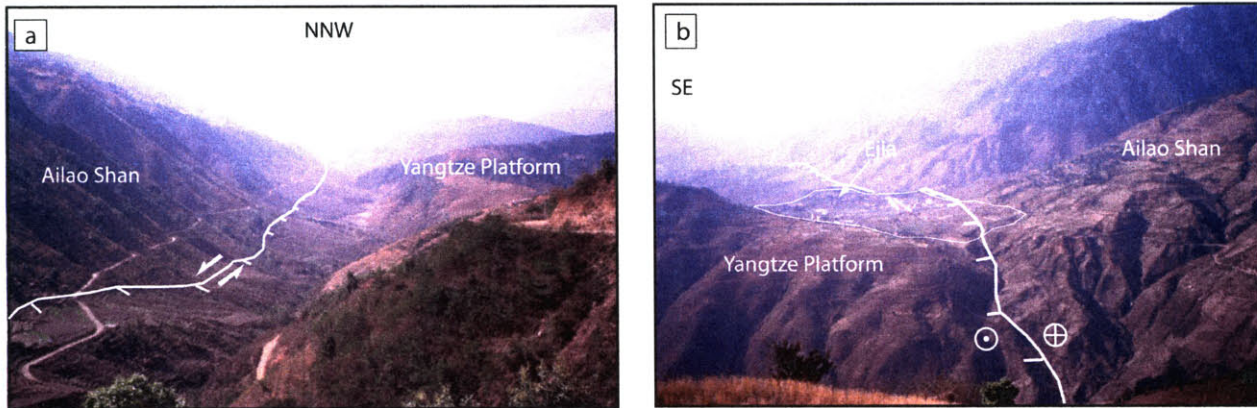


Figure 9. a) Red River fault northwest of Ejia, view to NNW. Fault has a clear dip-slip displacement here and well-developed triangular facets. Tributaries run along fault, but valley is partially filled by large alluvial fans from Ailao Shan. b) Ejia bench, former tributary valley floor. Viewpoints indicated in Figure 8.

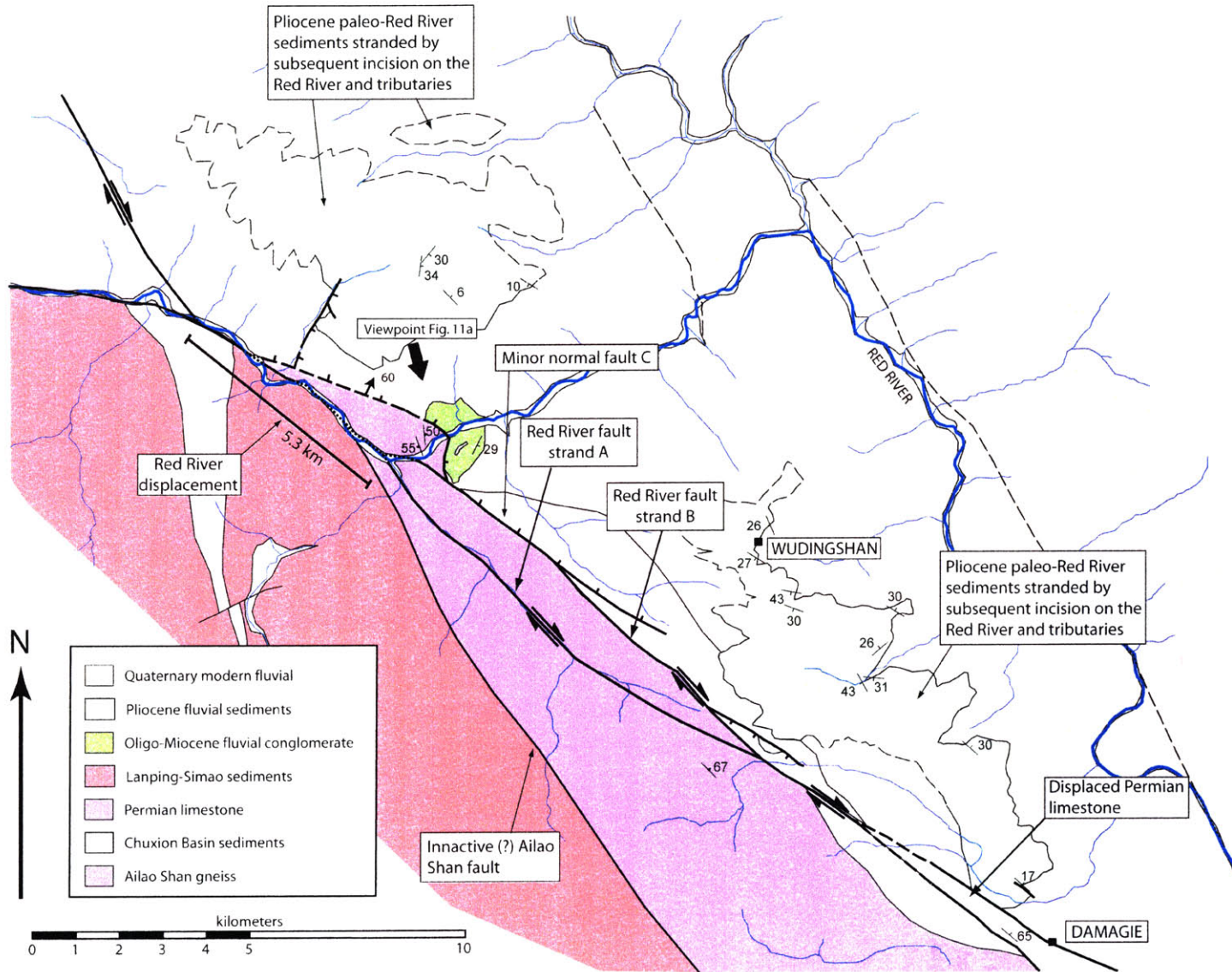


Figure 10. Generalized geologic map of Wudingshan region. Structures related to Red River fault indicated with labels and heavy weight line. Note Pliocene sediments which pre-date river incision, and slivers of Permian sediment offset at least 16 km on pre-Pliocene right-lateral faults (see also Fig. 12). See Figure 1b for location.

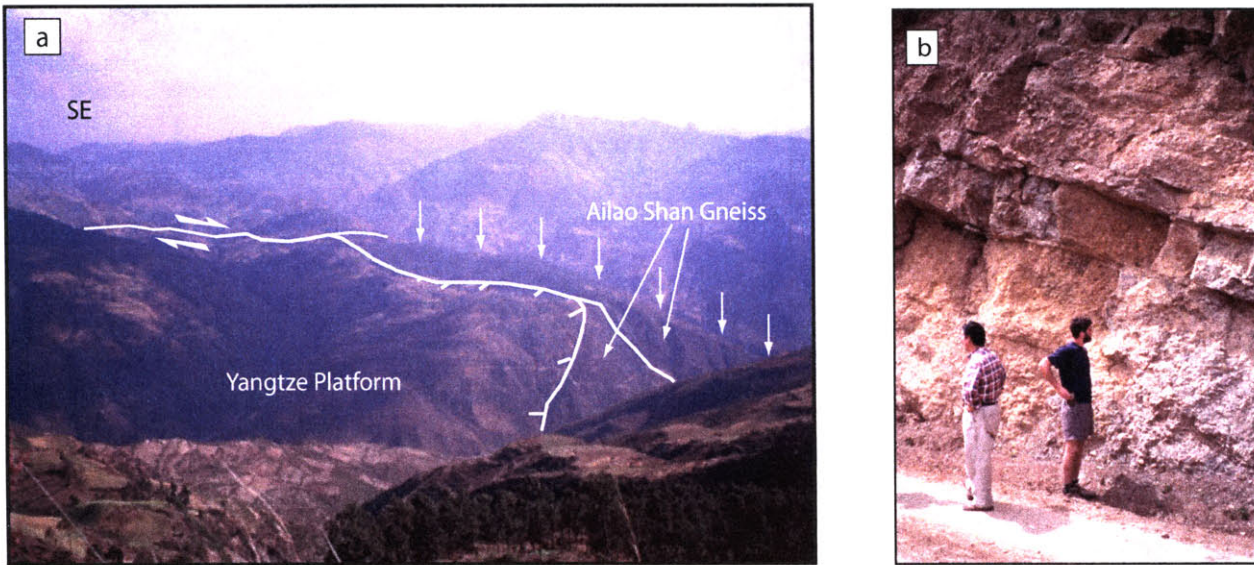


Figure 11. a) Wudingshan region, view to southeast. Southwest strand (Fault A, Fig. 10) is within Ailao Shan gneiss, marked by arrows. Northeast strand (Fault B, Fig 10) is between Ailao Shan gneiss, Yangtze platform rocks and Permian limestone. Small normal fault (Fault C, Fig. 10) merges with main strand and drops Yangtze platform rocks onto Ailao Shan gneiss. Pliocene sediments are deposited on hill to left (east) of photo. Viewpoint for photo marked in Figure 10. b) Paleo-Red River, Pliocene-age sediments preserved on hill near Wudingshan. These sediments pre-date river incision, and indicate that incision is in Pliocene time or younger.

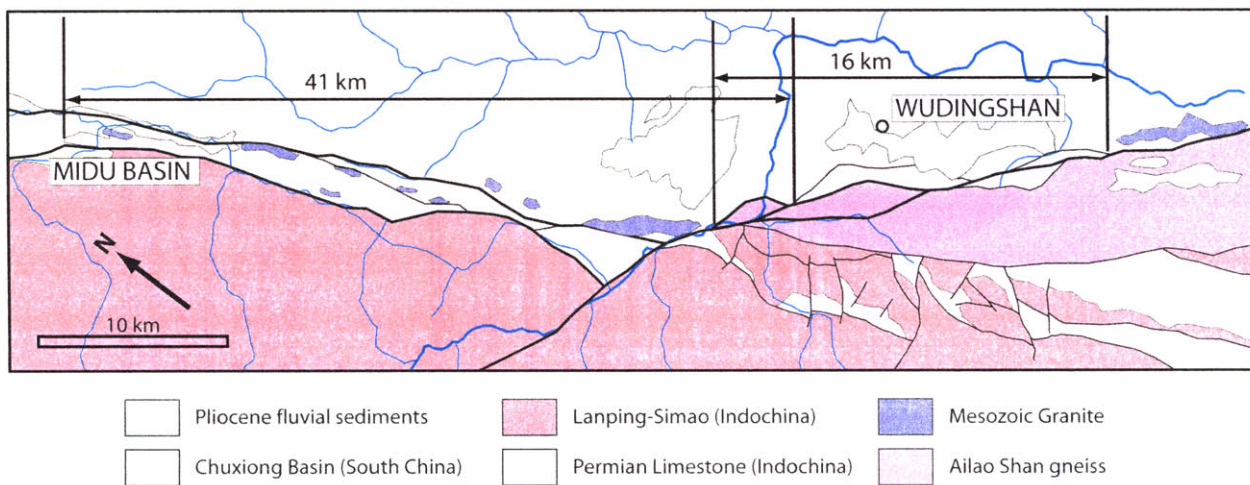


Figure 12. Offset geologic markers near northern termination of Ailao Shan gneiss and Wudingshan. Permian limestone is offset along inactive right-lateral faults which pre-date Pliocene deposits. Minimum displacement is 16 km, but displacement could be greater, up to 41 km or more if Permian continues beneath Midu basin. Mesozoic granites cannot be used to determine geologic offset because of an apparent contradiction between their apparent Triassic age and intrusive contact, and 700 km Cenozoic left-lateral displacement between Indochina and the Yangtze platform. See Figure 1a for location.

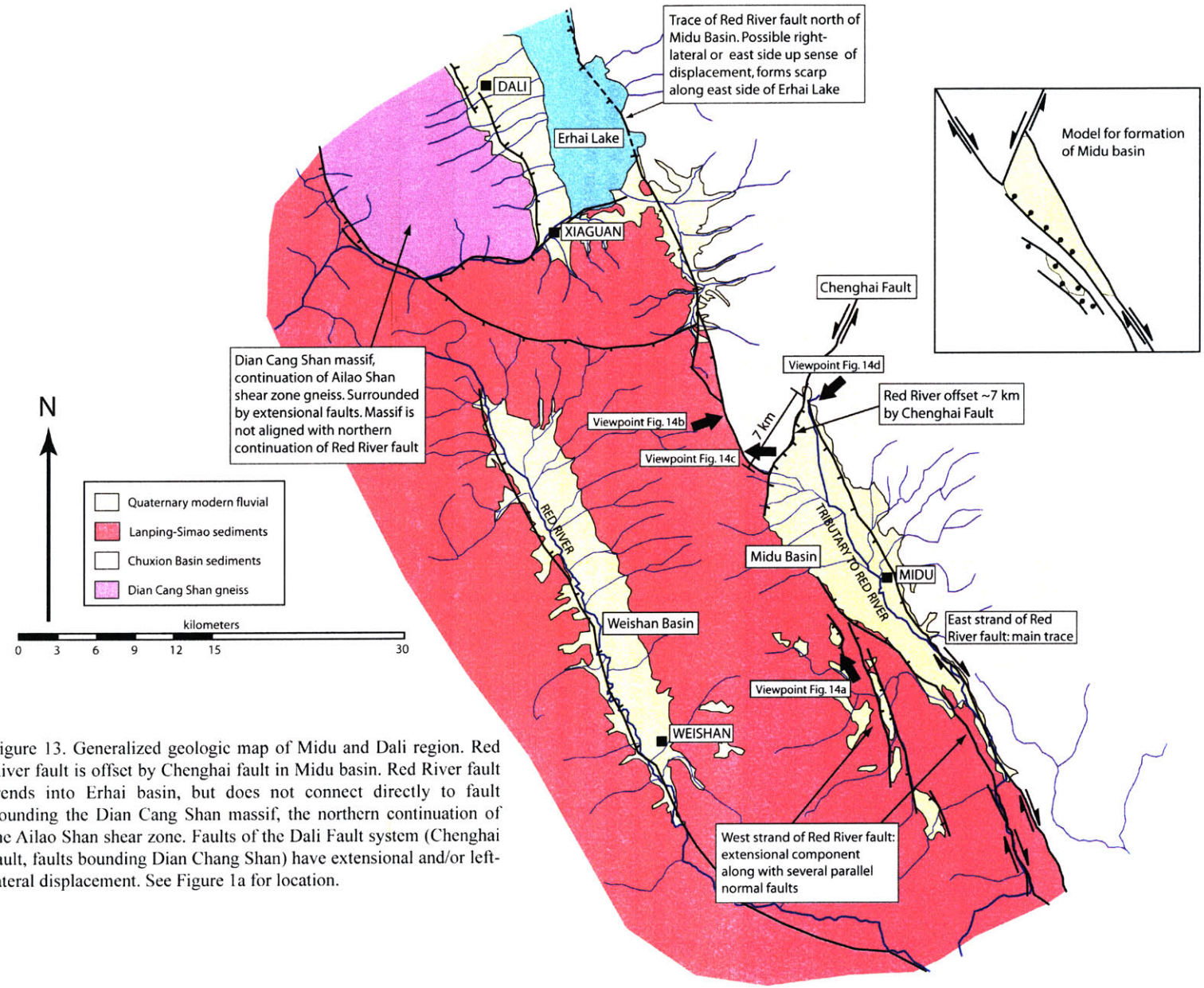


Figure 13. Generalized geologic map of Midu and Dali region. Red River fault is offset by Chenghai fault in Midu basin. Red River fault trends into Erhai basin, but does not connect directly to fault bounding the Dian Cang Shan massif, the northern continuation of the Ailao Shan shear zone. Faults of the Dali Fault system (Chenghai fault, faults bounding Dian Chang Shan) have extensional and/or left-lateral displacement. See Figure 1a for location.

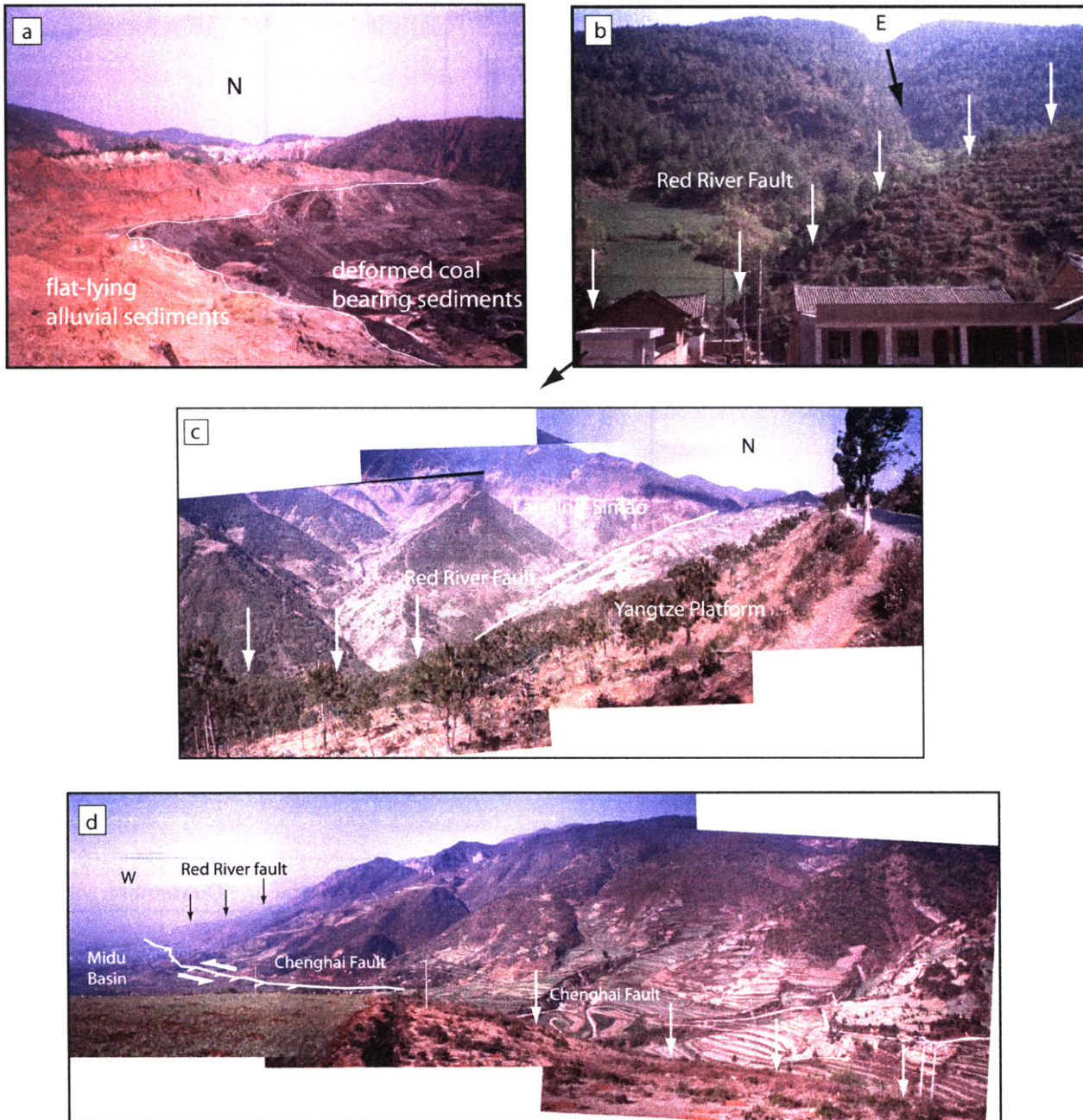


Figure 14. a) Small fault bounded basin southwest of Midu basin. Coal bearing sediments are deformed, overlain by flat-lying alluvial sediments. Basin outlet is to east, basin is currently being incised. Small basins like this suggest extensional faulting. b) Offset tributary north of Midu basin. White arrows mark fault. Black arrows marks tributary east and west of fault (on hillslope in background and in the lower left corner). c) Continuation of Red River fault north of Midu basin. Fault continuation behind hill marked with arrows. View to north. d) Chenghai fault at north end of Midu basin. Fault continuation behind hill marked with arrows. Red River fault continues north from Midu basin in valley marked in distance with black arrows. View to west. Photo viewpoints marked on Figure 13.

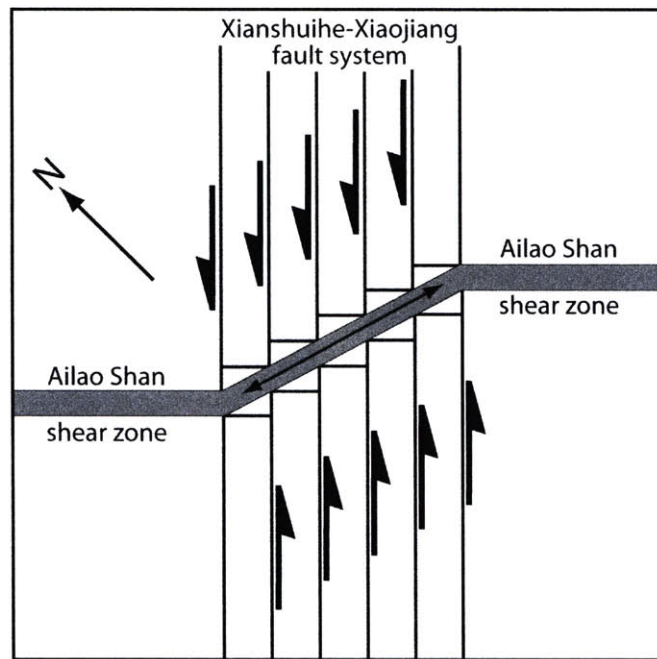


Figure 15. Model for transfer of shear across the Ailao Shan shear zone. Left-lateral shear is distributed across a region, while the Ailao Shan shear zone is stretched and rotated. A distributed fault network is necessary to accommodate transfer.

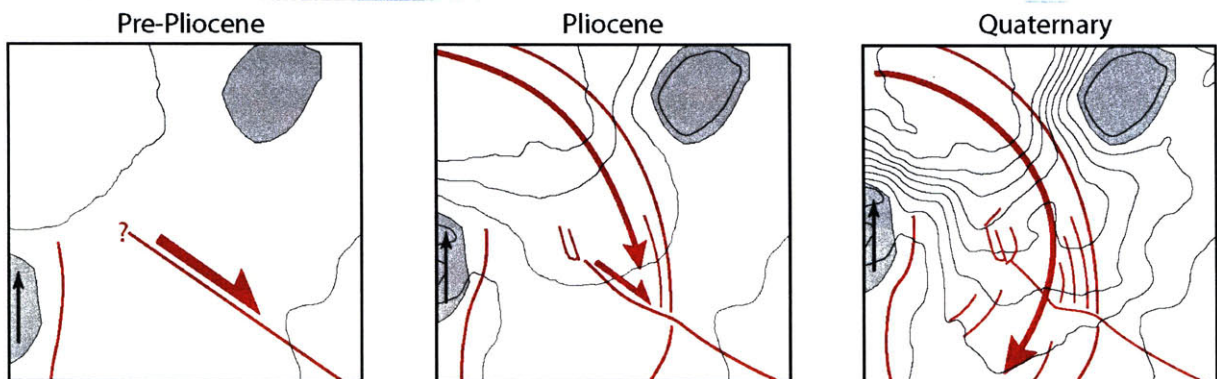


Figure 16. Proposed evolution of the eastern margin region. Red River fault decreases in importance as the margin grows, a detachment zone may develop in the mid to lower crust, and the Xianshuihe-Xiaojiang fault system accommodates rotation around the eastern Himalayan syntaxis. Sichuan basin (upper right) and syntaxis (left edge) indicated with shading. Syntaxis moves north at $\sim 35\text{mm/yr}$. Contours plotted at 500 m interval, calculated from smoothed topography for Quaternary, inferred for Pliocene and Pre-Pliocene.

**Geomorphic constraints on surface uplift,
exhumation, and plateau growth in the Red River region,
Yunnan Province, China**

L. M. Schoenbohm^{1*}

K. X. Whipple¹

B. C. Burchfiel¹

L. Chen²

¹Massachusetts Institute of Technology, Dept. of Earth, Atmospheric and Planetary Sciences, 77
Massachusetts Ave., Cambridge, MA 02139

²Yunnan Institute of Geological Sciences, 131 Baita Rd., Kunming, Yunnan, China

* E-mail: schoenbl@mit.edu

ABSTRACT

Field observations, digital elevation data and longitudinal profile analysis reveal a perched low-relief upland landscape in the Red River region, Yunnan Province, China, which correlates to an uplifted, regional low-relief landscape preserved over the eastern margin of the Tibetan Plateau. As with other major rivers of the plateau margin, the Red River has deeply incised the low-relief upland landscape, which we interpret to be the remnants of a pre-uplift or relict-landscape. We examine longitudinal river profiles for 97 tributaries to the Red River. Most profiles consist of three segments separated by sharp knickpoints: an upper, low-gradient channel segment, a steeper middle channel segment and a very steep lower channel segment. Upper channel segments correspond to the relict landscape and have not yet experienced river incision. Steeper middle and lower segments indicate onset of rapid, two-phase river incision, on the basis of which changes in external forcings, such as climate or uplift, can be inferred. In terms of two end-member scenarios, two-phase incision could be the result of pulsed plateau growth, in which relatively slow uplift during the first stage is followed by rapid uplift during the second phase, or it could reflect adjustments of the main channel to changing climate conditions against the backdrop of steady plateau growth. Reconstruction of the paleo-Red River indicates ~1400 m river incision, 1400-1500 m surface uplift and a maximum of 750 m vertical displacement across the northern Red River fault, elevating the northern Ailao Shan above the surrounding relict landscape. On the basis of stratigraphic constraints, incision along the Red River likely began in Pliocene time.

Keywords: Asia, landscape evolution, Red River fault, Ailao Shan shear zone, erosion surface, fluvial geomorphology, incision

INTRODUCTION

Tectono-geomorphic studies have yielded valuable insights in Asia, where continental scale strike-slip faults, extensive crustal thickening, surface uplift, and regional climatic interactions have shaped the dramatic modern landscape (Hallet and Molnar, 2001; Clark, 2003; Clark et al., in press). The eastern margin of the Tibetan Plateau has experienced extensive deformation

associated with the India-Asia collision, particularly along the Ailao Shan shear zone and the Red River fault in southeast China and Vietnam (Fig. 1). A number of studies have focused on the Ailao Shan shear zone (Harrison et al., 1992; Leloup and Kienast, 1993; Schärer et al., 1994; Leloup et al., 1995; Harrison et al., 1996; Wang P.L. et al., 1998; Zhang and Schärer, 1999; Wang P.L. et al., 2000; Leloup et al., 2001) and some work has evaluated the Red River fault (Allen et al., 1984; Wang E. et al., 1998; Replumaz et al., 2001). Absent in this research, however, is a significant consideration of the regional geomorphology.

In this study, we combine field observations with topographic data to understand aspects of the Cenozoic structural and geomorphic evolution of the Red River region of Yunnan Province, China. Geomorphic observations of the landscape can enhance our understanding of the regional geology and constrain tectonic models, specifically interactions among the active fault systems, the regional uplift history, and aspects of the unroofing history of the shear zone. We describe locally a low-relief upland landscape, continuous with a regional low-relief upland landscape developed over the eastern plateau margin (Clark, 2003), which is deeply incised by the Red River. We reconstruct the paleo-Red River tributary network developed on the low-relief landscape, and use this data to constrain the amount of surface uplift experienced in the Red River region, and the amount and distribution of dip-slip displacement on the Red River fault. Tributary morphology and channel parameters also allow us to explore geodynamic and climatic aspects of the landscape evolution of this region.

GEOLOGIC SETTING

The study area, in Yunnan province, China, lies east of the Eastern Himalayan Syntaxis and is currently affected by right-lateral shear and clockwise rotation as India moves northward into the Eurasian continent (Cobbold and Davy, 1988; Davy and Cobbold, 1988; Dewey et al., 1989; Holt et al., 1991; Wang and Burchfiel, 1997; Wang E. et al., 1998; Hallet and Molnar, 2001). The Red River fault and Ailao Shan shear zone are products of this deformation.

The vertically foliated gneisses of the Ailao Shan segment of the Oligo-Miocene Ailao Shan shear zone are bounded on the northeast by the active Red River fault and on the southwest by the probably inactive Ailao Shan fault (Fig. 1). Shearing began ~34 Ma (Gilley et al., 2003), and

was followed by rapid cooling between ~25 and ~17 Ma, diachronous along strike (Harrison et al., 1996). Additional zircon and apatite fission-track data indicate rapid cooling from 13 to 10 Ma (Bergman et al., 1997; Leloup et al., 2001), but it is unclear whether this cooling phase is continuous with that indicated by the Harrison et al. (1996) thermochronology, or if it represents a distinct cooling event. Shear sense indicators are consistently left-lateral (Leloup et al., 1995; Leloup et al., 2001) and estimates for the amount of offset fall in the range of 700 ± 200 km (Brias et al., 1993; Leloup et al., 1995; Wang P.L. et al., 1998; Leloup et al., 2001). The Ailao Shan shear zone likely accommodated southward extrusion of Indochina, but the exact nature of the associated crustal deformation is unclear (Tapponnier et al., 1982; Tapponnier et al., 1986; Tapponnier et al., 1990; Leloup et al., 1995; Wang and Burchfiel, 1997; Leloup et al., 2001).

In contrast to the ductile, left-lateral Ailao Shan shear zone, the Red River fault (Fig. 1) is a geomorphically prominent, right-lateral structure, approximately bounding the northeastern edge of the shear zone. The fault plane is vertical to slightly east dipping. Strike-slip estimates, based on geomorphic and geologic data, range from 5.5 to 54 km (Allen et al., 1984; Wang E. et al., 1998; Replumaz et al., 2001). The age of inception is also not well known, but estimates fall in the range 2 to 5 Ma (Allen et al., 1984; Wang E. et al., 1998; Replumaz et al., 2001). The fault is traceable from Vietnam northwest past the northern tip of the Ailao Shan and into the Midu basin (Fig. 1). A prominent feature of the Red River fault in map view is a major bend near its intersection with the left-lateral Xianshuihe-Xiaojiang fault system. Northwest of this bend, triangular facets, Quaternary sedimentary basins, and high peak elevations within the Ailao Shan have been interpreted to result from a dip-slip displacement on the Red River fault with the northeast side down (Allen et al., 1984; Replumaz et al., 2001; Leloup et al., 1995; Wang et al., 1998). Replumaz et al. (2001) observed triangular facets southeast of the bend as well, and on this basis infer that dip-slip displacement extends along the entire length of the fault in China. However, as pointed out by Allen et al. (1984), differential erosion along the gneissic foliation of the Ailao Shan, which is sub-vertical but often dips slightly valleyward, can create the appearance of triangular facets in the absence of true dip-slip displacement. Wang E. et al. (1998) argue that normal faulting does not continue south of the bend. Thus the amount and distribution of dip-slip along the fault is uncertain, but is important in interpreting the way in which the Red River fault interacts with other active fault systems in Yunnan, particularly the

Xianshuihe-Xiaojiang fault system, and in constraining the amount of exhumation of the Ailao Shan shear zone along the Red River fault.

In addition to deformation along strike-slip shear zones as a response to the India-Eurasia collision, the eastern margin of Tibet is argued to have experienced long wave-length surface uplift as a result of pressure-gradient driven flow of weak lower crust from beneath Tibet and inflation of adjacent regions (Royden, 1996; Royden et al., 1997; Clark and Royden, 2000). Surface uplift, exhumation of the Ailao Shan shear zone and displacement along the Red River fault and other active fault systems of Yunnan have all interacted to shape the modern landscape, which preserves an interpretable record of these processes.

TOPOGRAPHIC SETTING

A regionally extensive, perched, low-relief upland landscape extends from Tibet toward the South China Sea along the southeastern margin of the Tibetan Plateau, and is deeply dissected by major rivers which drain the Plateau, including the Mekong, Salween and Yangtze and their principle tributaries (Fig. 1b, Clark et al., 2002; Clark, 2003). This low-relief upland landscape continues into central and southern Yunnan where it is incised by the Red River (Figs. 1a and 2, Clark et al., 2002; Clark, 2003). In the Red River region, low-relief landscape patches are generally between 2000 and 2500 m, except for in the northwest Ailao Shan where average elevations are closer to 3000 m (Fig. 2a). To the southwest of the Red River, the low-relief landscape is best preserved on the northern segment of the Ailao Shan, and can be traced in discontinuous patches toward the southeast along the crest of the range. To the northeast of the Red River, on the Yunnan Plateau, the low-relief landscape is extensive, and is discussed by Wang E. et al. (1998).

The low-relief upland landscape, where developed on the Ailao Shan, exhibits a “hummocky” topography with rounded hills separated by meandering, low-gradient, gravel and sand bedded streams (Figs. 3 and 4a). Relief is generally less than 200 m but can reach a maximum of 500 m. Everywhere within the low-relief landscape, bedrock is deeply weathered, capped by a saprolite layer estimated to be ~200 m thick. The original gneissic foliation of the Ailao Shan shear zone is well preserved throughout the saprolite, indicating little disruption of the weathered material.

Because of the many small hills and the high porosity of the underlying material, the low-relief upland landscape is dry, uncultivated, and sparsely populated. Near Ejia (Figs. 1 and 3), the low-relief upland is developed on Ailao Shan gneiss and lower grade metamorphic rocks to the west, separated by the Ailao Shan fault (Bureau of Geology, Yunnan, 1990). To the east of the fault, the soil is well-drained saprolite, and supports the typical vegetation of the Ailao Shan, a mixture of grasses and conifers. In contrast, the phyllites to the west of the fault support a temperate rainforest because the clay-rich soils that have developed on the phyllites better retain moisture (Fig. 3). While the Ailao Shan fault does not appear to be active in a strike-slip sense here or elsewhere along the shear zone, it does form a scarp in this region, higher to the west, probably the result of differential weathering and erosion.

To the northeast of the Red River, the low-relief upland landscape is gently rolling and is developed on a variety of rocks of the Chuxiong basin and South China fold belt (Wang E. et al., 1998; Figs. 1 and 4b). The character of the landscape varies according to the lithology it is cut on; most notable is the hummocky topography and thick saprolite horizons which form over granites. Where developed on Triassic limestones, karst landforms and thick red muds are common. Strands of the Xianshuihe-Xiaojiang fault system locally disrupt the landscape and have created a number of small pull-apart basins (Fig. 1). The landscape is often gently warped down into these extensional basins (Wang E. et al., 1998).

The rolling topography of the perched low-relief landscape contrasts sharply with the deeply incised canyons of the Red River. The Red River flows in a deep valley along the Red River fault. Most tributaries, particularly those on the Ailao Shan side of the Red River, are short, steep bedrock rivers that flow straight and approximately perpendicular to the course of the main river (Fig. 4c). Most tributaries from the northeast are short, steep bedrock rivers as well, but a few tributaries (~4) are larger with a drainage area and morphology similar to the Red River itself. Hillslopes along the main river and in the tributary valleys are steep, with frequent landslides, discontinuous soils and sparse vegetation. Tributaries to the Red River that have their headwaters on the low-relief upland cross over one or more knickpoints, separating a low gradient alluvial channel above from a steep bedrock channel below.

We also observe a series of broad, moderately incised valleys cut into the low-relief upland landscape, but perched above the deeply incised valleys. These broad valleys are distinct from both the low-relief upland and the deep river gorges, and we refer to them as intermediate valleys that together form a discontinuous intermediate landscape. Relief within these valleys (between the approximate elevation of the low-relief landscape and the knickpoint above the deeply incised valleys) is generally less than 1000 m. The intermediate valleys are cultivated, soils are well developed and bedrock is deeply weathered.

In addition to field observations, we also identify the different landscape components using methods developed by Clark (2003), particularly through the combined use of topographic data, river profiles, slope and relief data, geologic maps and CORONA satellite imagery. Overlain slope-elevation maps are particularly useful for identifying low-slope areas at high elevations that correspond to the low-relief landscape and high-slope areas at moderate to low elevations that correspond to the incised valleys (Clark, 2003). Clark (2003) finds that slopes on the low-relief landscape are generally less than $\sim 10^\circ$, and relief is less than 600 m. We apply these methods to the Red River region, using 90 meter DEM data (see Fielding et al. (1994) for description of the data set). To the northeast of the Red River, on the Yunnan Plateau, large continuous areas of the low-relief landscape are indicated by prominent low-slope zones, although the extremely low slope areas generally are modern depositional basins along strands of the Xianshuihe-Xiaojiang fault system (Fig. 2). To the southwest of the Red River, the low-relief landscape is clear west of Ejia (Figs. 2 and 3) and can be identified in discontinuous patches along the crest of the Ailao Shan to the southeast. Low-slope regions southwest of the Ailao Shan and immediately along the Red River usually do not correspond to the low-relief landscape, but rather to valley bottoms and alluviated stretches of river (Fig. 2). Southwest of the Ailao Shan the low-relief, high elevation landscape is largely absent (Fig. 2) and appears to have been removed by erosion.

MODERN , INTERMEDIATE AND RELICT LANDSCAPES

The morphology of the southeastern margin of the Tibetan plateau, that of a deeply incised low-relief upland continuous with the Tibetan Plateau in the north and the South China coastal margin in the south, is suggestive of long wave-length surface uplift associated with

development of the Tibetan Plateau. Clark and Royden (2000) argue that this surface uplift is driven by flow of weak crustal material from beneath Tibet into adjacent regions, including the southeastern plateau margin. Injected material thickens the crust and results in isostatic surface uplift (Clark and Royden, 2000). The major rivers of the eastern margin have responded to this surface uplift through large-scale drainage reorganization (Clark et al., in press) and by incising deep gorges (Clark, 2003).

In this interpretation, the low-relief landscape we observe in the Red River region, and which Clark (2003) observes regionally, can be used as a sub-horizontal datum to track tectonic development of the region. An important component of this interpretation is that the low-relief landscape has not “re-graded” to present conditions; it’s isolation from the incised rivers is what allows it to record surface uplift and deformation. This is consistent with several field observations in the Red River region: the deep weathering, thick saprolite, low-gradient fluvial channels and low relief which characterize the low-relief surface suggest response to very different conditions than the incised valleys, which are characterized by exposed bedrock, landsliding, steep channels and high relief. Low temperature thermochronologic data elsewhere in eastern Tibet also indicate slow exhumation of an apparently correlative low-relief landscape (Kirby et al., 2002; Clark et al., 2000, Clark 2003), and much higher exhumation rates along major tributaries to the Yangtze River (Clark et al., 2000, Clark, 2003). The low-relief landscape continues to weather, erode and evolve, but those processes are isolated from modern base level.

In order to make clear the distinction between the base level conditions under which these two landscape components were formed, we adopt the terms “relict landscape” (after Clark, 2003) to describe the low-relief upland landscape, and “modern landscape” to describe the incised valleys. Additionally, we employ the term “intermediate landscape” for the broad, moderately incised valleys perched above the deeply incised valleys and below the relict landscape. In our usage, “relict” refers to the conditions under which the landscape was formed and should not be taken to imply a stagnancy of the landscape. We prefer this term to the more commonly used “erosion surface,” because “relict landscape” implies that a variety of geomorphic processes may have been acting on the landscape, potentially deposition as well as erosion, that the original relief structure may be complex and that the “age” may vary across the landscape.

One measure of the age of the relict landscape (Clark, 2003) is the age of formation of the surface, or the first time at which low-relief conditions were attained. The end of tectonic unroofing of the Ailao Shan shear zone provides an upper limit on this measure of the age of the landscape. Rapid cooling recorded by $^{40}\text{Ar}/^{39}\text{Ar}$ thermochronology between 25 and 17 Ma (Harrison et al., 1996) probably resulted from uplift and exhumation of the shear zone with correspondent high relief over the range. Cenozoic sediments preserved along the Red River to the northeast of the shear zone are coarse fluvial conglomerates derived from the Ailao Shan, and also indicate high relief within the range during this time (Wang E. et al., 1998). Limited fission-track data from the Ailao Shan shows rapid cooling between 13 and 10 Ma (Bergman et al., 1997). The relict landscape therefore is probably not older than 10 Ma and is certainly not older than 17 Ma. To the northeast on the Yunnan Plateau the landscape may have formed earlier: various parts of the relict landscape need only share the same historic base level conditions, not the same age. Folded Eocene and rarely Oligocene units are beveled by the relict landscape in the Chuxiong basin (Fig. 1) and capped by undeformed Pliocene age fossil-bearing sediments, indicating the relict landscape is younger than Eocene and older than Pliocene in this region (Wang et al., 1998; Clark, 2003). Flat-lying Eocene sediments overlie folded units of the South China Fold Belt (Fig. 1), therefore the relict landscape may older than Eocene in this region (Wang et al., 1998; Clark, 2003).

A second measure of the age of the relict landscape (Clark, 2003) is the age at which the river incision began and the relict landscape first became isolated from modern base level. The timing of initiation of river incision is difficult to determine because of the paucity of well preserved terraces within the Red River valley. However, sedimentologic evidence from near the northern termination of the Ailao Shan shear zone (Fig. 1) suggests incision in Pliocene time or later. At Damagie, fossil bearing Pliocene sediments are deposited on the relict landscape in what appears to be the paleo-Red River valley based on the flat basal unconformity, the fluvial facies and the slightly lower elevation (~200 m) compared to the surrounding relict landscape. These sediments are perched high above the Red River and have been incised on all sides by the main river and two tributaries. River incision must post-date deposition of these sediments, and therefore can have begun no earlier than Pliocene time.

MOTIVATION: RIVER RESPONSE TO UPLIFT AND DEFORMATION

Relict landscapes (or erosion surfaces as termed by many authors) have served as important markers of tectonic uplift and deformation in a number of studies (e.g., Epis and Chapin, 1975; Gregory and Chase, 1994; Clark and Royden, 2000; Spotila and Sieh, 2000; Clark, 2003; Clark et al., in press; for partial summaries, see Widdowson, 1997; and Phillips, 2002). However, the rivers of the southeastern margin of the Tibetan Plateau have also responded to surface uplift and deformation, and can be sensitive recorders of temporal and spatial variations in rock uplift rate (e.g., Whipple and Tucker, 1999; Snyder et al., 2000; Kirby and Whipple, 2001; Whipple and Tucker, 2002; Lague and Davy, 2003; Wobus et al., 2003; Whipple, in press).

We expect the Red River and its tributaries to respond to long wave-length surface uplift, tilting, and disruption of the relict landscape on a number of spatial and temporal scales. On the largest scale, from the headwaters of the Red River in central Yunnan to its outlet at the South China sea, the river should experience a long-wavelength tilt, but a relatively stable base level set by sea level. Surface uplift and tilting should cause a steepening of the river gradient, although channel response will also be influenced by climatic conditions. Further, although far-field base level does not change significantly, the evolution of tributaries to the Red River will depend on the “local” base level, or the elevation of the confluence of the tributary and the main river. Because tributary local base level is set by the gradient of the Red River, changes in uplift and climate conditions will be translated to the tributaries by adjustments in gradient along the main channel. It is our interpretation that each component of the landscape, the relict, intermediate and modern, formed under different rates of local base level fall. The modern, deeply incised lower channel segments are responding to the local modern rate of rock uplift relative to the base level set by the Red River, the intermediate landscape formed in response to an earlier local base level set by a paleo Red River, and the relict landscape formed under stable pre-uplift base level conditions. Therefore, both surface uplift patterns and spatial-temporal patterns of incision on the Red River (set by surface uplift, climate, and sediment and rock properties) influence the evolution of tributary channel profiles. Finally, disruptions along the active fault systems of the southeastern margin of the Tibetan Plateau can produce local variation in rock uplift rate, which will influence the morphology of local tributaries. In sum, incision along the Red River reflects

regional surface uplift, tilting, climate conditions, changes in tributary local base level, and disruption along the Red River fault.

In the next section, we turn to analysis of longitudinal profiles of tributaries to the Red River, because this can be used to constrain the history of incision of the Red River. Channel parameters (such as steepness and concavity) can help in evaluation of the temporal and spatial sequence of incision in the Red River region: stream-power bedrock incision modeling suggests that channel parameters should be linked to a range of external factors, including, most importantly, uplift rate and climate (Howard, 1980; Seidl and Dietrich, 1992; Howard et al., 1994; Whipple and Tucker, 1999; Whipple and Tucker, 2002). Further, a reconstructed paleo-drainage network is a basis for inferring the total amount of river incision. It can also provide a robust structural datum for measuring vertical displacement of the relict landscape across the Red River fault.

TRIBUTARY ANALYSIS

We begin with an abbreviated discussion of bedrock river incision theory, examine tributary morphology and channel parameters in the context of bedrock incision modeling, and finally reconstruct the drainage network of the relict landscape.

Longitudinal profile analysis

Typical river longitudinal profiles, for both bedrock and alluvial rivers, are concave and can be described by an empirical power law relationship between slope and area:

$$S=k_sA^{-\theta} \tag{1}$$

where S is slope, or channel gradient, k_s is the channel steepness index, A is upstream, contributing drainage area, and θ is the channel concavity index. For many landscapes, k_s varies with uplift rate, climate and lithology, but θ varies little (Snyder et al., 2000; Kirby et al., 2003). This empirical relationship is similar to that described by the stream-power incision model for bedrock river incision (Howard, 1980; Seidl and Dietrich, 1992; Howard et al., 1994; Whipple and Tucker, 1999; Whipple and Tucker, 2002), which we briefly discuss here as a framework to

guide our analysis. In the analysis we consider and discuss complexities in natural systems that may cause deviation from behavior expected for this simple model. The stream power incision model combines a power law relationship between shear stress and erosion, conservation of mass, conditions of steady, uniform flow, and empirical relations between discharge and channel width and discharge and basin area to arrive at the expression:

$$E = KA^m S^n \quad (2)$$

where E is erosion rate, K is a dimensional constant dependent on lithology, climate and sediment load, and m and n are positive constants related to basin hydrology, hydraulic geometry and erosion process. Relating channel elevation to the balance between uplift and erosion results in the expression:

$$dz/dt = U(x,t) - E(x,t) = U(x,t) - KA^m S^n \quad (3)$$

where U is uplift rate, x is horizontal distance along the channel and z is channel elevation. For an equilibrium channel, $dz/dt = 0$, Equation 3 can be solved for equilibrium slope (S_e):

$$S_e = (U/K)^{1/n} A^{-m/n} \quad (4)$$

Note that the form of this equation is identical to Equation 1, though it applies only to bedrock (or more precisely, detachment limited) channels. If the criteria inherent in the derivation of this model are met and a channel is in equilibrium, then the steepness index of a channel (k_s in Equation 1) is a function of the ratio between uplift (U) and erosion factors (K) to the $1/n$ power. There is strong empirical support for a positive correlation between steepness (k_s) and rock uplift rate (U) (e.g. Merritts and Vincent, 1989; Snyder et al., 2000; Kirby and Whipple, 2001; Whipple in press). If the U/K ratio increases uniformly along the channel, through either an increase in uplift rate or a decrease in erosivity, the channel will respond by forming a new equilibrium slope, starting at the basin outlet. The equilibration will proceed as an upstream-propagating wave of erosion (Weissel and Seidl, 1998; Whipple and Tucker, 1999). For the most part, the section upstream of this migrating “knickzone” is isolated from the change in uplift rate and will

maintain a profile in equilibrium with the old uplift rate while the section downstream of the knickpoint will be equilibrated to the new conditions. The equilibration process proceeds at a rate positively correlated to drainage area, and so the trunk stream equilibrates relatively quickly whereas headwater streams will maintain knickzones and non-equilibrated channel segments longer (Whipple and Tucker, 1999; Whipple 2001).

The ratio m/n in Equation 4, or the intrinsic concavity, corresponds to θ , observed concavity in Equation 1 if and only if the channel is in equilibrium and rock uplift, climatic conditions, and rock properties are spatially uniform. Intrinsic concavity should theoretically fall between 0.35 and 0.6 (Whipple and Tucker, 1999). Observed concavities, which may be influenced by non-uniform uplift, non-uniform lithology or variations in sediment flux and grain size (Sklar and Dietrich, 1998; Howard, 1998; Sklar and Dietrich, 2001; Whipple and Tucker, 2002; Kirby and Whipple, 2001), range from approximately 0.3 to 1.2 (Tucker and Whipple, 2002; Whipple, in press). If the concavity is significantly higher than this range, a variety of processes related to transient conditions could be in operation with important consequences (Whipple, in press).

Tributary morphology

Using a 90 m DEM, we extracted longitudinal profiles for 97 tributaries to the Red River in China, all those with a drainage area greater than 40 km² (Appendix Figs. 1 and 2). The profiles consist of one to several channel segments separated by knickpoints, and distinct channel parameters (see discussion in next section) can be defined for each segment. We analyzed channel segments according to their position within each profile and their channel parameters and found that tributary longitudinal profiles fall into three different morphologic categories. The dominant tributary form (78 of the 97, Fig. 5a and Appendix Fig. 2) consists of three segments: an upper segment which travels over the relict landscape with uniform concavity and low steepness, a middle segment with intermediate concavity and steepness, and a lower channel segment with high concavity and steepness (Table 1 and Appendix Table 1). For some tributaries, the upper segment is absent or poorly defined. In other cases, minor knickpoints or convex channel segments complicate segment classification. In general, however, the three-segment morphology is robust and is confirmed by our field observations of relict, intermediate, and modern landscapes described above (see Fig. 4). The second morphologic category consists

of profiles with only two channel segments (four of the 97, Fig. 5b, and Appendix Fig. 2), and the final category consists of profiles which have no discernable knickpoints at all (15 of the 97, Fig. 5c and Appendix Fig. 2). Fully equilibrated channels occur throughout the study area, but are concentrated on the Yunnan Plateau in the vicinity of the bend (Appendix Fig. 2)

Channel parameters

Intrinsic concavity was found using methods developed by Snyder et al. (2000), Kirby and Whipple (2000) and Kirby et al. (2003). In this procedure, channel drainage area is extracted from a DEM and corresponding slopes are calculated along the extracted channel, then these data are plotted in log-log slope-area space. A linear regression to the data yields the concavity index (the slope of the regression) and the steepness index (the y-intercept) (Fig. 5). Because steepness index is highly correlated to concavity, a normalized steepness index was also determined for each channel with a reference concavity (in our case, $\theta = 0.45$, though the exact value matters little, only that it is consistent for each analysis) to allow meaningful comparison of segments with different concavity.

In general, concavity and normalized steepness index for the upper and middle segments are consistent among all tributaries, and the minor variation in upper channel parameters may reflect the small sample size. In contrast lower channel segments exhibit high variability in these parameters (Table 1). Because the Red River flows directly along the Red River fault, and because we might reasonably expect different deformation patterns north and south of the major bend, we present averaged data for each set of segments as well as averaged data for the four quadrants defined by the river and the bend (Fig. 6). We also present data for the 15 tributaries with no knickpoints, which we label as “fully equilibrated” in Table 1.

A number of observations emerge from these data. First, there is only minor geographic variation in normalized steepness and concavity data for the upper and middle channel segments, which contrasts with significant variability in the lower channel segments. Second, average normalized steepness index increases from the upper channel segments to the middle to the lower segments. Finally, average concavity for the upper landscape segments (0.38 ± 0.19) falls within the range of commonly observed values (Tucker and Whipple, 2002) and average concavity for middle

channel segments (0.64 ± 0.37) is higher, but is still within the normally observed range. Lower segment concavities, however, are exceptionally high (3.54 ± 3.38).

Reconstruction of relict landscape channel profiles

Of the 97 total tributary longitudinal profiles, we identified well-developed “relict landscape” channel segments on 50 tributaries on the basis of low normalized steepness index, average concavity values, and their position above a prominent knickpoint. Each of these segments were evaluated for conditions that might affect channel gradient or knickzone propagation, particularly lithologic contrasts along the length of each channel. Such segments were excluded, as were segments with insufficient data to obtain a meaningful regression. Our final, conservative data set includes 12 tributaries from the Yunnan Plateau northeast of the Red River and 16 from the southwest, draining the Ailao Shan (Appendix Fig. 3 and Appendix Table 2).

The properties of these 28 channels were analyzed to estimate the pre-incision profiles to their confluence with the Red River. The mean concavity index (θ) for the upper channel segments is 0.38 (Table 1). Using this value, drainage area and slope data, and Equation 1, we obtained a steepness index (k_s) and uncertainty for each segment. From these values, we then projected the channel profile from the knickpoint downstream to the Red River confluence. This analysis provides an estimate of the paleo-longitudinal profile of each tributary corresponding to the drainage network developed on the relict landscape assuming no changes in drainage area. Because we use Equation 1, our analysis does not depend on the validity of bedrock incision modeling, but rather only on well-established empirical observation of a power-law relation between local slope and upstream drainage area.

The difference in elevation of the termination of the profile and that of the modern tributary-Red River confluence indicates the amount of subsequent incision: the reconstructed longitudinal profiles indicate 500-1600 m incision (Fig. 6a). The difference in elevation of the termination of the profile between tributaries from the Ailao Shan and from the Yunnan Plateau indicate the relative vertical displacement of the relict landscape by the Red River fault (Fig. 6b). Southeast of the bend in the Red River fault, tributaries from the Ailao Shan and Yunnan Plateau project to approximately the same elevation, indicating only minor if any offset across the fault. To the

northwest of the bend, however, displacement increases to a maximum of 750 m. Insufficient data in the vicinity of the bend hinders precise estimation of the offset in that area. Although tributary data do not extend to the northern tip of the Red River fault, field observations indicate vertical displacement must diminish toward the Midu basin as well (Fig. 1).

We also reconstructed the middle channel segment longitudinal profiles for 14 of the 28 tributaries with upper segments, and for 16 additional channel profiles with no upper segments, for a total of 30 projections (Fig. 6c., Appendix Fig. 3 and Appendix Table 2). We used a concavity of 0.64 (mean concavity for middle segments, Table 1). Data for tributaries with both upper and middle segment projections allows us to constrain the relative amount of river incision recorded by base level fall from the relict landscape channel to the middle segment, and from the middle segment to the modern river elevation (Table 2). Though the sparseness of this data limits inferences, approximately twice as much incision occurred from the middle to lower channel segments than from the relict landscape to middle channel segments, and appears to be greater north of the bend.

DISCUSSION

Key observations which emerge from our tributary analysis are (1) total amount and distribution of incision along the Red River (Fig. 6a); (2) a three-segment channel morphology for the majority of tributaries (Fig. 5 and Appendix Fig. 2); (3) high mean concavity (θ) for the lowermost channel segments (Table 1 and Appendix Table 1); (4) the relative offset of relict landscape tributaries across the Red River fault (Fig. 6b); and (5) geographic variation in normalized steepness index (k_s) and concavity (θ) for the lowermost channel segments (Table 1). The latter two factors yield information about activity along the Red River fault and will be addressed in the first section of the discussion. The first three factors relate to surface uplift and climatic interactions and will be addressed in a later section. Finally we will discuss implications of our observations for exhumation of the Ailao Shan shear zone and for growth of the eastern margin of the Tibetan Plateau.

Activity along the Red River fault

The Red River fault is clearly an active strike-slip fault, although previous workers have not been able to determine the magnitude of strike-slip or dip-slip displacement, spatial distribution or timing with certainty (Allen et al., 1984; Wang E. et al., 1998; Replumaz et al., 2001). Because the topographic relief of the relict landscape is significant relative to the amount of displacement we expect across the Red River fault, and as there may have been remnant relief along the crest of the Ailao Shan, topography alone is an insufficient datum for measuring vertical displacement. Using instead the reconstructed drainage network mitigates these problems, and allows us to place constraints on vertical displacement.

The longitudinal profiles of two directly opposing tributaries may have different concavities or steepness indices, but their downstream elevations must be the same, set by the elevation of the main channel (Playfair, 1802; Seidl and Dietrich, 1992). Once river incision begins, the upper portions of the opposing tributaries are isolated from each other and begin to record any differential offset occurring downstream of the knickpoint (see Fig. 6b inset). Reconstruction of relict landscape tributaries reveals that Ailao Shan tributaries are displaced vertically relative to Yunnan Plateau tributaries. Relative displacement is insignificant south of the bend, but increases toward the north to a maximum displacement of ~750 m near the town of Ejia (Fig. 6b). Absolute displacement may have occurred in the footwall (increasing the surface elevation of the Ailao Shan), in the hanging wall (downwarping the Yunnan Plateau), or both.

Mean normalized steepness index in the lowest channel segments (k_s) varies considerably by geographic region (Table 1): channels are steepest north of the bend in the Ailao Shan and south of the bend on the Yangtze Platform (390 ± 148 and 348 ± 176 respectively), and are less steep south of the bend in the Ailao Shan and north of the bend on the Yangtze Platform (277 ± 79 and 220 ± 76 respectively) (Fig. 1). Steepness in these channels varies as a function of lithology and rate of relative base level fall. Within the Ailao Shan, lithology is uniform. Therefore, variations in channel steepness probably reflect different uplift conditions: in the northern Ailao Shan, where uplift rate (and relative base level fall) is higher as a result of dip-slip displacement on the Red River fault, steepnesses are correspondingly higher (Equation 4, Table 1). Lower steepness north of the bend on the Yunnan Plateau may similarly result from downwarping of the hanging

wall by vertical displacement on the Red River fault, and downwarping may also be responsible for the high concentration of fully equilibrated channels on the Yunnan Plateau on either side of the bend near Yuanjiang (Appendix Fig. 2). However, this analysis is complicated by lithologic differences north and south of the bend which probably play an important role in determining channel steepness. Many of the tributaries from the Yunnan Plateau south of the bend drain cliff-forming Triassic limestones of the southern South China fold belt (Fig. 1), capable of supporting extremely steep channels. Further north, where tributaries drain the relatively erodible sediments of the Chuxiong red bed basin (Fig. 1), channel steepness indices are lower. Why the effect of lithology is not seen in the middle and relict landscape channel segments is unclear. One possibility is that the relict landscape and middle channel segments are in transport limited rather than detachment limited (bedrock) conditions, and therefore lithologic controls on channel morphology are masked (Whipple and Tucker, 2002).

The maximum gradient associated with regional tilting, which will affect tributary data, is $\sim 2 \times 10^{-3}$ (5000 m over 2500 km, Clark and Royden, 2000). However, because tilting is stronger near the plateau and gentler in more distal positions (Clark and Royden, 2000), because we do not know the original landscape gradient, and because the Red River runs slightly oblique to the plateau axis, tilting in the study area is probably less. On this basis, and from DEM analysis, we estimate tilting was of the order 1×10^{-3} . Over the 500 km of the study area, if we use this value, surface uplift at the northwest end of the study area is ~ 500 m greater than at the southwest end. This tilting does not affect relative displacement across the Red River fault, but does affect the paleo Red River profile recorded by tributaries from the Ailao Shan and Yunnan Plateau. The gradient recorded by the Yunnan plateau tributaries is $\sim 2 \times 10^{-4}$, less than our estimated tilting gradient. This is probably the result of downwarping of tributaries northwest of the bend along the Red River fault. The higher gradient recorded by Ailao Shan tributaries ($\sim 2 \times 10^{-3}$) may similarly result from relative uplift of the footwall along the Red River fault.

In summary, the dip-slip component of displacement along the Red River fault is less than 750 meters north of the bend and insignificant south of the bend, affecting both hanging wall and footwall elevations. This is not consistent with models for the Red River fault in which displacement extends along the entire length of the fault (Allen et al., 1984; Replumaz et al.,

2001). Further, a number of authors have suggested that significant unroofing of the Ailao Shan shear zone has occurred as a result of recent normal faulting along the Red River fault (Harrison et al., 1996; Leloup et al., 2001; Replumaz et al., 2001). Our tributary data and observations of landscape morphology indicate conclusively that no exhumation of the shear zone has occurred since establishment of the relict landscape, probably prior to Pliocene time.

River incision and surface uplift

The existence of a regional relict landscape at high elevations, which is continuous with the Tibetan Plateau, implies significant surface uplift of the southeastern plateau margin (Clark et al., 2002; Clark, 2003). We discuss incision along the Red River in the context of this regional uplift below.

Incision and surface uplift recorded by the Red River:

The Red River has incised the landscape between ~500 and ~1600 m (Fig. 6a), though tributaries on the Yangtze Plateau record less incision. Because both absolute elevations on the Ailao Shan and the Yunnan Plateau north of the bend have probably been affected by differential vertical displacement on the Red River fault, we cannot use the river incision recorded by these tributaries as a proxy for total river incision. South of the bend, however, tributaries on either side of the Red River are relatively unaffected by recent faulting, and these data indicate a weighted mean river incision of 1381 ± 88 m (Fig. 6a). Maximum surface uplift at the southern end of the study area is indicated by the current approximate elevation of the projected tributaries, or ~1500 m (Fig. 6b). Prior to surface uplift the paleo Red River was probably at a similar or lower elevation (<100 m) to the modern Red river, but the paleo Red River profile has been translated through surface uplift to its current elevation of ~1500 m (Fig. 6b). Surface uplift at this point is therefore 1400-1500 m (the amount of uplift necessary to elevate the paleo Red River profile from 0 m (the minimum original profile elevation) or ~100 m (the maximum original profile elevation) to ~1500 m, the approximate elevation today). Total surface uplift must increase upstream toward Tibet.

Incision and surface uplift recorded by tributaries to the Red River:

Multiple segment tributary longitudinal profiles (Fig. 5 and Appendix Fig. 2) indicate a complicated incision pattern. Knickpoints can result from a variety of processes, which we will explore below. However, it is unlikely that the knickpoints in this study result from river capture events. Clark et al. (in press) argue that prior to regional uplift, most of the major rivers of eastern Tibet, including the Mekong, Salween, Yangtze and tributaries to the Yangtze, drained through the Red River to the South China Sea. The modern drainage pattern is a result of river captures driven by uplift of the southeastern margin. However, the morphology of the Yangtze and other rivers (Clark et al., in press) suggest that these captures occurred immediately prior to regional uplift and river incision, and therefore excavation of the Red River valley was accomplished exclusively by the Red River, regardless of its prior drainage history. Knickpoints within the Red River basin are therefore most likely unrelated to large-scale drainage reorganization.

In a detachment-limited bedrock river, knickpoints can also result from a change in uplift rate (U) or other conditions such as precipitation or erosion mechanism (K) (Equation 4). An increase in uplift rate initiates the migration up the profile of a steep channel segment, separated from the upstream segments by a knickpoint (Weissel and Seidl, 1998; Whipple and Tucker, 1999). The steepness of the newly forming channel segment will depend on the term $(U/K)^{1/n}$ from Equation 4. Sudden base level fall can also produce migrating knickpoints, but channel segments above and below the knickpoint will have the same steepness index and concavity assuming the background rate of base level fall is unchanged (Whipple and Tucker, 1999).

The three segment tributary morphology (Fig. 5a) is thus most simply interpreted as pulsed surface uplift (Fig. 7a): during the first phase of incision, uplift rate increased, isolating the upper, relict landscape channel and developing the intermediate channel with higher mean normalized steepness (Table 1); during the second phase of incision, uplift rate increased further, isolating the intermediate channel and initiating the modern, lower channel segment with yet higher mean normalized steepness (Table 1). We can make this interpretation, however, only if tributary local base level remains constant throughout development of the region, that is, if the Red River maintains a relatively constant gradient during uplift. Even though the Red River is

constantly incising, if the gradient is stable, absolute base level for each tributary will be constant in time, and changes in uplift rate will be directly translated to the tributaries.

However, it is unlikely that the main Red River profile is unaffected by regional uplift and climate change. The trunk river has considerable latitude in adjusting to changes in external conditions: including possible changes in channel width, sinuosity, percent alluvial cover, bed material size, bed roughness, and gradient. A crucial factor in determining the evolution of tributary longitudinal profiles therefore is the nature of the response of the main river to changes in uplift rate (U) and climate and erosion conditions (related to K).

If surface uplift rate has been constant during river incision, we may infer changes in gradient of the Red River on the basis of tributary morphology. Local base level change brought about by changing absolute elevation along the trunk channel effectively enhances or detracts from the regional uplift rate. The following scenario would produce three-segment channels (Fig. 7b). As uplift rate first increased, the Red River steepened, increasing absolute elevation at every point along the channel. During this period, the effects of increased uplift rate on channel steepness were dampened by rising local base level on the trunk channel. Following this, climate change, possibly a shift in the Quaternary to more erosive conditions (Gregory and Chase 1994; Molnar, 2001), or a surface-uplift-induced intensification of the monsoon (Ruddiman and Kutzbach 1989), triggered downcutting of the main channel and the establishment of the new profile at lower absolute elevations. Base level fall initiated the lower channel segments and enhanced the effect of regional surface uplift, resulting in very steep channels.

Incision history may also be reflected in the high concavity of the lower channel segments, which have a mean concavity of 3.54 ± 3.38 , compared to middle segment values of 0.64 ± 0.37 and upper segment values of 0.38 ± 0.19 (Table 1). The effects of transient adjustment, alluviation near the tributary junction with the main river, data noise, lithology, sediment supply (Sklar and Dietrich, 1998; Howard, 1998; Sklar and Dietrich, 2001; Whipple and Tucker, 2002), bed armoring (Siedl et al., 1994), other spatially correlated effects (Kirby and Whipple, 2001; Kirby et al., 2003), or a transient response to rapid base level fall (Gasparini, in press) could increase observed channel concavities, and may account for increases in concavity of the order

observed in the lower tributary segments. However, temporal variations in uplift rate can also affect the concavity of a channel by producing a series of equilibrium channel segments that sweep up the profile in succession (Royden et al., 2000; Whipple and Tucker, 1999). If uplift rate decreases with time, channel segments formed earlier, during higher uplift conditions, in the upper parts of the channel, will be steeper. Later formed channel segments, near the tributary outlet, will be less steep. If the decrease in uplift rate is smooth, the result will appear as a highly concave channel profile. High lower channel segment concavity (Table 1) suggests declining uplift rate with time during the second phase of incision (Fig. 7a). Alternatively, incision along the trunk channel during the second phase of incision may initially have been rapid, during the period of base level fall, but has fallen to more moderate values toward the present (Fig. 7b).

In summary, we assign the upper knickpoints and abandonment of the relict landscape to rapid onset of uplift-driven river incision. Two end-member scenarios emerge for subsequent development of the Red River basin, one in which tributary morphology is entirely driven by changes in uplift rate with time, the other in which uplift rate is constant in time, and tributary morphology is the result of adjustments of the trunk channel to external forcings such as climate factors. We know of no geodynamic reason why plateau growth might be pulsed, but the possibility is certainly intriguing and worth further investigation. We do, however, strongly suspect that climate change over the duration of river incision is important. Short term climate fluctuations would likely damp out over the duration of development of the Red River drainage. However, global climate and monsoonal patterns and intensity do vary over longer timescales, and monsoon intensity may have been enhanced by the uplift of the plateau surface (Ruddiman and Kutzbach, 1989). Although the quantitative relation between climate and river erosivity is not well known, increased flood discharges associated with an intensification of the monsoon ought to enhance river incision rates and importantly influence landscape evolution in the region.

As an interesting side note, channels with fewer channel segments (Figs. 5a and 5b) may result from variable rates of knickpoint migration. If the knickpoint separating the middle and lower segments migrates quickly up the channel, it may overtake the upstream knickpoint separating the upper and middle segments, erasing the middle segment entirely from the profile (Fig. 5b). It may also migrate beyond the uppermost knickpoint, overtaking both the middle and upper

segments (Fig. 5c). Knickpoint migration rate, in the stream-power bedrock incision model, is sensitive to U , K and n (Equation 4; Whipple and Tucker, 1999; Weissel and Seidl, 1998; Royden et al., 2000). As the three tributaries shown in Figure 5 are closely spaced within the relatively uniform gneisses of the Ailao Shan, to a first order we would expect very similar values of U , K and n for each tributary, and therefore expect tributary morphology to be nearly identical. That this is not the case underlines the sensitivity of knickpoint migration to what we suspect are only small variations in factors that control erosion parameters.

Exhumation of the Ailao Shan shear zone

Development of an extensive, low-relief landscape indicates that a period of regional erosion and relief reduction followed exhumation of the shear zone. During its exhumation the Ailao Shan was a high range, shedding debris into a fluvial system along its northeastern edge (Wang E. et al., 1998). The high relief within the Ailao Shan during its unroofing stages was reduced to low-relief and was deeply weathered by the time river incision began in the Pliocene or later. However, because the shape of the modern Red River basin is inherited from the relict landscape, and because the Ailao Shan is a modern drainage divide, the Ailao Shan must have remained a subtle topographic high even after reduction to low relief.

While the Ailao Shan has experienced surface uplift since formation of the relict landscape, the preservation of the relict landscape indicates that the range has not been structurally or erosionally exhumed. We cannot assess the role of a possible paleo-Red River fault in exhumation of Ailao Shan prior to formation of the relict landscape, but we have demonstrated that dip-slip displacement along the modern Red River fault plays no role in exhumation of the shear zone, counter to the findings of several other workers (Leloup et al., 1995; Harrison et al., 1996; Leloup et al., 2001, Gilley et al., 2003). Additionally, river incision is not extensive enough to have reset low temperature thermochronometers as it has elsewhere on the eastern margin of the Tibetan Plateau (Xu and Kamp, 2000; Clark and Royden, 2000; Kirby et al., 2002). Therefore, all thermochronologic data showing rapid cooling relate to earlier, pre-relict landscape exhumational events. In particular, fission track data (Bergman et al., 1997) which indicate rapid cooling at ~10 Ma cannot be linked to initiation of normal faulting on the modern Red River fault as it is by Leloup et al. (2001).

Plateau growth

In the Red River region, river incision in the Pliocene or later probably closely followed the initiation of growth of the eastern margin of the Tibetan Plateau. Plateau growth may have been in two stages, based on the three-segment tributary morphology, but this may also be the result of factors such as climate change in the Quaternary. Total surface uplift near the Chinese-Vietnamese border at the southern end of the study area is 1400-1500 m. The paleo Red River defines the base of the relict landscape, but relief within the relict landscape is up to 500 m, and average elevation of the relict at the southeast end of the study area is ~1800 m. Subtracting from this the amount of surface uplift, average elevations were probably only a few hundred meters above sea level prior to surface uplift.

Pliocene initiation of incision in the Red River region is somewhat later than the initiation of river incision inferred from thermochronologic data from elsewhere along the plateau margin. Kirby et al. (2002) infer uplift of the plateau adjacent to the Sichuan basin in late Miocene or early Pliocene time (10-12 Ma in the Longmen Shan, west edge of Sichuan basin, and 5-7 Ma in the Min Shan, north edge of Sichuan basin) on the basis of rapid cooling recorded in (U-Th)/He and $^{40}\text{Ar}/^{39}\text{Ar}$ data. Rapid river incision in late-Miocene time (7-13 Ma) is implied by the apatite (U-Th)/He data of Clark (2003). The Red River region is farther southeast along the plateau margin from Tibet than these other study areas (see Fig. 1), and thus probably experienced less overall surface uplift and that uplift may have occurred more recently. A delay in the initiation of incision along the Red River compared to regions proximal to Tibet suggests outward growth of the Plateau.

CONCLUSIONS

We describe a low-relief upland landscape in the areas adjacent to the Red River in Yunnan Province, China, continuous with a landscape developed over the entire eastern margin of the Tibetan Plateau (Clark et al., 2002; Clark, 2003; Clark et al., in press), which we interpret as a relict landscape: a landscape with a morphology that reflects past rather than present base level conditions. The relict landscape is cut by the active fault systems of Yunnan, including the Red River fault, and it is deeply incised by the Red River. Tributaries to the Red River record incision and tectonic deformation of the region, including ~1400 m river incision, ~1400-1500 m surface

uplift, up to 750 m dip-slip offset across the northern portion of the Red River fault, and two phases of river incision.

The following history for structural and geomorphic development of the region emerges. The Ailao Shan shear zone was active, and actively unroofing, until at least 17 Ma (Harrison et al., 1996) and possibly as recently as 10 Ma (Bergman et al., 1997; Leloup et al., 2001). After that time, deep weathering and erosion reduced the area to low relief (<500 m) and low average elevation, sharing base level with the regional low-relief landscape identified by Clark (2003). At some point, possibly in the Pliocene, the area began to undergo regional uplift and tilting, and the Red River responded by incising a deep valley into the now elevated low-relief landscape, forming the relict landscape. Regional uplift is almost certainly related to uplift of the Tibetan Plateau, and a plausible mechanism has been suggested by Royden (1996), Royden et al. (1997), and Clark and Royden (2000), in which the extrusion of weak lower crustal material from beneath Tibet causes the inflation and uplift of the eastern margin of the Tibetan Plateau.

Structural deformation produced at most 750 m of uplift of the northern Ailao Shan, tapering toward zero south of the bend and at the northern termination of the fault in the Midu basin. The relict landscape has not been erosionally or structurally removed from the Ailao Shan, and therefore no unroofing of the Ailao Shan shear zone has occurred along the Red River fault or any other structure since the formation of the relict landscape.

The spatial and temporal pattern of river incision reflects both regional uplift and climate conditions. The tributary three-segment morphology could indicate two phases of plateau growth: relatively slow growth during the first phase, then a pulse of rapid uplift during the second phase. More likely, however, the two-stage incision history results from adjustments of the trunk channel to changing conditions of uplift and climate. The trunk channel may have initially increased in gradient as a response to regional uplift, then rapidly cut down to a new equilibrium profile after a trigger to more erosive conditions, such as climate change in the Quaternary or monsoonal strengthening. While we cannot rule out the intriguing possibility of pulsed plateau growth, we acknowledge that climatic conditions almost certainly will play a role in the development of any river system of this size and over this length of time.

ACKNOWLEDGEMENTS

This research was supported by the Continental Dynamics program at the National Science Foundation (EAR-0003571). We thank Marin Clark and Wiki Royden for helpful discussion of this work, Sinan Akciz, Will Ouimet and Christopher Studnicki-Gizbert for discussion and manuscript reviews, Michael Stewart, Josh Feinberg and Yin Jiyun for invaluable assistance in the field, and driver Kou Jianle for five safe field seasons. This paper benefited from thorough reviews by F. Pazzaglia and J. O'Connor.

REFERENCES CITED

- Allen, C.R., Gillespie, A.R., Han Yuan, Sieh, K.E., Zhang Buchun, Zhu Chengnan, 1984, Red River and associated faults, Yunnan Province, China: Quaternary geology, slip rates, and seismic hazard: *Geological Society of America Bulletin*, v. 95, p. 686-700.
- Allen, C.R., Luo, Z., Qian H., Wen X., Zhou H., Huang W., 1991, Field study of a highly active fault zone: the Xianshuihe-Xiaojiang fault of southwestern China: *Geological Society of America Bulletin*, v. 103, p. 1178-1199.
- Baldwin, J.A., Whipple, K.X., and Tucker, G.E., 2003, Implications of the shear-stress river incision model for the timescale of post-orogenic decay of topography: *Journal of Geophysical Research*, v. 108(B3), 2158, doi:10.1029/2001JB000550.
- Bergman, S.C., Leloup, P.H., Tapponnier, P., Schärer, U., and O'Sullivan, P., 1997, Apatite fission track thermal history of the Ailao Shan-Red River shear zone, China: paper presented at meeting, European Union of Geoscience, Strasbourg, France
- Brias, A., Patriat, P., and Tapponnier, P., 1993, Updated interpretation of magnetic anomalies and seafloor spreading stages in the South China Sea, implications for the Tertiary tectonics of SE Asia: *Journal of Geophysical Research*, B, v. 98, p. 6299-6328.
- Bureau of Geology and Mineral Resources of Yunnan Province, 1990, in *Regional Geology of Yunnan Province*, Beijing, Geological Publishing House, 728 p.
- Chapin, C.E., and Kelley, S.A., 1997, The Rocky Mountain erosion surface in the Front Range of Colorado: *Colorado Front Range Guidebook-1997*, p. 101-114.
- Chen Z., Burchfiel, B.C., Liu Y., King, R.W., Royden, L.H., Tang W., Wang E., Zhao J., and Zhang X., 2000, Global Positioning System measurements from eastern Tibet and their implications for India/Eurasia intercontinental deformation: *Journal of Geophysical Research* B, vol. 105, p. 16,215-16,227.
- Clark, M.K., House, M., Royden, L.H., Burchfiel, B.C., X Zhang, W. Tang, Z Chen, 2000, River incision and tectonic uplift in eastern Tibet from low-temperature apatite U-Th/He thermochronology, EOS, Transactions, American Geophysical Union, Fall Meeting Suppl., v. 81, n. 48, p. F1142.
- Clark, M.K., and Royden, L.H., 2000, Topographic ooze: Building the eastern margin of Tibet by lower crustal flow: *Geology*, v. 28, p. 703-706.
- Clark, M.K., Royden, L.H., Burchfiel, B.C., Whipple, K.X., House, M.A., Zhang X., 2002, Preservation of a low-relief, regionally continuous erosion surface in southeastern Tibet: evidence for the transient condition of the southeastern plateau margin: *Geological Society of America Abstracts with Program*, paper no. 182-11.
- Clark, M.K., Schoenbohm, L.M., Royden, L.H., Whipple, K.X., Burchfiel, B.C., Zhang, X., Tang, W., Wang, E., Chen, L., , Surface Uplift, tectonics, and erosion of eastern Tibet from large-scale drainage patterns: *Tectonics*.
- Clark, M.K., 2003, Late Cenozoic Uplift of Southeastern Tibet [PhD Thesis]: Massachusetts Institute of Technology, 226 p.
- Cobbold, P.R., and Davy, P., 1988, Indentation tectonics in nature and experiment 2. Central Asia: *Geological Institute, University of Uppsala*, v. 14, p. 143-162.
- Davy, P., and Cobbold, P.R., 1998, Indentation tectonics in nature and experiment 1. Experiments scaled for gravity: *Geological Institute, University of Uppsala*, v. 14, p. 129-141.
- Dewey, J., Cande, S., and Pitman, W.C., III, 1989, Tectonic evolution of the India-Eurasia collision zone: *Eclogae geologicae Helveticae*, v. 82, p. 717-734.
- Epis, R.C., and Chapin, C.E., 1975, Geomorphic and tectonic implications of the Post-Laramide Late Eocene erosion surface in the Southern Rocky Mountains: *Geological Society of America Memoir* 144, p. 45-74.
- Fielding, E., Isacks, B., Barazangi, M., Duncan, C., 1994, How flat is Tibet?: *Geology*, v. 22, p. 163-167.
- Gasparini, N.M., Tucker, G.E., and Bras, R.L., in press, Network-scale dynamics of grain-size sorting: Implications for downstream fining, stream-profile concavity, and drainage basin morphology: *Earth Surface Processes and Landforms*.
- Gilley, L.D., Harrison, T.M., Leloup, P.H., Ryerson, F.J., Lovera, O.M., Wang J-H, 2003, Direct dating of left-lateral deformation along the Red River shear zone, China and Vietnam: *Journal of Geophysical Research*, v. 103, No. B2, 10.1029/2001JB001726.
- Gregory, K.M., and Chase, C.B., 1994, Tectonic and climatic significance of a late Eocene low-relief high-level geomorphic surface, Colorado: *Journal of Geophysical Research* B, v. 99, p. 20,141-20,160.
- Hallet, B., and Molnar, P., 2001, Distorted drainage basins as markers of crustal strain east of the Himalaya: *Journal of Geophysical Research*, B, v. 106, p. 13,697-13,709.
- Harrison, T.M., W Chen, Leloup, P.H., Ryerson, F.J., and Tapponnier, P., 1992, An early Miocene transition in deformation regime within the Red River fault zone, Yunnan, and its significance for the Indo-Asian tectonics: *Journal of Geophysical Research*, v. 97, p. 7159-7182.
- Harrison, T.M., Leloup, P.H., Ryerson, F.J., Tapponnier, P., Lacassin, R., and Chen Wenji, 1996, Diachronous initiation of transtension along the Ailao Shan-Red River shear zone, Yunnan and Vietnam, in Yin, A., and Harrison, T.M., eds., *The Tectonic Evolution of Asia*, Cambridge University Press, New York, p. 208-226.
- Holt, W.E., Ni, J.F., Wallace, T.C., Haines, A.J., 1991, The active tectonics of the Eastern Himalayan Syntaxis and surrounding regions: *Journal of Geophysical Research* B, v. 96, p. 14,595-14632.
- Howard, A.D., 1980, Thresholds in river regimes, in Coats, D.R., and Vitek, J.D., eds., *Thresholds in geomorphology*: Boston, Massachusetts., Allen and unwin, p. 227-258.
- Howard, A.D., 1994, A detachment-limited model of drainage basin evolution: *Water Resources Research*, v. 30, p. 2261-2285.

Chapter 4- Surface uplift, exhumation and plateau growth

- Howard, A.D., 1998, Long profile development of bedrock channels: Interaction of weathering, mass wasting, bed erosion, and sediment transport, *in* Tinkler, K., and Wohl, E.E., eds., *Rivers over rock: Fluvial processes in bedrock channels*: American Geophysical Union Geophysical Monograph 107, p. 297-319.
- Kirby, E., and Whipple, K.X., 2001, Quantifying differential rock-uplift rates via stream profile analysis: *Geology*, v. 29, p. 415-418.
- Kirby, E., Reiners, P.W., Krol, M.A., Whipple, K.X., Hodges, K.V., Farley, K.A., Wenqing Tang, Zhiliang Chen, 2002, Late Cenozoic evolution of the eastern margin of the Tibetan Plateau: Inferences from $^{40}\text{Ar}/^{39}\text{Ar}$ and (U/Th)/He thermochronology: *Tectonics*, v. 21, 10.1029/2000TC001246.
- Kirby, E., Whipple, K.X., Tang W., and Chen Z., 2003, Distribution of active rock uplift along the eastern margin of the Tibetan Plateau: Inferences from bedrock channel longitudinal profiles, *Journal of Geophysical Research*, v. 108, doi:10.1029/2001JB000861.
- Lauge, D., and Davy, P., 2003, Constraints on the long-term colluvial erosion law by analyzing slope-area relationships at various tectonic uplift rates in the Siwalik Hills (Nepal): *Journal of Geophysical Research*, v. 106, no. B11, p. 26561-26591.
- Leloup, P.H., and Kienast, J.R., 1993, High temperature metamorphism in a major Tertiary ductile continental strike-slip shear zone: The Ailao Shan-Red River (P.R.C.): *Earth and Planetary Science Letters*, v. 118, p. 213-234.
- Leloup, P.H., Harrison, T.M., Ryerson, F.J., Chen Wenji, Li Qi, Tapponnier, P., and Lacassin, R., 1993, Structural, petrological and structural evolution of a Tertiary ductile strike-slip shear zone, Diangcang Shan, Yunnan: *Journal of Geophysical Research*, v. 98, p. 6715-6743.
- Leloup, P.H., Lacassin, R., Tapponnier, P., Schärer, U., Zhong Dalai, Liu Xiaohan, Zhang Liangshang, Ji Shaocheng, Phan Trong Trinh, 1995, The Ailao Shan-Red River shear zone (Yunnan, China), Tertiary transform boundary of Indochina: *Tectonophysics*, v. 251, p. 3-84.
- Leloup, P.H., Arnaud, N., Lacassin, R., Kienast, J.R., Harrison, T.M., Phan Trong, T.T., Replumaz, A., and Tapponnier, P., 2001, New constraints on the structure, thermochronology, and timing of the Ailao Shan-Red River shear zone, SE Asia: *Journal of Geophysical Research*, B, v. 106, p. 6683-6732.
- Merritts, D.J. and Vincent, K.R., 1989, Geomorphic response of coastal stream to low, intermediate, and high rates of uplift, Mendocino junction region, northern California: *GSA Bulletin*, v. 101, p. 1373-1388.
- Mears, B., Jr., 1993, Geomorphic history of Wyoming and high-level erosion surfaces, in Snoke, A.W., Steidtmann, J.R., and Roberts, S.M., eds. *Geology of Wyoming: Geological Survey of Wyoming Memoir No. 5*, p. 608-626.
- Metcalfe, I., 1996, Pre-Cretaceous evolution of SE Asian terranes, in Hall, R., and Blundell, D., eds., *Tectonic evolution of Southeast Asia*: London, Geological Society Special Publications No. 106, p. 97-122.
- Molnar, P., 2001, Climate change, flooding in arid environments, and erosion rates: *Geology*, v. 29, p. 1071-1074.
- Phillips, J.D., 2002, Erosion, isostatic response, and the missing peneplains: *Geomorphology*, v. 45, p. 225-241.
- Playfair, J., 1802, *Illustrations of the Huttonian Theory of the Earth*: Dover, London.
- Replumaz, A., Lacassin, R., Tapponnier, P., and Leloup, P.H., 2001, Large river offsets and Plio-Quaternary dextral strike-slip rate on the Red River fault (Yunnan, China): *Journal of Geophysical Research*, B, v. 106, 819-836.
- Roe, G.H., Montgomery, D.R., Hallet, B., 2002, Effects of orographic precipitation variations on the concavity of steady-state river profiles: *Geology*, v. 30, p. 143-146.
- Royden, L.H., 1996, Coupling and decoupling of crust and mantle in convergent orogens: Implications for strain partitioning in the crust: *Journal of Geophysical Research*, B, v. 101, p. 17 679-17 705.
- Royden, L.H., Burchfiel, B.C., King, R.W., Wang, E., Chen Z., Shen F., Liu Y., 1997, Surface deformation and lower crustal flow in eastern Tibet: *Science*, v. 276, p. 788-790.
- Royden, L.H., Clark, M.K., Whipple, K.X., 2000, Evolution of river elevation profiles by bedrock incision: analytical solutions for transient river profiles related to changing uplift and precipitation rates, *Eos Transaction, AGU*, 81(48), Fall Meeting Supplement.
- Ruddiman, W.F. and Kutzbach, J.E., 1989, Forcing of Late Cenozoic northern hemisphere climate by plateau uplift in southern Asia and the American west: *Journal of Geophysical Research*, v. 94, p. 18409-18427.
- Schärer, U., Zhang L., Tapponnier, P., 1994, Duration of strike-slip movements in large shear zones: the Red River belt, China: *Earth and Planetary Science Letters*, v. 126, p. 379-397.
- Seidl, M.A., and Dietrich, W.E., 1992, The problem of channel erosion into bedrock, *in* Schmidt, K.H., and de Ploey, J., eds., *Functional geomorphology*: Catena, suppl. 23, p. 101-124.
- Siedl, M.A., Dietrich, W.E., and Kirchner, J.W., 1994, Longitudinal profile development into bedrock: an analysis of Hawaiian channels: *Journal of Geology*, v. 102, p. 457-474.
- Sklar, L.S., and Dietrich, W.E., 1998, River longitudinal profiles and bedrock incision models: Stream power and the influence of sediment supply, *in* Tinkler, K., and Wohl, E.E., eds., *Rivers over rock: Fluvial processes in bedrock channels*: American Geophysical Union Geophysical Monograph 107, p. 237-260.
- Sklar, L.S., and Dietrich, W.E., 2001, Sediment and rock strength controls on river incision into bedrock: *Geology*, v. 29, p. 1087-1090.
- Snyder, N.P., Whipple, K.X., Tucker, G.E., and Merritts, D.J., 2000, Landscape response to tectonic forcing: DEM analysis of stream profiles in the Mendocino triple junction region, northern California: *Geological Society of America Bulletin*, v. 112, p. 1250-1263.
- Spotila, J.A., and Sieh, K., 2000, Architecture of transpressional thrust faulting in the San Bernardino Mountains, southern California, from deformation of a deeply weathered surface: *Tectonics*, v. 19, p. 589-615.

Chapter 4- Surface uplift, exhumation and plateau growth

- Tapponnier, P., Peltzer, G., Armijo, R., Le Dain, A.-Y., and Cobbold, P., 1982, Propagating extrusion tectonics in Asia: New insights from simple experiments with plasticine: *Geology*, v. 10, p. 611-616.
- Tapponnier, P., Peltzer, G., and Armijo, R., 1986, On the mechanics of the collision between India and Asia, *in* Coward, M.P., and Ries, A.C., eds., *Collision Tectonics*, Geological Society Special Publication 19, p. 115-157.
- Tapponnier, P., Lacassin, R., Leloup, P.H., Schärer, U., D. Zhong, X. Liu, S. Ji, L. Zhang and J. Zhong, 1990, The Ailao Shan/Red River metamorphic belt: Tertiary left-lateral shear between Indochina and south China: *Nature*, v. 343, p. 431-437.
- Tucker, G.E., and Whipple, K.X., 2002, Topographic outcomes predicted by stream erosion models: Sensitivity analysis and intermodel comparison: *Journal of Geophysical Research*, v. 107, doi:10.1029/2001JB000162.
- U.S. Geological Survey, 1993, Digital elevation models, data user guide, 5: Reston, VA, U.S. Geological Survey, p. 1-50.
- Wang, Erchie, and Burchfiel, B.C., 1997, Interpretation of Cenozoic tectonics in the Right-Lateral accommodation zone between the Ailao Shan shear zone and the Eastern Himalayan Syntaxis: *International Geology Review*, v. 39, p. 191-219.
- Wang, Erchie, Burchfiel, B.C., Royden, L.H., Chen Liangzhong, Chen Jishen, Li Wenxin, Chen Zhiliang, 1998, Late Cenozoic Xianshuihe-Xiaojiang, Red River and Dali fault systems of southwestern Sichuan and central Yunnan, China: Boulder, Colorado, Geological Society of America Special Paper 327.
- Wang, Pei-Ling, Ching-Hua Lo, Tung-Yi Lee, Sun-Lin Chung, Ching-Ying Lan, Nguyen Trong Yem, 1998, Thermochronological evidence for the movement of the Ailao Shan-Red River shear zone: A perspective from Vietnam: *Geology*, v. 26, p. 887-890.
- Wang, Pei-Ling, Ching-Hua Lo, Sun-Lin Chung, Tung-Yi Lee, Ching-Ying Lan, Trang Van Thang, 2001, Onset timing of left-lateral movement along the Ailao Shan-Red River shear zone: $^{40}\text{Ar}/^{39}\text{Ar}$ dating constraint from the Nam Dinh Area, northeastern Vietnam: *Journal of Asian Earth Sciences*, v. 18, p. 281-292.
- Weissel, J.K., and Seidl, M.A., 1998, Inland propagation of erosional escarpments and river profile evolution across the southeast Australian passive continental margin, *in* Tinkler, K., and Wohl, E.E., eds., *Rivers over rock: Fluvial processes in bedrock channels*: American Geophysical Union Geophysical Monograph 107, p. 189-206.
- Whipple, K.X., 2001, Fluvial landscape response time; how plausible is steady-state denudation?: *American Journal of Science*, v. 301, p. 313-325.
- Whipple, K.X., in press, Bedrock rivers and the geomorphology of active orogens: *Annual Review of Earth and Planetary Sciences*, v. 32.
- Whipple, K.X., and Tucker, G.E., 1999, Dynamics of the stream-power river incision model: Implications for height limits of mountain ranges, landscape response timescales, and research needs: *Journal of Geophysical Research*, v. 104, p. 17 661-17 674.
- Whipple, K.X., and Tucker, G.E., 2002, Implications of sediment-flux-dependent river incision models for landscape evolution: *Journal of Geophysical Research*, v. 107, no. B2, 10.1029/2000JB000044.
- Widdowson, M., 1997, The geomorphological and geological importance of paleosurfaces, *in* Widdowson, M., ed., *Paleosurfaces: Recognition, Reconstruction and Paleoenvironmental Interpretation*, Geological Society Special Publication No. 120, p. 1-12.
- Wobus, C.W., Hodges, K.V., and Whipple, K.X., 2003, Has focused denudation sustained active thrusting at the Himalayan topographic front? *Geology*, v. 31, p. 861-864.
- Xu, G. and Kamp, P.J.J., 2000, Tectonics and denudation adjacent to the Xianshuihe fault, eastern Tibetan plateau: constraints from fission track thermochronology: *Journal of Geophysical Research B*, v. 105, p. 19 231 – 19 251.
- Zhang, Lian-Sheng and Schärer, U., 1999, Age and origin of magmatism along the Cenozoic Red River shear belt, China: *Contributions to Mineralogy and Petrology*, v. 134, p. 67-85.

TABLE 1. NORMALIZED STEEPNESS AND CONCAVITY VALUES

Upper Segment					
Concavity [†]	Ailao Shan/SW	Yunnan Plateau/NE	Steepness [‡]	Ailao Shan/SW	Yunnan Plateau/NE
North of bend	0.42 ± 0.22 (n=11) [§]	0.36 ± 0.22 (n=6)	North of bend	32 ± 16 (n=11)	44 ± 15 (n=6)
South of bend	0.32 ± 0.08 (n=5)	0.40 ± 0.18 (n=6)	South of bend	40 ± 21 (n=5)	29 ± 7 (n=6)
Average	0.38 ± 0.19 (n=28)		Average	35 ± 16 (n=28)	
Middle Segment					
Concavity	Ailao Shan/SW	Yunnan Plateau/NE	Steepness	Ailao Shan/SW	Yunnan Plateau/NE
North of bend	0.74 ± 0.48 (n=20)	0.56 ± 0.23 (n=18)	North of bend	112 ± 70 (n=20)	95 ± 37 (n=18)
South of bend	0.51 ± 0.26 (n=29)	0.74 ± 0.40 (n=31)	South of bend	126 ± 53 (n=29)	100 ± 48 (n=31)
Average	0.64 ± 0.37 (n=98)		Average	109 ± 54 (n=98)	
Lower Segment					
Concavity	Ailao Shan/SW	Yunnan Plateau/NE	Steepness	Ailao Shan/SW	Yunnan Plateau/NE
North of bend	3.07 ± 1.96 (n=22)	2.34 ± 1.96 (n=15)	North of bend	390 ± 148 (n=22)	220 ± 76 (n=15)
South of bend	3.50 ± 4.36 (n=29)	4.64 ± 3.45 (n=27)	South of bend	277 ± 79 (n=29)	348 ± 176 (n=27)
Average	3.54 ± 3.38 (n=93)		Average	314 ± 141 (n=93)	
Fully Equilibrated					
Concavity	Ailao Shan/SW	Yunnan Plateau/NE	Steepness	Ailao Shan/SW	Yunnan Plateau/NE
North of bend	0.51 ± 0.23 (n=2)	0.50 ± 0.14 (n=7)	North of bend	157 ± 122 (n=2)	129 ± 25 (n=7)
South of bend	0.54 ± 0.21 (n=3)	0.53 ± 0.09 (n=3)	South of bend	159 ± 56 (n=3)	161 ± 25 (n=3)
Average	0.51 ± 0.14 (n=15)		Average	145 ± 46 (n=15)	

Note: Mean concavity and normalized steepness indices for upper, middle, lower and fully equilibrated channel segments for entire drainage network (in bold) and by quadrant. Quadrants are: north and south of bend to the southwest of the Red River (Ailao Shan) and north and south of the bend to the northeast of the Red River (Yunnan Plateau), see figure 6c. Note increasing normalized steepness and concavity from upper to middle to lower segments, and high variability of lower segments.

[†]Concavity determined by linear regression to selected slope-area data using a 20 m contour interval.

[‡]Normalized steepness index determined by linear regression to slope-area data with a fixed concavity of 0.45.

[§]Number of tributaries used in average. In some cases, more than one middle or lower channel segment can be identified in each tributary, separated by knickpoints and with slightly different steepness and concavity. Channel parameters for each segment were retained and used to determine mean values. This results in some cases in a greater number of channel segments than there are actual channels

TABLE 2. PHASE II to PHASE I INCISION RATIO

	Ailao Shan/SW	Yunnan Plateau/NE
North of Bend	3.0 ± 0.2 (n=4) [†]	2.8 ± 0.5 (n=3)
South of Bend	1.1 ± 0.3 (n=3)	1.6 ± 0.2 (n=4)
Average	2.3 ± 0.1 (n=14)	

Note: Incision during each phase determined by fitting upper and middle channel segments using a concavity of 0.38 and 0.64 respectively (Table 1), projecting the channels to their intersection with the paleo-Red River, then subtracting modern river elevations.

[†]Number of tributaries used in average.

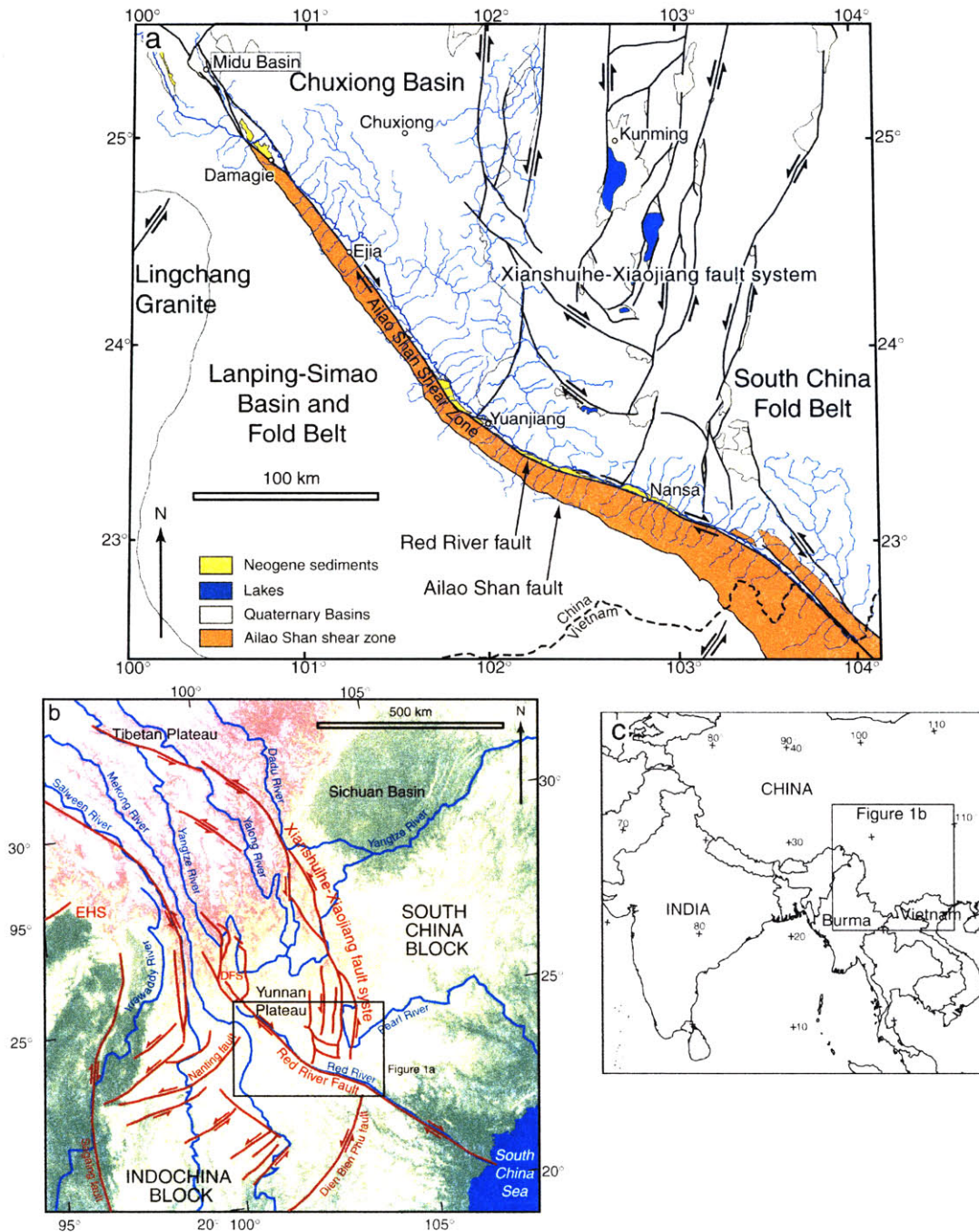


Figure 1. (a) Geologic map of field area. South China block shown in shades of blue, Indochina block in shades of green, separated by the Ailao Shan shear zone and Red River fault. The South China fold belt is of mixed lithology but in the vicinity of the Red River contains massive Triassic limestones. Chuxiong basin rocks are dominantly Mesozoic to early Cretaceous sedimentary rocks, as are rocks of the Lanping-Simao fold and thrust belt. The Red River drainage network is traced in blue. Active faults are marked with a heavy-weight black line. The inactive Ailao Shan fault, which marks the southern boundary of the Ailao Shan shear zone and is shown with a medium-weight line. (b) Map of the eastern margin of the Tibetan Plateau. EHS = Eastern Himalayan Syntaxis, DFS = Dali Fault system. Data for map from ~1 km resolution GTOPO30 DEM (USGS 1993). The Yunnan Plateau is a physiographic feature, part of the southeastern margin of the Tibetan Plateau. Figure 1a location indicated by box.

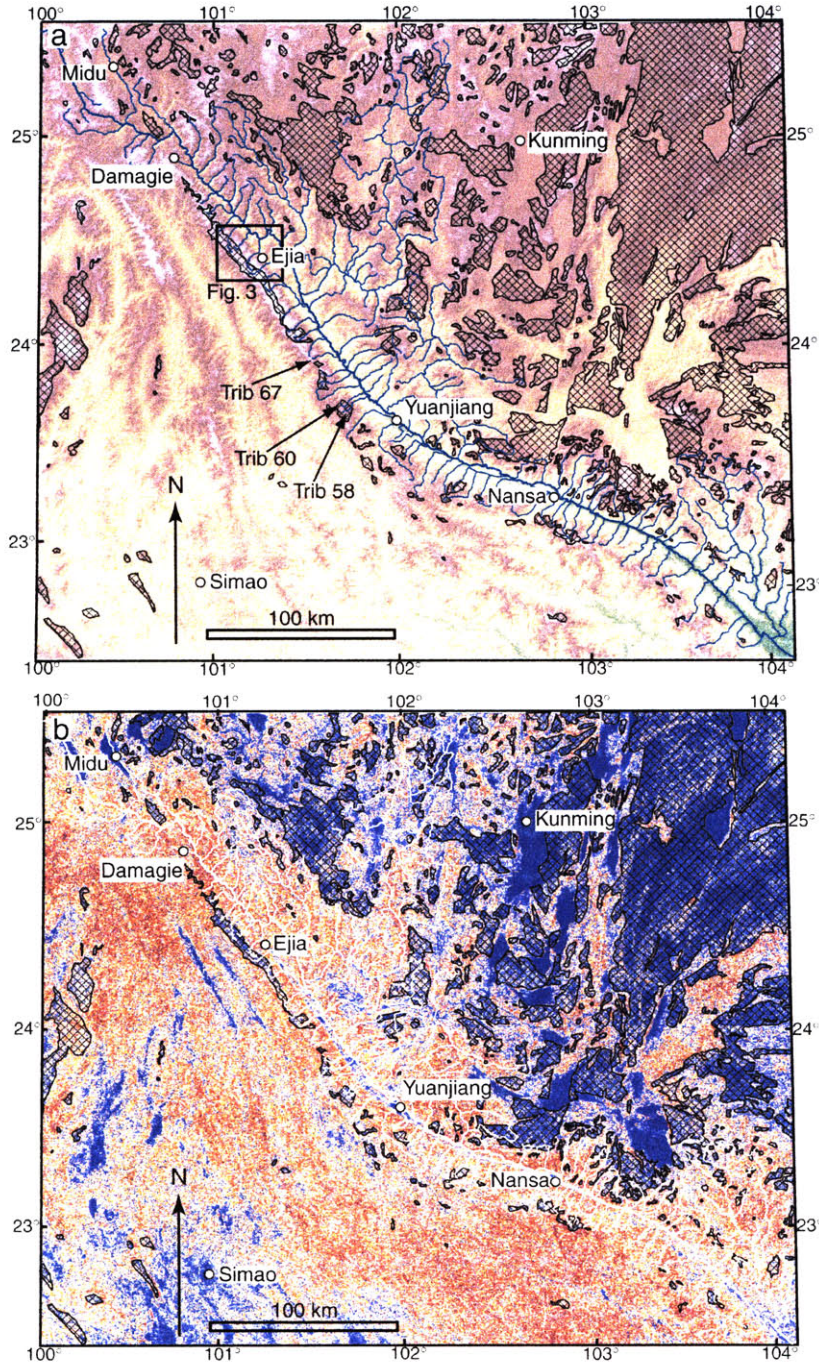


Figure 2. (a) DEM of field area, view covers same geographic area as shown in Figure 1a. The Ailao Shan is the prominent range to the immediate west and southwest of the Red River. The prominent bend in the Red River fault is centered approximately at the town of Yuanjiang. The Red River fault parallels the course of the Red River and terminates in the Midu basin. The relict landscape is indicated by patterned polygons, identified by the correspondence of high elevation and low slope areas. (b) Slope map of same area. Low slopes ($< 12^\circ$) are shown in blue, and reds and browns indicate increasing slope. The relict landscape is clearly visible as low-slope regions, and is indicated by patterned polygons. Areas of low slope which do not correspond to the relict landscape are Quaternary basins along strands of the Xianshuihe-Xiaojiang fault system (see Fig. 1a) or river valley bottoms.

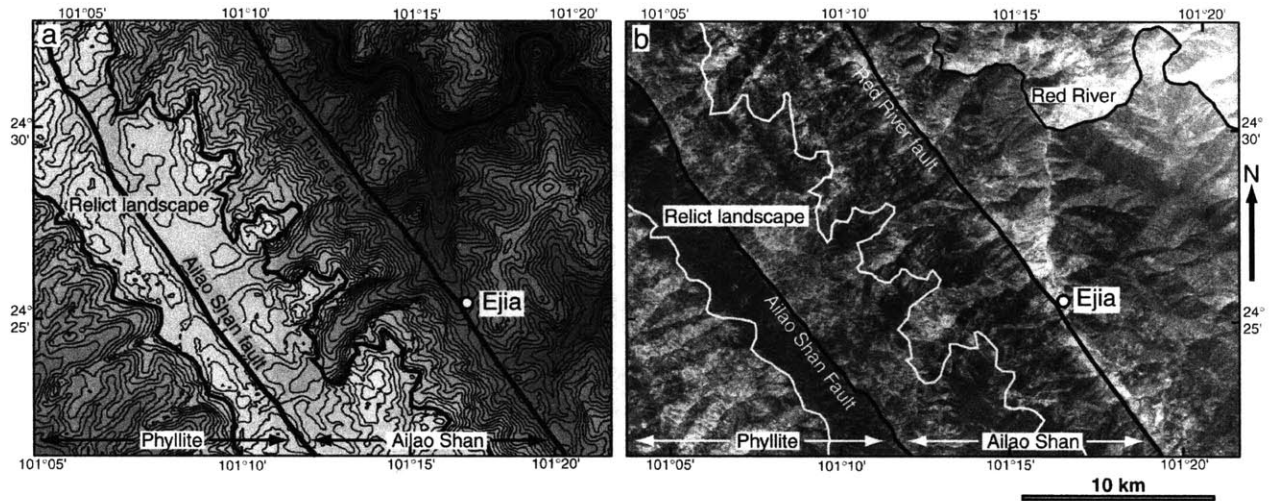


Figure 3. Relict landscape to the west of Ejia, location indicated in Figure 2a. (a) Topographic map shaded with DEM. Also indicated are the Red River fault, Ailao Shan fault, Ailao Shan gneisses and phyllite. The relict landscape is clearly discernible as a high, flat area, and is outlined with a medium weight line. Red River is in the upper right hand corner. (b) CORONA aerial photographs of same area as Figure 3a. Erosion surface outlined in white. Note vegetation contrast between Ailao Shan gneisses (light color) and phyllites (dark).

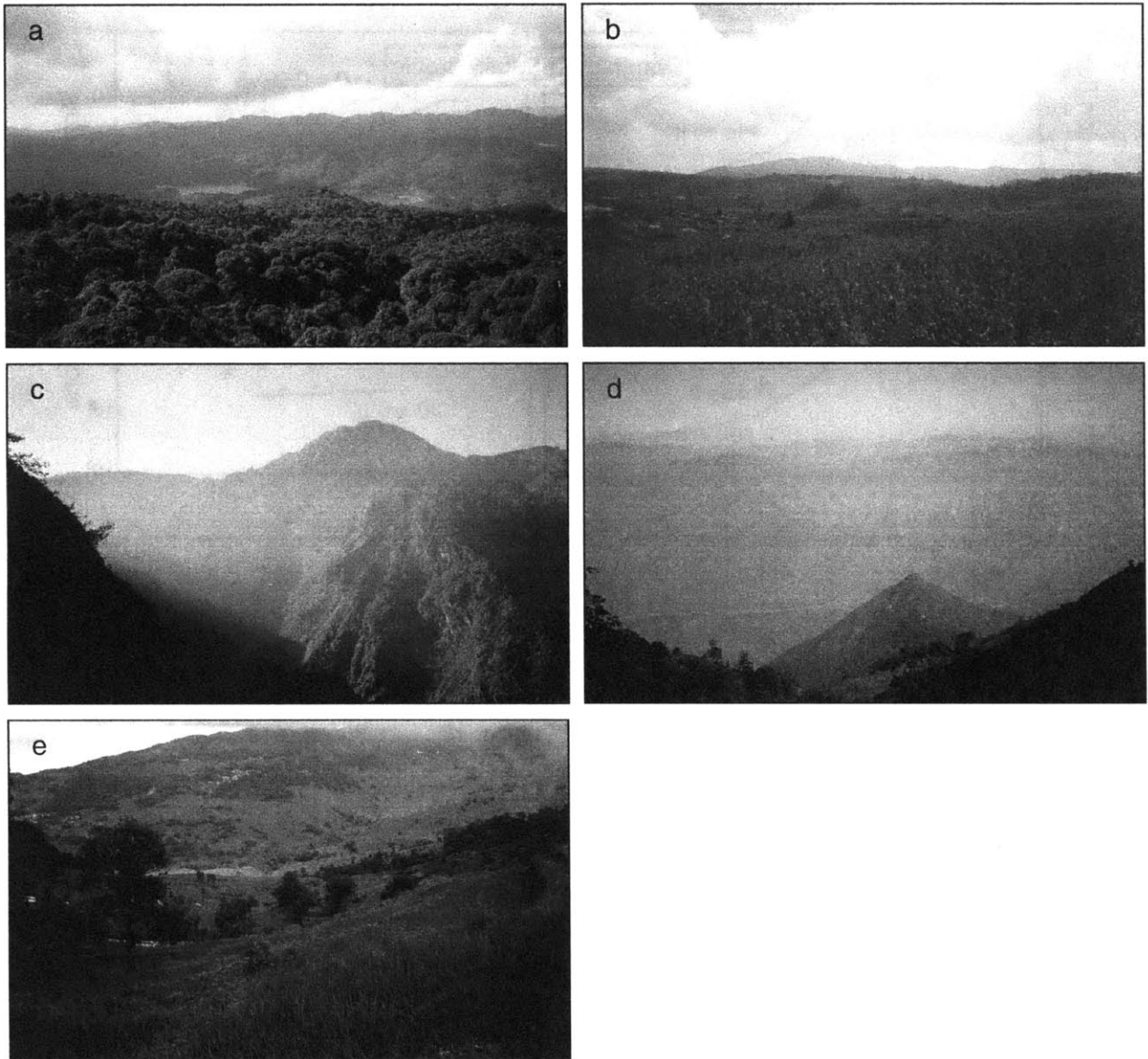


Figure 4. (a) Low-relief upland landscape developed on the Ailao Shan to the west of Ejia. Relief in photo is of the order ~200 m, view to the north. (b) Low-relief upland landscape on the Yunnan Plateau to the northeast of the Red River. (c) Deeply incised tributary to the Red River north of Ejia. Relief in photo is of the order ~1200 m. (d) View to the northeast over the Red River valley. Red River is the light colored sub-horizontal feature in the valley bottom. Photo taken from the low-relief upland landscape on the Ailao Shan, Yunnan Plateau can be seen in the far distance. (e) Intermediate valley system, below the low-relief upland landscape but perched above deeply incised lower channel.

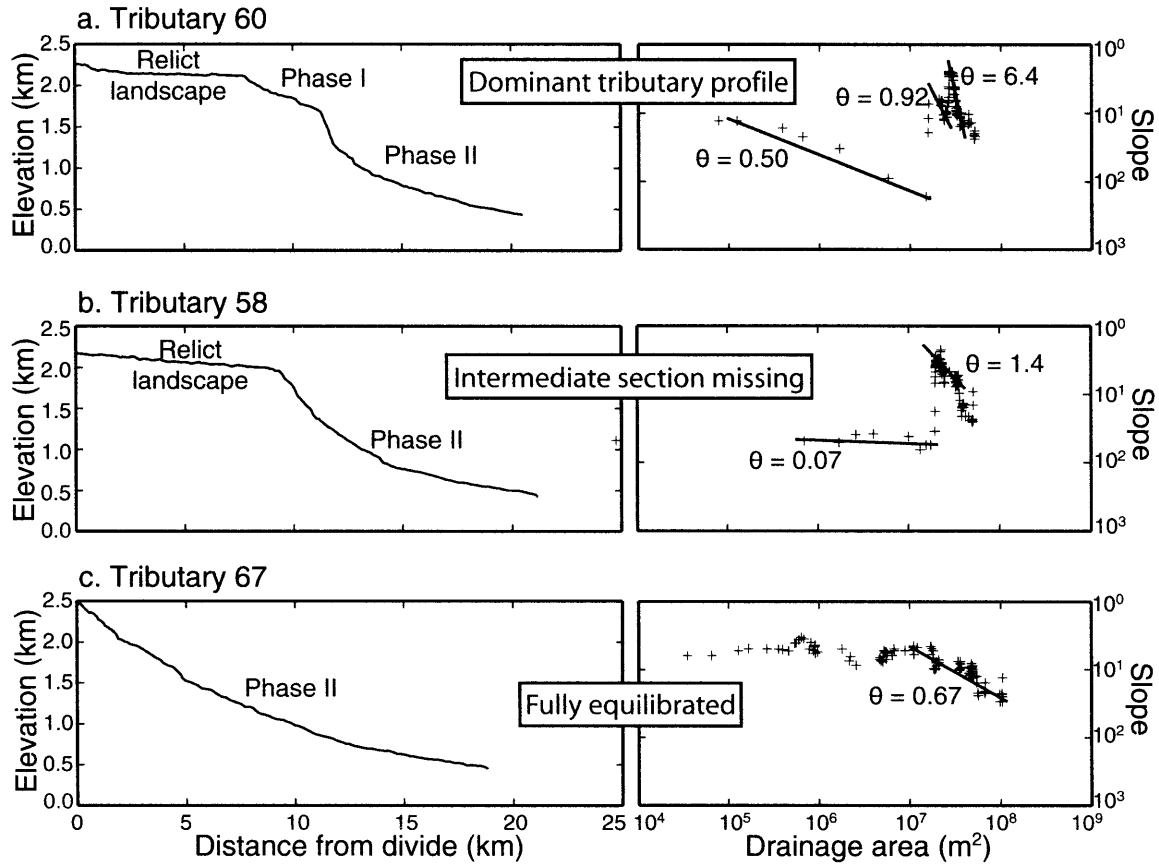


Figure 5. Longitudinal profiles and slope-area data extracted from 90 m DEM (see Fielding et al. (1994) for dataset details) for three representative tributaries, locations shown in Figure 2a. Best fit concavity, from Equation 1, is indicated on slope-area plots. (a) Tributary 60, an example of the 3-segment dominant tributary form. (b) Tributary 58, example in which the intermediate channel segment has been removed by headward erosion of lower segment. (c) Tributary 67, an example of a fully equilibrated channel with no major knickpoints.

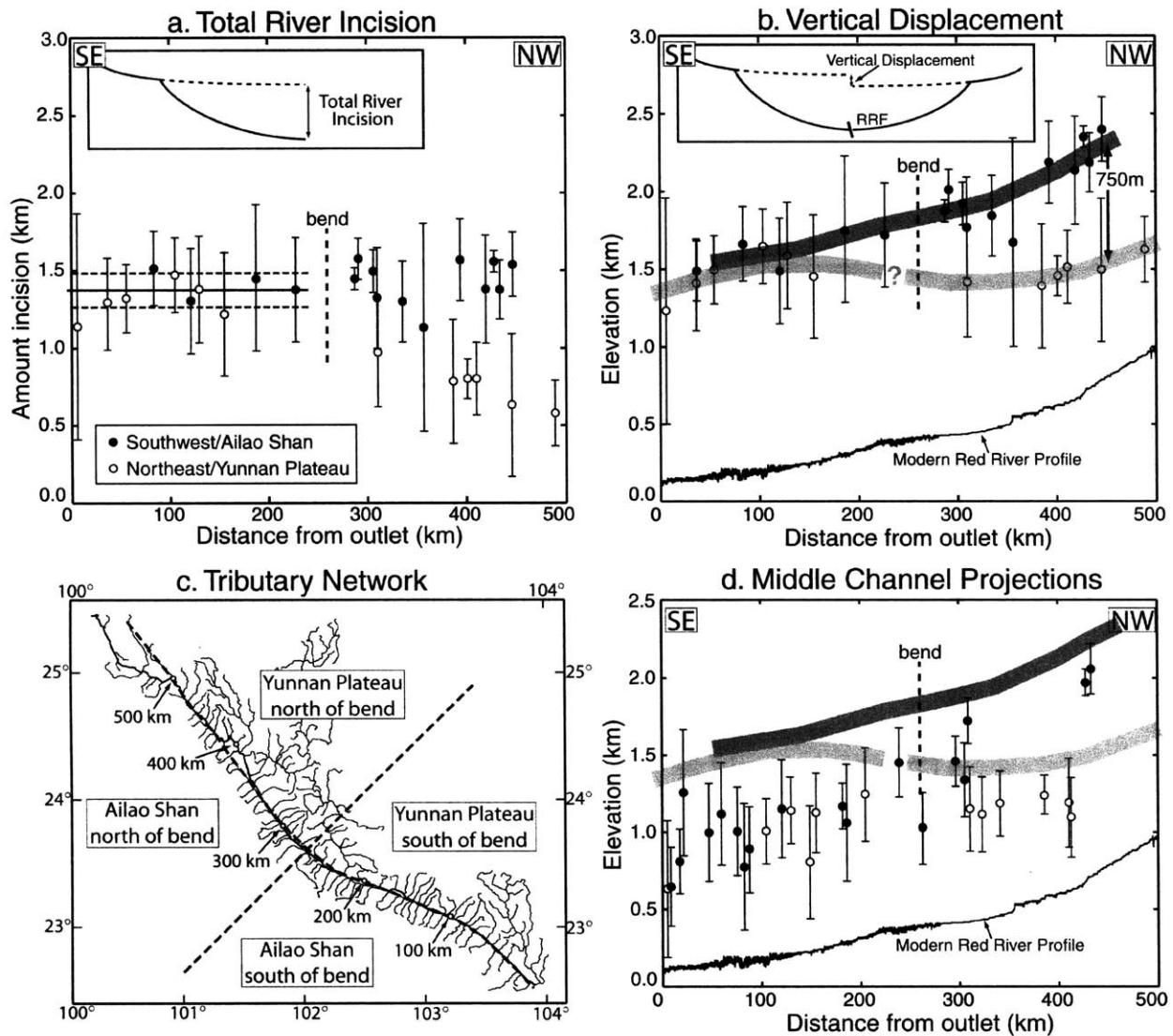


Figure 6. Projected channel segment data plotted against distance from the basin outlet near the Chinese-Vietnamese border, with the bend at approximately 260 km upstream from basin outlet. (a) River incision, calculated by projecting upper segments and subtracting modern river elevations (see inset). Regression of data south of bend shown at 1381 ± 88 m. (b) Projected upper segment elevations. Interpreted vertical displacement across the Red River fault (see inset) shown by thick lines. A maximum vertical displacement of ~750 m is recorded. Longitudinal profile of Red River also shown. (c) Approximate distances upstream from outlet and location of bend shown in relation to the Red River tributary network. (d) Projected middle segment elevations. Upper segment displacement lines and Red River longitudinal profile shown, same as for 6b. Incision is approximately two times greater from the middle to lower segments than from the upper to middle segments.

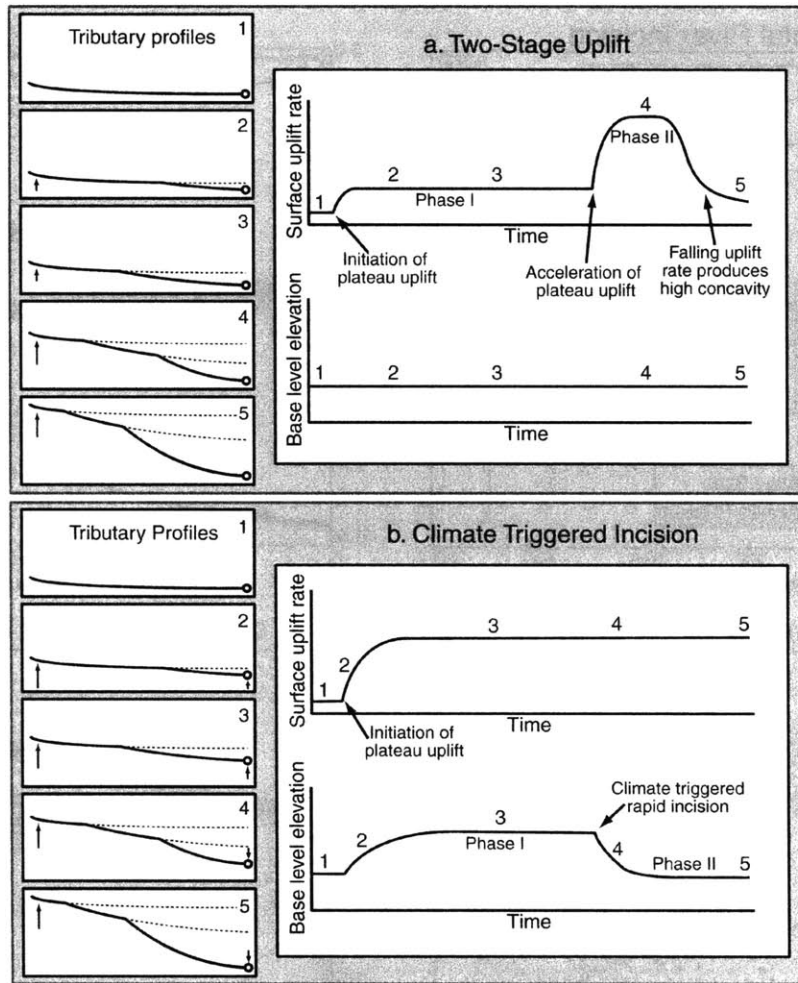


Figure 7: End-member scenarios resulting in two-phase incision. Time slices shown on left with numbers corresponding to positions along time axis on graphs on right. (a) Two stage-uplift history. In this scenario, tributary base level (therefore the profile of the main channel) is constant with time. Pulses in plateau growth are directly translated to tributary morphology. (b) Constant uplift rate with climate interactions. In this scenario, the main channel adjusts to plateau uplift by changing its gradient and therefore increasing local tributary base level (times 2 and 3). Rapid river incision is triggered, likely by climatic conditions, and the main channel returns to a lower gradient, causing tributary base level fall (times 4 and 5). Base level changes, against a background of constant uplift, result in the two-phase river incision.

APPENDIX

In this appendix, we expand our discussion of our methods for identifying and projecting channel segments. We extracted channel profiles for 97 tributaries to the Red River with drainage area $>40 \text{ km}^2$ from 90 m DEM data (Appendix Figs. 1 and 2, see Fielding et al., 1994 for dataset details). Channel segments were identified, and a concavity (θ) and normalized steepness (k_s) determined for each using methods developed by Snyder et al. (2000), Kirby and Whipple (2000) and Kirby et al. (2003). Concavity was determined by a linear best fit to slope-area data on a log-log plot over the drainage area corresponding to the channel segment. Because steepness index is highly correlated to concavity, a normalized steepness was determined over the same drainage area, but with a fixed concavity of 0.45. The actual value we use matters little, but this value is within the range of commonly reported concavities (Tucker and Whipple, 2002).

Channel segment categorization

Channel segments within each profile were then categorized as upper, middle or lower segments (Appendix Fig. 2 and Table 1). We used a number of criteria in this identification, including position along the channel, channel concavity and normalized steepness, and relationship to our field and DEM-based observations of the various landscape components.

Upper segments are consistently low in concavity (most in the range 0.2 to 0.6) and low in slope (most in the range 20 to 60), and of course always occur in the uppermost part of the tributary profile. Some channel segments which fit these criteria, however, were rejected because they corresponded to a region where, based on DEM analysis or field observation, the relict landscape has been removed. In such cases, these channel segments were categorized instead as middle segments.

Middle channel segments usually have a concavity less than 1 (for 89% of channel segments) and a normalized steepness index less than 150 (for 82% of channel segments). An upper channel segment may be present upstream of the middle segment and a lower channel segment is always present downstream. In many cases, we identified two middle channel segments which have slightly different channel parameters and are separated by an internal knickpoint. These internal knickpoints may reflect a wide range of factors, including, most importantly, lithology

and data noise, but given the regional coherence of the three-segment pattern and the relative consistency of channel parameters across these internal knickpoint, we do not think this causes difficulty for our overall analysis. In these cases, parameters for both segments are retained in Appendix Table 1 and for determination of mean parameters.

Lower channel segments must exist in every tributary profile. Concavity in these segments is usually greater than 1 (for 87% of channel segments) and normalized steepness is greater than 150 (for 94% of channel segments). We also observed a number of examples in which segments we categorize as lower channel segments are separated by an internal knickpoint. Again, we do believe this causes difficulty for our analysis.

In a number of channels (15), which we refer to as “fully equilibrated” channels, we observed no discernible knickpoints.

Channel segment projection

We were able to fit and project upper and middle channel segments for 28 and 30 profiles respectively (Appendix Table 2 and Fig. 3). Using mean concavity values of 0.38 for the upper segments and 0.64 for the lower segments, we obtained a linear best fit to the slope-drainage area data over a specified drainage area range corresponding to the channel segments (same as for determining steepness index with a fixed concavity, described above). Uncertainty was determined based on the standard deviation of slope and area data and propagated through the steepness index calculation. Using this steepness index, the input concavity and the drainage area data downstream of the channel segment, we projected the channel profile to its confluence with the Red River. We repeated this for the maximum and minimum steepness index values based on the steepness index uncertainty. Total incision, incision recorded by the upper channel segments (stage 1), incision recorded by the middle channel segments (stage 2) and the ratio of stage 2 to stage 1 incision are calculated (Appendix Table 2). All possible upper and middle channel segments were projected. Reasons for not projecting channels include: (1) insufficient data for a meaningful regression; (2) too much scatter in the data for a meaningful regression; (3) drainage area is too large, different processes may be operating on these channels compared to shorter

tributaries, and therefore comparison is inappropriate; or (4) there are multiple channel segments.

REFERENCES

- Fielding, E., Isacks, B., Barazangi, M., Duncan, C., 1994, How flat is Tibet?: *Geology*, v. 22, p. 163-167.
- Kirby, E., and Whipple, K.X., 2001, Quantifying differential rock-uplift rates via stream profile analysis: *Geology*, v. 29, p. 415-418.
- Kirby, E., Whipple, K.X., Tang W., and Chen Z., 2003, Distribution of active rock uplift along the eastern margin of the Tibetan Plateau: Inferences from bedrock channel longitudinal profiles, *Journal of Geophysical Research*, v. 108, doi:10.1029/2001JB000861.
- Snyder, N.P., Whipple, K.X., Tucker, G.E., and Merritts, D.J., 2000, Landscape response to tectonic forcing: DEM analysis of stream profiles in the Mendocino triple junction region, northern California: *Geological Society of America Bulletin*, v. 112, p. 1250-1263.
- Tucker, G.E., and Whipple, K.X., 2002, Topographic outcomes predicted by stream erosion models: Sensitivity analysis and intermodel comparison: *Journal of Geophysical Research*, v. 107, doi:10.1029/2001JB000162.

APPENDIX TABLE 1.
NORMALIZED STEEPNESS AND CONCAVITY VALUES, ALL
CHANNEL SEGMENTS

Tributary Number	Upper Concavity [†]	Upper Steepness [‡]	Middle Concavity	Middle Steepness	Lower Concavity	Lower Steepness	Channel location and type [§]
1 (u,m)	0.63	31	0.73	197	14.00	419	Yunnan Plateau
					4.20	273	
2 (m)			0.52	126	1.10	279	Ailao Shan
					9.10	162	
3 (m)			0.42	106	2.00	256	Ailao Shan
					10.00	164	
4 (m)			0.44	158	0.57	294	Ailao Shan
					2.50	302	
5 (u)	0.49	20	0.24	86	1.40	164	Yunnan Plateau
					2.80	201	
6 (u)	0.38	66			2.30	453	Ailao Shan
7			0.38	95	3.00	302	Yunnan Plateau
8 (m)			0.40	125			Ailao Shan
9 (u)	0.21	29	0.63	203			Yunnan Plateau
10 (m)			0.50	139	1.20	213	Ailao Shan
					1.70	301	
					1.40	293	
11			0.62	72	7.20	656	Yunnan Plateau
			0.88	160			
12 (m)			0.45	131	0.57	246	Ailao Shan
13					0.52	145	YP equilibrated
14			1.30	137	1.90	389	Yunnan Plateau
					1.60	201	
15 (u,m)	0.30	36	0.84	140	6.40	288	Ailao Shan
					2.10	293	
16			0.23	26	4.50	145	Yunnan Plateau
			0.73	93	7.90	313	
17 (m)			0.40	139			Ailao Shan
18			1.50	90	4.50	143	Yunnan Plateau
					3.20	515	
19			0.50	45	11.00	534	Yunnan Plateau
			1.00	164			
20			0.23	129	4.50	341	Ailao Shan
21 (u,m)	0.45	24			4.30	453	Yunnan Plateau
22					0.32	161	AS equilibrated
23			0.72	74	6.30	687	Yunnan Plateau
			1.40	141			
26			0.90	103	0.42	243	Ailao Shan
27 (u,m)	0.22	56	0.29	163	0.84	246	AS equilibrated
					2.20	241	
28			0.55	19	8.30	514	Yunnan Plateau
			0.74	97			
29 (u,m)	0.43	31	1.20	80	3.30	106	Yunnan Plateau
					3.80	465	

Chapter 4 Appendix- Surface uplift, exhumation, and plateau growth

Tributary Number	Upper Concavity [†]	Upper Steepness [‡]	Middle Concavity	Middle Steepness	Lower Concavity	Lower Steepness	Channel location and type [§]
30			0.26	67	1.50	318	AS equilibrated
			0.63	172	3.00	373	
31			0.37	61	2.60	252	Yunnan Plateau
			0.18	161			
32					0.73	213	AS equilibrated
33			0.20	46	0.18	183	Yunnan Plateau
			1.00	175			
34			0.34	124	5.70	186	Ailao Shan
			0.40	275			
35 (m)			0.39	118	1.50	205	Yunnan Plateau
36			0.40	106	2.10	179	Ailao Shan
			1.00	147			
37 (u,m)	0.17	41	1.00	99	2.20	309	Yunnan Plateau
					10.00	297	
38			0.72	63	3.50	414	Yunnan Plateau
			1.30	71			
39 (m)			0.32	51	0.93	312	Ailao Shan
40			1.20	80	2.70	479	Yunnan Plateau
			0.40	90			
41 (u,m)	0.43	23	1.00	107	3.00	438	Ailao Shan
42 (m)			1.50	141	8.90	667	Yunnan Plateau
43			0.44	59	2.30	325	Ailao Shan
			1.20	187			
44			0.53	85	0.37	102	Yunnan Plateau
45			0.47	52	4.30	375	Ailao Shan
			0.41	132			
46 (u)	0.27	18	0.39	107	2.70	334	Ailao Shan
47			0.32	59			Yunnan Plateau
			0.62	86			
48 (m)			0.70	64	4.00	277	Ailao Shan
49					1.70	160	Ailao Shan
50					0.45	149	NE equilibrated
51			0.18	98	1.80	123	Ailao Shan
			0.36	244			
52					0.63	190	NE equilibrated
53					0.57	102	AS equilibrated
54			0.53	50	23.00	305	AS
			0.23	144			
55 (m)			0.35	94	2.00	234	AS
56					0.51	163	YP equilibrated
57					0.48	142	YP equilibrated
58 (u)	0.07	21			1.40	473	AS two segment
59					0.40	95	YP equilibrated

Chapter 4 Appendix- Surface uplift, exhumation, and plateau growth

Tributary Number	Upper Concavity [†]	Upper Steepness [‡]	Middle Concavity	Middle Steepness	Lower Concavity	Lower Steepness	Channel location and type [§]
60 (u)	0.50	15	0.92	247	6.40	417	Ailao Shan
61 (m)			0.74	66	3.30	271	Ailao Shan
62					3.20	326	
63					0.52	111	YP equilibrated
64 (u,m)	0.56	26	1.10	125	4.30	496	Ailao Shan
65 (u,m)	0.91	45	0.80	70	5.20	608	Ailao Shan
66 (u,m)	0.30	32	0.30	93	0.97	169	Yunnan Plateau
67					0.67	243	AS equilibrated
68 (m)			0.70	90	1.80	159	Yunnan Plateau
69 (u)	0.30	46	0.52	101	4.20	457	Ailao Shan
70 (m)			0.50	86			Yunnan Plateau
71			0.46	68	5.50	593	Ailao Shan
72			0.25	135			
73			0.39	56	3.00	482	Ailao Shan
74 (u)	0.55	64	1.50	249			
75			0.69	71	5.60	362	Yunnan Plateau
76 (u,m)	0.28	29	0.19	130			
77			0.69	262	4.20	357	Ailao Shan
78 (u)	0.37	38	0.59	36			Yunnan Plateau
79 (u)	0.23	54	0.46	67	2.20	214	Yunnan Plateau
80 (u,m)	0.27	31	0.51	41	5.60	253	Yunnan Plateau
81 (m)					1.70	459	AS two segment
82 (u)	0.38	40	0.90	180	1.20	203	Yunnan Plateau
83 (u,m)	0.19	7	0.64	103	6.60	190	Yunnan Plateau
84 (u,m)	0.47	24	0.60	117	1.00	160	Yunnan Plateau
85					1.30	212	Yunnan Plateau
86					1.20	179	Yunnan Plateau
87 (u)	0.80	57					Ailao Shan
88 (u)	0.31	24	0.44	73	1.10	411	Ailao Shan
			0.86	60	1.60	300	Ailao Shan
			0.44	83	5.40	682	
			0.82	131	2.10	266	Yunnan Plateau
			0.28	44			
			1.30	95	6.60	535	Ailao Shan
			0.86	175			
			0.72	85	2.60	409	Yunnan Plateau
			0.40	131			
					0.73	281	AS two segment

Chapter 4 Appendix- Surface uplift, exhumation, and plateau growth

Tributary Number	Upper Concavity [†]	Upper Steepness [‡]	Middle Concavity	Middle Steepness	Lower Concavity	Lower Steepness	Channel location and type [§]
92					0.26	144	YP equilibrated
93			0.10	66	0.15	205	Yunnan Plateau
94					0.31	208	Ailao Shan
95			0.97	66			Yunnan Plateau
96					0.72	105	YP equilibrated
100			0.30	160	0.84	186	Ailao Shan
101 (u)	0.29	63	0.62	141	1.40	150	Yunnan Plateau
106			0.36	25	2.00	156	Ailao Shan
108			0.62	43	1.50	265	Ailao Shan
109			0.67	90			Ailao Shan
112			2.20	103	0.35	71	AS equilibrated

Note: See Figure DR1 for channel locations and Figure DR2 for tributary morphology. Tributaries for which upper segments are projected are marked with a u, and for which middle segments are projected are marked with an m. Projection data given in DR Table 2 and Figure DR3.

[†]Concavity determined by linear regression to selected slope-area data using a 20 m contour interval.

[‡]Normalized steepness index determined by linear regression to slope-area data but with a fixed concavity of 0.45.

[§] Channels to the southwest of the Red River are designated as “Ailao Shan” and channels to the northeast are “Yunnan Plateau.” Fully equilibrated channels (no internal knickpoints or segmentation) from the southwest are labeled “AS equilibrated” and from the northeast are “YP equilibrated.” Channels with a two segment morphology (upper and lower channels only) all four within the Ailao Shan, are labeled “AS two segment.”

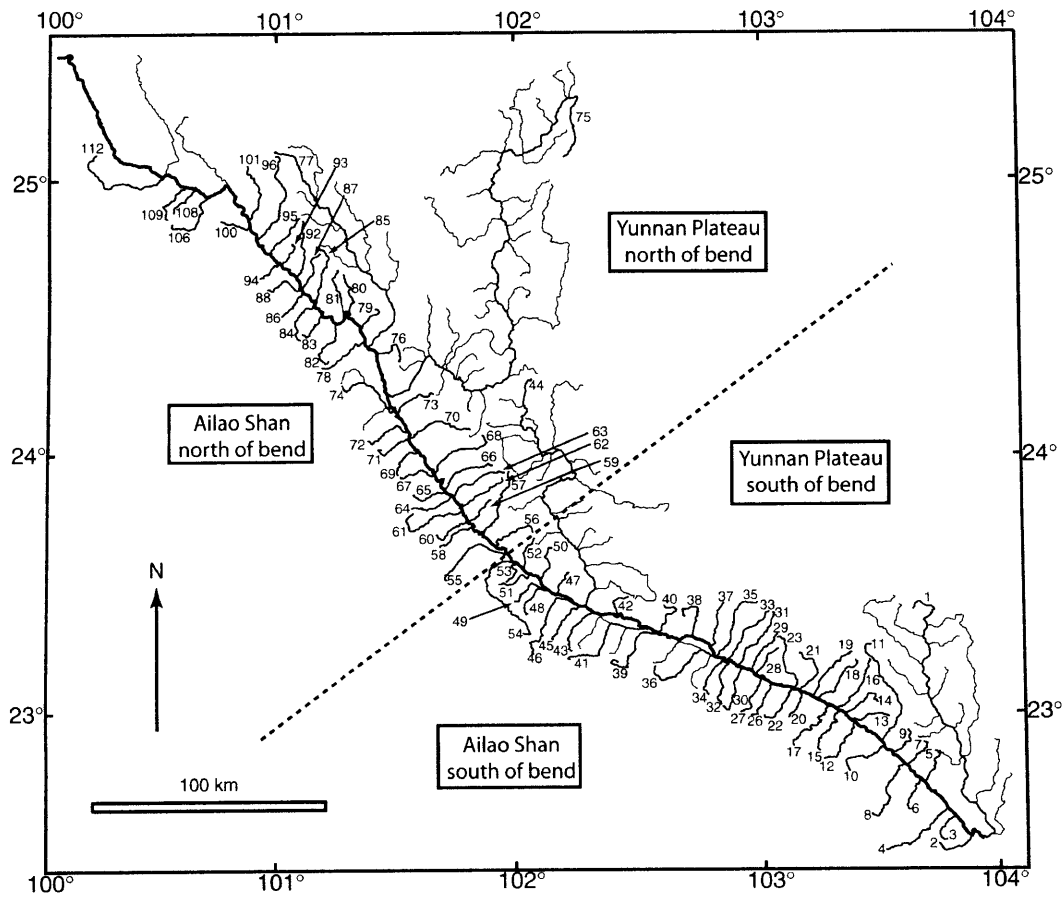
APPENDIX TABLE 2.
PROJECTED CHANNEL SEGMENT VALUES AND RIVER INCISION

Trib. number	River elev (m)	Upper proj. elev (m) [†]	Middle proj. elev (m) [‡]	Total incision (m)	1 st stage incision (m)	2 nd stage incision (m)	Incision ratio 2 nd :1 st stage	Channel location
1	91	1234 ± 732	631 ± 446	1143 ± 732	603 ± 857	540 ± 446	0.90 ± 0.74	Yunnan Plateau
5	110	1407 ± 299		1297 ± 299				Yunnan Plateau
6	108	1485 ± 201		1377 ± 201				Ailao Shan
9	172	1499 ± 228		1327 ± 228				Yunnan Plateau
15	146	1662 ± 240	780 ± 421	1516 ± 240	882 ± 485	634 ± 421	0.72 ± 0.48	Ailao Shan
21	183	1652 ± 239	1004 ± 211	1469 ± 239	648 ± 319	821 ± 211	1.27 ± 0.33	Yunnan Plateau
27	189	1490 ± 348	1154 ± 322	1301 ± 348	336 ± 474	965 ± 322	2.87 ± 0.96	Ailao Shan
29	207	1592 ± 343	1142 ± 213	1385 ± 343	450 ± 404	935 ± 213	2.08 ± 0.47	Yunnan Plateau
37	232	1453 ± 398	1126 ± 263	1221 ± 398	327 ± 477	894 ± 263	2.73 ± 0.80	Yunnan Plateau
41	301	1751 ± 472	1061 ± 384	1450 ± 472	690 ± 608	760 ± 384	1.10 ± 0.56	Ailao Shan
46	340	1721 ± 340		1381 ± 340				Ailao Shan
58	426	1876 ± 65		1450 ± 65				Ailao Shan
60	432	2012 ± 133		1580 ± 133				Ailao Shan
64	426	1924 ± 143	1335 ± 246	1498 ± 143	589 ± 285	909 ± 246	1.54 ± 0.42	Ailao Shan
65	441	1770 ± 322	1730 ± 141	1329 ± 322	40 ± 352	1289 ± 141	32.23 ± 3.55	Ailao Shan
66	435	1412 ± 355	1148 ± 270	977 ± 355	264 ± 446	713 ± 270	2.70 ± 1.02	Yunnan Plateau
69	541	1845 ± 261		1304 ± 261				Ailao Shan
74	541	1675 ± 679		1134 ± 679				Ailao Shan
76	605	1394 ± 408	1237 ± 130	789 ± 408	157 ± 428	632 ± 130	4.03 ± 0.83	Yunnan Plateau
78	619	2189 ± 267		1570 ± 267				Ailao Shan
79	653	1459 ± 139		806 ± 139				Yunnan Plateau
80	710	1517 ± 244	1190 ± 288	807 ± 244	327 ± 377	480 ± 288	1.47 ± 0.88	Yunnan Plateau
82	752	2136 ± 348		1384 ± 348				Ailao Shan
83	792	2352 ± 64	1968 ± 79	1560 ± 64	384 ± 102	1176 ± 79	3.06 ± 0.21	Ailao Shan
84	806	2187 ± 195	2053 ± 162	1381 ± 195	134 ± 254	1247 ± 162	9.31 ± 1.21	Ailao Shan
87	855	1496 ± 468		641 ± 468				Yunnan Plateau
88	860	2401 ± 216		1541 ± 216				Ailao Shan
101	1046	1629 ± 225		583 ± 225				Yunnan Plateau

Note: Errors are 1 sigma, calculated for projections as described in data repository text and propagated through incision and incision ratio determinations. See Figure DR1 for channel locations and Figure DR3 for channel morphology.

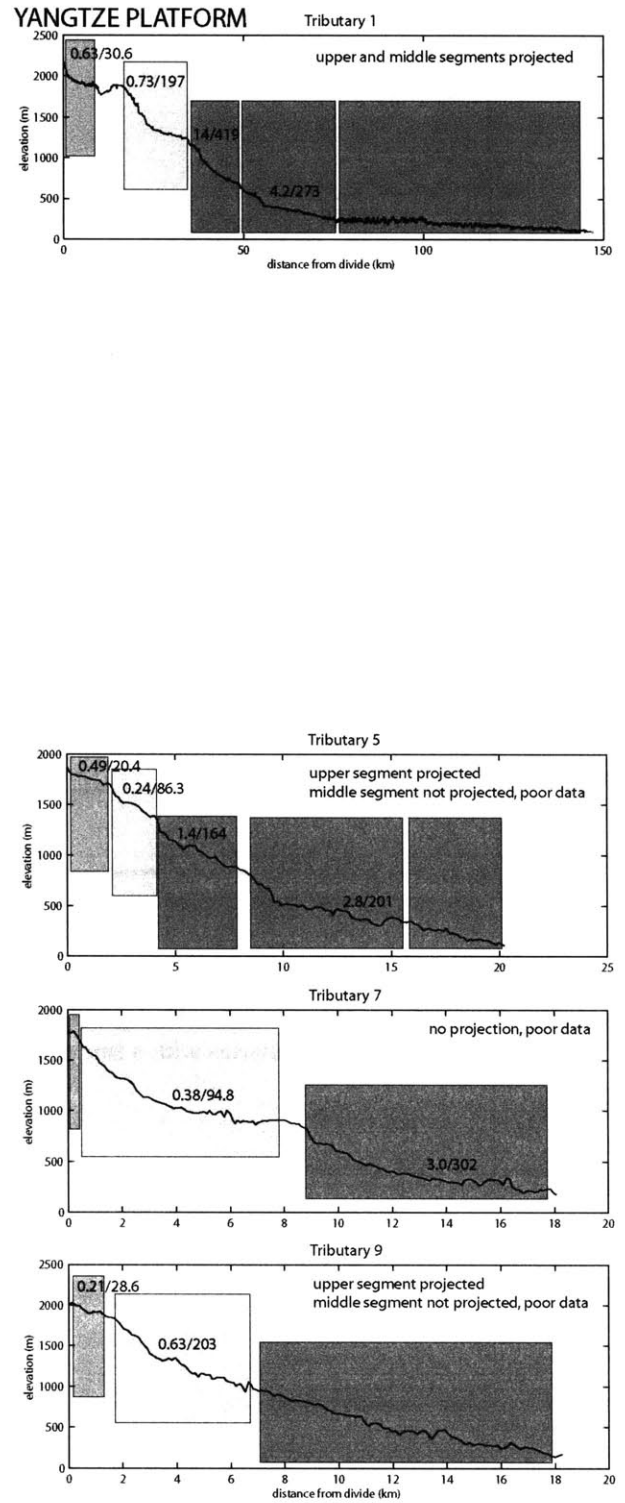
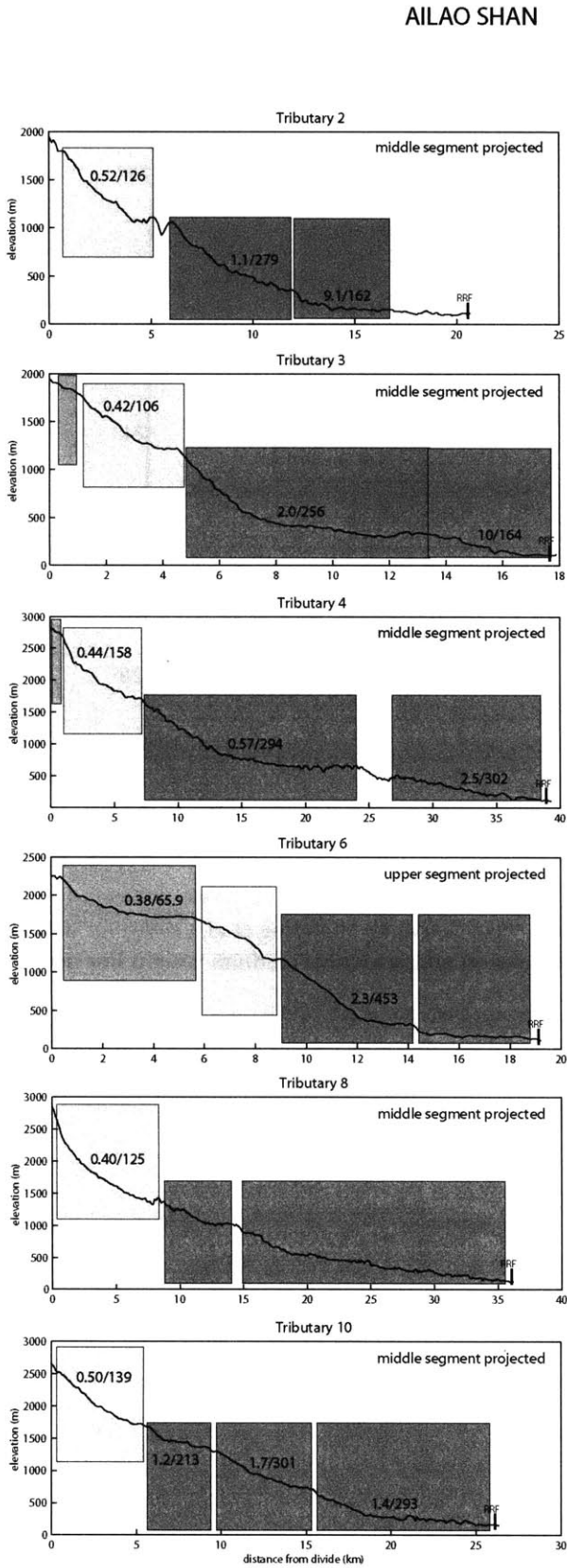
[†]Elevation at projected upper channel segment at intersection with Red River.

[‡]Elevation of projected middle channel segment at intersection with Red River.



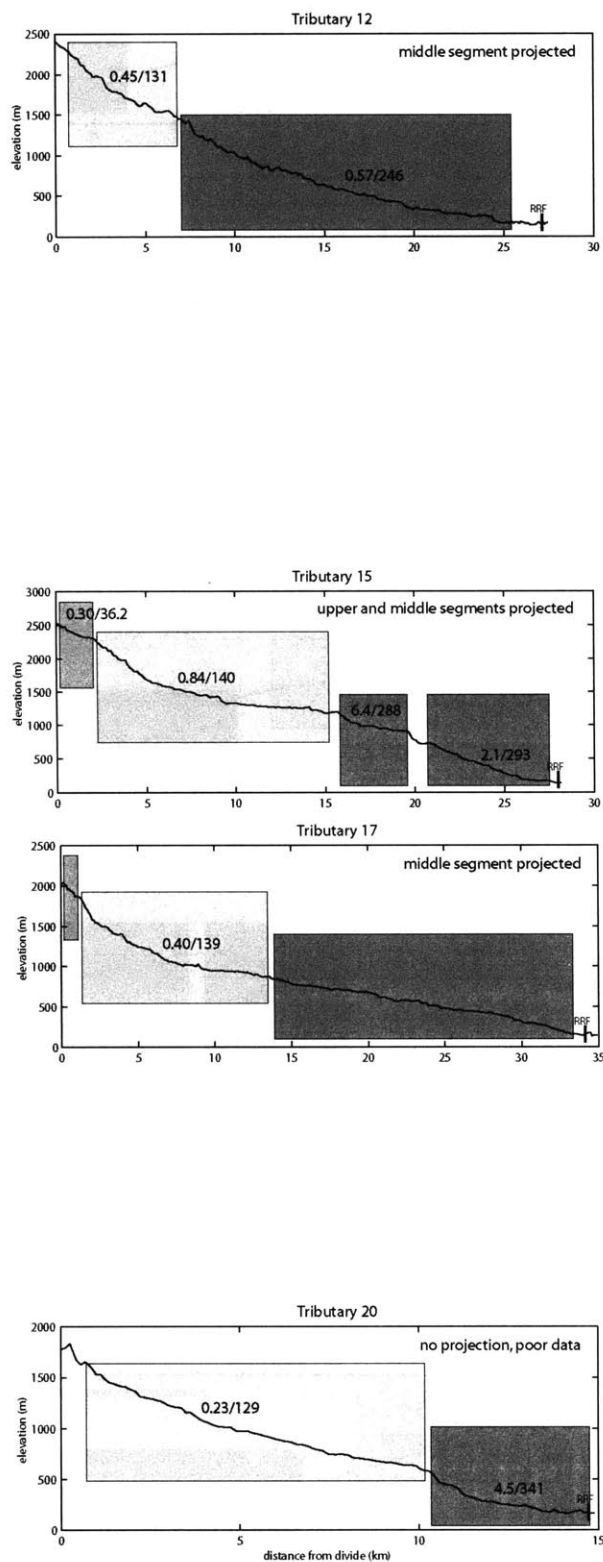
Appendix Figure 1. Red River drainage network derived from 90 m DEM (see Fielding et al. (1994) for dataset details). Trunk channel shown with a heavy weight line, analyzed tributaries with a medium weight line and additional, non-analyzed tributaries with a fine weight line.

Chapter 4 Appendix- Surface uplift, exhumation, and plateau growth

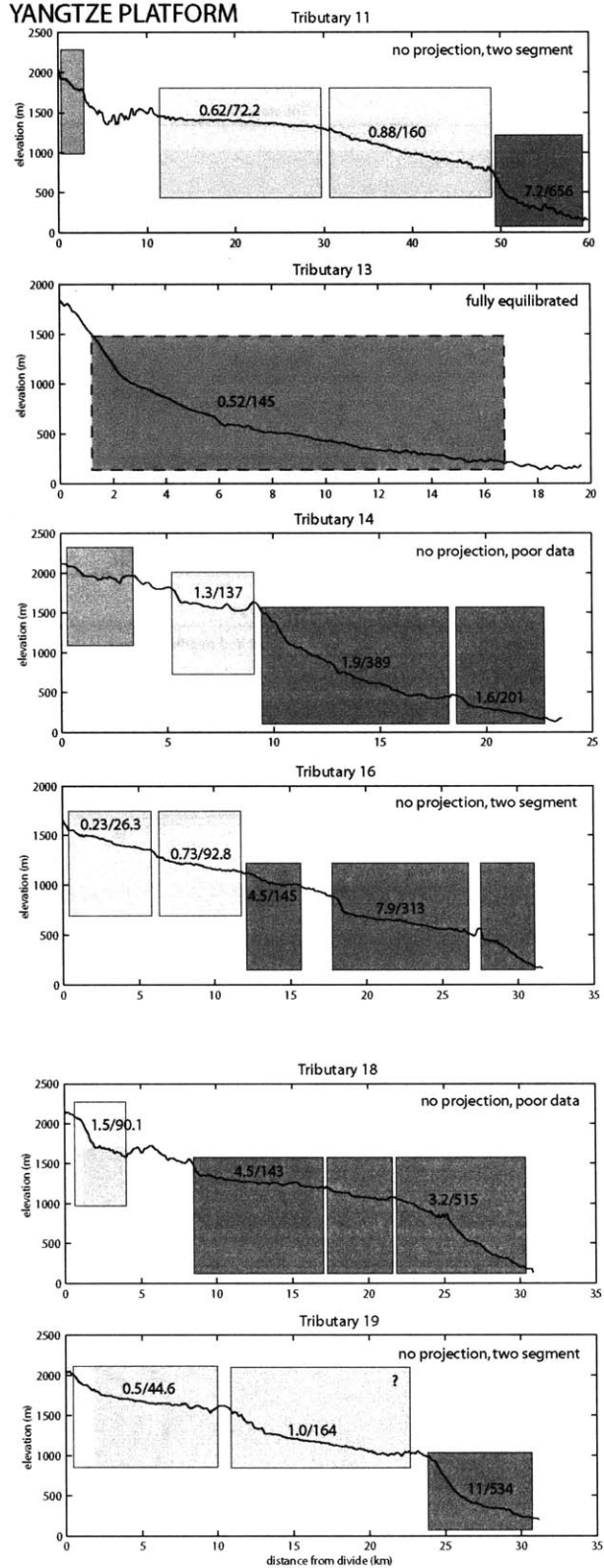


Appendix Figure 2.1. Caption on Fig. 2.10

AILAO SHAN

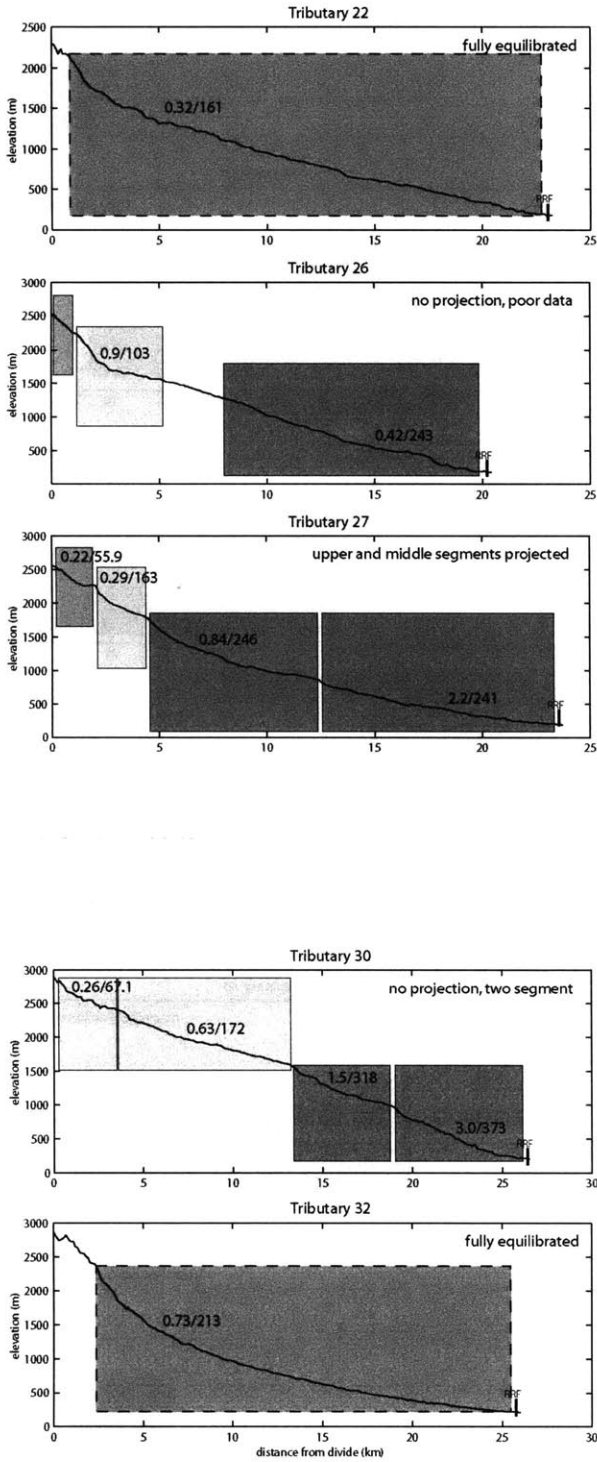


YANGTZE PLATFORM

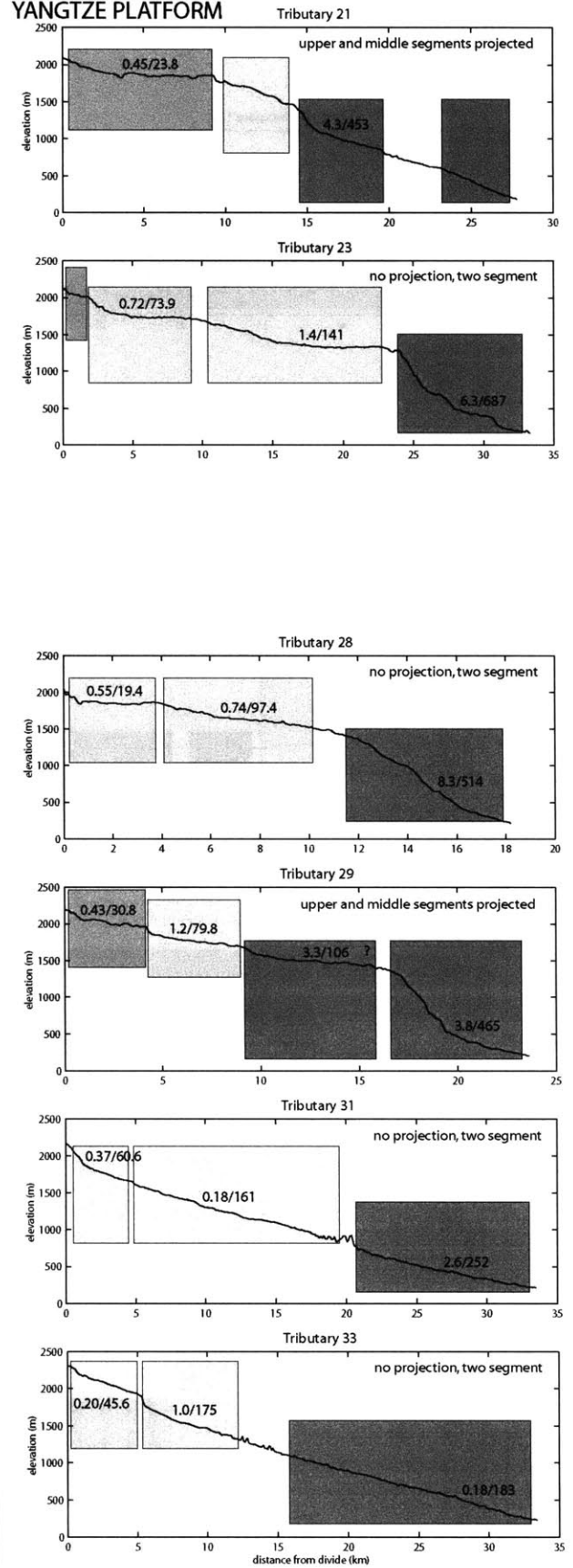


Appendix Figure 2.2. Caption on Fig. 2.10

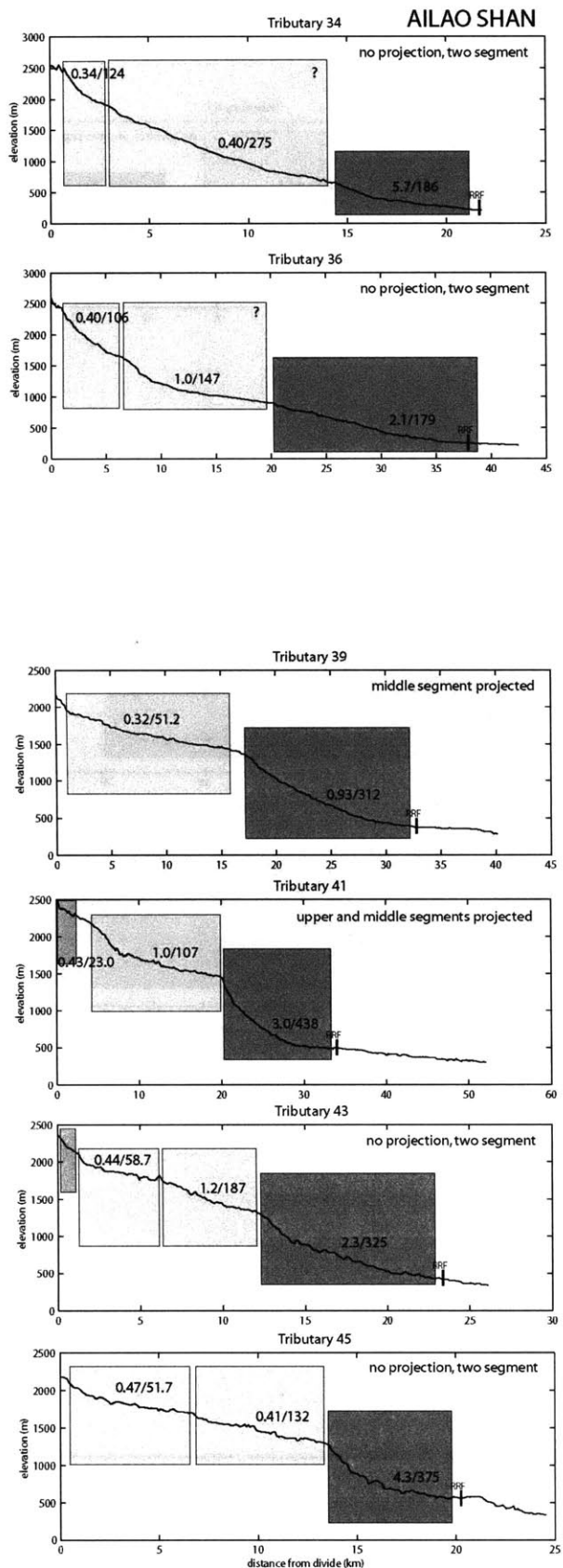
AILAO SHAN



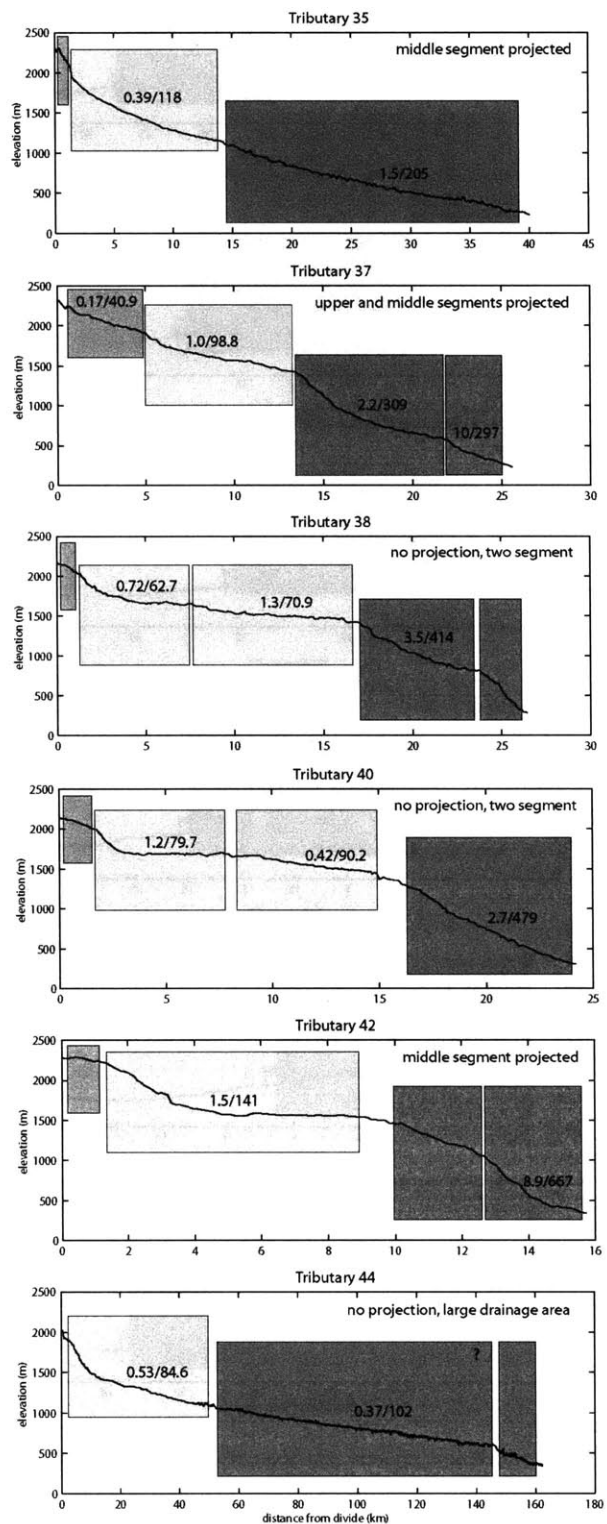
YANGTZE PLATFORM



Appendix Figure 2.3. Caption on Fig. 2.10

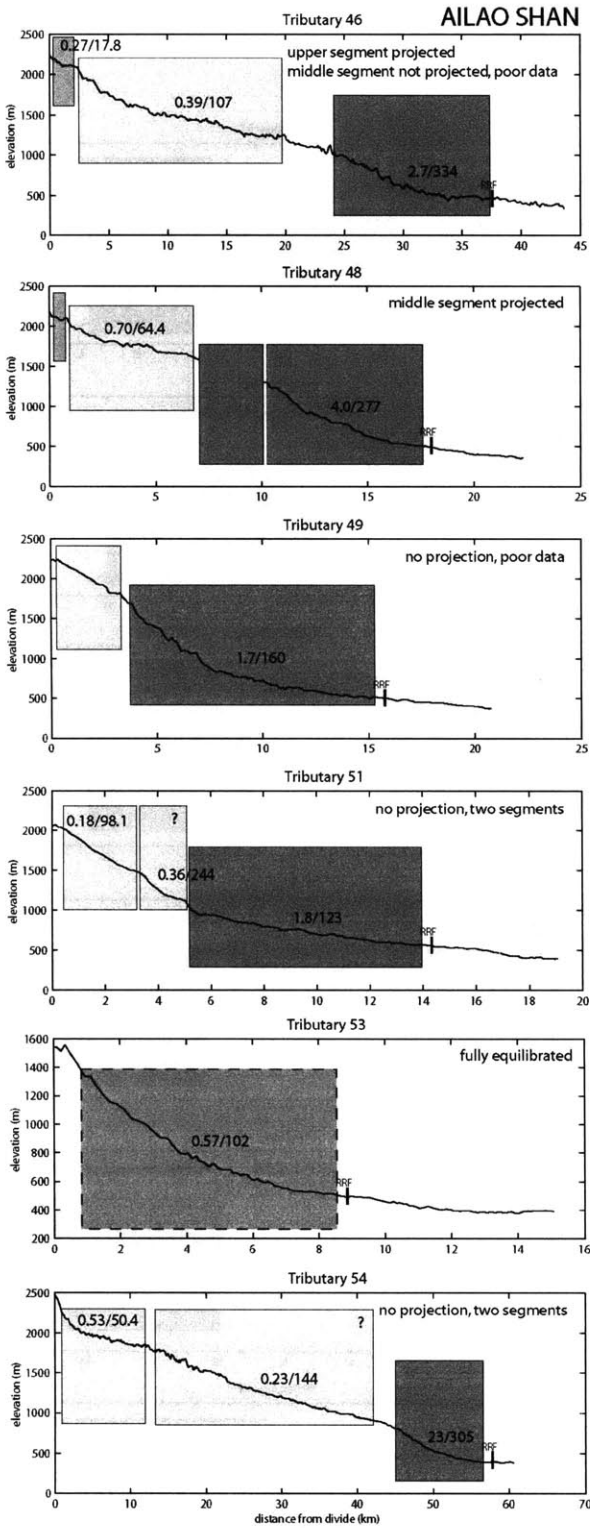


YANGTZE PLATFORM

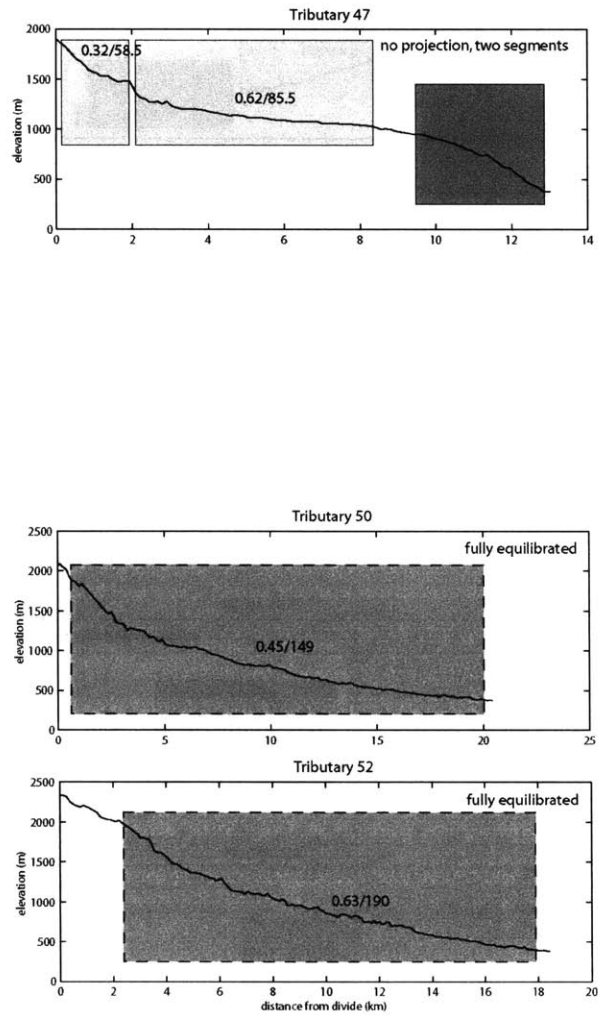


Appendix Figure 2.4. Caption on Fig. 2.10

Chapter 4 Appendix- Surface uplift, exhumation, and plateau growth

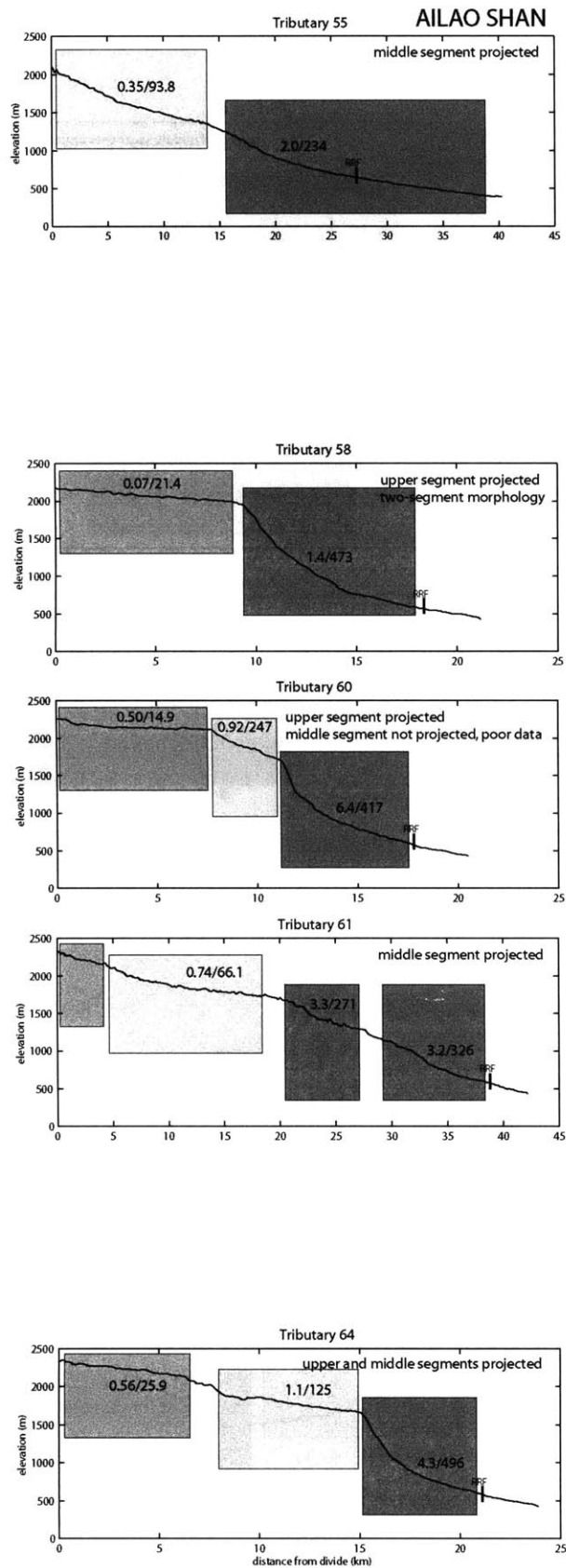


YANGTZE PLATFORM



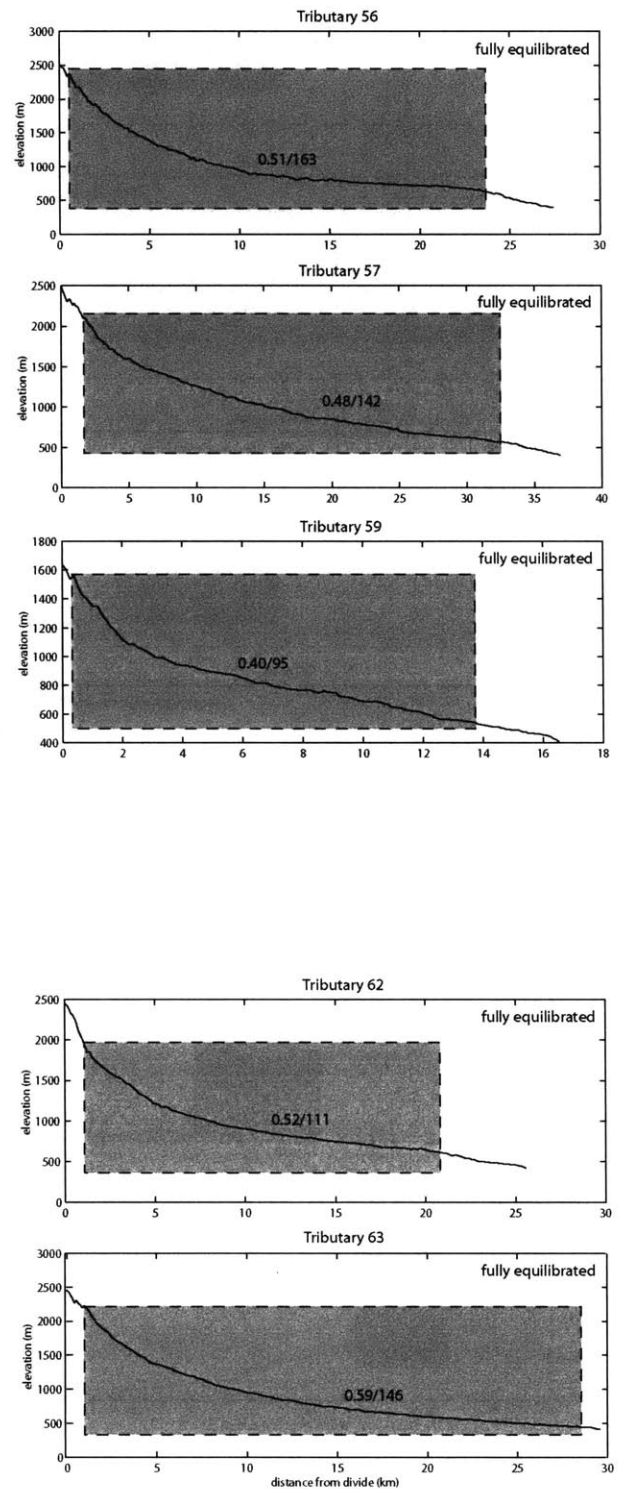
BEND

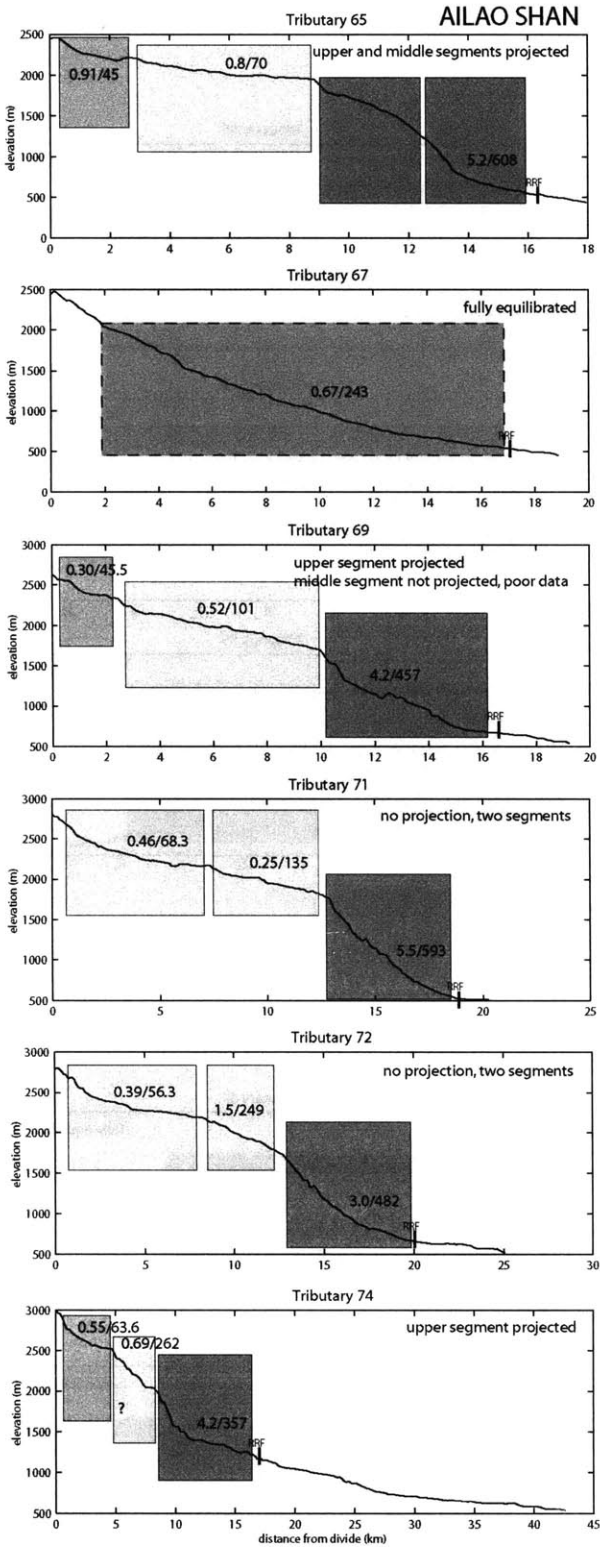
Appendix Figure 2.5. Caption on Fig. 2.10



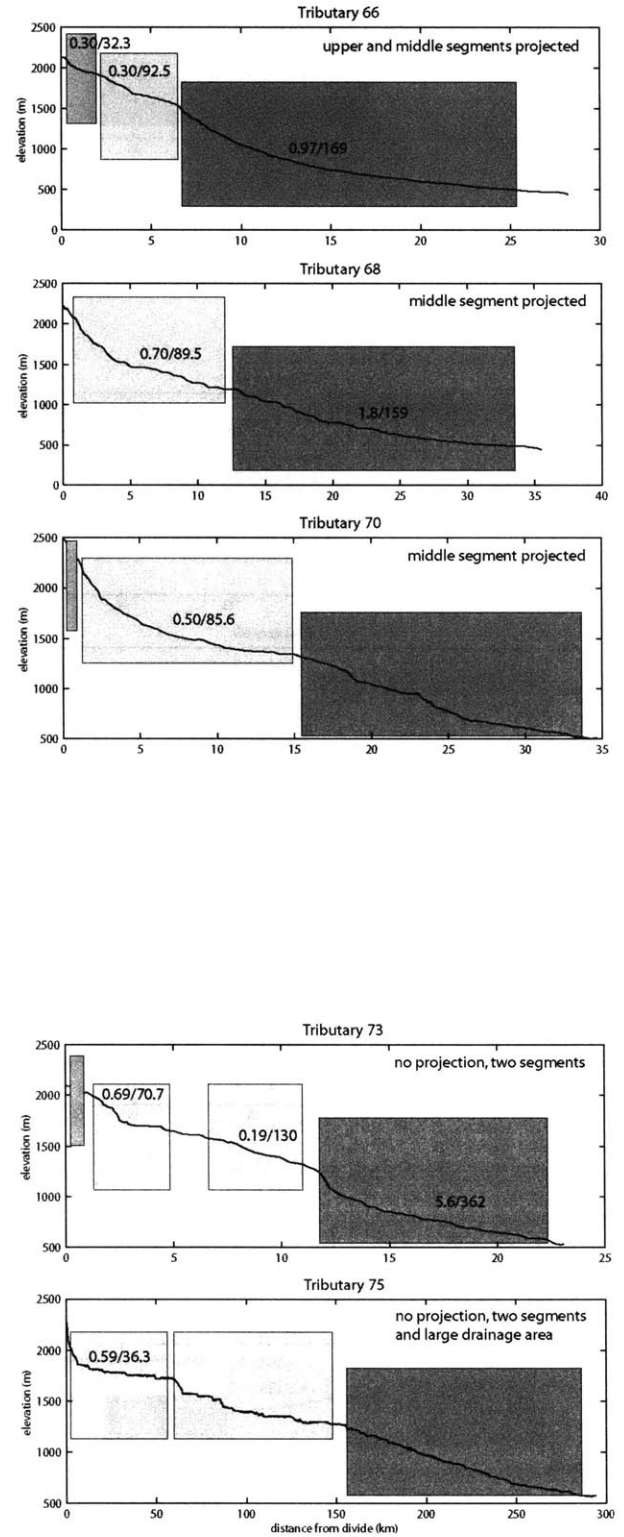
Appendix Figure 2.6. Caption on Fig. 2.10

YANGTZE PLATFORM



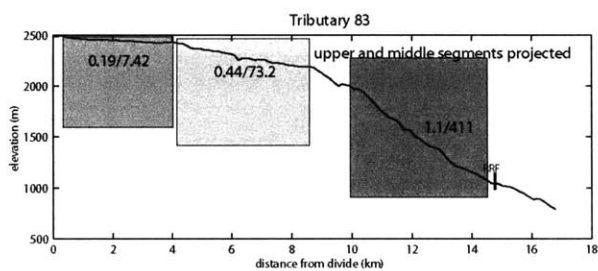
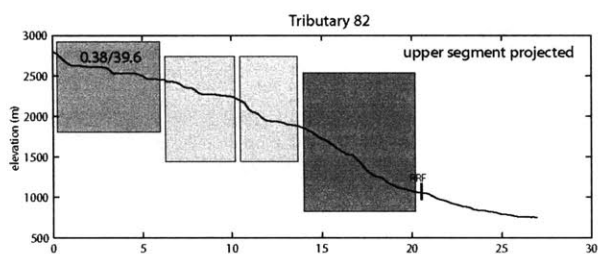
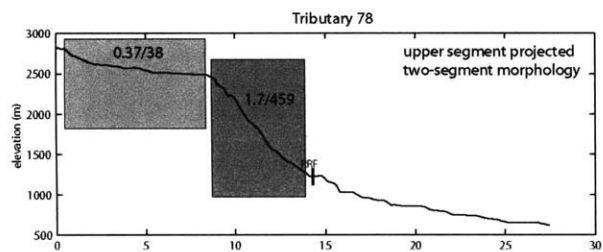


YANGTZE PLATFORM

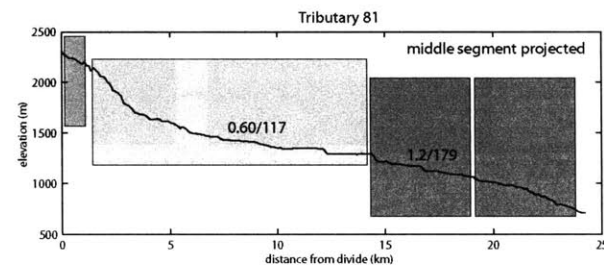
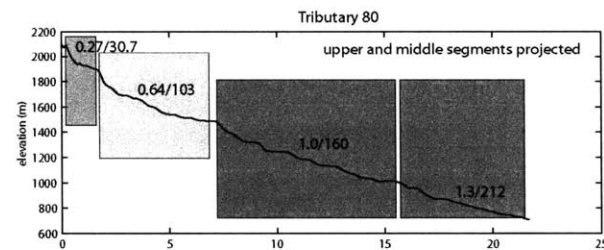
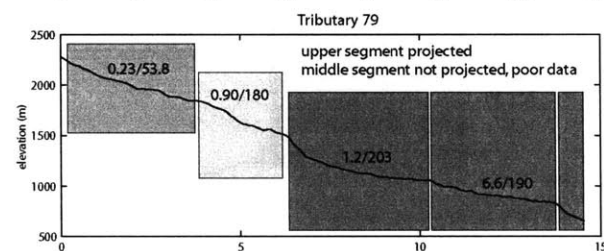
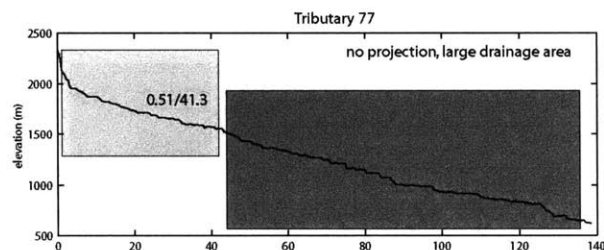
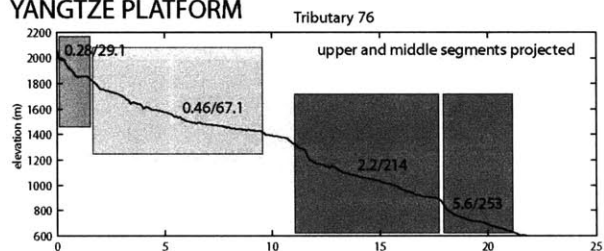


Appendix Figure 2.7. Caption on Fig. 2.10

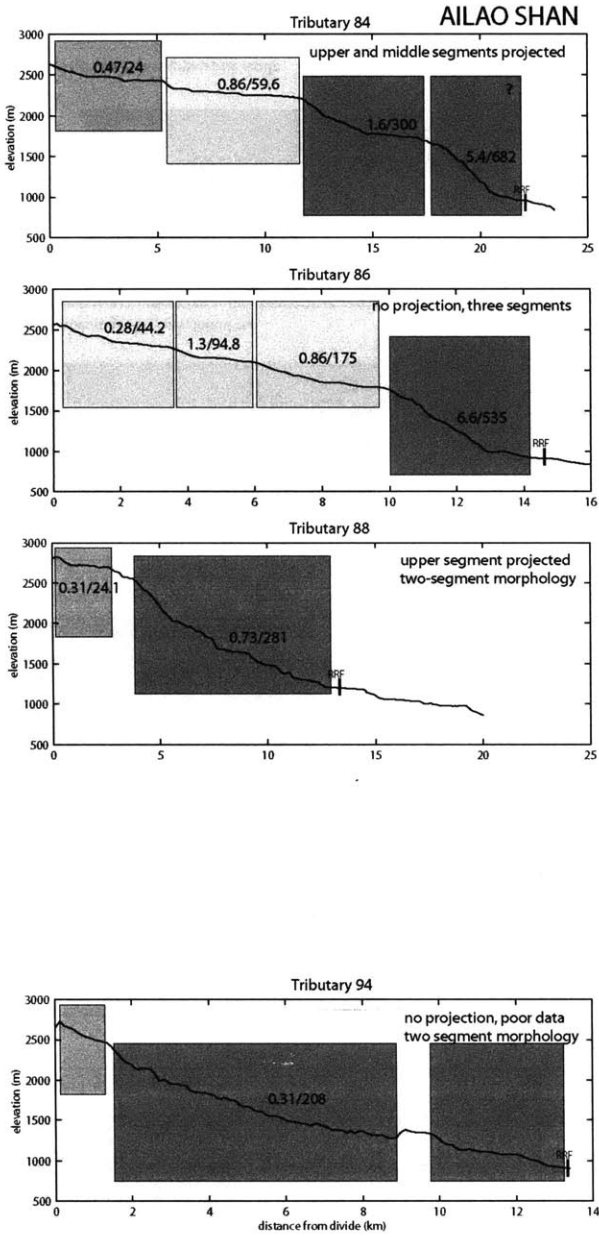
AILAO SHAN



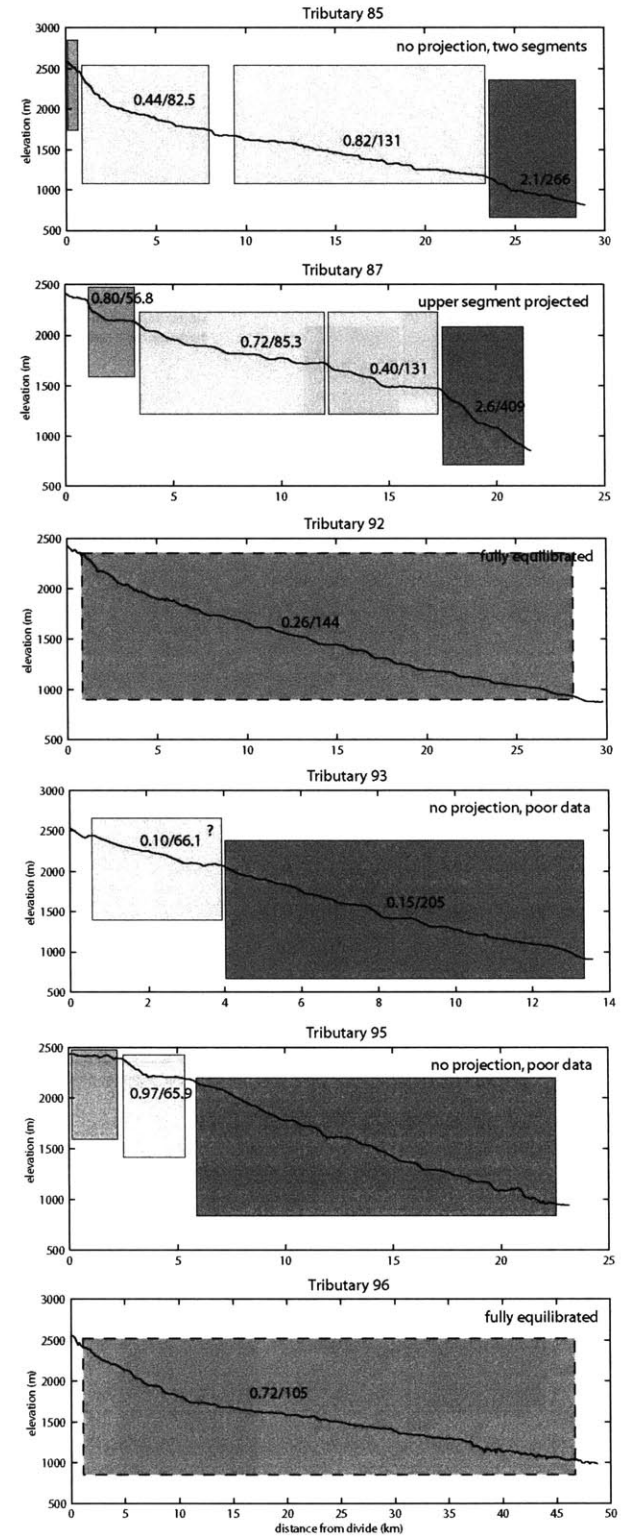
YANGTZE PLATFORM



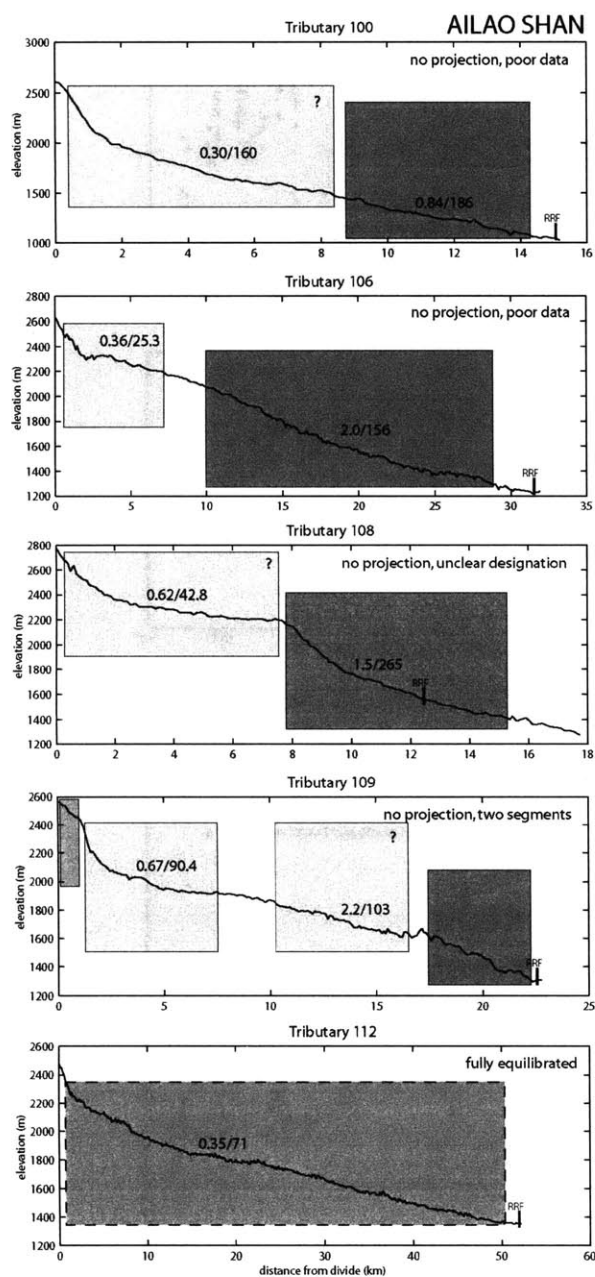
Appendix Figure 2.8. Caption on Fig. 2.10



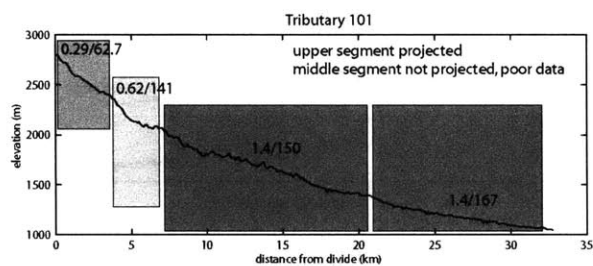
YANGTZE PLATFORM



Appendix Figure 2.9. Caption on Fig. 2.10

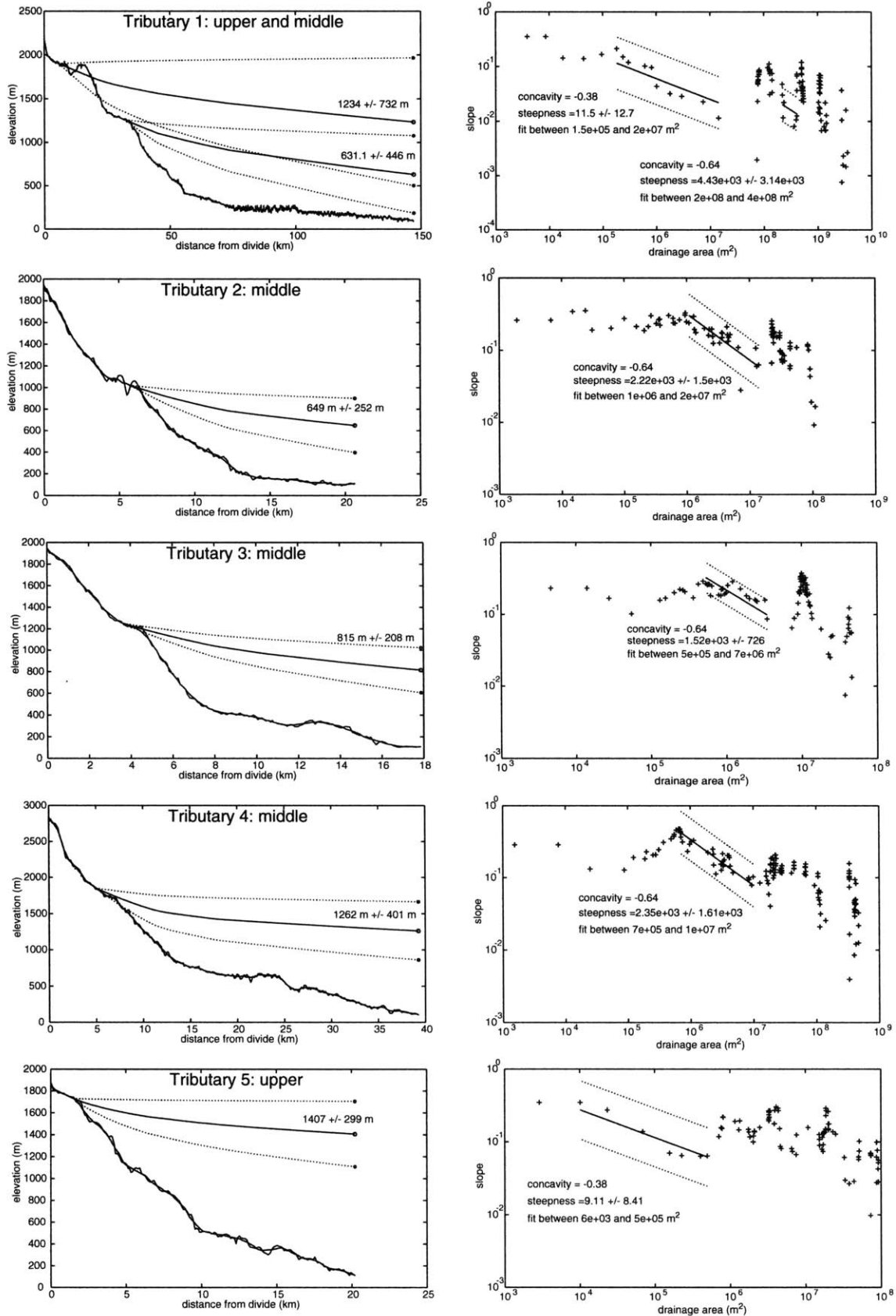


YANGTZE PLATFORM



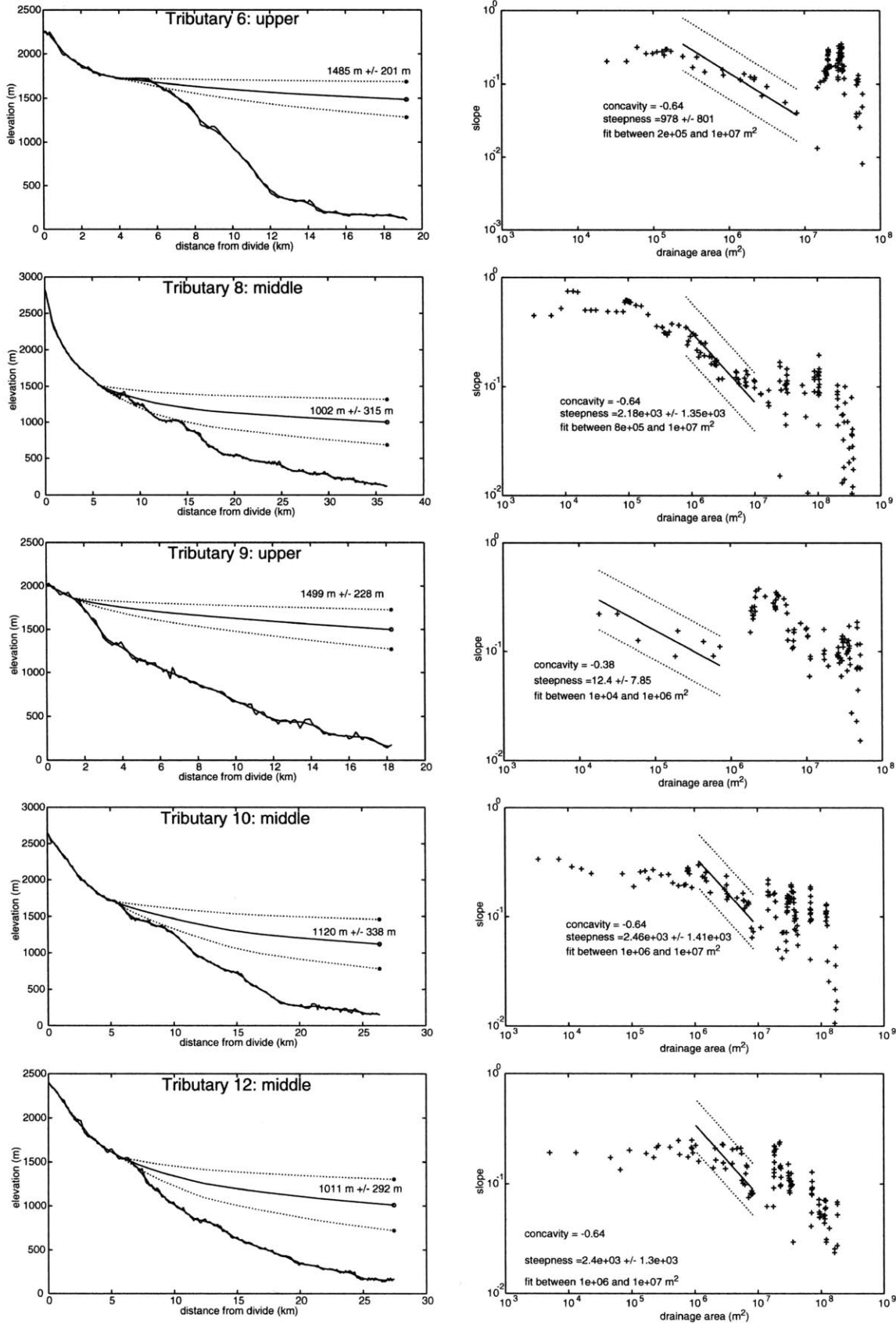
Appendix Figure 2.10. Longitudinal profiles for 97 tributaries to the Red River in China, tributary locations shown in Appendix Figure 1. Channel segment categorization is indicated by colored boxes, with medium gray for upper channel segments, light gray for middle channel segments and dark gray for lower channel segments. Fully equilibrated channels are indicated with a medium dark gray box with a dashed border. Numbers within each box indicate the concavity and the normalized steepness index (separated by a slash) for each channel segment. This data is tabulated in Appendix Table 1. Channel segment boxes without steepness index or concavity values correspond to cases in which the channel segment was too short and therefore contained too few data points for a meaningful regression, or cases in which there was too much scatter in the data for a meaningful regression. Tributaries are labeled if they are fully equilibrated, if they are of the two-segment morphology, or if a channel segment is projected. If an appropriate channel segment is not projected, the reason is given in the label. See text for further explanation. Tributaries are arranged roughly according to upstream distance with Ailao Shan tributaries on the left hand side of the figure and Yangtze Plateau tributaries on the right hand side. Position of the Red River fault marked on Ailao Shan tributaries. Bend in the Red River fault occurs approximately between tributaries 54 and 55.

Chapter 4 Appendix- Surface uplift, exhumation, and plateau growth



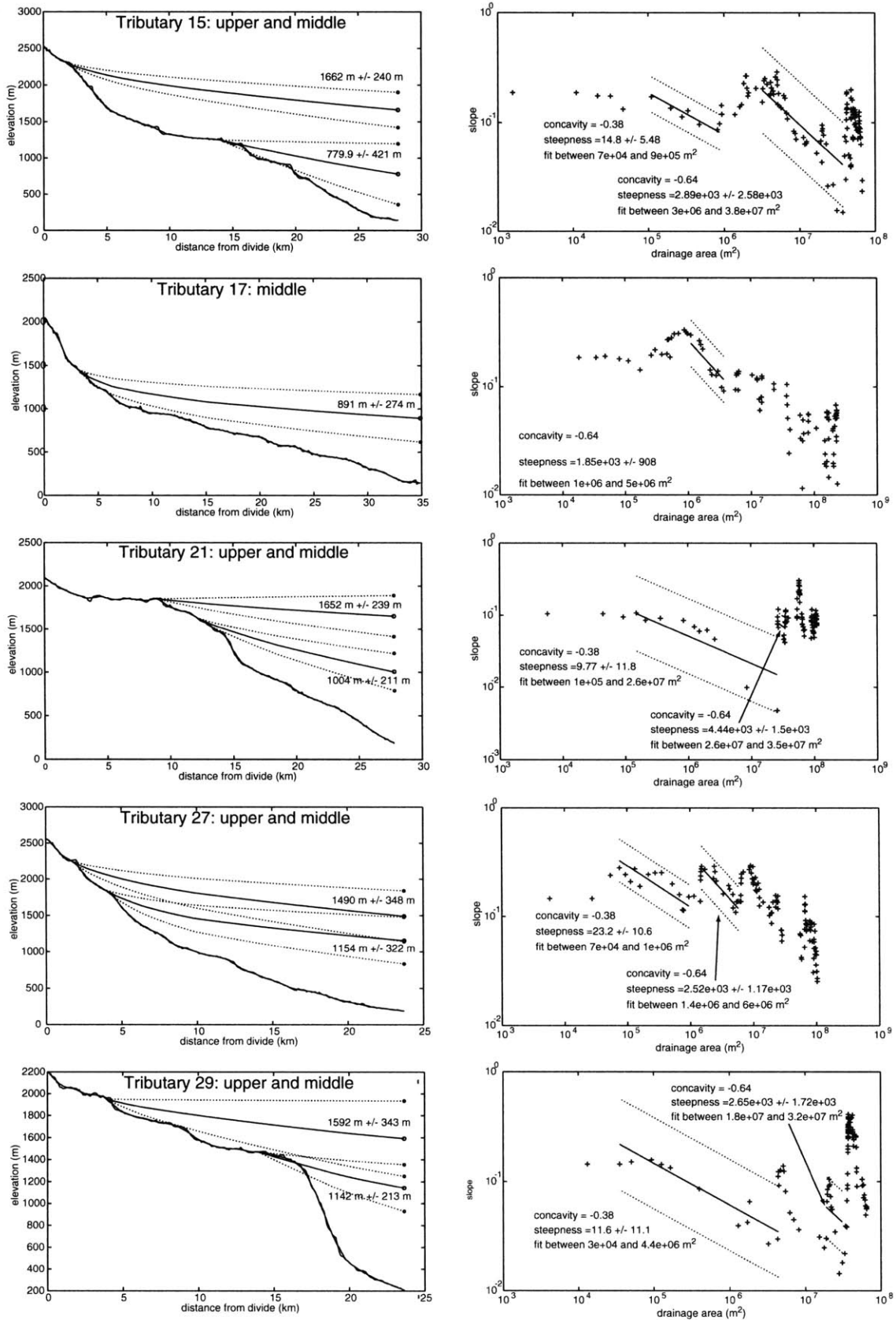
Appendix Figure 3.1. Caption on Fig. 3.9

Chapter 4 Appendix- Surface uplift, exhumation, and plateau growth



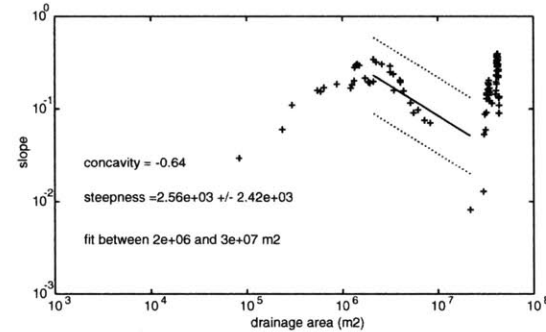
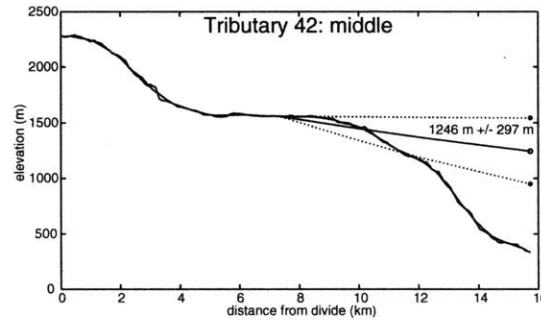
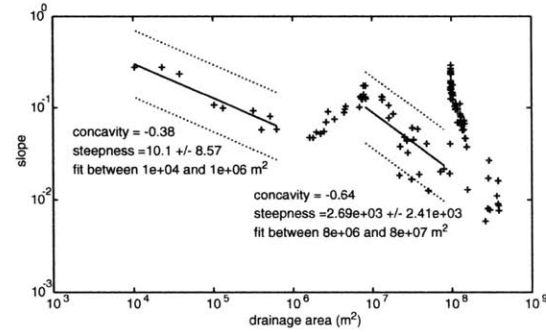
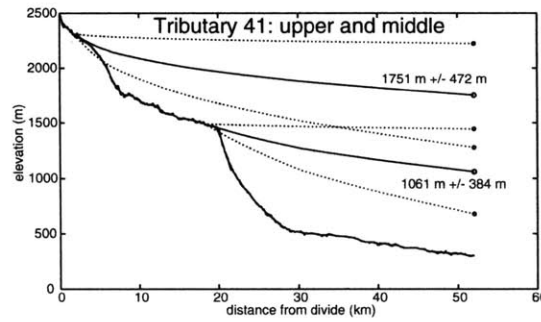
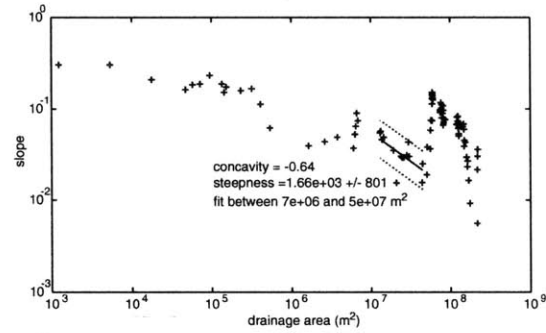
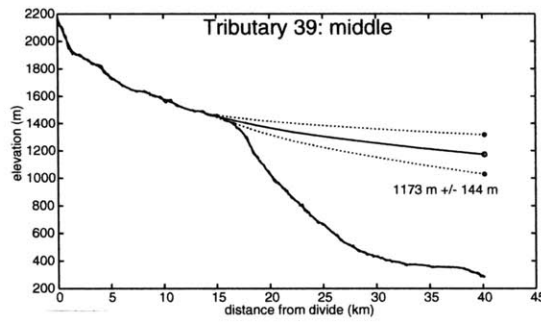
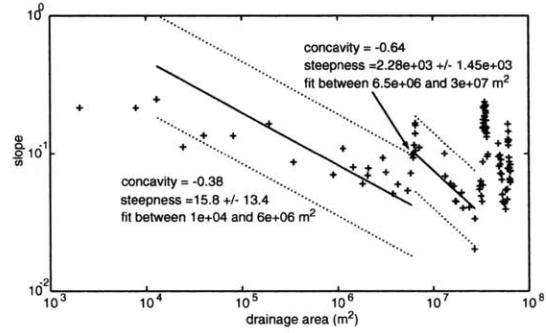
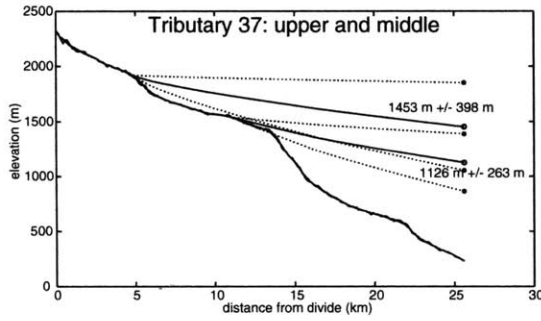
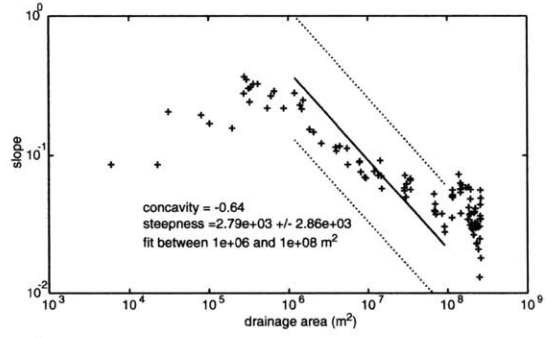
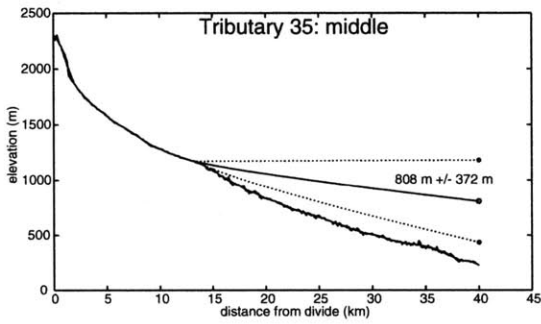
Appendix Figure 3.2. Caption on Fig. 3.9

Chapter 4 Appendix- Surface uplift, exhumation, and plateau growth



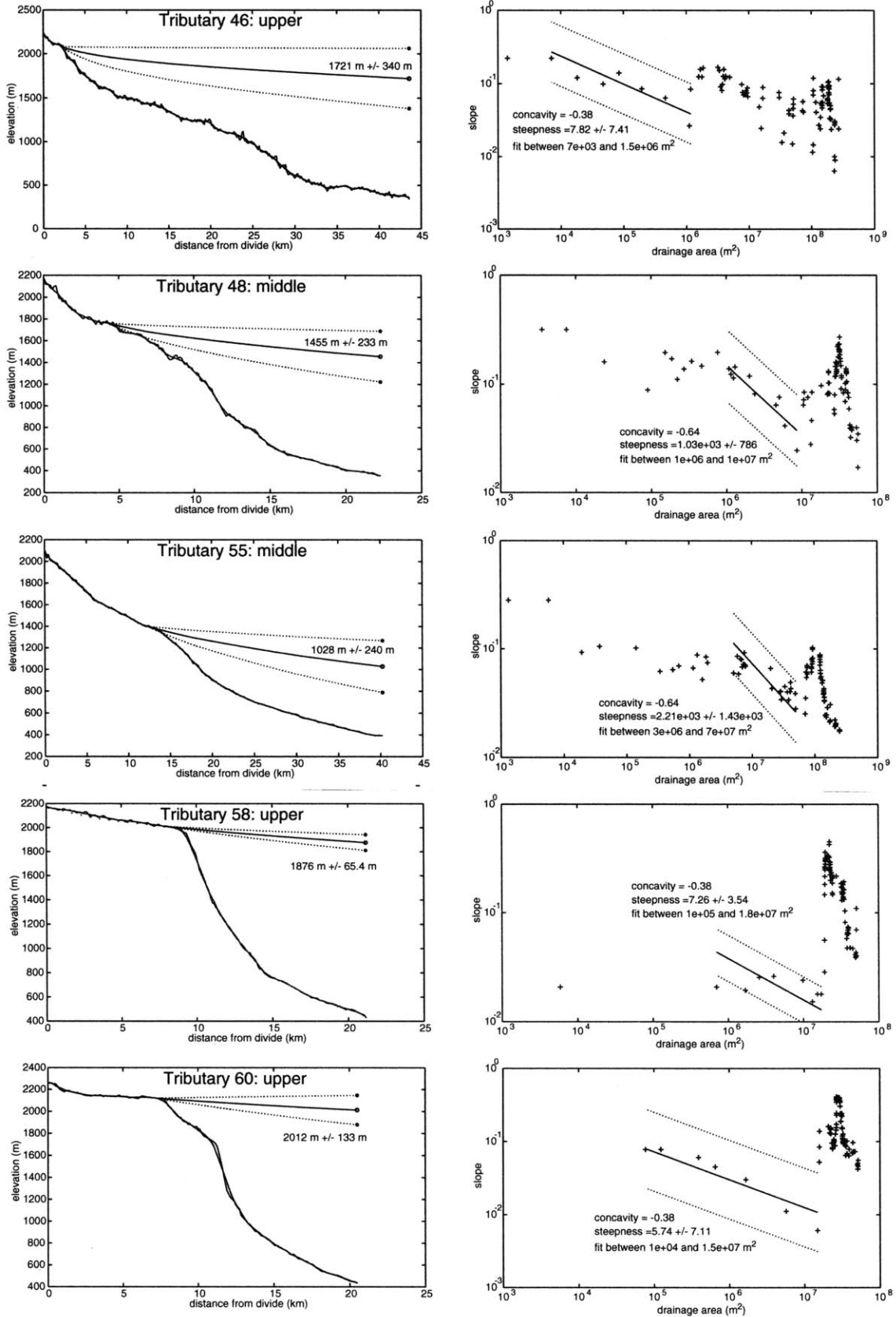
Appendix Figure 3.3. Caption on Fig. 3.9

Chapter 4 Appendix- Surface uplift, exhumation, and plateau growth

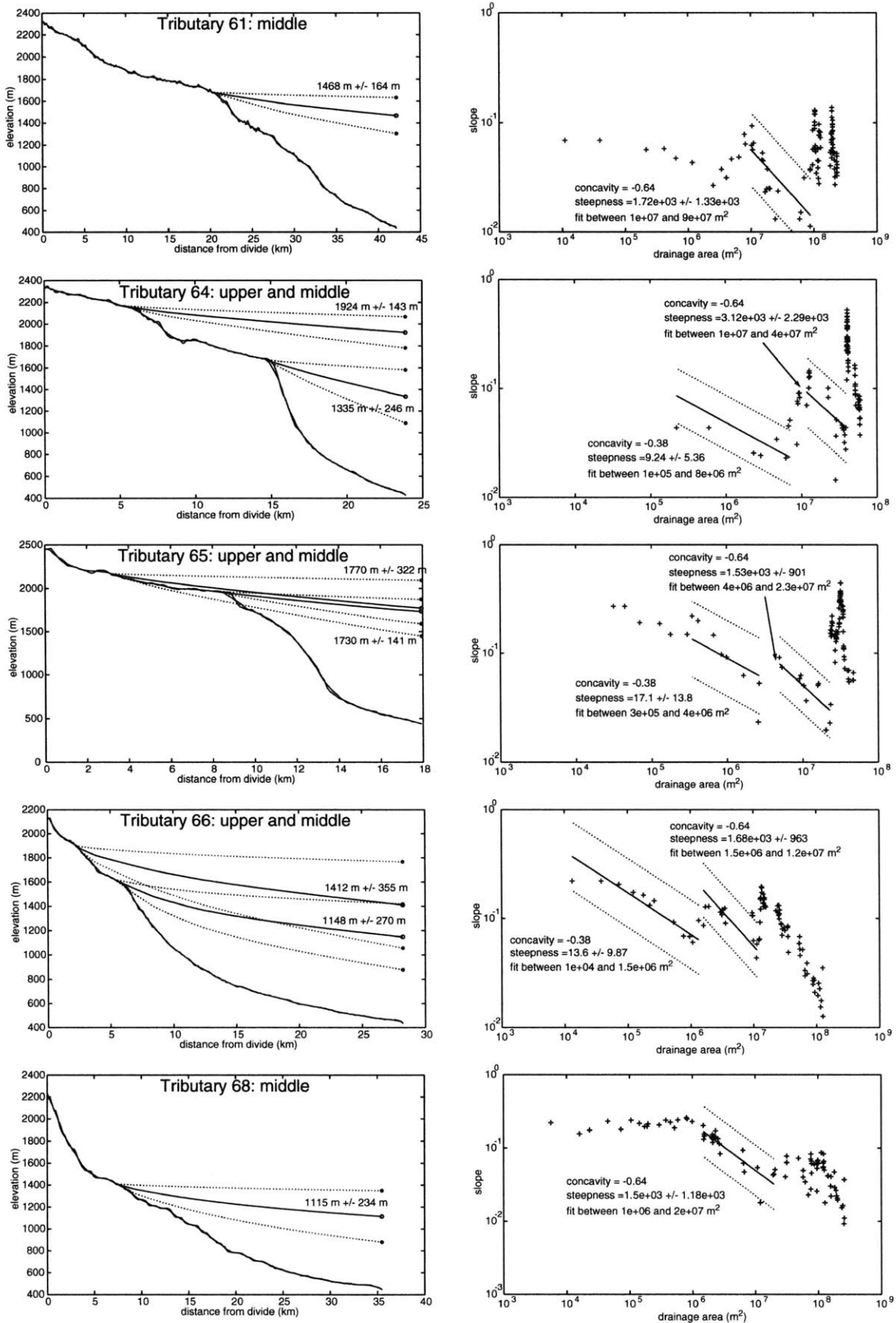


Appendix Figure 3.4. Caption on Fig. 3.9

Chapter 4 Appendix- Surface uplift, exhumation, and plateau growth

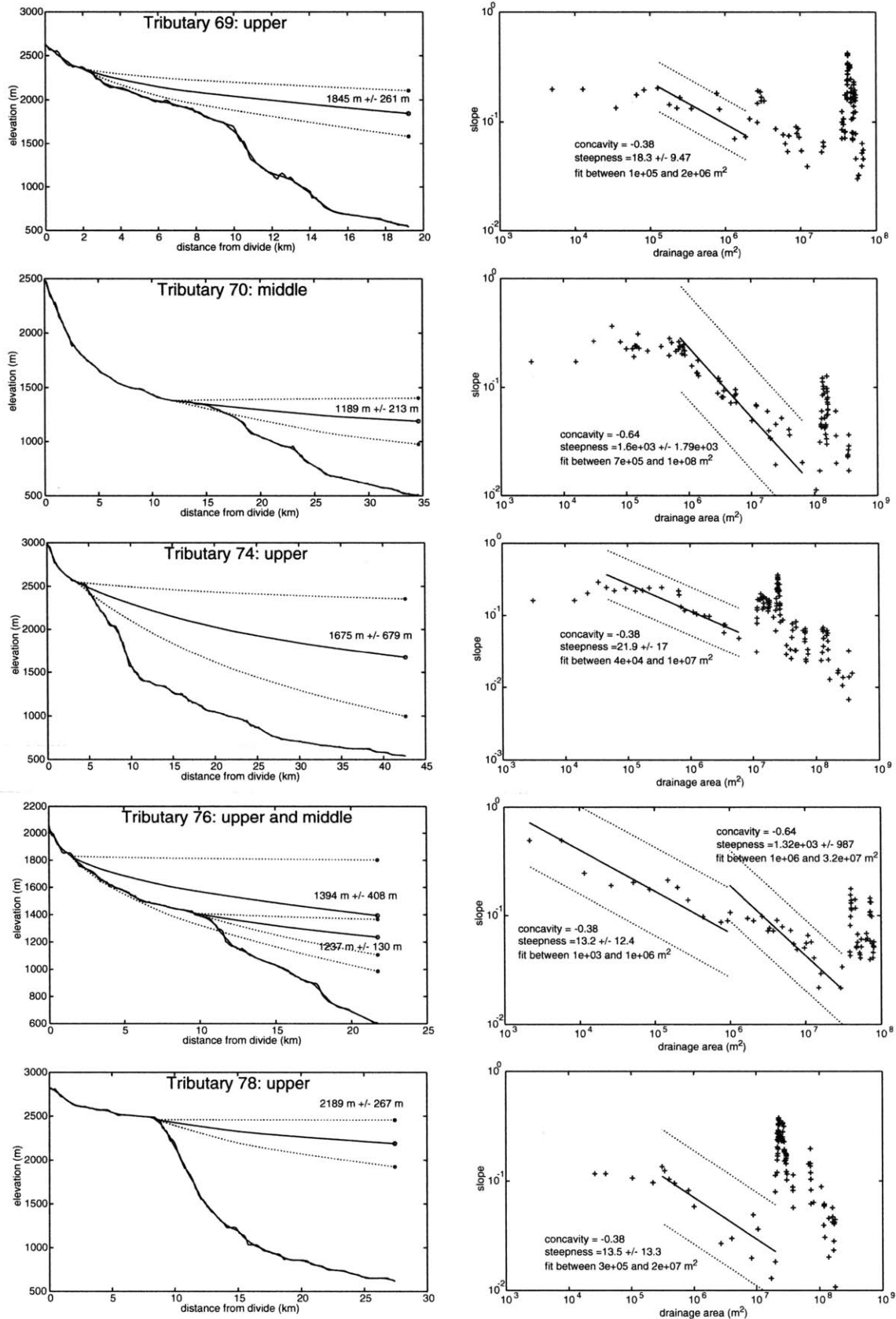


Appendix Figure 3.5. Caption on Fig. 3.9



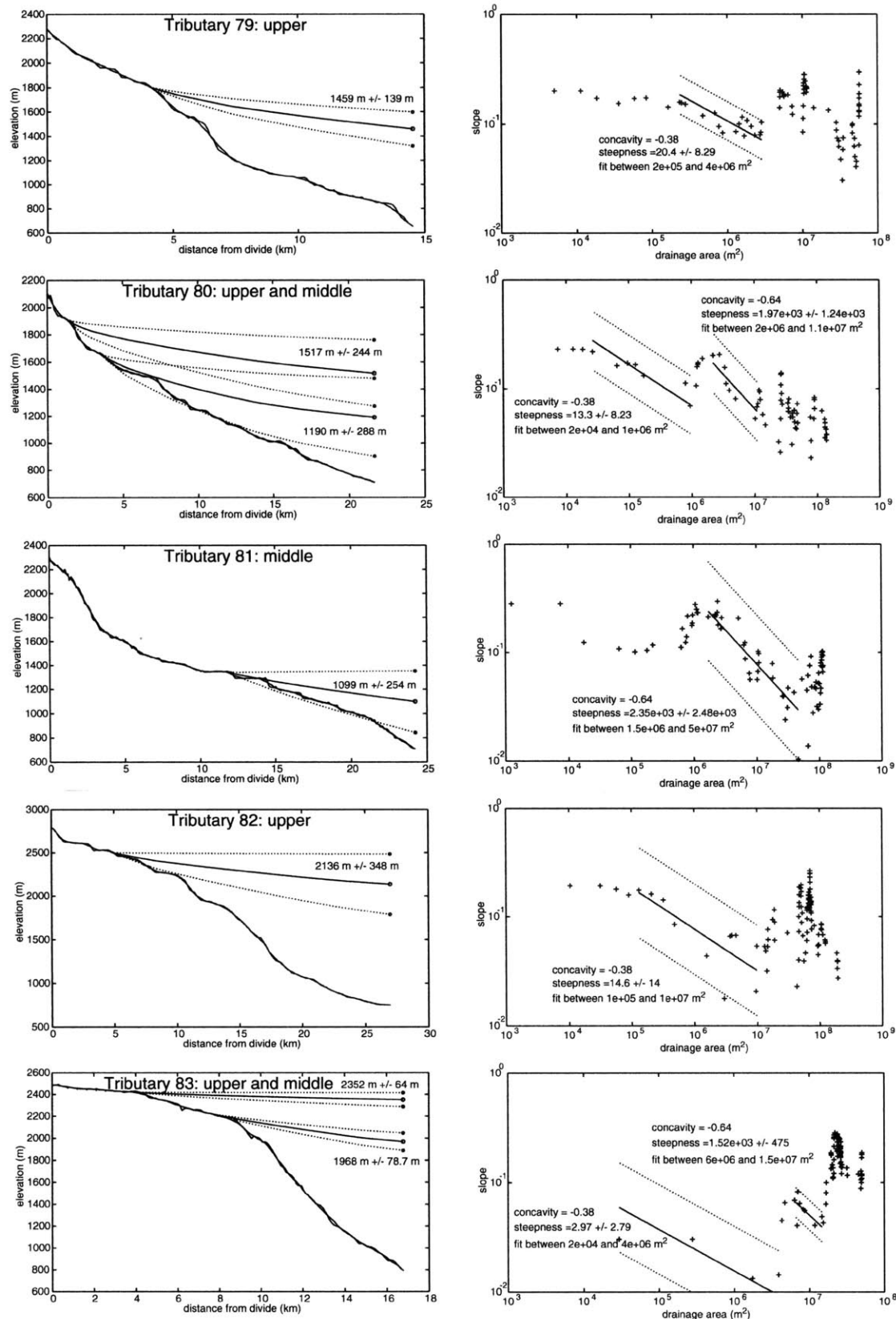
Appendix Figure 3.6. Caption on Fig. 3.9

Chapter 4 Appendix- Surface uplift, exhumation, and plateau growth

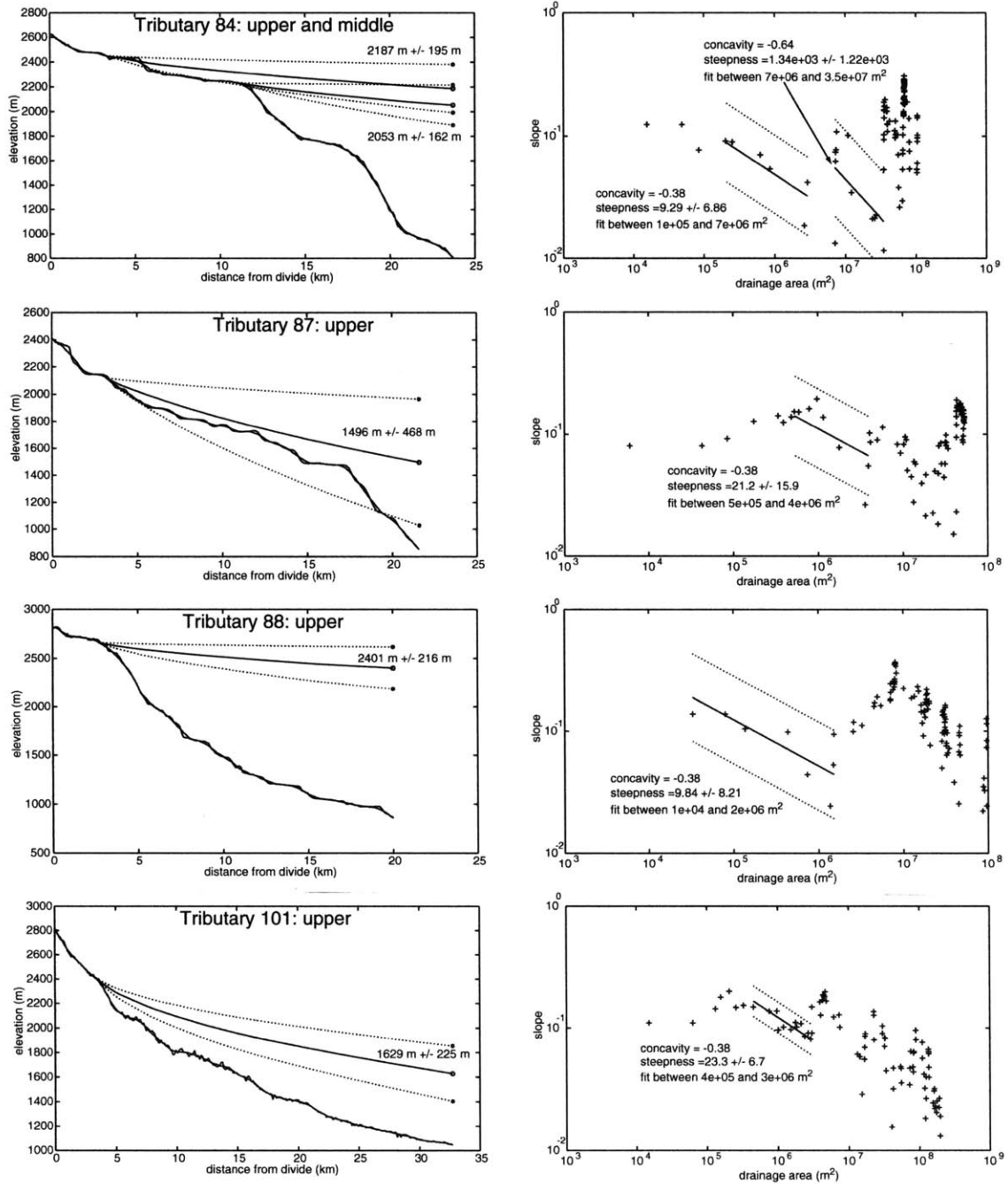


Appendix Figure 3.7. Caption on Fig. 3.9

Chapter 4 Appendix- Surface uplift, exhumation, and plateau growth



Appendix Figure 3.8. Caption on Fig. 3.9



Appendix Figure 3. Projected channel segments for 44 tributaries to the Red River. Longitudinal profile data shown in plots on left hand side with projected channel segments for upper and/or middle channel segments indicated with a solid line, and uncertainty indicated with dashed line. Elevations of projected intersections with the Red River are tabulated in Appendix Table 2. Slope-area data for longitudinal profiles shown in plots on right hand side with fit used to determine steepness index indicated with solid lines and uncertainty indicated with dashed lines. Concavity and steepness values differ between Appendix Table 1/Figure 2 and Appendix Figure 3 because concavity for Appendix Figure 2 is determined by a best fit to the data and steepness is determined with a fixed concavity of 0.45, while for Appendix Figure 3, concavity is a fixed value of 0.38 for upper segments and 0.64 for middle segments, and steepness values are determined using these fixed concavities.

**Cosmogenically determined incision rates along the
Red River, Yunnan Province, China**

L. M. Schoenbohm^{1*}

Darryl Granger²

¹Massachusetts Institute of Technology, Dept. of Earth, Atmospheric and Planetary Sciences, 77
Massachusetts Ave., Cambridge, MA 02139

²Purdue University

* E-mail: schoenbl@mit.edu

ABSTRACT

Cosmogenic ^{26}Al and ^{10}Be are used to investigate incision rates along the Red River, Yunnan Province, China. We determine a basin-wide, spatially averaged erosion rate for four tributaries to the Red River and burial ages for sediment deposited in two caves 32 and 60 m above the river. Sample localities are spaced over 400 km along the length of the river. Results indicate a background incision rate of ~ 0.05 to 0.10 mm/a. This is consistent with observations that despite a long-term (Plio-Quaternary) incision rate minimum of ~ 0.26 mm/a, incision rates have been declining towards the present. Additionally, we observe an approximate doubling of incision rates to ~ 0.20 mm/a correlated with uplift gradients produced by dip-slip displacement on the Red River fault. Incision rates thus reflect the dynamics of the eastern margin of the Tibetan Plateau: regional surface uplift and climate change which have shaped the background river incision pattern, and vertical displacements along active faults which affect river incision rates locally.

INTRODUCTION

The deeply incised rivers of the southeastern margin of the Tibetan Plateau are sensitive reflectors of regional climate change, plateau growth and active tectonic displacement. The southeast plateau margin has experienced long wave-length surface uplift (Clark and Royden, 2000; Clark 2003), possibly as a result of flow of weak mid to lower crustal material from beneath the Tibetan plateau into adjacent regions (Royden, 1996; Royden, 1997; Clark and Royden, 2000 and Clark, 2003). The rivers which traverse the southeastern margin, primarily the Yangtze and tributaries, the Mekong, the Salween and the Red River (Fig. 1), have responded to this surface uplift by deeply incising the landscape (Clark, 2003; Clark et al., in press; Schoenbohm et al., in press and Chapter 4). River incision has also been affected by regional climate change and by displacement of the landscape along active strike-slip faults.

The Red River, flowing southeasterly along the axis of the southeast plateau margin, has been well studied in the context of these interactions. Total river incision, and thus minimum surface uplift in this region, is ~ 1400 meters (Schoenbohm et al., in press and Chapter 4). Fossil-bearing paleo-Red River sediments deposited prior to uplift and subsequently incised by the modern Red River indicate that river incision initiated during Early Pliocene time or later (Schoenbohm et al.,

in press and Chapter 4) Long term incision rate is thus a minimum of ~ 0.26 mm/a. However, tributary analysis suggests a complicated incision history, likely affected by regional climate variations, with declining incision rate toward the present (Schoenbohm et al., in press and Chapter 4). Further, an extensional component to oblique slip along the Red River fault has caused relative uplift of the landscape to the southwest of the river. Maximum displacement is ~ 750 m near the town of Ejia, and declines to the southeast toward the cities of Yuanjiang and Nansa, and to the north toward the Midu Basin (Figs. 1 and 2). Incision rates on tributaries to the Red River likely reflect this gradient in uplift rate.

In this study, we employ cosmogenic ^{26}Al and ^{10}Be to constrain incision rates along the Red River in Yunnan Province, China. We calculate a basin-wide erosion rate for four tributaries from the southwest side of the river near the towns of Nansa, Yuanjiang and Ejia (Fig. 1). We also calculate incision rate along the trunk channel from sediment buried in caves 32 to 60 m above the modern river near the town of Wudingshan (Fig. 1). Results are interpreted in terms of the interaction of plateau growth, climate change and displacements along the Red River fault.

BACKGROUND AND SAMPLES

Cosmic rays interact with material at the Earth's surface, producing measurable quantities of rare radionuclides such as ^{26}Al and ^{10}Be in quartz. Cosmic rays attenuate rapidly in rock, and thus the concentration of cosmogenic radionuclide in a sample is a measure of the time that sample has spent in the accumulation zone in the Earth's near surface. In this study, we use two distinct cosmogenic dating techniques: basin-wide erosion rate determination and burial dating.

Basin-wide erosion rate

A spatially averaged erosion rate can be calculated for a basin upstream of a sediment sampling site. If the basin is in approximate steady state, the average erosion rate is the incision rate of that tributary. A single quartz grain on an eroding hillside within a basin accumulates cosmogenic nuclide as it passes upwards into the accumulation zone, approaches the surface and eventually is eroded and transported to the sample site. If erosion rate is relatively high, radionuclide decay during exposure is negligible. The final concentration of nuclide within a grain (N , at/g) reflects the erosion rate (E , cm/a), the cosmic ray attenuation length ($L \sim 60$ cm), and the cosmogenic

Chapter 5- Cosmogenically determined incision rate along the Red River

nuclide production rate (P , at/g/a) at the site of origin (Lal, 1991). This relationship is expressed by:

$$E = \frac{L \cdot P}{N} \quad (1)$$

Sediment collected from a stream contains grains that have originated from upstream parts of the basin. If all parts of the basin contribute sediment proportionately to their erosion rate, the sample can be used to calculate an average erosion rate (Lal and Arnold, 1985; Brown et al., 1995; Granger et al., 1996; Bierman et al., 1996) according to the equation:

$$E_{ave} = \frac{L \cdot P_{ave}}{N_{sample}} \quad (2)$$

where E_{ave} (cm/a) is the spatially averaged, basin-wide erosion rate, N_{sample} (at/g) is the measured nuclide concentration in the multi-grain sample and P_{ave} (at/g/a) is the basin-wide, average production rate. The timescale over which this rate is averaged is related to the residence time of a grain within the accumulation zone, or L/E_{ave} (Granger et al., 1996).

A number of factors must be taken into account when calculating a basin-wide erosion rate. Production rate values for ^{26}Al and ^{10}Be in quartz are relatively well known at sea-level and high-latitude (SLHL), but must be scaled to the sample latitude and altitude because the flux of cosmic rays at the surface of the earth depends on magnetic shielding and on the depth of atmosphere through which the cosmic rays pass. Shielding of the sample site by obstructions of the horizon must also be accounted for, as such obstructions block cosmic rays from reaching the sample site. Sediment storage, dissolution or chemical weathering, non-proportional contribution from all parts of basin and mass wasting are all factors which can compromise the determination of an accurate basin-wide erosion rate, and thus must be avoided when sampling or accounted for in the calculations (Brown et al., 1995; Granger et al., 1996; Bierman et al., 1996).

Burial dating

Dating of sediment deposited in caves above the modern river level allows the calculation of river incision rates (Granger et al., 1997, Granger et al., 2001). During exposure to cosmogenic rays, quartz grains in sediment accumulate ^{26}Al and ^{10}Be at a characteristic ratio of ~ 6.1 , though with very long exposure the ratio declines towards ~ 2.7 as radio-decay of nuclide becomes more important (Lal, 1991) (Fig. 3). If that sediment is then shielded from cosmic rays, new production will cease and concentrations of cosmogenic nuclide will decline according to the nuclide half-life (Fig. 3). Shielding may occur if the sample is buried in a sedimentary deposit, or, of interest here, if sediment is deposited deeply within a cave at paleo-river level. Both the pre-burial nuclide concentration and the time since shielding began are unknown, and thus concentration data for two nuclides (in this case, the $^{26}\text{Al}:$ ^{10}Be pair) are needed to solve for the burial age (Granger and Muzikar, 2001).

A number of simplifying assumptions can be made about the pre-burial and burial conditions, for each set of which a slightly different set of equations is used. These are thoroughly discussed by Granger and Muzikar (2001). For this study, we consider relatively rapid pre-burial erosion (> 0.01 mm/a) and nuclide produced both by the dominant mechanism (neutron spallation reactions) and by muon interactions (relatively less reactive, lower mass particles) which comprise a small but significant fraction of production at the Earth's surface. The equation for burial age for this set of assumptions comes from equations 25 and 26 of Granger and Muzikar (2001), solved for the time since burial (t):

$$t = \frac{1}{\lambda_{Be}} \cdot \ln \left[\frac{N_{Be}}{N_{Al}} \cdot \frac{A_0 L_0 + A_1 L_1 + A_2 L_2 + A_3 L_3}{B_0 L_0 + B_1 L_1 + B_2 L_2 + B_3 L_3} \cdot \exp(\lambda_{Al} \cdot t) \right] \quad (3)$$

where λ_{Al} and λ_{Be} are the decay constants of ^{26}Al and ^{10}Be (1/a), N_{Al} and N_{Be} are measured nuclide concentrations (at/g), the A and B terms (for ^{26}Al and ^{10}Be respectively) are the production rate of cosmogenic nuclide through various neutron and muon interactions and the L

terms are the attenuation length of each production mechanism. Values for A , B and L terms are given in Granger and Smith (2000). This equation must be solved iteratively.

SAMPLING AND METHODS

Basin-wide erosion rate sampling

We collected ~ 1 kg sand from each of four tributaries to the Red River (see Fig. 1 for locations). Tributaries to the Red River in general are steep, narrow bedrock channels. The hillslopes show evidence for frequent mass-wasting events and are mantled by only thin and patchy soils. We observed no significant terraces within the basins at stream level or above. Our field observations thus suggest that sediment storage and chemical dissolution are unlikely to affect the results of our calculations: erosion is dominantly mechanical, and grains are transported rapidly from their source to the sampling site with insignificant post-erosion decay or exposure. All four sampled tributary basins lie almost entirely within the Ailao Shan gneiss. Lithology is uniform on the hundreds of meters scale, and thus within reasonable limits, all parts of the basin should be contributing equally to the final sediment composition. The exception may be for the smaller basin near Ejia (basin 3, Fig. 1) which is small enough that the heterogeneities within the Ailao Shan gneisses, particularly occasional significant marble horizons, may affect the calculated erosion rate, as will be discussed further below. Also, the headwaters of the large basin near Ejia (basin 4, Fig. 1) lie above the deeply incised valley within a rolling upland characterized by deep weathering and chemical dissolution (Schoenbohm et al., in press and Chapter 4). We deliberately sampled this basin to observe the affect of this part of the landscape on the cosmogenic results, as will be discussed further below. Mass wasting is common in all four tributaries and could potentially pose a problem if we inadvertently sampled sediment dominated by a recent mass-wasting event, though we did not observe any apparent recent landslide deposits immediately upstream from our sampling locations.

Calculation of an average production rate for each basin requires knowledge of the basin morphology. We extracted the basin upstream of each sampling site from a 90m digital elevation model (DEM, see Fielding et al., 1994 for data description). For each pixel within the basin we calculated first a production rate scaled for latitude and altitude after Stone (2000), and using the SLHL production rates of $P_{Be} = 5.1 \pm 0.3$ at/g/a and $P_{Al} = 31.1 \pm 1.9$ at/g/a (Stone, 2000 and

references therein). We also calculated a shielding factor using a method modified from Balco (personal communication 2003), in which, for each pixel, the surrounding pixels are binned into azimuthal increments of 30°. A maximum angular relationship is found within each bin and assigned as the angle to the horizon (h) over that azimuthal interval. Total shielding is the integral $\sin(h)^{3.3}$ over the entire horizon. In the case of basin-wide erosion rate, shielding is relatively unimportant, as only horizon angles over ~30° significantly affect production rate, and such steep angles are uncommon on the basin-scale. The maximum correction factor for shielding in our samples basins is ~3%.

Cave samples

Near the town of Wudingshan, close to the northern end of the Red River, we collected ~0.5 kg material from the floor of two neighboring caves 32 and 60 m above the modern river (Caves 1 and 2 respectively). Both caves are shallow, with limited deposits on the cave floor of carbonate and organic debris, mud, and some sand. Samples were cleaned and sieved extensively to separate the quartz fraction, and final quartz yields were quite low (<100 g). Sediment cannot have been deposited in the cave until the river was at or below the elevation of the cave, regardless of the sediment source (washed into the cave during the river flood stage, deposited by subterranean channels linked to the river or washed in from the surface by groundwater flow). Thus the age of the sediment is a minimum measure of the age of the cave.

We make several reasonable assumptions about the pre-burial and post-burial conditions. First, we assume that sediment washed into the cave reflects the erosion conditions upstream of that point in the Red River drainage, just as if the sediment was sampled for basin-wide erosion rate. Erosion rates along the main Red River are at least ~0.01 mm/a (based on our results for tributary basin-wide erosion rate, Table 1). The contribution of muon-produced nuclide is non-negligible, and equation 3, which accounts for muon production, should be used (Granger and Muzikar, 2001). We also assume that sediment was deposited deeply enough within the cave that it experienced no significant post-burial exposure. This is reasonable, as both samples were collected ~ 5 m from the mouth of the caves. The cliffs in which the caves are located are nearly vertical, therefore the thickness of rock above the sample sites is several tens of meters, substantial enough to block nearly all incoming cosmic rays (Granger et al., 1997).

Sample preparation and analysis

Samples were treated with aquaregia to dissolve CaCO_3 and organic material and magnetically separated. Samples were then treated with a dilute HF/HNO_3 solution in an ultrasonic bath over a period of several days up to two weeks to purify the sample and remove the outer portion of sand grains contaminated with atmospheric beryllium (after Kohl and Nishizumi, 1992). The remaining sample was then dissolved in hot, concentrated hydrofluoric and nitric acid, fumed in sulfuric acid to remove fluorides and chemically separated to form pure aluminum and beryllium. Samples were analyzed at the Lawrence Livermore National Laboratory AMS facility. During sample preparation, incomplete purification resulted in the loss of the beryllium sample for the large Ejia basin (Basin 4). All aluminum samples analyzed in this study yielded low currents during AMS analysis, resulting in very large uncertainties for ^{26}Al concentration. This may also be responsible for low $^{26}\text{Al}:^{10}\text{Be}$ ratios for the Nansa (Basin 1) and the small basin near Ejia (Basin 3).

RESULTS AND DISCUSSION

Results are presented in Table 1, and graphically in Figures 2 and 3. In general, erosion rates are lower than expected (~ 0.1 mm/a) given the average long-term minimum incision rate (~ 0.26 mm/a) calculated from the total amount and maximum age of river incision. However, these rates are consistent with the observation based on tributary longitudinal profile concavity data that incision rates may be declining towards the present (Schoenbohm et al., in press and Chapter 4). We discuss individual results from southeast to northwest.

Nansa (Basin 1): The spatially averaged basin-wide erosion rate for the tributary near the town of Nansa yields the lowest incision rate of all four basins (Table 1). Aluminum data is poor for this sample (Fig. 3), and we thus prefer the erosion rate determined with ^{10}Be for this basin, 0.05 ± 0.01 mm/a.

Yuanjiang (Basin 2): Erosion rate for this sample is higher. ^{26}Al and ^{10}Be data yield similar erosion rates of 0.13 ± 0.02 mm/a.

Ejia (Basin 3): This sample yields a very low erosion rate. Because of poor Al data (Fig. 3), we use the ^{10}Be erosion rate of 0.06 ± 0.01 mm/a. However, this basin is small, increasing the potential importance of basin inhomogeneities (Basin 3 area is ~ 4 km² compared to 83 km², 29 km² and 29 km² for Basins 1, 2 and 4 respectively). For example, the presence of a marble horizon (which would contribute no quartz to the integrated basin sample) in lower portion of basin would increase the proportion of quartz sediment derived from higher in the basin where production rates are also higher. The result would be a lowering of the apparent basin-wide erosion rate. Because of this potential problem, and because erosion rates are so much lower for this basin than for the flanking basins (Basins 2 and 4), we place little weight on this data during further analysis.

Ejia (Basin 4): Erosion rate in this basin is 0.19 ± 0.06 mm/a, though unfortunately we were only able to calculate an erosion rate from the aluminum data as beryllium was lost during sample processing. Because of low AMS aluminum yields in this study, erosion rates calculated from ^{26}Al data in general are slightly higher than those calculated from ^{10}Be data, and so the ^{26}Al -based erosion rate for this basin may be artificially elevated by up to $\sim 25\%$. Even with this possible overestimation taken into account, the erosion rate for this basin is significantly higher than for any other in this study. The headwaters of this basin drain a high-altitude, deeply weathered, low-relief landscape (Schoenbohm et al., in press and Chapter 4). If a significant sand component derived from the low-relief landscape was present in the basin-integrated sample, we would expect higher concentrations of cosmogenic nuclide, both from long exposure in the presumably slowly eroding landscape (Schoenbohm et al., in press and Chapter 4), and from higher production rates at the higher altitude of the low-relief landscape. Such high concentrations of nuclide in sediment would lead to the calculation of lower erosion rates. However, erosion rate for this basin is the highest calculated in this study. It therefore appears that little material is contributed from the low-relief landscape to the total sediment flux, perhaps because the dominant weathering process is chemical dissolution, streams flowing across the low-relief landscape are low-gradient and transport relatively little sediment, or the sediment contribution from the low-relief landscape is overwhelmed by material from the incised valleys.

Wudingshan (Cave 2): At 60 m above the modern river, this sample yields a burial age of 0.69 ± 0.63 Ma, and therefore an incision rate along the Red River of 0.09 ± 0.08 mm/a. Though the very large uncertainties (resulting from low-current yield during aluminum analysis) limit the usefulness of this data, this incision rate is consistent with basin-wide erosion rate data.

Wudingshan (Cave 1): The lower cave sample, collected from a nearby cave 32 m above the modern river, was extremely small (~ 7 g purified and cleaned quartz), and reliability of this data is thus very low. Results (2.54 ± 1.1 Ma burial age and 0.01 ± 0.01 mm/a incision rate) are inconsistent with Cave 2 results and basin-wide erosion rates. We therefore discard this data for further analysis.

Basin-wide data averages erosion rates over the timescale 3,000 to 12,000 years (attenuation length L divided by the range of erosion rates, ~ 0.05 mm/a to ~ 0.2 mm/a), which is considerably shorter than the averaged timescale of Cave 2, which is $\sim 700,000$ years. Schoenbohm et al., (in press and Chapter 4) argue that incision rates are declining with time, therefore Cave 2 might be expected to yield a higher incision rate than basin-wide erosion rate samples. However, uncertainty on Cave 2 data and the lack data from the same location over both timescales does not allow for further analysis of this topic.

Despite large uncertainties and differing timescales, several interesting points emerge from data presented in this study. From southeast to northwest, excluding data from the smaller basin near Ejia (Basin 3) and Cave 1, incision rates are: 0.05 ± 0.01 mm/a, 0.13 ± 0.02 mm/a, 0.19 ± 0.06 mm/a and 0.9 ± 0.08 mm/a (Table 1, Fig. 2). These incision rates are broadly consistent with the pattern of displacement along the Red River fault. The southwest side of the river, the footwall of the Red River fault, experienced a maximum 750 vertical displacement near the town of Ejia, with displacements decreasing to the southeast towards the town of Nansa, and decreasing to the northwest towards Wudingshan the Midu basin (Figs. 1 and 2, Schoenbohm et al., in press and Chapter 4). Our data suggest a background modern incision rate in the range 0.05-0.1 mm/a, with an approximate doubling of that in the zone of maximum vertical displacement to near 0.2 mm/a.

CONCLUSIONS

The long-term average incision rate along the Red River on the southeastern margin of the Tibetan Plateau is ~ 0.26 mm/a (from the total amount and maximum age of river incision, Schoenbohm et al., in press and Chapter 4). However, tributary analysis suggests a complicated incision history with declining incision rates towards the present, related to plateau geodynamics and regional climate change (Schoenbohm et al., in press and Chapter 4). Further, uplift gradients resulting from oblique slip on the Red River fault (Schoenbohm et al., in press and Chapter 4) should influence incision rates on tributaries to the Red River. These observations are confirmed and informed by cosmogenic ^{26}Al and ^{10}Be basin-wide erosion rate and burial data presented in this study. Our conclusions are:

1. A background incision rate of 0.05 to 0.1 mm/a is consistent with lower incision rates along the Red River today than the long-term average. It follows that at some point in the Pliocene or Quaternary, erosion rates must have been higher, perhaps dramatically, than the long-term average incision rate.
2. Though uncertainties are large and caution must be used in interpreting out data, there is a suggestion of a correlation of incision rate to vertical displacement along the Red River fault, with a doubling of incision rate to ~ 0.2 mm/a in the area of most significant normal displacement.

REFERENCES

- Balco, G., personal communication, Cosmogenic Isotope Laboratory, Quaternary Research Center and Department of Earth and Space Sciences, University of Washington, <http://depts.washington.edu/cosmolab/math.html>.
- Bierman, P., and Steig, E.J., 1996, Estimating rates of denudation using cosmogenic isotope abundances in sediment: *Earth Surface Processes and Landforms*, v. 21, p. 125-139.
- Brown, E.T., Stallard, R.F., Larsen, M.C., Raisbeck, G.M., and Yiou, F., 1995, Denudation rates determined from the accumulation of *in situ*-produced ^{10}Be in the Luquillo Experimental Forest, Puerto Rico: *Earth and Planetary Science Letters*, v. 129, p. 193-202.
- Clark, M.K., and Royden, L.H., 2000, Topographic ooze: Building the eastern margin of Tibet by lower crustal flow: *Geology*, v. 28, p. 703-706.
- Clark, M.K., Schoenbohm, L.M., Royden, L.H., Whipple, K.X., Burchfiel, B.C., Zhang, X., Tang, W., Wang, E., Chen, L., in press, Surface Uplift, tectonics, and erosion of eastern Tibet from large-scale drainage patterns: *Tectonics*.
- Clark, M.K., 2003, Late Cenozoic Uplift of Southeastern Tibet [Ph.D. Thesis]: Massachusetts Institute of Technology, 226 p.
- Fielding, E., Isacks, B., Barazangi, M., Duncan, C., 1994, How flat is Tibet?: *Geology*, v. 22, p. 163-167.

Chapter 5- Cosmogenically determined incision rate along the Red River

- Granger, D.E., Fabel, D., and Palmer, A., 2001, Pliocene-Pleistocene incision of the Green River, Kentucky, determined from radioactive decay of cosmogenic ^{26}Al and ^{10}Be in Mammoth Cave sediments: GSA Bulletin, v. 113, p. 825-836.
- Granger, D.E., Kirchner, J.W., and Finkel, R.C., 1996, Spatially averaged long-term erosion rates measured from *in situ*-produced cosmogenic nuclides in alluvial sediment: Journal of Geology, v. 104, p. 249-257.
- Granger, D.E., Kirchner, J.W., and Finkel, R.C., 1997, Quaternary downcutting rate of the New River, Virginia, measured from differential decay of cosmogenic ^{26}Al and ^{10}Be in cave-deposited alluvium: Geology, v. 25, p. 107-110.
- Granger, D.E., and Muzikar, P., 2001, Dating sediment burial with *in situ*-produced cosmogenic nuclides: theory, techniques and limitations: Earth and Planetary Science Letters, v. 188, p. 269-281.
- Granger, D.E., and Smith A.L., 2000, Dating buried sediments using radioactive decay and muonogenic production of ^{26}Al and ^{10}Be : Nuclear Instrumentation and Methods in Physics Research B, v. 172, p. 822-826.
- Kohl, C.P., and Nishizumi, K., 1992, Chemical isolation of quartz for measurement of *in-situ*-produced cosmogenic nuclides: Geochimica et Cosmochimica Acta, v. 56, p. 3583-3587.
- Lal, D., 1991, Cosmic ray labeling of erosion surfaces: *in situ* nuclide production rates and erosion models: Earth and Planetary Science Letters, v. 104, p. 424-439.
- Lal, D., and Arnold, J.R., 1985, Tracing quartz through the environment: Proceedings of the Indian Academy of Science Earth and Planetary Science, v. 94, p. 1-5.
- Royden, L.H., 1996, Coupling and decoupling of crust and mantle in convergent orogens: Implications for strain partitioning in the crust: Journal of Geophysical Research, B, v. 101, p. 17 679-17 705.
- Royden, L.H., Burchfiel, B.C., King, R.W., Wang, E., Chen Z., Shen F., Liu Y., 1997, Surface deformation and lower crustal flow in eastern Tibet: Science, v. 276, p. 788-790.
- Schoenbohm, L.M., Whipple, K.X., Burchfiel, B.C., Chen, L., in press, River incision into a relict landscape along the Ailao Shan shear zone and Red River fault, Yunnan Province, China: GSA Bulletin.
- Stone, J., 2000, Air pressure and cosmogenic isotope production: Journal of Geophysical Research, v. 105, p. 23,753-23,759.

Chapter 5- Cosmogenically determined incision rate along the Red River

Table 1.

¹⁰ Be	P Be ¹ (at/g/a)	(+/-)	¹⁰ Be (10 ⁶ at/g)	(+/-)	Erosion rate ² (mm/a)		(+/-)	Ave. Elev (m)	Latitude (dd)	Longitude (dd)	
Basin 1	10.8	1.3	0.1395	0.0085	0.05	0.01		1410	23.25	102.83	
Basin 2	11.5	1.3	0.0530	0.0043	0.13	0.02		1481	23.63	101.90	
Basin 3	18.6	2.2	0.1799	0.0073	0.06	0.01		2227	24.36	101.31	
	P Be (at/g/a)	(+/-)	¹⁰ Be (10 ⁶ at/g)	(+/-)				Cave ³ height (m)			
Cave 1	9.4	1.1	0.0704	0.0066				32			
Cave 2	9.5	1.1	0.0366	0.0028				60			
²⁶ Al	P Al ¹ (at/g/a)	(+/-)	²⁶ Al (10 ⁶ at/g)	(+/-)	Erosion rate ² (mm/a)		(+/-)	Ave. Elev (m)	Latitude (dd)	Longitude (dd)	
Basin 1	66.1	6.6	0.6833	0.0858	0.06	0.01		1410	23.25	102.83	
Basin 2	70.0	7.0	0.3298	0.0400	0.13	0.02		1481	23.63	101.90	
Basin 3	113.9	11.4	0.9778	0.0757	0.07	0.01		2227	24.36	101.31	
Basin 4	141.2	14.2	0.4584	0.1272	0.19	0.06		2572	24.38	101.30	
	P Al (at/g/a)	(+/-)	²⁶ Al (10 ⁶ at/g)	(+/-)	Incision rate ⁴ (mm/a)	(+/-)	Burial age ⁵ (Ma)	(+/-)	Cave Elev. (m)	Latitude (dd)	Longitude (dd)
Cave 1	57.29	6.71	0.1257	0.0660	0.01	0.01	2.54	1.10	1190	24.58	100.84
Cave 2	58.08	6.81	0.1665	0.0473	0.09	0.08	0.69	0.63	1209	24.98	100.84

Note: Cosmogenic ²⁶Al and ¹⁰Be data, production rates and calculation results. All errors are propagated at 1 sigma uncertainty. Best values for erosion rate (basin-wide average) and incision rate (burial dating of cave sediment) are in bold. See Figure 1 for basin locations.

¹Average production rate for basin-wide erosion rate calculated from basin DEM. A scaled production rate and shielding factor are calculated for each pixel in the DEM, then averaged. Scaling algorithms and production rate values at SLHL from Stone (2000). For Cave 1 and 2, production rate scaled to elevation and latitude of cave.

²Erosion rate calculated using equation (2) in text. All errors are propagated at 1 sigma uncertainty. ¹⁰Be data is more reliable for this study, as aluminum yields were low during AMS analysis, possibly due to Ca interference.

³Cave height above river.

⁴Incision rate calculated from burial age and height above river.

⁵Burial age calculated for pre-burial erosion rate >0.01 mm/a, muon production and no post-burial exposure using equation (3) in text after Granger and Muzikar (2001).

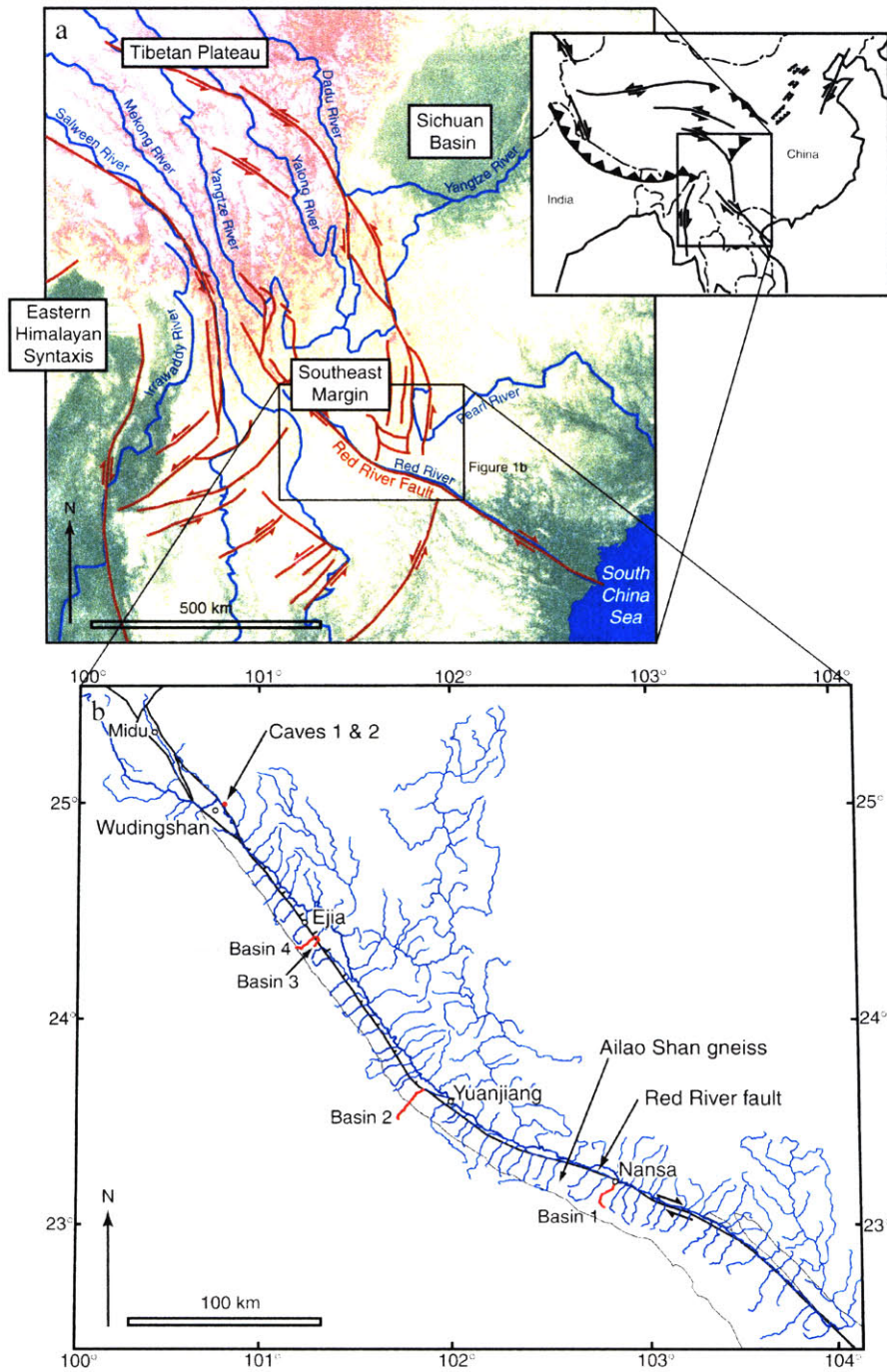


Figure 1. (a) Map of the eastern margin of the Tibetan Plateau with figure 1b location marked by box. Active faults are indicated in red and major rivers in blue. Location shown in inset. (b) The Red River and tributaries in China. Cities and towns referred to in text are marked with open circles and labeled. Sampled locations and tributaries are marked in red. Ailao Shan gneisses are shaded gray and the Red River fault is marked with a heavy line. Slip on the Red River fault is dominantly right-lateral, but between Yuanjiang and Wudingshan there is a significant component of normal slip. This segment is indicated with short dashed lines perpendicular to the fault on the hanging wall.

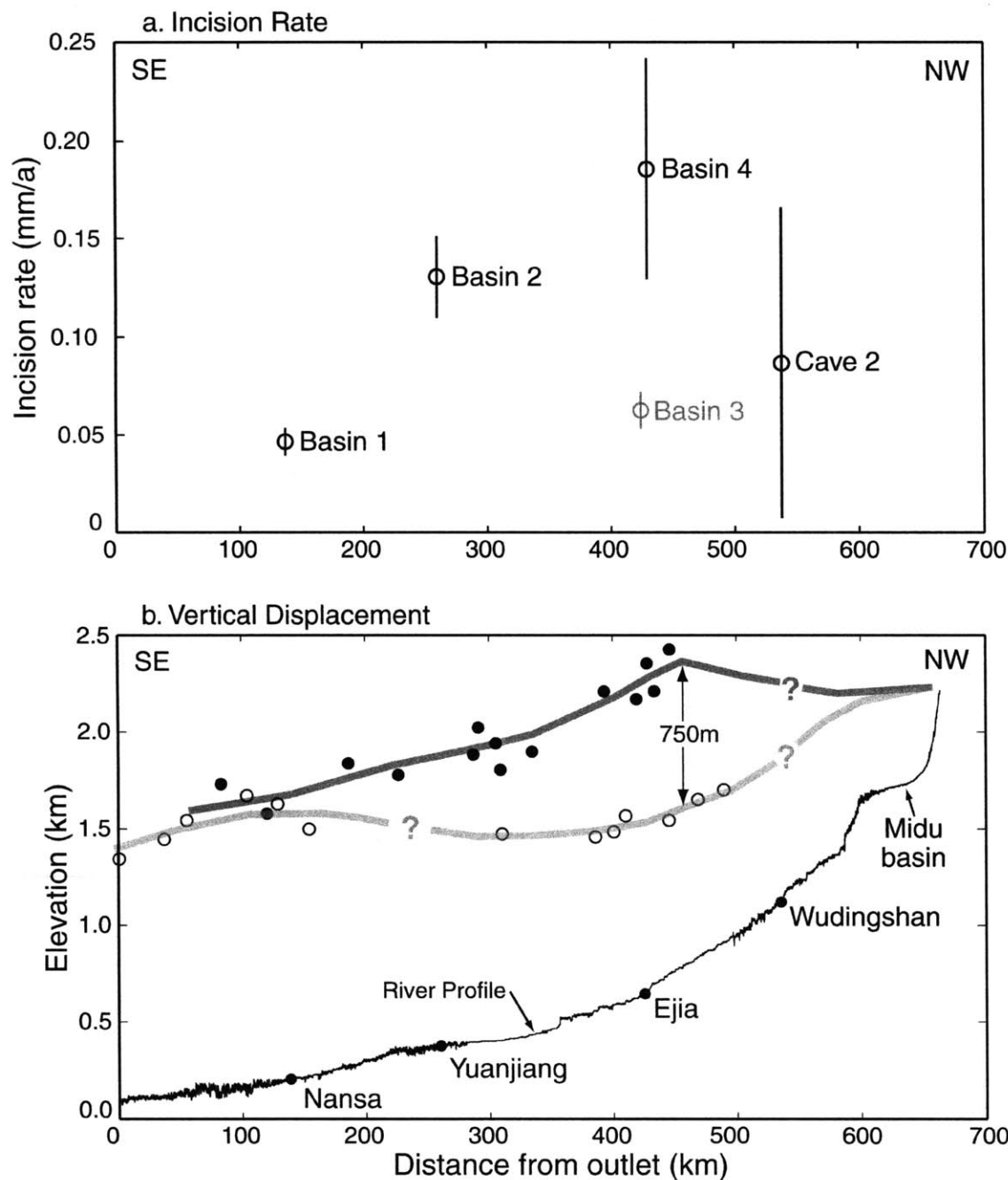


Figure 2. (a) Incision rate plotted against distance along Red River. 1 sigma uncertainty indicated by bar. Basin 3 data is grayed because it may be less reliable. Incision rates roughly correlate to uplift gradients along the Red River fault. (b) Vertical displacement along across the Red River fault plotted against distance upstream from a point near the Chinese-Vietnamese border (same horizontal scale as Figure 2a). Cities referred to in the text are plotted on the Red River longitudinal profile. Displacement is constrained by using the reconstructed drainage system of the low-relief landscape as a datum (Schoenbohm et al., in review). Open circles are data for tributaries northeast of the Red River and solid circles are for data from the southwest side. Schoenbohm et al. (in review) argue that most absolute displacement occurred in the footwall of the Red River fault, the southwest side of the river. Maximum displacement is near Ejia, and becomes negligible towards Midu in the northwest and Nansa in the southeast.

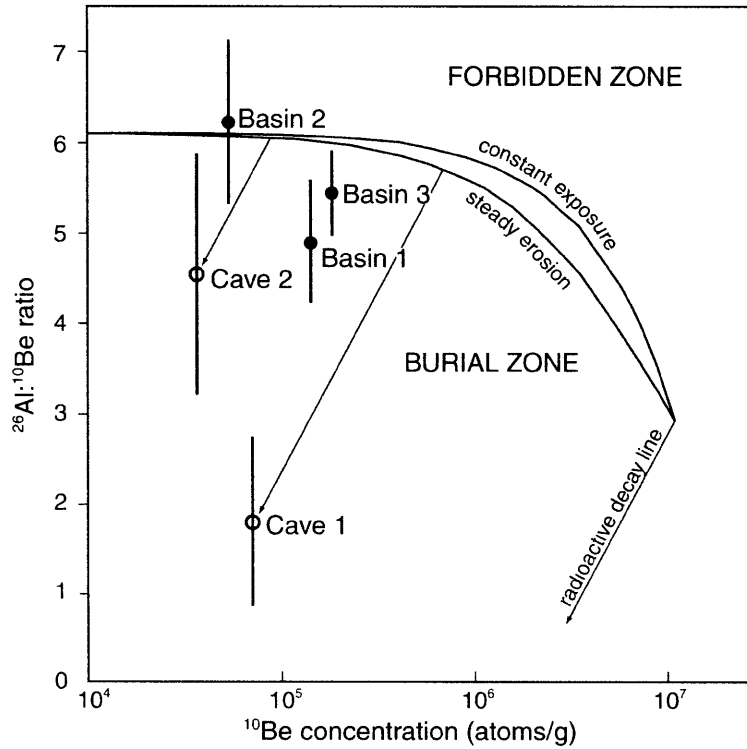


Figure 3. Banana diagram: ^{10}Be concentration plotted against the $^{26}\text{Al}:^{10}\text{Be}$ ratio. 1 sigma uncertainty in the $^{26}\text{Al}:^{10}\text{Be}$ ratio indicated by bar. Uncertainty in ^{10}Be concentration is less than the symbol width. When first exposed, nuclide is produced in a sample at the $^{26}\text{Al}:^{10}\text{Be}$ production rate ratio of ~ 6.1 . As exposure time lengthens, radioactive decay of ^{26}Al and ^{10}Be according to different half lives (longer for ^{10}Be) causes the nuclide ratio to decrease towards ~ 2.7 (Lal, 1991). The upper envelope of the "banana" describes samples that have experienced no erosion and the lower envelope describes samples undergoing steady state erosion. It is theoretically impossible to produce sample with a nuclide ratio in the "forbidden zone" through cosmogenic means. If a sample is buried, the $^{26}\text{Al}:^{10}\text{Be}$ ratio declines along a radioactive decay line. The $^{26}\text{Al}:^{10}\text{Be}$ ratio for Cave 1 and Cave 2 indicates both the steady state erosion rate experienced by sediment prior to burial, and the burial age. Basin-wide erosion rate data should overlap, within error, with the envelope defined by the constant exposure and steady state erosion lines. Burial in a terrace prior to sampling can cause basin-averaged sediment to plot in the "burial zone," but we do not observe field data in support of sediment storage. Instead, we attribute the low $^{26}\text{Al}:^{10}\text{Be}$ ratios to poor aluminum data. Basin 4 is not shown here because only ^{26}Al data is available for that sample.

**Depth dependence of cosmogenic
 ^3He and ^{21}Ne in Antarctic sandstone bedrock:
implications for exposure and erosion history**

L. M. Schoenbohm^{1*}

M. D. Kurz²

R. Ackert²

E J Brook⁴

E T Brown³

¹Massachusetts Institute of Technology, Dept. of Earth, Atmospheric and Planetary Sciences, 77
Massachusetts Ave., Cambridge, MA 02139

² Woods Hole Oceanographic Institution, MS 25, Clark 4, Woods Hole, MA 02543

³ Large Lakes Observatory, RLB 207, University of Minnesota, Duluth, MN 55812

⁴ Geology Dept., Washington State University, 14204 NE Salmon Creek Ave., Vancouver, WA
98686

* E-mail: schoenbl@mit.edu

ABSTRACT

We present new ^{21}Ne , ^3He depth dependence data in quartz for sandstone bedrock cores collected from Mt. Fleming and Arena Valley in the Dry Valleys region, Antarctica and compare these data to previously published ^{26}Al and ^{10}Be data (Brown et al., 1992; Brook, 1994). Measured ^{21}Ne and ^3He attenuation lengths for the Mount Fleming core are 140 ± 5 and $144 \pm 7 \text{ g/cm}^2$ (1σ) respectively, similar to values determined for ^{10}Be and ^{26}Al in both cores. ^{21}Ne and ^3He attenuation lengths for the Arena Valley core are significantly longer, 166 ± 3 and $196 \pm 5 \text{ g/cm}^2$ (1σ) respectively. We attribute these exceptionally long attenuation lengths to the combined impacts of exposure history and nuclide production through muon interactions. The attenuation length of muon production is approximately an order of magnitude greater than that of neutron production. Higher erosion rates increase the proportion of total muon-produced cosmogenic nuclide in the near surface, thus increasing apparent attenuation length. Modeling can place constraints on erosion history and muon production rate values in quartz for ^{21}Ne and ^3He . We find that erosion rates at the Arena Valley site were higher in the past. Good fits to the data are obtained for moderate erosion rates ($\sim 1 \text{ m/Ma}$), persistent over several million years, followed by low erosion rate conditions for the last 1.3 Ma. Prolonged, low erosion rate conditions ($< 1 \text{ m/Ma}$) punctuated by a short period of rapid erosion just prior to 1.3 Ma also produce good model fits to the data. Our results illustrate the potential of cosmogenic nuclide depth profiles for unraveling complex exposure histories.

INTRODUCTION

Cosmic ray exposure dating is a powerful tool for understanding sediment accumulation and burial histories, determining erosion rates, and dating geomorphic surfaces. Cosmic rays interact with matter at the surface of the Earth, dominantly by neutron induced nuclear spallation, but also through higher-energy muon interactions, to produce measurable quantities of cosmogenic nuclide. The flux of cosmic radiation attenuates exponentially with depth in rock, therefore the accumulation of *in situ* cosmogenic nuclide in a sample records the residence time of a rock in the near surface ($\sim 2 \text{ m}$). The application of cosmogenic dating techniques is not significantly

limited by analytical capabilities, but rather by uncertainties in production rate, muon production mechanisms, depth dependence, and geological and geomorphic uncertainties.

In this study we investigate one of these uncertainties, the depth-dependence of cosmogenic nuclide production, and explore the consequent implications for production mechanisms and chronology of surface processes. Seventeen samples from two ~1.25 meter long sandstone cores collected from the Antarctic Dry Valleys (Fig. 1) were analyzed for ^3He and ^{21}Ne concentration. ^{10}Be and ^{26}Al data are available for both cores in Brown et al. (1992) and Brook (1994). In this study, the depth dependence, or attenuation length, was calculated for ^{21}Ne and ^3He concentration depth profiles, and were found to significantly deviate from theoretical predictions for production by neutron spallation for one of the cores. Several explanations for this deviation are explored in the discussion. As confirmed by modeling, the proportion of nuclide resulting from muon interactions strongly affects the depth dependence, and the muogenic component can be increased through high and varied erosion rates. We model the results as a function of the integrated erosion and exposure history and explore methods that can constrain these histories.

BACKGROUND

Production Mechanisms

The flux of cosmic radiation at the surface of the Earth consists dominantly of neutrons with a minor component of negatively charged mu-mesons (muons). The depth dependence of production in rock is often described as an exponential decrease with depth with respect to overlying mass, by the equation:

$$P = P_0 e^{-x/L} \quad (1)$$

where P is production rate as a function of depth x , P_0 is production rate at the surface, and L is the attenuation length. In rock, there are several nuclear mechanisms by which neutrons and muons produce cosmogenic nuclides, each with a distinct depth dependence, or attenuation length. The dominant production mechanism is *nuclear spallation*, in which incoming neutrons with energies greater than the binding energy of the target nuclei split the target into a varying

number of daughter nuclei (Lal and Peters, 1967; Lal, 1988). The attenuation length is usually assumed to be 140-160 g/cm², or about 60-75 cm in sandstone (Brown et al. 1992). A second production mechanism is *negative muon capture*, in which slow negative muons are captured onto target nuclei (Lal, 1988). This reaction in itself can produce cosmogenic nuclide, depending on the target nuclei, but thermal neutrons ejected during the reaction and subsequently involved in thermal neutron capture reactions also produce nuclide (Lal, 1988). As negative muons are weakly interacting particles, production by muons is a less important reaction at the earth's surface (~2-3% of total production), and the attenuation length is significantly longer (Granger and Smith, 2000; Stone, 2000; Granger and Muzikar, 2001), thus this mechanism becomes more important with depth. A final production mechanism, *muon spallation*, involving fast muons, is similar to neutron spallation, has a very long attenuation length, and a similarly low production rate (Lal, 1988; Granger and Smith, 2000).

Production mechanisms and attenuation lengths for ^{26}Al and ^{10}Be are discussed elsewhere (Lal, 1988; Heisinger, 1998; Granger and Smith, 2000; Heisinger et al. 2002a; Heisinger et al. 2002b; Braucher et al. 2003). Principle reactions for production of cosmogenic ^3He in quartz are (1) spallation and (2) thermal neutron capture: $^6\text{Li}(n,\alpha)^3\text{H} \rightarrow ^3\text{He} + \beta^-$ (Lal, 1988). Nucleogenic ^3He is also produced indirectly from U and Th decay via thermal neutron capture on ^6Li . A correction must be made for this component. Cosmogenic neon is produced in quartz by (1) spallation: $\text{Si}(n,4p,xn)\text{Ne}$, (2) thermal neutron capture: $^{24}\text{Mg}(n,\alpha)^{21}\text{Ne}$ and (3) negative muon capture on Na, Mg, Al (Lal, 1988). Additional nucleogenic neon is produced through thermal neutron capture on Mg in a similar way to ^3He and by (4) alpha interactions: $^{18}\text{O}(\alpha,n)^{21}\text{Ne}$, $^{19}\text{F}(\alpha,n)^{22}\text{Na} \rightarrow ^{22}\text{Ne} + \beta^-$.

Accumulation Equations

The accumulation of cosmogenic nuclide in rock, from Granger and Smith (2000), is described by:

$$N = N_{inh} \exp(-\lambda t) + [P_n \exp(-x/L_n) / (\lambda + \varepsilon/L_n)] \cdot [1 - \exp(-t(\lambda + \varepsilon/L_n))] + P_m \cdot A_l \exp(-x/L_{ml}) / (\lambda + \varepsilon/L_{ml}) \cdot [1 - \exp(-t(\lambda + \varepsilon/L_{ml}))]$$

$$\begin{aligned}
 &+ P_{-m} \cdot A_2 \cdot \exp(-x/L_{-m2}) / (\lambda + \varepsilon / L_{-m2}) \cdot [1 - \exp(-t (\lambda + \varepsilon / L_{-m2}))] \\
 &+ P_{fm} \cdot \exp(-x/L_{fm}) / (\lambda + \varepsilon / L_{fm}) \cdot [1 - \exp(-t (\lambda + \varepsilon / L_{fm}))]
 \end{aligned} \tag{2}$$

where N is the concentration of nuclide as a function of time (t) and depth (x). Depth is usually expressed in units corrected for density, or in g/cm^2 . P_n , $P_{-m} \cdot A_1$, $P_{-m} \cdot A_2$ and P_{fm} are terms for production by different mechanisms at the surface, ε is erosion rate, L_n , L_{-m1} , L_{-m2} and L_{fm} are attenuation lengths for each production mechanism, and λ is the radiogenic decay constant. The first term of equation (2) expresses inheritance, which includes nucleogenic components and nuclide accumulated during prior exposure of the sample. The subsequent terms each account for the exponential decrease in production rate with depth and time dependent decay and removal by erosion of the nuclide; term 2 for neutron spallation, terms 3 and 4 for negative muon capture and term 5 for fast muon interactions. Equation (2) can be simplified for stable nuclides ($\lambda = 0$). A minimum age (t_{eff}) can be determined by assuming zero erosion, and a model erosion rate can be found by assuming the steady-state case, in which removal of nuclide by erosion and/or radio-decay equals production (Lal, 1991).

Attenuation length

The depth dependence measured in rock, the apparent attenuation length, is a product of the combined depth profiles for neutron and muon produced nuclide. Neutron produced nuclide dominates the upper part of the profile, while muon produced nuclide becomes increasingly important below ~ 2 m depth (Lal, 1988). Attenuation length is affected by latitude, with longer attenuation lengths at the equator where the energy spectrum is harder (Lal, 1988; Brown et al., 1992). Erosion also can play a role by increasing the relative proportion of muon-produced nuclide in the upper part of the profile, increasing apparent attenuation length (Brook 1994, Hall and Richmond 1974). Apparent attenuation length data from other studies are compiled for comparison in Table 1. Olinger et al. (1992) measured the attenuation length of both ^{10}Be and ^{21}Ne in the Bandolier tuff in New Mexico and obtained values significantly longer than expected, potentially because the profile was ~ 7 m long and muon produced nuclide was an important component of the measured profile. The data of Sarda et al. (1993) agree well with Kurz (1986) for attenuation length in basalt and such longer attenuation lengths are expected at the low

latitudes of both studies. Kurz (1986) explains long ^3He attenuation in basalt by a similar mechanism as we invoke below, a combination of erosion and muon production. Brown et al. (1992) report attenuation length data for one core considered here. Other studies have constrained muon-produced nuclide depth dependence through studies of cliff face exposures (e.g. Stone et al., 1998; Braucher et al., 2003).

The attenuation length for nuclide accumulation due to neutron induced spallation alone (L_n) has not been independently measured in rock, but because neutron production dominates the upper ~2 meters of a given profile, the attenuation length is probably close to but slightly lower than apparent attenuation length measured for this interval, estimates for which fall in the range 140-160 g/cm^2 (see also Table 1), with lower attenuation lengths at high latitudes (Brown et al., 1992, Granger and Smith, 2000). For this study we use a neutron spallation attenuation length at the low end of this range, 140 g/cm^2 , the same as the lowest value we measure for apparent attenuation length in this study (^{21}Ne at Mt. Fleming, see results below). For negative muon capture attenuation length, yield data from Heisinger (1998) and muon stopping functions modified from Stone et al. (1998) provide a 5th order polynomial function for the depth attenuation of this production mechanism (Granger and Smith, 2000). Granger and Smith (2000) simplify this function as the sum of two exponential terms, an approximation which is valid to better than 2% over the depth range of interest. This results in two attenuation lengths for negative muon capture (equation (2), terms 3 and 4), both significantly longer than for neutron spallation alone (of $L_{-m1} = 738$ and $L_{-m2} = 2688$ g/cm^2). The attenuation length for fast muon interactions can be approximated by a single exponential function, based on the data of Heisinger (1998), and is accurate to 3% over the depth range of interest, with an attenuation length of $L_{fm} = 4360$ g/cm^2 (Granger and Smith, 2000). Braucher et al. (2003) measured a slightly longer attenuation length for fast muon production ($L_{fm} = 5300$ g/cm^2).

Production Rates

The production rates used in this study are scaled according to Stone (2000) from values given at sea-level and high-latitude (SLHL) to the altitude and latitude of our sample sites. ^{26}Al and ^{10}Be production rates in quartz are relatively well known; 5.1 ± 0.3 at/g·a (1σ , SLHL) for ^{10}Be and

31.1 ± 1.9 at/g·a (1σ , SLHL) for ^{26}Al (Stone, 2000 and references therein). ^3He production rate has been determined in a variety of materials by a number of authors (Kurz 1987, Kurz et al. 1990, Cerling and Craig 1994, Cerling 1990, Licciardi et al. 1999, Ackert et al. 1998, and Dunai and Wijbrans 2000). We use the value reported in Licciardi et al., 1999, in which $\text{P}^3\text{He}(\text{olivine})=116 \pm 3$ at/g·a (1σ , SLHL). This value can be adjusted for production in quartz with $\text{P}^3\text{He}(\text{quartz})/\text{P}^3\text{He}(\text{olivine}) = 1.19$ (Masarik and Reedy, 1996) to 138 ± 4 at/g·a (1σ , SLHL). The production rate of ^{21}Ne in quartz is 20 ± 4 at/ g·a (1σ , SLHL) based on values given in Niederman (2000) but scaled using Stone (2000) rather than Dunai (2000).

Diffusive loss

Helium diffusive loss from quartz is a major obstacle to its successful use as a chronometer. Trull et al. (1995) found severe (approaching total) helium losses in Death Valley beach terraces. Trull et al. (1991) determined the diffusion coefficient of ^3He in quartz with step heating experiments and found relatively low diffusivity, suggesting that other mechanisms (possibly cracks acting as grain boundaries, and/or diffusion paths produced by spallation tracks) are involved in ^3He diffusion. Diffusion is highly temperature dependent, but even in Antarctica, with below zero annual mean temperatures, diffusional loss appears significant (Brook et al. 1993, Staudacher and Allegre 1991). To date, no studies have suggested measurable diffusive loss of cosmogenic neon.

METHODS AND RESULTS

Two cores were collected from the Transantarctic Mountains of Antarctica during 1989-90 and 1990-91 (Figure 1). Both cores were taken from localities with no significant shielding or snow cover. The Arena Valley core, KBA89-77, was collected from a flat, exposed bedrock surface above the east wall of Arena Valley at 1700 m altitude. The 1.09 m deep core is of the Beacon Heights Orthoquartzite, an upper Devonian formation of the Beacon Supergroup (McElroy and Rose, 1987). It is a mature sandstone with well-rounded, well-sorted, frosted quartz grains up to ~1 mm in diameter, and is 95% quartz with minor matrix components. Most grains (77%) have a single extinction and appear fresh, though they often contain small inclusion trails. A few grains display undulose extinction, subgrain development and minor grain impingement, suggesting a small component of pre-depositional or diagenetic metamorphism. With regard to this study,

undulose extinction or subgrain development, not detectable with grain hand picking techniques employed here, might provide fast diffusion pathways and reduce effective grain size.

The Mount Fleming core, BAK90-79, was collected near the summit of Mt. Fleming at an altitude of 2065 m and is from the Feather Conglomerate, a Permo-Triassic formation of the Beacon Supergroup (McElroy and Rose, 1987). This 1.25 m core is a coarse grained immature sandstone with poorly sorted angular quartz up to 2 mm with frequent quartz cement overgrowths with well developed crystal facets. Quartz content is lower (67% and 70% respectively in two adjacent samples) and grains are of poorer quality than the Arena Valley core, with undulose extinction and subgrain development. Mica, highly degraded feldspar crystals and an abundance of matrix minerals also distinguish this core from the Arena Valley core.

Cores were subsampled and weighed in 3-8 cm lengths and gently disaggregated with a mortar and pestle (samples were not crushed aggressively to avoid breaking grains). Average density for each core was determined by weighing and measuring volume; densities are 2.28 g/cm^3 and 2.09 g/cm^3 for the Arena Valley (KBA89-77) and Mount Fleming (BAK90-79) respectively. Samples were cleaned in water using an ultrasonic probe to remove adhering clay minerals, dried in acetone and dry sieved. The largest available size fraction of each core (0.5-0.71mm for KBA89-77 and 0.71mm-1mm for BAK90-79) were hand picked for clear grains with no inclusions, cracks, adhering matrix material or other obvious defects. Preference was given to well rounded grains as this is an indication of whole grains rather than fragments. The picked grains (~50mg) were weighed after a final cleaning in acetone.

Grains were heated to 600 and then 1500°C in a Modifications Limited Model TC-9 low-Ar blank double vacuum furnace. Exceptions to this heating schedule were for KBA89-77-10, which was heated in three steps, and KBA89-77-4, which had a high blank after the 1500° step. All gas for this sample was extracted by 1600°C . A blank was analyzed for each temperature step, and air standards were analyzed between each sample and blank run. Extracted gas was analyzed on a gas source MAP215-50 mass spectrometer with a Nier type source. Ne and He blanks were

usually less than 5% of the sample, but a few approach 40% of the sample. Uncertainties reflect the high blanks and replicates were analyzed in most cases.

Results for Ne and He are presented in Tables 2 and 3. Seventeen analyses were performed including 8 replicate analyses which agree within 2σ . To correct for nucleogenic ^3He we used the $^3\text{He}/^4\text{He}$ nucleogenic ratio determined by Trull et al., (1991) in a Beacon Supergroup sandstone sample: $0.011 \pm 0.004 \times \text{Ra}$ (1σ , $\text{Ra} = 1.384 \times 10^{-6}$). This ratio depends on the Li, Th and U content of the rock. Correction for radiogenic ^3He is usually $\sim 1\%$ of the sample. The correction for nucleogenic neon is similarly small. Yatsevich and Honda (1997) determined that the $^{21}\text{Ne}_n/^4\text{He}$ ratio in crustal rocks is 4.5×10^{-8} . Correction based on this ratio is less than 3% for both cores except for one sample (KBA89-77-4, for which the correction is 7%). In addition to Ne and He data produced in this study, both cores were previously analyzed for ^{26}Al and ^{10}Be concentrations; data and methods are given in Brown et al. (1992) and Brook (1994). ^3He data from Brook (1994) are not used in this study because they are in general agreement, and because the ^4He concentration, which is important for nucleogenic corrections for ^{21}Ne and ^3He , is variable among replicate analyses, and ^{21}Ne data must therefore be compared to ^3He data from the same core.

^{10}Be and ^{26}Al data for both cores are separately published in Brown et al., (1992) and Brook (1994). For this study, ^{10}Be data was reduced by a factor of 0.875 (Middleton et al., 1993) to account for difference between the $^{10}\text{Be}/^9\text{Be}$ standard used in Gif-sur-Yvette where the ^{10}Be and ^{26}Al measurements were made and that used for calculating ^{10}Be production rates.

Exponential profiles were fit to the data for all four cosmogenic nuclides using a linear regression method (York 1969). Depth profiles for KBA89-77 and BAK90-79 are shown in Figure 2. Attenuation lengths with respective Mean Square Weighted Deviation (MSWD, Wendt and Carl, 1991) values are listed in Table 4. MSWD values are low for all depth profiles except ^3He data for KBA89-77 which has an MSWD=9.58. In fact a few values are too low (the expected MSWD is one) indicating possible over-estimation of analytical errors. If errors were overestimated, then MSWD values are artificially low as are uncertainties on attenuation lengths.

Despite this, it is clear from inspection of the data (Figure 2) that the ^3He and ^{21}Ne depth profiles differ significantly for the Arena Valley (KBA89-77) and Mount Fleming (BAK90-79) cores.

DISCUSSION

Helium diffusional loss

Helium loss can be approximated by comparing the observed ^3He concentration with concentration predicted by using equation (2) and the best estimates of erosion rate and age for each core. Results of this calculation indicate there is significant ^3He loss in these cores: approximately 31% minimum helium loss in the Arena Valley core, and 18% minimum loss in the Mount Fleming core. Greater ^3He loss in the Arena Valley core is consistent with the smaller analyzed grain size; because volume-diffusion related loss is grain size dependent, greater loss is expected in smaller grains. Brook (1994) also report lower ^3He concentrations for smaller grain size in the Mount Fleming core. However, grain quality is lower for the Mount Fleming core and subgrain boundaries may provide fast diffusion pathways thereby reducing the effective grain size. Diffusional loss dependence on grain size is probably slightly offset by the poor grain quality, so a clear relationship between grain size and loss can not be determined from this study. $^3\text{He}/^{21}\text{Ne}$ ratios for both cores are listed in Table 4. A lower $^3\text{He}/^{21}\text{Ne}$ ratio may reflect ^3He diffusional loss, and this relationship is true here with a lower $^3\text{He}/^{21}\text{Ne}$ ratio corresponding to the core with presumed greatest ^3He loss (Arena Valley). Despite sub-zero annual mean temperatures in Antarctica, diffusional loss of ^3He in quartz is significant, though the problem is less severe for larger grain sizes. ^{21}Ne does not seem to suffer from diffusional loss problems.

Age and erosion rate determinations

Minimum ages, assuming zero erosion, and erosion rates assuming steady state erosion are given in Table 4, though ^3He data are probably unreliable because of diffusional loss. Erosion rates are in the same range (222 to 921 mm/Ma) as found in other Antarctic erosion rate studies (e.g. Nishiizumi et al. 1991, ~1000 mm/Ma; Brook et al. 1995, ~50-120 mm/Ma; Summerfield et al. 1999, 133-164 mm/Ma). Minimum ages for each location (1.28 ± 0.33 Ma and 2.56 ± 0.51 Ma in Arena Valley and Mount Fleming respectively) are also consistent with other localities in the Dry

Valleys (Ivy-Ochs et al., 1995; Bruno et al., 1997). Surfaces as old as Miocene have been identified nearby (Schäfer et al., 1999).

The Mount Fleming core (BAK90-79) gives the same steady state erosion rate (~ 0.5 m/Ma) for ^{26}Al and ^{10}Be within 1σ uncertainty. This indicates that concentrations of ^{26}Al and ^{10}Be have probably reached saturation, that is, production of new nuclide is balanced by decay and removal by erosion, such that concentration does not change with time. Age information is lost in this case, but the assumption of steady state erosion is validated, yielding a mean steady state erosion rate of 476 ± 74 mm/Ma. ^{21}Ne may be saturated as well, though as a stable nuclide, saturation means a balance between production and erosional removal, and takes longer to achieve. ^{21}Ne also preserves the most age information, and therefore for a minimum age, we adopt 2.56 ± 0.51 Ma determined from ^{21}Ne data, though the surface may be older than this.

The exposure history of the Arena Valley core (KBA89-77) is apparently more complex, as discussed below, and the most recent exposure is affected by previous accumulation of cosmogenic nuclides. The inherited component is particularly of concern for the stable nuclides as there is no decay to “erase” the samples’ memory for prior exposure. For this core we therefore rely on ^{26}Al and ^{10}Be data. As the ^{26}Al half life is shorter, this nuclide is likely to reach saturation first, and therefore gives the best approximation of steady state erosion rate, 222 ± 67 mm/Ma. Using this erosion rate, we calculate an age with ^{10}Be concentrations of 1.28 ± 0.33 Ma.

Attenuation length

Apparent attenuation lengths for the Arena Valley and Mount Fleming cores, including the first reported for ^{21}Ne in quartz, are presented in Table 4. Measured attenuation lengths are close to expected values in the Mount Fleming core (BAK90-79) and for ^{26}Al and ^{10}Be in the Arena Valley core (KBA89-77). ^{21}Ne and ^3He apparent attenuation lengths for the Arena Valley core, however, are significantly longer than expected at 166 ± 3 and 196 ± 5 g/cm² (1σ) respectively. The ^3He apparent attenuation length is in fact the longest ever reported for any nuclide in any target. In the following discussion we examine the role of diffusional loss, compositional

differences, and a combination of erosion and muon production in producing the high apparent attenuation lengths.

Diffusion

Volume diffusion is temperature dependent, thus solar heating of rock, which produces a temperature gradient from the surface, can produce a corresponding gradient in the rate of diffusion. The resultant preferential diffusion from the top of the core would increase the apparent attenuation length. Helium loss does appear to be greater for the Arena valley core. However, diffusional loss is has not been reported for ^{21}Ne , and thus cannot explain the anomalously long ^{21}Ne attenuation length measured in the Arena Valley core. Further, studies of solar heating in Antarctica show that significant temperature changes (up to 25°C) can occur in exposed rock, but such heating only penetrates a few cm into the surface, not enough to effect the changes seen in the Arena Valley core (McKay and Friedman 1985). Further, Brook (1994) report identical attenuation length for different grain size fractions for the Mount Fleming core, despite greater diffusional loss for the smaller size fraction. Diffusion is clearly an important factor in the concentration of ^3He , but probably does not play a significant role in determining attenuation length.

Composition

Production rate is composition dependent, therefore changes in composition with depth can cause anomalously long attenuation lengths. In the case of ^3He production, ^6Li is the important element for thermal neutron capture of spallation-produced and muogenic thermal neutrons. An increase in Li concentration with depth would increase thermal neutron capture on ^6Li and correspondingly ^3He production rate at depth, increasing apparent attenuation length. Data on compositional variation with depth is not available for this study. However, production rate dependence on composition is small, causing only about 20% production rate difference between quartz and olivine targets (Masarik and Reedy 1996). It is unlikely that compositional variations in the core are significant enough to explain the anomalously long attenuation lengths of ^3He and ^{21}Ne in the Arena Valley core.

Non depth-dependent composition variations, however, can also affect the apparent attenuation length. In the case of ^3He , muon production is a function of Li content. Because of the longer muon attenuation lengths relative to neutron production, a higher muogenic component of the total production leads to a longer apparent attenuation length. Composition differences between the cores do indicate slightly higher Li content in the Arena Valley core (3.28 ppm v. 5.0 ppm; Brook, 1994), and thus potentially more muogenic production in that core. However, as will be explored in the next section, this compositional difference alone is not significant enough to explain the anomalously long attenuation lengths of ^{21}Ne and ^3He found in the Arena Valley core.

Erosion and Muon production

Apparent attenuation length is the result of combined neutron and muon production. Under low erosion rate conditions the muogenic component of total nuclide production is low and the apparent attenuation length in the near surface is thus very close to that for neutron production alone. Deeper in the profile, attenuation lengths are longer, but concentrations are insignificant compared to concentrations in the near surface. As erosion rate increases, material from depth is brought to the surface more quickly, causing total concentrations to decrease, but increasing the relative proportion of muon produced nuclide in the near surface. The result is a longer apparent attenuation length. This affects the stable nuclides (^{21}Ne and ^3He) more strongly than the radionuclides (^{26}Al and ^{10}Be), because decay erases nuclide originally produced deeper below the surface and “inherited” through erosion. Each erosion rate condition is associated with a characteristic steady state attenuation length and surface concentration. If erosion rate at a site changes, during the transition between steady state cases, the attenuation length and concentrations associated with the former erosion conditions will be preserved for some time, affecting the profile as it develops towards steady state under the new erosion conditions. Because of this relationship between erosion rate and apparent attenuation length, important information about exposure history can be gained by modeling apparent attenuation lengths. We believe this to be the primary factor responsible for the anomalously long Arena Valley attenuation lengths, and explore this further below.

Construction of Model. To investigate the range of erosion histories which might produce the exceptionally long attenuation lengths observed for the stable nuclides in the Arena Valley core, we construct a simple model based on Equation (2). The model allows the user to input a variable erosion rate with time over a 10 Ma period. Values for P_n , P_{-m} , A_1 , A_2 , P_{fm} , L_n , L_{-m1} , L_{-m2} , and L_{fm} for ^{26}Al and ^{10}Be are given by Granger and Smith (2000). (Revised values for fast muon attenuation length (L_{fm}) are published in Braucher et al. (2003) but were not used because as our modeling reveals, fast muon production rate (B) is relatively unimportant in producing good model results for ^{21}Ne and ^3He). A_1 , A_2 and all three muonogenic attenuation lengths (L_{-m1} , L_{-m2} , and L_{fm}) are related only to muon interactions with quartz and so can be used for describing any nuclide. Muon production rates P_{-m} (for negative muon production), and P_{fm} (for fast muon production), however, are particular to the nuclide, and values of P_{-m} and P_{fm} for ^3He and ^{21}Ne are not known. Instead, we constrained these values through iterative modeling, as will be further explained below.

The ability of each model run to reproduce the measured nuclide data for the Arena Valley core was assessed by calculating an MSWD value for the model fit to the measured data for each nuclide. This value was then normalized by dividing by the optimum MSWD values given in Table 4. To obtain a good fit, the model must reproduce both the final concentration and the final attenuation length of the measured data. We evaluated these semi-independently by calculating an MSWD value for the model fit to the actual measured data, which assesses our ability to reproduce measured concentrations (and to a lesser extent, the attenuation length), and by calculating an MSWD value for the model fit to data in which both are normalized to a concentration of 1 at the surface, which assesses only the quality of the fit to the attenuation length. This was particularly necessary, as our Helium data has been affected by significant diffusional loss, and thus measured concentrations are always lower than those produced in our model. These results were examined individually, then a final, averaged MSWD value was calculated for each model run by averaging the MSWD values for Al, normalized Al, Be, normalized Be, Ne, normalized Ne and normalized He data. Normalized MSWD values of less than 2 for a given erosion history yield acceptable fits, that is, the MSWD is twice that of the best

fit MSWD, and a perfect fit would yield a normalized MSWD value of 1. Best fits obtained through our modeling were close to 1.03.

In order to constrain unknown or poorly known parameters built into the model, we made a few necessary simplifying assumptions. Primarily, we assumed a strictly three phase erosion history, though future versions of this model may incorporate a greater number of erosion steps. The final phase, phase III, is constrained by ^{26}Al and ^{10}Be erosion rate and minimum age data for the Arena Valley core to a low erosion rate of ~ 0.2 m/Ma for a period of ~ 1.3 Ma (Table 4). The erosion rates during phase I and phase II are variables in our model. We also vary the length of phase I and II, exploring five pairs (I=8.6 Ma, II=0.1 Ma; I=8.5 Ma, II=0.2 Ma; I=8.2 Ma, II= 0.5 Ma; I=7.7 Ma, II=1 Ma; and I=6.7 Ma, II=2 Ma). Nuclide concentrations approach steady state values within a few million years. For this reason, we only explored phase II durations up to 2 Ma. For longer phase II durations, steady state values are reached before phase III begins and phase I erosion rate conditions matter little or not at all to the final profile: the scenario collapses to a two-stage erosion history set by phase II and phase III conditions. This scenario is accounted for by modeling scenarios in which phase I and phase II erosion rates are the same, and so does not need to be modeled separately by increasing phase II duration to more than 2 Ma. For similar reasons it is acceptable to run the model for only 10 Ma total duration, as a longer total duration would not affect the profiles (in fact, a shorter duration could be used). P_{-m} and P_{fm} production rate values for ^{21}Ne and ^3He are also varied during certain model runs.

We began by assuming arbitrary values for P_{-m} and P_{fm} , then calculating a field of normalized MSWD values for combinations of phase I and phase II erosion rates varying over three orders of magnitude, from ~ 44 m/Ma to 0.04 m/Ma, for five different phase II durations (0.1 Ma, 0.2 Ma, 0.5 Ma, 1.0 Ma and 2.0 Ma). We then ran a series of models in which the best fit combination of phase I and II erosion rates and phase II duration was held fixed while values of P_{-m} and P_{fm} for both ^{21}Ne and ^3He were varied over three orders of magnitude, obtaining a best fit for a combination of these values. We iterated several times, first holding constant P_{-m} and P_{fm} values while allowing the erosion history to vary, then holding constant the erosion history and finding the best combination of P_{-m} and P_{fm} values. The solution converged after six iterations. It is worth

noting that our results rely heavily on ^{21}Ne data, as the other nuclides are fit reasonably well by most erosion scenarios (excluding the case of low erosion rates for both phase I and II).

Erosion History. Erosion history results for the best production rate values ($P_{\text{mNe}} = 0.001$ at/g/yr, $P_{\text{fmNe}} = 1$ at/g/yr, $P_{\text{mHe}} = 0.16$ at/g/yr, $P_{\text{fmHe}} = 0.001$ at/g/yr at SLHL) are plotted in column 1 of Figure 3 for five different phase I and II durations. Combinations of phase I and II erosion rates which fall within the lowermost contour only produce acceptable fits to the measured data (normalized MSWD < 2), and best fits for each scenario are indicated. The lowest averaged normalized MSWD value is produced for the erosion history: ~ 7 m/Ma erosion for 6.7 Ma, followed by erosion at ~ 0.7 m/Ma for 2 Ma and finally erosion at ~ 0.2 m/Ma for 1.3 Ma (Fig. 3). It is immediately apparent from the results for all phase II durations that low values for both phase I and phase II erosion rates are strongly ruled out: erosion rate must have been higher at some point in the past than it is today, at least ~ 1 m/Ma for either phase I or II.

The best model results are obtained for scenarios in which the erosion history essentially collapses to two rather than three phases. This happens either when phase II duration is very short, in which case it has only a minimal effect on the overall evolution of the profile (Fig. 3a), or when phase II duration is very long, in which case the profile approaches steady state during phase II and the inherited component from phase I matters little to the profile evolution (Fig. 3e). Scenarios with intermediate phase II durations represent intermediate cases (Figs. 3b, 3c, 3d). In this scenario, long attenuation lengths are produced by moderately high erosion rates during the initial phase (phase I or II) while concentrations are kept relatively low. During the final phase (phase III), a decrease in erosion rate allows concentrations to rise and attenuation lengths to fall slightly to values which fit the ^3He and ^{21}Ne data for the Arena Valley core. In this case, the erosion rate was approximately 5 times higher (~ 1 m/Ma) prior to 1.3 Ma (phase III).

The data can also be fit by a very different scenario (Figs. 3a, 3b) which consists of a long period of erosion at very low erosion rate during phase I, followed by a sharp but short increase in erosion rate during phase II, followed by a 1.3 Ma period under low erosion rate conditions in phase III. During the long initial exposure, nuclide concentrations build up significantly both in

the near surface, where neutron production dominates, and deeper, where muon production is significant and attenuation lengths are long. During phase II, rapid exhumation brings this deeper material to the surface. Concentrations are lowered, but attenuation length is increased. The final period allows accumulation of neutron produced nuclide, reducing the apparent attenuation length, but the memory of the long attenuation length material is retained, and the resultant attenuation lengths are still quite long, in the range observed for ^3He and ^{21}Ne in the Arena Valley core. Removal of 1 to 3 meters of material during phase II yields the best results.

Throughout our modeling, we assume a fixed erosion rate and duration for phase III based on values determined using ^{26}Al and ^{10}Be data (Table 4). 1.3 Ma is a minimum age, and therefore phase III duration must be at least this long or longer. During the low erosion rate conditions of phase III, attenuation length falls. Therefore if the duration of phase III is longer than 1.3 Ma, the preceding erosion history would have to be even more dramatic (higher phase I and II erosion rates or more removal of material during phase II) in order to produce long enough attenuation lengths in the near surface by the close of phase II conditions to survive during phase III conditions.

Production Rate Values. Production rate results for several different erosion histories are shown in columns 2 and 3 of Figure 3. Acceptable values fall within the lowermost contour (MSWD<2). Results are robust regardless of erosion history, as demonstrated by the nearly identical results for 5 significantly different erosion histories. High values of P_{-m} for both ^{21}Ne and ^3He are precluded, and best fits are obtained for $P_{-m}\text{Ne}=0.001$ at/g/a and $P_{-m}\text{He}=0.16$ at/g/a at SLHL. For both nuclides, P_{fm} values are relatively unconstrained, though for the case of the best fit erosion history values are $P_{fm}\text{Ne}=1$ at/g/a and $P_{fm}\text{He}=0.001$ at/g/a at SLHL.

Arena Valley. In the case of the Arena Valley core, erosion rate was clearly higher at some point in the past. A simple two-stage history, in which erosion rate prior to 1.3 Ma was approximately five times higher produces a profile which closely matches our measured data (Fig. 4a). However, good fits are also obtained for low background erosion rates punctuated by a period of rapid erosion just prior to 1.3 Ma (Fig. 4b). These findings have strong implications for the

geomorphic history of the Dry Valleys region of Antarctica. In the first case, a large scale shift in erosion rate at 1.3 Ma could imply a regional change in climate conditions. A period of punctuated erosion suggests local scouring of a region, possibly due to glacial erosion. Regardless, our data and modeling indicate there was a significant change in the erosion conditions at the Arena Valley site prior to or at 1.3 Ma which begs a geomorphic explanation. This observation is particularly interesting in the context of other studies which indicate a period of prolonged stability in the Dry Valleys region (Summerfield et al., 1999; Ivy-Ochs et al., 1995; Bruno et al., 1997; Schäfer et al., 1999; Sugden et al., 1999). Further studies of this kind should help in developing an understanding of the landscape evolution of the Dry Valleys over the last few million years.

Mount Fleming. Using production rate values determined for the Arena Valley core and a simple erosion history, we are unable to adequately model measured data for the Mount Fleming core. Muon production rates are composition dependent, in which case values could be different at the Mount Fleming site. However, attenuation lengths at the Mount Fleming site are very low, and even for the unlikely case of zero values for muon production we cannot fit the measured data. It is therefore possible that this site experienced a more complicated erosion history as well.

Implications. The success of our modeling in placing meaningful and significant constraints on both production rate values and erosion histories is encouraging. This is perhaps the most significant implication of our efforts: with refined production models and densely sampled data (every ~10 cm in this study) for multiple nuclides, erosion histories may be successfully extracted from depth profile data. We also were able to obtain values for negative muon production (P_m) for ^{21}Ne and ^3He . It is difficult for us to assess whether the values for $P_m^{21}\text{Ne}$ and $P_m^3\text{He}$ are appropriate only to the Arena Valley site, or if they may be generally applied. Significant theoretical and experimental studies specifically focused on the problem of muon production rates for ^{21}Ne and ^3He in quartz are necessary to fully constrain these values. Until this work is undertaken, our modeling provides approximate production rates.

CONCLUSION

In this study, we analyzed ^{21}Ne and ^3He concentrations in two sandstone cores from the Dry Valley Regions of Antarctica. Combined with ^{26}Al and ^{10}Be data from Brown et al. (1992) and Brook (1994), we determined steady state erosion rate values, minimum ages and apparent attenuation lengths. For the Mount Fleming core, minor diffusional loss (estimated at 18%) has affected ^3He concentrations. Data for the other nuclides indicates a protracted period (at least 2.56 ± 0.51 Ma) of relatively slow erosion (476 ± 74 mm/Ma). Attenuation lengths for all four nuclides are within the normally observed range (140-160 g/cm², Brown et al., 1992).

In contrast, the Arena Valley core appears to have experienced a more complicated erosion history. Diffusional loss of ^3He is more significant, approximately 31%. ^{26}Al and ^{10}Be data yield an erosion rate of 222 ± 67 mm/Ma over the past 1.28 ± 0.33 Ma. However, the exceptionally long attenuation lengths measured for ^{21}Ne and ^3He (166 ± 3 and 196 ± 5 1σ respectively) indicate a complicated prior exposure history. Modeling the combined effects of erosion rate and muon production, our results indicate that erosion rate for this core was higher prior to ~ 1.3 Ma with good results obtained for erosion rates approximately 5 times greater in the past. Model scenarios in which a long period of slow erosion is punctuated by rapid removal of surface material at approximately ~ 1.3 Ma also produce good results. Regardless, the Arena valley site must have experienced higher erosion rates in the past with a significant change to modern low erosion rate conditions occurring at approximately ~ 1.3 Ma.

In addition to constraining the erosion history of the Arena Valley site through our modeling efforts, we were also able to constrain preliminary values for negative muon production for ^{21}Ne and ^3He ($P_{-m}\text{Ne}=0.001$ at/g/a and $P_{-m}\text{He}=0.16$ at/g/a at SLHL), though it remains to be seen if these values can be applied to other sites, and will be supported by theoretical and experimental studies of muon production. An important implication of this study is that it may be possible with refined accumulation models, dense sampling, and data for multiple nuclides, to extract a specific exposure history for a sample.

REFERENCES

- Ackert, R.P., Singer, B.S., Guillou, H., Kurz, M.D., 1998, Cosmogenic ^3He production rates over the last 125,000 years; calibration against $^{40}\text{Ar}/^{39}\text{Ar}$ and unspiked K-Ar ages of lava flows: Geological Society of America Abstracts with Programs, v. 30, p. 299.
- Braucher, R., Brown, E.T., Bourles, D.L. and Colin, F., 2003, In situ produced ^{10}Be measurements at great depths: implications for production rate by fast muons: Earth and Planetary Science Letters, v. 211, p. 251-258.
- Brook, E.J., 1994, Surface Exposure Geochronology Using Cosmogenic Nuclides: Applications in Antarctic Glacial Geology: Doctoral Dissertation, Woods Hole Oceanographic Institution MIT Joint Program in Oceanography/Applied Ocean Science and Engineering, WHOI-93-50, 232 p.
- Brook, E.J., Brown, E.T., Kurz, M.D., Ackert, R.P., Raisbeck, G.M., and Yiou, F., 1995, Constraints on age, erosion and uplift of Neogene glacial deposits in the Transantarctic Mountains using in situ cosmogenic ^{10}Be and ^{26}Al : Geology, v. 23, p. 1063-1066.
- Brook, E.J., Kurz M.D., Denton, G.H., and Ackert, R.P.Jr., Denton, G.H., Brown, E.T., Raisbeck, G.M., and Yiou, F., 1993, Chronology of Taylor Glacier advances in Arena Valley, Antarctica, using in situ cosmogenic ^3He and ^{10}Be : Quaternary Research, v. 39, p. 11-23.
- Brown, E.T., Brook, E.J., Raisbeck, G.M., Yiou, R., Kurz, M., 1992, Effective attenuation lengths of cosmic rays producing ^{10}Be and ^{26}Al in quartz: implications for exposure age dating: Geophysical Research Letters, v. 19 p. 369-372.
- Bruno, L.A., Baur, H., Graf, T., Schlüchter, C., Signer, P., and Wieler, R., 1997, Dating of Sirius Group tillites in the Antarctic Dry Valleys with cosmogenic ^3He and ^{21}Ne : Earth and Planetary Science Letters, v. 147, p. 37-54.
- Cerling, T.E., 1990, Dating geomorphological surfaces using cosmogenic ^3He : Quaternary Research, v. 33, p. 148-156.
- Cerling, T.E., and Craig, H., 1994, Cosmogenic ^3He production rates from 39N to 46N latitude, western USA and France: Geochimica et Cosmochimica Acta, v. 58, p. 249-255.
- Dunai, T., 2000, Scaling factors for production rates of in situ produced cosmogenic nuclides: a critical reevaluation: Earth and Planetary Science Letters, v. 176, p. 157-169.
- Dunai, T., and Wijbrans, J.R., 2000, Long term cosmogenic ^3He production rates (152 ka-1.35 Ma) from $^{40}\text{Ar}/^{39}\text{Ar}$ dated basalt flows at 29°N latitude: Earth and Planetary Science Letters, v. 176, p. 147-156.
- Granger, D., and Muzikar, P., 2001, Dating sediment burial with in situ-produced cosmogenic nuclides: theory, techniques and limitations: Earth and Planetary Science Letters, v. 188, p. 269-281.
- Granger, D., and Smith A., 2000, Dating buried sediments using radioactive decay and muonogenic production of ^{26}Al and ^{10}Be : Nuclear Instrumentation and Methods in Physics Research B, v. 172, p. 822-826.
- Hall, H.E., and Richmond, M.E., 1974, Stopping rate and energy loss of cosmic ray muons in sand: Journal of Geophysical Research, v. 35, p. 5503-5506.
- Heisinger, B.P., 1998, Myonen-induzierte Produktion von Radionukliden, Ph.D. thesis, Tech. Univ. München, 153 p.
- Heisinger, B., Lal, D., Jull, A.J.T., Kubik, P., Ivy-Ochs, S., Neumaier, S., Knie, K., Lazarev, V., and Nolte, E., 2002a, Production of selected cosmogenic radionuclides by muons: 1. Fast muons: Earth and Planetary Science Letters, v. 200, p. 345-355.
- Heisinger, B., Lal, D., Jull, A.J.T., Kubik, P., Ivy-Ochs, S., Knie, K and Nolte, E., 2002b, Production of selected cosmogenic radionuclides by muons: 2. Capture of negative muons: Earth and Planetary Science Letters, v. 200, p. 357-369.
- Ivy-Ochs, S., Schlüchter, C., Kubik, P., Dittrich-Hannen, B., and Beer, J., 1995, Minimum ^{10}Be exposure ages of early Pliocene for the Table Mountain plateau and the Sirius Group at Mount Fleming, Dry Valleys, Antarctica: Geology, v. 23, p. 1007-1010.
- Kurz, M.D., 1986, In situ production of terrestrial cosmogenic helium and some applications to geochronology: Geochimica et Cosmochimica Acta, v. 50, p. 2855-2862.
- Kurz, M.D., 1987, Erratum: Correction to Kurz (1986b), Geochimica et Cosmochimica Acta, v. 51, p. 1019.
- Kurz, M.D., Colodner, D., Trull, T.W., Moore, R.B., and O'Brien, K., 1990, Cosmic ray exposure dating with in situ produced cosmogenic ^3He : Results from young lava flows: Earth and Planetary Science Letters, v. 97, p. 177-189.
- Lal, D., 1988, In situ-produced cosmogenic isotopes in terrestrial rocks: Ann. Rev. Earth Planet. Sci., v. 16, p. 355-388.

Chapter 6- Depth dependence of cosmogenic ^3He and ^{21}Ne

- Licciardi, J.M., Kurz, M.D., Clark, P.U., Brook, E.J., 1999, Calibration of cosmogenic ^3He production rates from Holocene lava flows in Oregon, USA, and effects of the Earth's magnetic field: *Earth and Planetary Science Letters*, v. 172, p. 261-271.
- Masarik, J., and Reedy, R.C., 1996, Monte Carlo simulation of the in-situ-produced cosmogenic nuclides: *Radiocarbon*, v. 38, p. 163.
- McElroy, C.T., and Rose, G., 1987, *Geology of the Beacon Heights Area: Southern Victoria Land, Antarctica*: New Zealand Geological Survey Miscellaneous Series Map 15, DSIR, Wellington, New Zealand.
- McKay, C.P., and Friedman, E.I., 1985, The cryptoendolithic microbial environment in the Antarctic cold desert: temperature variations in nature: *Polar Biology* v. 4, p. 19-25.
- Niedermaier, S., Graf, Th., Kim, J., Kohl, C., Marti, K., and Nishiizumi, K., 1994, Cosmic-ray-produced ^{21}Ne in terrestrial quartz: the neon inventory of Sierra Nevada quartz separates: *Earth and Planetary Science Letters*, v. 125, p. 341-355.
- Nishiizumi, K., Kohl, C.P., Arnold, J.R., Klein, J., Fink, D., and Middleton, R., 1991, Cosmic ray produced ^{10}Be and ^{26}Al in Antarctic rocks: exposure and erosion history: *Earth and Planetary Science Letters*, v. 104, p. 440-454.
- Nishiizumi, K., Winterer, E.L., Kohl, C.P., Klein, J., Middleton, R., Lal, D., and Arnold, J.R., 1989, Cosmic ray production rates of ^{10}Be and ^{26}Al in quartz from glacially polished rocks: *Journal of Geophysical Research*, v. 94, p. 17907-17915.
- Olinger, C.T., Poths, J., Nishiizumi, K., Kohl, C.P., Finkel, R.C., Caffè, M.W., Southon, J., and Proctor, I., 1992, Attenuation Lengths of Cosmogenic Production of ^{26}Al , ^{10}Be and ^{21}Ne in Bandolier Tuff: *EOS* v. 73(14), p. 185.
- Sarda, P., Staudacher, T., Allegre, C.J., and Lecomte, A., 1993, Cosmogenic neon and helium at Reunion: measurement of erosion rate: *Earth and Planetary Science Letters*, v. 119, p. 405-417.
- Schäfer, J., Ivy-Ochs, S., Wielier, R., Leya, I., Baur, H., Denton, G., and Schlüchter, C., 1999, Cosmogenic noble gas studies in the oldest landscape on earth: surface exposure ages of the Dry Valleys, Antarctica: *Earth and Planetary Science Letters*, v. 167, p. 215-226.
- Staudacher, T., and Allegre, C.J., 1991, Cosmogenic neon in ultramafic nodules from Asia and in quartzite from Antarctica: *Earth and Planetary Science Letters*, v. 106, p. 87-102.
- Staudacher, T., Allegre, C., 1990, Cosmogenic ^{21}Ne : a new tracer in geochemistry: *EOS*, v. 71 fall meeting, p. 1668.
- Stone, J., 2000, Air pressure and cosmogenic isotope production: *Journal of Geophysical Research*, v. 105, p. 23,753-23,759.
- Stone, J.O.H., Evans, J.M., Fifield, L.K., Allan, G.L., and Cresswell, R.G., 1998, Cosmogenic chlorine-36 production in calcite by muons: *Geochimica et Cosmochimica Acta*, v. 62, p. 433-454.
- Sugden, d., Summerfield, M., Denton, G., Wilch, T., McIntosh, W., Marchant, D., Rutherford, R., 1999, Landscape development in the Royal Society Range, southern Victoria Land, Antarctica: stability since the mid-Miocene: *Geomorphology*, v. 28, p. 181-200.
- Summerfield, M.A., Stuart, F.M., Cockburn, H.A.P., Sugden, D.E., Denton, G.H., Dunai, T., Marchant, D.R., 1999, Long-term rates of denudation in the Dry Valleys, Transantarctic Mountains, southern Victoria Land, Antarctica based on in-situ-produced cosmogenic ^{21}Ne : *Geomorphology*, v. 27, p. 113-129.
- Trull, T.W., Brown, E.T., Marty, B., Raisbeck, G.M., Yiou, F., 1995, Cosmogenic ^{10}Be and ^3He accumulation in Pleistocene beach terraces in Death Valley, California, USA: Implications for cosmic-ray exposure dating of young surfaces in hot climates: *Chemical Geology* v. 119, p. 191-207.
- Trull, T.W., Kurz, M.D., and Jenkins, W.J., 1991, Diffusion of cosmogenic ^3He in olivine and quartz: Implications for surface exposure dating: *Earth and Planetary Science Letters*, v. 103, p. 241-256.
- Wendt, I., and Carl, C., 1991, The statistical distribution of the mean squared weighted deviation: *Chemical Geology*, v. 86, p. 275-285.
- Yatsevich, I., and Honda, M., 1997, Production of nucleogenic neon in the Earth from natural radioactive decay: *Journal of Geophysical Research*, B, Solid Earth and Planets, v. 102, p. 10291-10298.
- York, D., 1969, Least squares fitting of a straight line with correlated errors: *Earth and Planetary Science Letters*, v. 5, p. 320-324.

TABLE 1. Compiled attenuation length data

Isotope	attenuation in g/cm^2	location	reference
^{21}Ne	178	Los Alamos, NM	Olinger et al. (1992)
^{10}Be	172		
^3He	170 ± 2	Hawaii	Kurz (1986)
	165 ± 7		
	164 ± 3		
	110 ± 10		
	185 ± 10		
^3He	165.5 ± 6.2	Reunion Island	Sarda et al. (1993)
^{21}Ne	159 ± 10		
all errors 1σ			

Chapter 6- Depth dependence of cosmogenic ^3He and ^{21}Ne

TABLE 2. BAK90-79 He and Ne data

Sample Name	depth g/cm ²	$^{20}\text{Ne}/^{22}\text{Ne}$	$^{21}\text{Ne}/^{22}\text{Ne}$	^{20}Ne 10 ⁹ at/g	$^{21}\text{Ne}_{\text{total}}$ Mat/g	$^{21}\text{Ne}_n$ Mat/g	$^{21}\text{Ne}_c$ Mat/g	4He 10 ¹² at/g	$^3\text{He}/^4\text{He}$ Ra	$^3\text{He}_{\text{total}}$ Mat/g	$^3\text{He}_r$ Mat/g	$^3\text{He}_c$ Mat/g
1,2-i-600C	9.14 ± 0.03	0.0957 ± 0.0011	16.45 ± 0.83	120.18 ± 6.34	0.07 ± 0.01	120.11 ± 6.34	1.58 ± 0.18	441.44 ± 33.06	963.51 ± 131.96	0.02 ± 0.01	963.49 ± 131.96	
1,2-i-1500C	8.97 ± 0.02	0.1077 ± 0.0008	20.65 ± 1.04	181.20 ± 9.29	0.10 ± 0.01	181.10 ± 9.29	2.12 ± 0.26	0.66 ± 0.92	1.92 ± 2.71	0.03 ± 0.01	1.89 ± 2.71	
total	13.6 ± 5			301.38 ± 11.25	0.17 ± 0.01	301.22 ± 11.25	3.69 ± 0.32	188.89 ± 23.07	965.43 ± 131.99	0.06 ± 0.02	965.38 ± 131.99	
1,2-ii-600C	9.63 ± 0.08	0.0607 ± 0.0069	16.21 ± 0.87	53.34 ± 11.95	0.25 ± 0.02	53.08 ± 11.95	5.61 ± 0.34	105.28 ± 5.33	817.20 ± 64.38	0.09 ± 0.03	817.12 ± 64.38	
1,2-ii-1500C	8.49 ± 0.03	0.1434 ± 0.0014	18.28 ± 0.98	246.44 ± 13.65	0.94 ± 0.06	245.50 ± 13.65	20.87 ± 1.23	0.80 ± 0.05	23.15 ± 1.89	0.32 ± 0.12	22.83 ± 1.90	
total	13.6 ± 5			299.78 ± 18.15	1.19 ± 0.06	298.58 ± 18.15	26.48 ± 1.27	22.93 ± 1.85	840.35 ± 64.40	0.40 ± 0.12	839.95 ± 64.40	
1,2-iii-600C	9.65 ± 0.03	0.0565 ± 0.0005	21.91 ± 1.13	62.37 ± 3.37	0.20 ± 0.01	62.17 ± 3.37	4.42 ± 0.22	133.82 ± 2.05	818.24 ± 43.15	0.07 ± 0.02	818.17 ± 43.15	
1,2-iii-1500C	8.83 ± 0.03	0.1166 ± 0.0008	25.86 ± 1.33	256.46 ± 13.44	0.82 ± 0.04	255.64 ± 13.44	18.15 ± 0.91	1.76 ± 0.06	44.31 ± 2.74	0.28 ± 0.10	44.03 ± 2.74	
total	13.6 ± 5			318.82 ± 13.85	1.02 ± 0.04	317.81 ± 13.85	22.56 ± 0.94	27.62 ± 1.53	862.55 ± 43.23	0.34 ± 0.10	862.20 ± 43.23	
6-600C	9.77 ± 0.04	0.0484 ± 0.0007	11.26 ± 0.57	22.31 ± 1.37	0.08 ± 0.01	22.23 ± 1.37	1.76 ± 0.26	175.98 ± 22.79	429.50 ± 84.73	0.03 ± 0.01	429.48 ± 84.73	
6-1500C	9.05 ± 0.02	0.1002 ± 0.0007	21.71 ± 1.10	170.84 ± 8.83	0.54 ± 0.03	170.30 ± 8.83	12.00 ± 0.64	4.61 ± 0.29	76.60 ± 6.34	0.18 ± 0.07	76.41 ± 6.34	
total	84.3 ± 4.3			193.15 ± 8.93	0.62 ± 0.03	192.53 ± 8.93	13.76 ± 0.69	26.57 ± 4.21	506.10 ± 84.97	0.21 ± 0.07	505.89 ± 84.97	
8-600C	9.70 ± 0.03	0.0494 ± 0.0005	13.65 ± 0.69	28.73 ± 1.64	0.13 ± 0.01	28.60 ± 1.64	2.88 ± 0.26	95.24 ± 5.37	380.11 ± 40.00	0.04 ± 0.02	380.07 ± 40.00	
8-1500C	9.18 ± 0.03	0.0874 ± 0.0007	16.65 ± 0.84	105.90 ± 5.50	0.63 ± 0.04	105.27 ± 5.50	13.97 ± 0.79	0.41 ± 0.12	7.87 ± 2.28	0.21 ± 0.08	7.65 ± 2.28	
total	132 ± 4			134.63 ± 5.74	0.76 ± 0.04	133.87 ± 5.74	16.85 ± 0.83	16.63 ± 1.69	387.98 ± 40.06	0.26 ± 0.08	387.72 ± 40.06	
11-i-600C	9.79 ± 0.03	0.0434 ± 0.0004	13.58 ± 0.68	19.97 ± 1.14	0.33 ± 0.02	19.64 ± 1.14	7.29 ± 0.43	32.76 ± 1.25	330.42 ± 23.25	0.11 ± 0.04	330.30 ± 23.25	
11-i-1500C	9.50 ± 0.02	0.0660 ± 0.0008	19.88 ± 1.00	77.46 ± 4.23	0.45 ± 0.03	77.00 ± 4.23	10.11 ± 0.63	1.29 ± 0.24	18.08 ± 3.55	0.15 ± 0.06	17.93 ± 3.55	
total	174.7 ± 4			97.42 ± 4.38	0.78 ± 0.03	96.64 ± 4.38	17.39 ± 0.76	14.48 ± 0.85	348.50 ± 23.52	0.26 ± 0.07	348.23 ± 23.52	
11-ii-600C	9.83 ± 0.03	0.0474 ± 0.0006	11.82 ± 0.59	22.07 ± 1.32	0.29 ± 0.01	21.78 ± 1.32	6.38 ± 0.32	32.06 ± 0.92	283.03 ± 16.47	0.10 ± 0.04	282.94 ± 16.47	
11-ii-1500C	9.42 ± 0.04	0.0714 ± 0.0007	16.90 ± 0.85	75.95 ± 4.02	0.63 ± 0.03	75.32 ± 4.02	14.04 ± 0.71	0.82 ± 0.05	15.88 ± 1.22	0.21 ± 0.08	15.67 ± 1.22	
total	174.7 ± 4			98.02 ± 4.23	0.92 ± 0.03	97.10 ± 4.23	20.41 ± 0.78	10.58 ± 0.56	298.91 ± 16.51	0.31 ± 0.09	298.60 ± 16.51	
14-600C	9.85 ± 0.04	0.0369 ± 0.0004	16.19 ± 0.82	12.96 ± 0.97	0.15 ± 0.01	12.81 ± 0.97	3.33 ± 0.17	30.54 ± 0.71	140.70 ± 7.89	0.05 ± 0.02	140.65 ± 7.89	
14-1500C	9.64 ± 0.02	0.0503 ± 0.0003	20.13 ± 1.20	44.49 ± 2.36	1.40 ± 0.08	43.09 ± 2.36	31.03 ± 1.74	0.15 ± 0.01	6.32 ± 0.67	0.47 ± 0.17	5.85 ± 0.69	
total	253.4 ± 8.1			57.45 ± 2.55	1.55 ± 0.08	55.91 ± 2.55	34.36 ± 1.75	3.09 ± 0.21	147.02 ± 7.92	0.52 ± 0.17	146.50 ± 7.92	

Note: Errors given as 1sigma machine counting statistics error or propagated error.

TABLE 3. KBA89-77 He and Ne data

Sample Name	depth (g/cm ²)	$^{20}\text{Ne}/^{22}\text{Ne}$	$^{21}\text{Ne}/^{22}\text{Ne}$	^{20}Ne 10 ⁹ at/g	$^{21}\text{Ne}_{\text{total}}$ Mat/g	$^{21}\text{Ne}_{\text{n}}$ Mat/g	$^{21}\text{Ne}_{\text{c}}$ Mat/g	4He 10 ¹² at/g	$^3\text{He}/^4\text{He}/$ Ra	$^3\text{He}_{\text{total}}$ Mat/g	$^3\text{He}_{\text{r}}$ Mat/g	$^3\text{He}_{\text{c}}$ Mat/g
1-i-600C		9.65 ± 0.03	0.0527 ± 0.0004	21.29 ± 0.34	52.19 ± 1.23	0.13 ± 0.01	52.05 ± 1.23	2.97 ± 0.22	64.79 ± 4.68	266.48 ± 27.84	0.05 ± 0.02	266.44 ± 27.84
1-i-1500C		9.54 ± 0.03	0.0593 ± 0.0004	29.70 ± 0.47	94.30 ± 1.97	0.50 ± 0.01	93.80 ± 1.97	11.14 ± 0.20	0.07 ± 0.15	1.15 ± 2.25	0.17 ± 0.06	0.99 ± 2.25
total	2.7 ± 2.7			50.99 ± 0.58	146.49 ± 2.32	0.63 ± 0.01	145.86 ± 2.32	14.11 ± 0.30	13.70 ± 1.30	267.64 ± 25.99	0.21 ± 0.08	267.42 ± 25.99
1-ii-600C		9.80 ± 0.04	0.0406 ± 0.0004	24.42 ± 0.35	28.93 ± 1.13	0.17 ± 0.00	28.76 ± 1.13	3.70 ± 0.05	54.89 ± 0.82	280.87 ± 5.50	0.06 ± 0.02	280.81 ± 5.50
1-ii-1500C		9.54 ± 0.03	0.0558 ± 0.0005	40.29 ± 0.57	113.11 ± 2.63	1.00 ± 0.01	112.11 ± 2.63	22.25 ± 0.24	0.42 ± 0.03	13.03 ± 0.94	0.34 ± 0.12	12.70 ± 0.95
total	2.7 ± 2.7			64.72 ± 0.67	142.04 ± 2.86	1.17 ± 0.01	140.88 ± 2.86	25.95 ± 0.24	8.18 ± 0.16	293.90 ± 6.46	0.40 ± 0.14	293.51 ± 6.47
1-iii-600C		9.79 ± 0.02	0.0405 ± 0.0004	22.35 ± 0.36	26.31 ± 0.97	0.19 ± 0.00	26.12 ± 0.97	4.27 ± 0.05	46.89 ± 0.96	277.09 ± 6.63	0.07 ± 0.02	277.02 ± 6.63
1-iii-1500C		9.50 ± 0.02	0.0580 ± 0.0004	38.54 ± 0.63	117.61 ± 2.50	2.30 ± 0.03	115.31 ± 2.50	51.15 ± 0.56	0.31 ± 0.02	21.66 ± 1.34	0.78 ± 0.28	20.88 ± 1.37
total	2.7 ± 2.7			60.88 ± 0.72	143.92 ± 2.68	2.49 ± 0.03	141.43 ± 2.68	55.42 ± 0.56	3.89 ± 0.09	298.75 ± 7.80	0.84 ± 0.31	297.91 ± 7.81
2c-i-600C		9.75 ± 0.02	0.0435 ± 0.0005	12.00 ± 0.20	17.84 ± 0.66	0.16 ± 0.01	17.68 ± 0.66	3.55 ± 0.12	50.14 ± 1.32	246.45 ± 10.36	0.05 ± 0.02	246.40 ± 10.36
2c-i-1500C		9.43 ± 0.03	0.0712 ± 0.0005	19.74 ± 0.33	88.37 ± 1.86	0.36 ± 0.01	88.01 ± 1.86	8.06 ± 0.26	0.82 ± 0.07	9.16 ± 0.79	0.12 ± 0.04	9.04 ± 0.80
total	48.8 ± 3.4			31.74 ± 0.39	106.21 ± 1.97	0.52 ± 0.01	105.69 ± 1.97	11.61 ± 0.29	15.91 ± 0.63	255.61 ± 11.99	0.18 ± 0.06	255.43 ± 11.99
2c-ii-600C		9.81 ± 0.04	0.0421 ± 0.0005	15.46 ± 0.18	20.62 ± 0.78	0.18 ± 0.00	20.44 ± 0.78	4.06 ± 0.04	46.45 ± 1.05	261.06 ± 6.54	0.06 ± 0.02	260.99 ± 6.54
2c-ii-1500C		9.48 ± 0.03	0.0635 ± 0.0007	23.91 ± 0.28	87.11 ± 1.94	1.04 ± 0.01	86.08 ± 1.94	23.02 ± 0.23	0.27 ± 0.03	8.68 ± 0.83	0.35 ± 0.13	8.33 ± 0.84
total	48.8 ± 3.4			39.37 ± 0.33	107.74 ± 2.09	1.22 ± 0.01	106.52 ± 2.09	27.08 ± 0.24	7.20 ± 0.18	269.74 ± 7.19	0.41 ± 0.15	269.32 ± 7.19
4-600C		9.87 ± 0.04	0.0371 ± 0.0004	23.12 ± 0.26	19.02 ± 0.96	0.63 ± 0.01	18.39 ± 0.96	14.06 ± 0.28	9.89 ± 0.35	192.39 ± 7.78	0.21 ± 0.08	192.17 ± 7.78
4-1500C		9.67 ± 0.03	0.0498 ± 0.0005	36.11 ± 0.40	77.70 ± 1.99	6.05 ± 0.16	71.65 ± 1.99	134.34 ± 3.63	0.03 ± 0.01	6.10 ± 1.20	2.05 ± 0.75	4.06 ± 1.42
4-1550C								8.09 ± 0.15				
4-1600C								1.56 ± 0.04				
total	89.5 ± 4.7			59.22 ± 0.47	96.72 ± 2.20	6.68 ± 0.16	90.04 ± 2.21	158.05 ± 3.65	0.90 ± 0.06	196.51 ± 13.80	2.41 ± 0.88	194.10 ± 13.83
6-i-600C		9.82 ± 0.05	0.0395 ± 0.0003	8.93 ± 0.10	9.54 ± 0.29	0.52 ± 0.01	9.02 ± 0.29	11.67 ± 0.17	8.92 ± 0.16	144.05 ± 3.26	0.18 ± 0.06	143.87 ± 3.26
6-i-1500C		9.49 ± 0.03	0.0568 ± 0.0019	22.40 ± 0.24	65.50 ± 4.64	1.50 ± 0.02	64.01 ± 4.64	33.24 ± 0.48	0.44 ± 0.03	20.25 ± 1.32	0.51 ± 0.18	19.74 ± 1.34
total	141.4 ± 3.4			31.33 ± 0.26	75.05 ± 4.65	2.02 ± 0.02	73.03 ± 4.65	44.91 ± 0.51	2.64 ± 0.06	164.29 ± 3.96	0.68 ± 0.25	163.61 ± 3.97

Chapter 6- Depth dependence of cosmogenic ^3He and ^{21}Ne

TABLE 3 continued

Sample Name	depth (g/cm ²)	$^{20}\text{Ne}/^{22}\text{Ne}$	$^{21}\text{Ne}/^{22}\text{Ne}$	^{20}Ne 10 ⁹ at/g	$^{21}\text{Ne}_{\text{total}}$ Mat/g	$^{21}\text{Ne}_n$ Mat/g	$^{21}\text{Ne}_c$ Mat/g	4He 10 ¹² at/g	$^3\text{He}/^4\text{He}/\text{Ra}$	$^3\text{He}_{\text{total}}$ Mat/g	$^3\text{He}_r$ Mat/g	$^3\text{He}_c$ Mat/g
6-ii-600C		9.91 ± 0.05	0.0399 ± 0.0006	13.34 ± 0.17	14.68 ± 0.81	0.27 ± 0.00	14.41 ± 0.81	6.03 ± 0.07	20.02 ± 0.42	167.16 ± 4.03	0.09 ± 0.03	167.07 ± 4.03
6-ii-1500C		9.64 ± 0.02	0.0551 ± 0.0008	17.96 ± 0.22	48.62 ± 1.61	2.17 ± 0.02	46.45 ± 1.61	48.14 ± 0.50	0.08 ± 0.01	5.06 ± 0.75	0.73 ± 0.27	4.33 ± 0.79
total	141.4 ± 3.4			31.29 ± 0.28	63.30 ± 1.80	2.44 ± 0.02	60.86 ± 1.80	54.17 ± 0.50	2.30 ± 0.06	172.22 ± 4.57	0.82 ± 0.30	171.40 ± 4.58
8-i-600C		9.95 ± 0.04	0.0336 ± 0.0005	10.50 ± 0.11	4.90 ± 0.48	0.23 ± 0.01	4.67 ± 0.48	5.06 ± 0.13	14.24 ± 0.45	99.78 ± 4.07	0.08 ± 0.03	99.70 ± 4.07
8-i-1500C		9.69 ± 0.03	0.0503 ± 0.0003	20.79 ± 0.23	45.63 ± 0.86	0.56 ± 0.01	45.07 ± 0.86	12.48 ± 0.32	0.75 ± 0.03	13.01 ± 0.68	0.19 ± 0.07	12.82 ± 0.68
total	184.3 ± 2.9			31.29 ± 0.25	50.53 ± 0.98	0.79 ± 0.02	49.74 ± 0.98	17.54 ± 0.35	4.65 ± 0.17	112.79 ± 4.61	0.27 ± 0.10	112.52 ± 4.61
8-ii-600C		9.89 ± 0.04	0.0381 ± 0.0004	10.46 ± 0.11	9.57 ± 0.40	0.26 ± 0.00	9.31 ± 0.40	5.81 ± 0.07	12.48 ± 0.36	100.42 ± 3.08	0.09 ± 0.03	100.34 ± 3.08
8-ii-1500C		9.69 ± 0.02	0.0457 ± 0.0005	20.50 ± 0.22	35.29 ± 1.06	0.66 ± 0.01	34.63 ± 1.06	14.69 ± 0.15	0.15 ± 0.03	3.09 ± 0.58	0.22 ± 0.08	2.87 ± 0.58
total	184.3 ± 2.9			30.96 ± 0.25	44.86 ± 1.13	0.92 ± 0.01	43.94 ± 1.13	20.51 ± 0.17	3.65 ± 0.11	103.52 ± 3.23	0.31 ± 0.11	103.20 ± 3.23
10-600C		9.85 ± 0.02	0.0385 ± 0.0002	18.83 ± 0.94	18.22 ± 1.00	0.30 ± 0.01	17.93 ± 1.00	6.57 ± 0.19	9.74 ± 0.85	88.56 ± 8.18	0.10 ± 0.04	88.46 ± 8.18
10-900C		9.86 ± 0.05	0.0384 ± 0.0004	12.88 ± 0.65	12.32 ± 0.81	0.19 ± 0.01	12.13 ± 0.81	4.32 ± 0.15	0.42 ± 0.44	2.51 ± 2.65	0.07 ± 0.02	2.45 ± 2.65
10-1500C		9.79 ± 0.07	0.0408 ± 0.0009	3.16 ± 0.16	3.79 ± 0.34	0.05 ± 0.01	3.75 ± 0.34	1.04 ± 0.14	1.61 ± 1.49	2.32 ± 2.17	0.02 ± 0.01	2.31 ± 2.17
total	244.6 ± 4.3			34.87 ± 1.15	34.33 ± 1.34	0.54 ± 0.01	33.80 ± 1.34	11.93 ± 0.28	5.66 ± 0.46	93.40 ± 7.92	0.18 ± 0.07	93.22 ± 7.92

Note: Errors given as 1sigma machine counting statistics error or propagated error.

TABLE 4. Summarized attenuation length, age, erosion rate and other core data

attenuation	Arena Valley (KBA89-77)		Mt. Fleming (BAK90-79)	
	g/cm ²		g/cm ²	
^{26}Al	153 ± 13	MSWD = 0.8442	152 ± 8	MSWD = 0.2551
^{10}Be	145 ± 6	MSWD = 1.5603	147 ± 5	MSWD = 1.0473
^3He	196 ± 5	MSWD = 9.5834	144 ± 7	MSWD = 2.6464
^{21}Ne	166 ± 3	MSWD = 3.6145	140 ± 5	MSWD = 0.3209
age and erosion	age Ma	erosion rate mm/Ma	age Ma	erosion rate mm/Ma
^{26}Al	1.40 ± 0.23	222 ± 67	1.01 ± 0.12	419 ± 81
^{10}Be	1.19 ± 0.10	413 ± 54	1.25 ± 0.11	425 ± 58
^3He	0.71 ± 0.02	921 ± 68	1.01 ± 0.04	714 ± 56
^{21}Ne	1.51 ± 0.42	435 ± 126	2.08 ± 0.58	345 ± 100
Best estimate	1.65 ± 0.60*	222 ± 67 [†]	2.08 ± 0.58 [‡]	422 ± 69 [°]
$^3\text{He}/^{21}\text{Ne}$	2.06 ± .06		2.96 ± .17	
grain size	0.5-0.71 mm		0.71-1.0 mm	
density	2.28 g/cm ²		2.09 g/cm ²	
location	161°50' E	77°49' S	160°11' E	77°33' S

Note: all errors are 1 σ propagated uncertainty

* ^{10}Be age using best erosion rate estimate.

[†] Steady state erosion rate using Al data. Al may be in saturation, but Be and Ne are not.

[‡] ^{21}Ne age using best erosion rate estimate. Al and Be are saturated and Ne may be as well, so this is a minimum estimate.

[°] Mean of Al, Be steady state erosion rate determination.

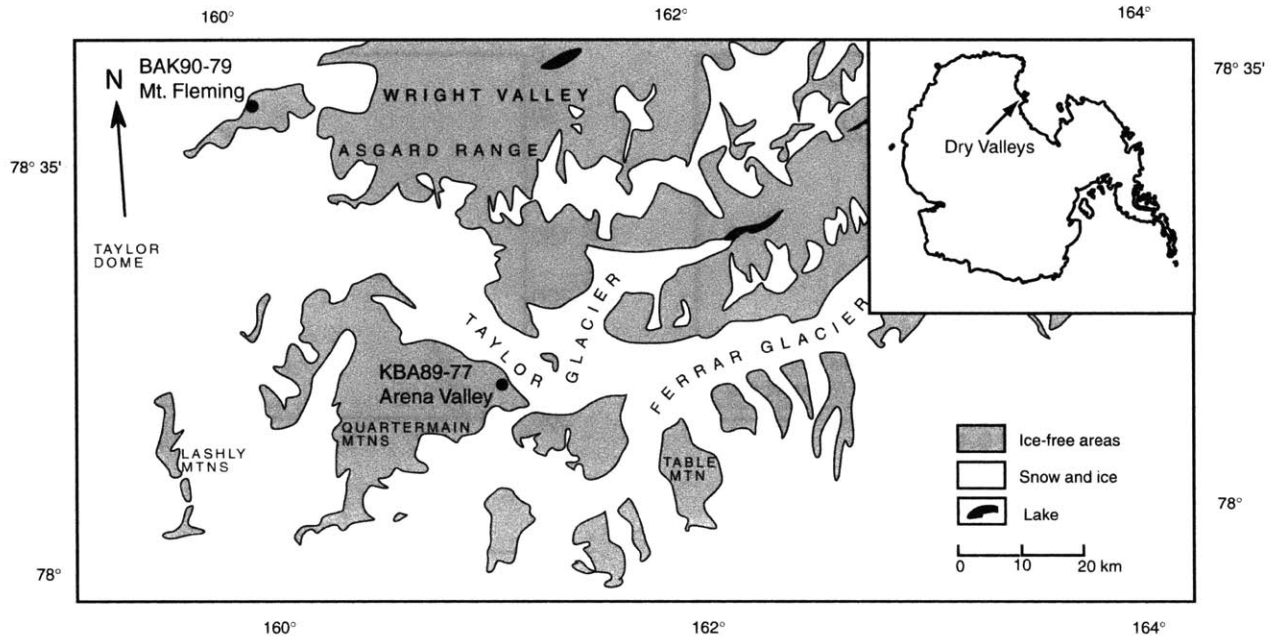


Figure 1. Map of the Dry Valleys in the Transantarctic Mountains shows locations of two cores drilled in sandstone (EB, RA and MK) in 1989 and 1990. KBA89-77 was collected at 1700 m altitude on a plateau above Arena Valley. BAK90-79 was collected at 2065 m altitude from near the summit of Mt. Fleming. Inset shows approximate location in Antarctica of the Dry Valleys.

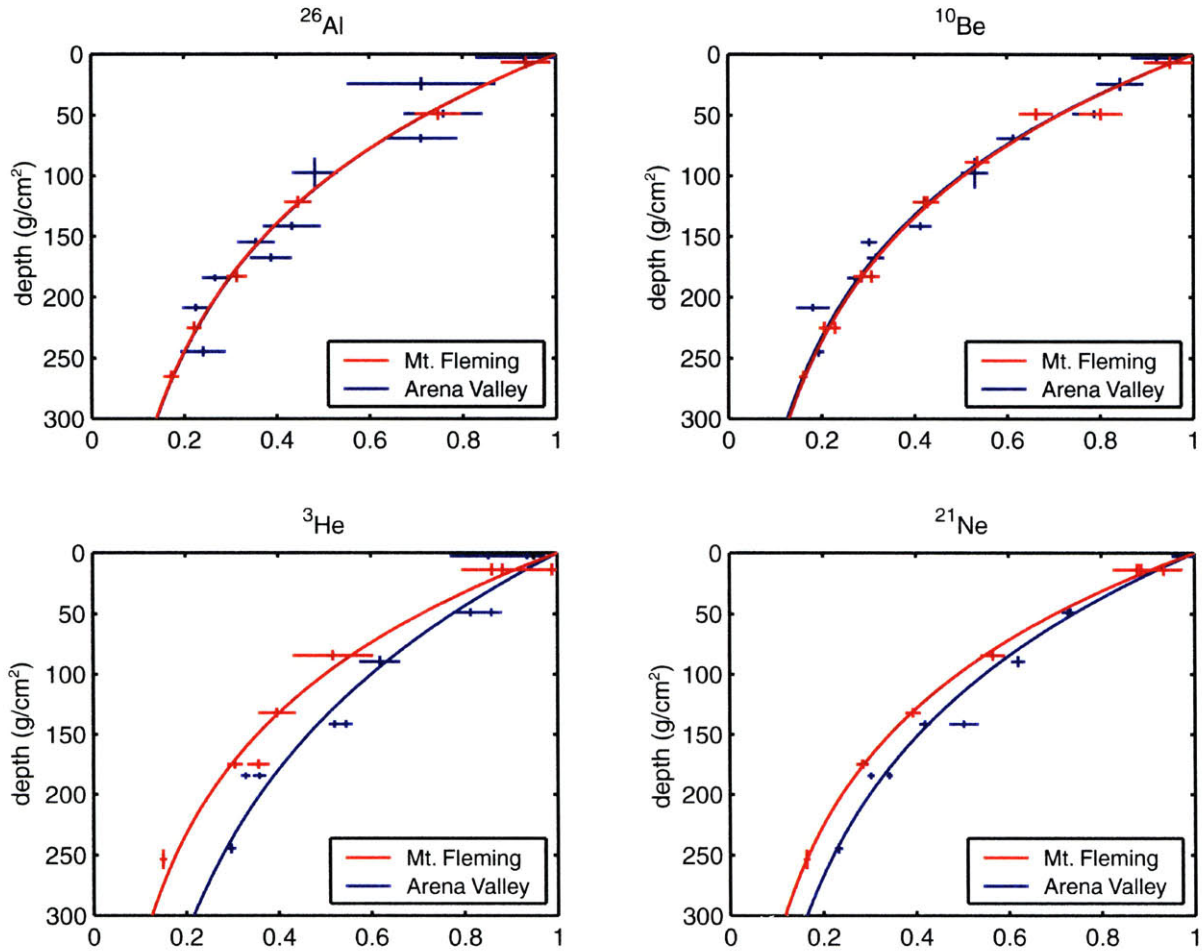


Figure 2. Depth profiles for Arena Valley (KBA89-77) and Mt. Fleming (BAK90-79). Profiles for each cosmogenic isotope are plotted individually with Arena Valley in blue and Mt. Fleming in red. Data points are plotted at 1 sigma uncertainty. Exponential depth profiles are fitted with a York linear regression (York 1969). Attenuation lengths and values of MSWD are in listed in Table 3. Note that for ^{26}Al and ^{10}Be depth profiles are nearly identical, but for ^{21}Ne and ^3He attenuation lengths are significantly longer for the Arena Valley Core

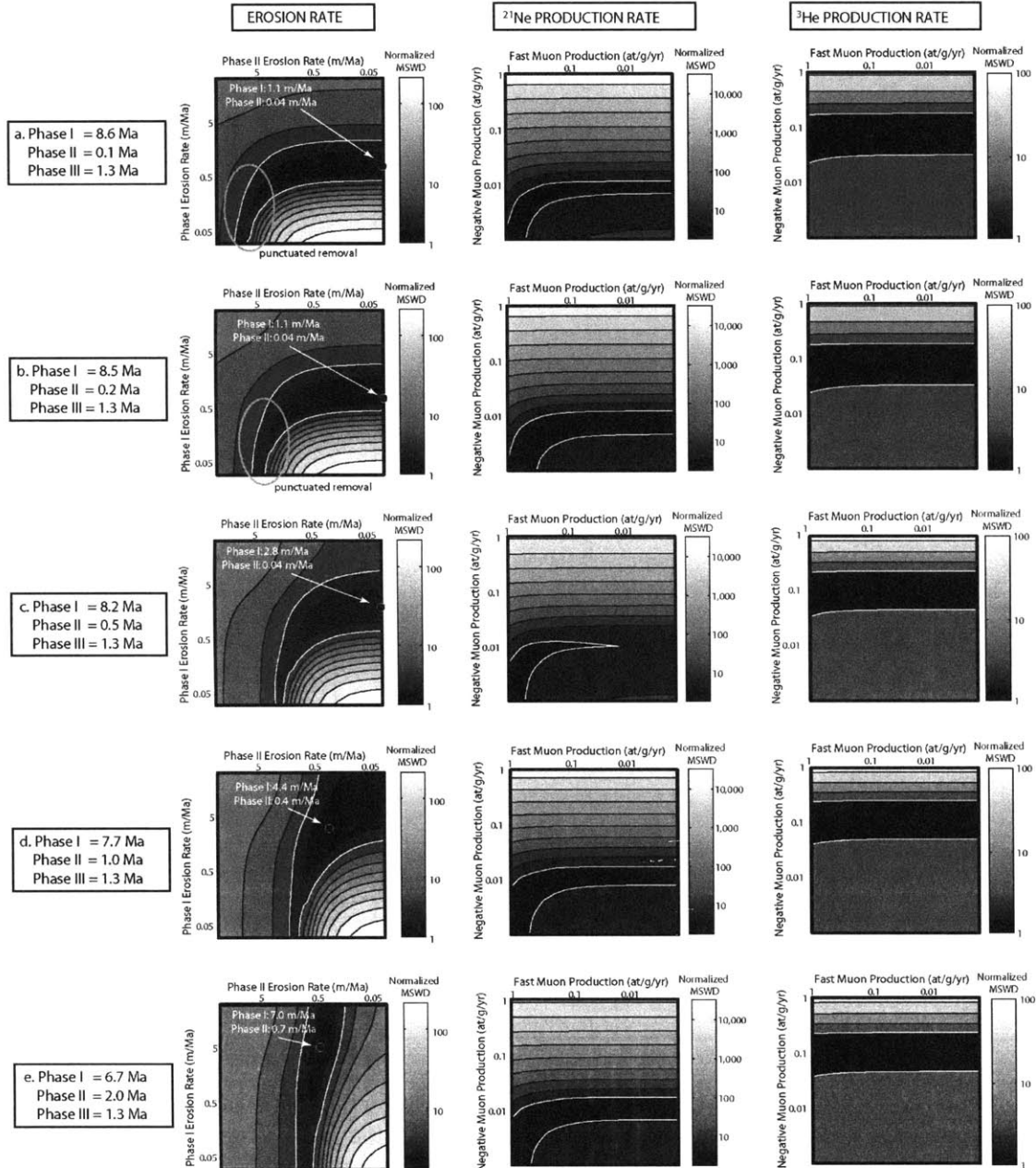
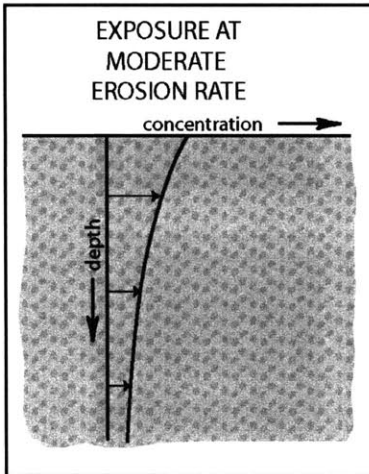


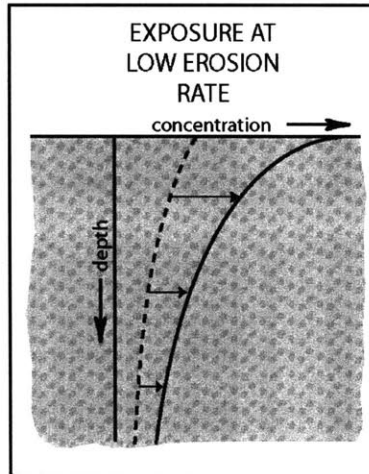
Figure 3. Column 1: Contoured, normalized MSWD values for combinations of Phase I and Phase II erosion rates for muon production values of $P_{-m}^{21}\text{Ne} = 0.001$, $P_{im}^{21}\text{Ne} = 1$, $P_{-m}^{3\text{He}} = 0.16$ and $P_{im}^{3\text{He}} = 0.001$ at/g/yr at SLHL. Normalized MSWD values were calculated for Al, of Al, Be, normalized Be, Ne, normalized Ne and averaged. Erosion histories which fall within the lowest contour, marked in white, have a normalized MSWD value less than 2, and provide acceptable fits to the measured data. Best solutions are labeled and marked with a circle. Normalized MSWD values are unacceptably high for low phase I and phase II erosion rates in all scenarios. Best model fits are obtained for erosion rates ~ 5 times higher prior to 1.3 Ma (~ 1 m/Ma) but good results are also obtained for the case of punctuated removal (see a and b). Columns 2 and 3: Contoured, normalized MSWD values for combinations of negative muon and fast muon production for ^{21}Ne and ^3He for the five best fit scenarios identified in column 1. Normalized MSWD values were calculated for normalized He and averaged for normalized Ne. Negative muon production (P_{-m}) is strongly selected for both ^{21}Ne and ^3He , but fast muon production (P_{im}) has little impact on evolution of the profile, and so the value is not well constrained by this study. We obtain best fits for $P_{-m}^{21}\text{Ne} = 0.001$ at/g/yr (must be less than ~ 0.01 at/g/yr) and for $P_{-m}^{3\text{He}} = 0.16$ at/g/yr (must be in the range ~ 0.2 to 0.07 at/g/yr) at SLHL.

CASE 1

Phase I and II: 10 to 1.3 Ma

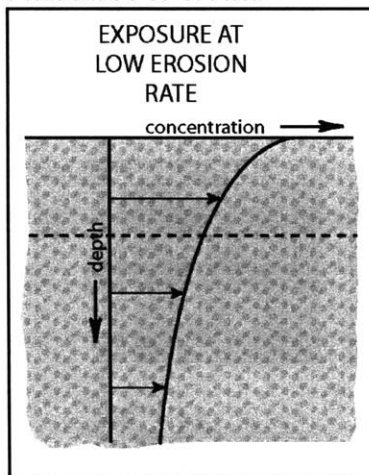


Phase III: 1.3 to 0 Ma

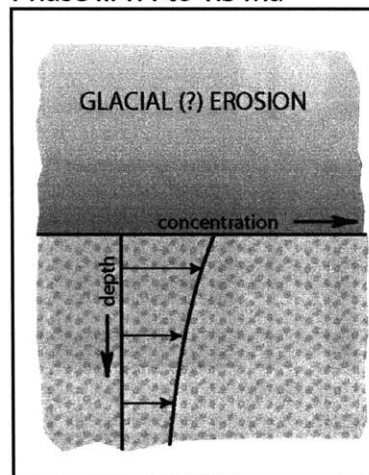


CASE 2

Phase I: 10 to 1.4 Ma



Phase II: 1.4 to 1.3 Ma



Phase III: 1.3 to 0 Ma

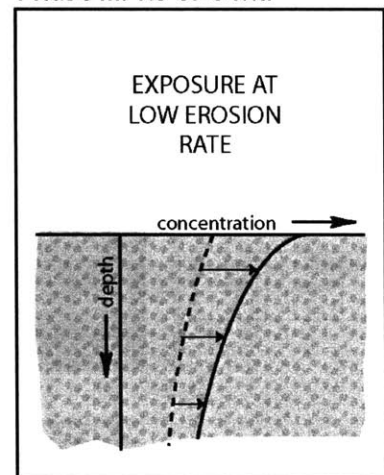


Figure 4. Model erosion histories. Modeling suggests two possible erosion histories. In the first, a long period of moderate erosion produces long attenuation length. In the final phase, erosion rate decreases by ~ 5 times. Concentration increases and attenuation length decreases, but the long signal is retained. In the second case, low erosion rates are punctuated by rapid removal of ~ 1 m surface material. Long attenuation lengths result from bringing long attenuation length material from depth to close to the surface. During final exposure (phase III), attenuation length decreases as concentration increases, but the long attenuation length signal is retained.

Conclusion

Tectonic synthesis

In addition to developing techniques of quantitative landscape analysis, this thesis is concerned with understanding the Cenozoic tectonic and landscape evolution of the Red River region in the context of unanswered questions about the role of major strike-slip shear zones in accommodating the India-Asia collision, the growth of the southeast margin of the Tibetan plateau, and, ultimately, the nature of deformation of continental crust. From this body of work, the following Cenozoic history for the Red River region emerges.

Shearing along the Ailao Shan shear zone began ~34 Ma, recorded by monazite inclusions in synkinematic garnet (Gilley et al., 2003). The earliest indication of deformation to the northeast of the Ailao Shan shear zone in the geologic record is the left-lateral displacement and minor exhumation of Yangtze platform rocks. Lacustrine rocks were subsequently deposited on these exhumed slivers, probably in pull-apart or sag basins along the expression of the shear zone at the surface. This deformation likely occurred in Early Oligocene time. $^{40}\text{Ar}/^{39}\text{Ar}$ thermochronologic results indicate rapid exhumation from before ~25 to at least 17 Ma (Harrison et al., 1996), a period which corresponds to the deposition of fluvial sediments in a narrow basin adjacent to the northeast margin of the shear zone. The oldest strata within this basin record the erosion and subsequent deposition of Yangtze platform rocks originally capping the shear zone gneiss, and later strata record the arrival of the shear zone gneiss at the Earth's surface. Displacement along the northeast margin of the shear zone is limited to ~190 km after the deposition of the later strata, which are probably of Early Miocene age. These sediments underwent shortening during deposition, consistent with a relationship between exhumation of the shear zone and coeval shortening in the Lanping-Simao fold and thrust belt to the southwest of the Ailao Shan, indicating a regionally transpressive setting. The paleo Red River was also established during rapid exhumation of the shear zone and may have played a role in shaping the temporal and spatial patterns of exhumation.

After cessation of tectonic exhumation of the Ailao Shan shear zone, the Red River region was erosionally reduced to low-relief, probably less than a few hundred meters elevation. As the southeastern margin of the Tibetan plateau grew, the major rivers of the plateau, including the

Red River, began to incise, isolating the low-relief “relict” landscape from “modern” base level conditions. River incision and surface uplift began 5-13 Ma near Tibet (Kirby et al., 2002; Clark, 2003) but did not begin in the Red River region until Pliocene time (<5.3 Ma), suggesting progressive southeastward growth of the plateau margin. Pulsed river incision likely reflects climate variation against a backdrop of relatively steady plateau growth. Incision rates are declining toward the present, confirmed by cosmogenic incision rate data.

The Red River fault appears to have been active before river incision and therefore probably before the onset of surface uplift in the Red River region; geologic data tentatively record at least 16 km pre-Pliocene right-lateral displacement. Since that time, geomorphic data record a displacement of ~25 km, yielding a minimum Pliocene and Quaternary slip-rate of ~5 mm/a, although slip-rates appear to be lower at present (Allen et al., 1984; Weldon et al., 1994; Rangin et al., 1995; Duong and Feigl, 1999). The Red River fault is deflected but not cut by the Xianshuihe-Xiaojiang fault system, which accommodates rotation of crustal fragments around the eastern Himalayan syntaxis. The distributed nature of the Xianshuihe-Xiaojiang fault system at the intersection with the Red River fault is probably what allows the transfer of displacement across the strong crustal anisotropy formed by the Red River fault and the Ailao Shan shear zone without obvious through-going structures. The Xianshuihe-Xiaojiang fault system and the Dali fault system probably initiated in early Pliocene time, synchronous with surface uplift. This suggests a kinematic link between plateau growth and the initiation of a new system of surface faults, possibly through the development of a detachment zone in the mid to lower crust.

Implications

How do the results of this thesis relate to questions about the role of strike-slip faulting and plateau growth in accommodating the India-Eurasia collision? The Ailao Shan shear zone was clearly an important structure during mid-Cenozoic time and there is little doubt that it accommodated at least a few hundred kilometers of displacement. However, exhumation of the shear zone is linked to regional transpression, particularly within the Lanping-Simaofold and thrust belt, and a number of faults to the northeast of the shear zone also show evidence for mid-Cenozoic left-lateral displacement. Deformation was thus not confined exclusively to the Ailao Shan shear zone but was expressed throughout the southeast margin of the plateau. Although the

Chapter 7- Conclusion

structure of the crust is probably very different today than when the Ailao Shan shear zone was active, the active faults of the southeastern plateau region also suggest distributed deformation. Material currently does not appear to be extruding along the Red River fault, but rather is rotating around the eastern Himalayan syntaxis, internally deforming and extending. Although the Ailao Shan shear zone and Red River fault define important crustal anisotropies, both are passively rotated by displacement along the Xianshuihe-Xiaojiang fault system. Further, observations outlined in this thesis are consistent with growth of the southeastern margin of the Tibetan plateau through the influx of weak mid to lower crust from beneath Tibet, and additionally provide evidence for southeastward progression of uplift through time. Growth of the plateau margin clearly has had profound effects on the structural and geomorphic evolution of the Red River region.

From this study, and from the innumerable studies referenced herein, the picture emerges of a dynamically deforming region, influenced by pre-existing crustal anisotropies, evolving with time both as a result of the intrusion of weak lower crust, and of the migration of the eastern Himalayan syntaxis from a position southwest to a position northwest of the region. Continental deformation cannot be treated in a simplistic way, as either the lateral translation of rigid blocks, or as a continuum. Field studies such as this are important for building more realistic and comprehensive models for deformation associated with the India-Eurasia collision.

Future work

As with most scientific inquiry, this thesis raises as many questions as it answers. One outstanding issue is the evolution of the region in late Miocene time, when geomorphic geologic and geochronologic records are vague. $^{40}\text{Ar}/^{39}\text{Ar}$ feldspar model data indicate rapid cooling of the Ailao Shan shear zone through $\sim 200^\circ\text{C}$ by 17 Ma (Harrison et al., 1996). The low-relief landscape must have been established after this time, but before the onset of river incision in Pliocene time or later, probably indicating a period of relative tectonic quiescence. However, limited apatite and zircon fission-track data apparently record rapid exhumation in the interval 10-13 Ma (Bergman et al., 1997; Leloup et al., 2001). Additionally, the Red River fault was active prior to Pliocene time, responsible for a minimum of 16 km displacement. What caused these thermal and structural events? How do these events relate to the regional landscape and

Chapter 7- Conclusion

tectonic development? A combination of additional apatite and zircon fission-track and (U-Th)/He thermochronology could help answer these questions by establishing the low temperature cooling history of the Ailao Shan shear zone, defining a minimum age for the “relict” landscape, and placing existing fission-track data in context.

Field relationships northwest and southeast of the areas mapped for this thesis also bear further study. The relationship between extension in the Dali region and right-lateral displacement on the Red River fault remains unclear, but could probably be resolved through more detailed field mapping and additional thermochronology. The low-relief upland landscape is preserved on many of the faulted blocks of the Dali region, and could be used to reconstruct the pre-extension landscape. Near the Vietnamese border, the relationship between the Ailao Shan shear zone and Day Nui Con Voi is also unclear, although detailed mapping is impeded by poor exposure and poor access (and big snakes). The northern termination of the Day Nui Con Voi is particularly interesting, as Chinese maps (Bureau of Geology, Yunnan, 1990) indicate Triassic sediments in depositional contact with shear zone gneiss. This contact may be accessible by road at certain times of the year. Mapping along the Red River southwest of Nansa would also be useful to establish the southwestward extent of Ailao Shan clasts within the Cenozoic strata; this could provide additional constraints on the amount of left-lateral displacement that post-dates deposition of these sediments.

Data presented in this thesis indicate the progressive southeastward propagation of the southeastern margin of the Tibetan plateau. This observation, coupled with topographic data and river incision data elsewhere on the southeast plateau margin, can be used to place important constraints on the pattern of plateau growth and the flux-rate of possible lower crustal material extruding from beneath Tibet into the southeast margin region.

Finally, as demonstrated in chapter 6 of this thesis, cosmogenic dating is a valuable tool for constraining erosion history, but could be improved through better knowledge of production rates and attenuation lengths for both neutron and muon related nuclide production. Also, the results which indicate higher erosion rates at the sampling site in the Dry Valleys region prior to 1.3 Ma have important implications for erosion processes in extreme environments, for regional

climate change and for the glacial history of the Transantarctic mountains and West Antarctic ice sheet. Similar studies for other bedrock surfaces in the Dry Valleys region could help resolve these issues.

Concluding remarks

This thesis is wide ranging, incorporating results from field mapping, satellite image interpretation, DEM analysis, river longitudinal profile analysis, sedimentology, paleobotany and cosmogenic dating, and exploring problems from the exhumation of mid-crustal rocks to the evolution of fluvial systems to erosion in Antarctica. It is unified by the goal of understanding the tectonic and landscape evolution of the Red River region, by questions of fundamental crustal dynamics, and by a growing awareness of the insight gained into tectonic processes through landscape analysis.

References

- Allen, C.R., Gillespie, A.R., Han Yuan, Sieh, K.E., Zhang Buchun, Zhu Chengnan, 1984, Red River and associated faults, Yunnan Province, China: Quaternary geology, slip rates, and seismic hazard: Geological Society of America Bulletin, v. 95, p. 686-700.
- Bergman, S.C., Leloup, P.H., Tapponnier, P., Schärer, U., and O'Sullivan, P., 1997, Apatite fission track thermal history of the Ailao Shan-Red River shear zone, China: paper presented at meeting, European Union of Geoscience, Strasbourg, France
- Bureau of Geology and Mineral Resources of Yunnan Province, 1990, in Regional Geology of Yunnan Province, Beijing, Geological Publishing House, 728 p.
- Clark, M.K., 2003, Late Cenozoic Uplift of Southeastern Tibet [PhD Thesis]: Massachusetts Institute of Technology, 226 p.
- Duong, C.C., and Feigl, K.L., 1999, Geodetic measurement of horizontal strain across the Red River fault near Tha Ba, Vietnam, 1963-1994: Journal of Geodesy, v. 73, p. 298-310.
- Gilley, L.D., Harrison, T.M., Leloup, P.H., Ryerson, F.J., Lovera, O.M., Wang J-H, 2003, Direct dating of left-lateral deformation along the Red River shear zone, China and Vietnam: Journal of Geophysical Research, v. 103, No. B2, 10.1029/2001JB001726.
- Harrison, T.M., Leloup, P.H., Ryerson, F.J., Tapponnier, P., Lacassin, R., and Chen Wenji, 1996, Diachronous initiation of transtension along the Ailao Shan-Red River shear zone, Yunnan and Vietnam, *in* Yin, A., and Harrison, T.M., eds., The Tectonic Evolution of Asia, Cambridge University Press, New York, p. 208-226.
- Leloup, P.H., Arnaud, N., Lacassin, R., Kienast, J.R., Harrison, T.M., Phan Trong, T.T., Replumaz, A., and Tapponnier, P., 2001, New constraints on the structure, thermochronology, and timing of the Ailao Shan-Red River shear zone, SE Asia: Journal of Geophysical Research, B, v. 106, p. 6683-6732.
- Rangin, C., Klein, M., Roques, D., Le Pichon, X., and Trong, L.V., 1995, The Red River fault system in the Tonkin Gulf, Vietnam: Tectonophysics, v. 243, p. 209-222.
- Weldon, R., Sieh, K., Zhu, C., Han, Y., Yang, J., and Robinson, S., 1994, Slip rate and recurrence interval of earthquake on the Hong He (Red River) Fault, Yunnan, P.R.C.: International Workshop on Seismotectonics and Seismic hazard in SE Asia, p. 244-248.